# Uncertainties in modelling the Antarctic ice sheet during the warm Pliocene and 21st century

O'Neill, Jamie

*Awarding institution:*
King's College London

# Uncertainties in modelling the Antarctic ice sheet during the warm Pliocene and 21$^{st}$ century


**James O'Neill**

Supervisor: Dr Tamsin Edwards
Dr. Lauren Gregoire

The Department of Geography
King's College London

This dissertation is submitted for the degree of
*Doctor of Philosophy*

March 2023

# Acknowledgements

First, I want to thank my supervisors Tamsin Edwards and Lauren Gregoire. I have been incredibly lucky to have such supportive supervisors, who have been so generous in sharing their time and expertise. I cannot thank them enough for all the help they have given me. I would also like to thank Aisling Dolan and Tina van de Flierdt for their help with the Pliocene aspects of this PhD. I would like to thank Sam Kachuck, Dan Martin, Steph Cornford, Niall Gandy and Andreas Wernecke who have provided invaluable guidance and advice. Thanks also to Richard Rigby for his help with technical aspects of this project. I would like to extend my gratitude to Ilan Kelman, for his support and enthusiasm at the start of the project. I also want to thank Bridget Wade, whose supervision and encouragement with my MSci thesis gave me the confidence to apply for a PhD.

I want to thank the London NERC DTP for funding this PhD, and for giving me the opportunity to make some great friends. Will and James, thank you for your friendship, it's one of the things I cherish most from this PhD. Thanks also to Mike and Renee, and everyone at King's for making my time there a good one.

I'm incredibly grateful to have such a loving family, to who I owe everything. So Mum, Dad, Sam and Hannah, thank you. Finally, thank you Katy for being patient and endlessly supportive, it means the world to me.

# Abstract

Antarctica is one of the largest potential sources of sea level rise under a warming climate. Ice sheet response to warming is governed by internal ice sheet dynamics, complex feedbacks with atmosphere and ocean processes and the bedrock on which it sits. The impact of these processes on ice sheet evolution is challenging to characterise and timescale-dependent. These challenges are a source of uncertainty in projections of ice sheet evolution under anthropogenic climate change, and reconstructions of ice sheet dynamics under past warm climates. This thesis will explore uncertainties in modelling the Antarctic ice sheet (AIS) under $21^{st}$ century warming and a period of past climate change: the warm Pliocene, using the BISICLES ice sheet model.

First, projections of AIS sea level contribution by 2100 are presented, under low and very high emissions scenarios, using a range of climate and ice sheet modelling choices. These find a range of plausible sea level contributions (-53 mm to 125 mm AIS contribution to sea level), dependent on choice of climate forcing and sensitivity of the ice sheet to ocean warming. Next, developments in BISICLES for simulating the AIS in the warm Pliocene are presented. Aspects of the model setup, including Glacial Isostatic Adjustment and hydrology coupled basal sliding, needed for multi-millennial palaeo-ice sheet simulations are added and tested in a 30-member perturbed parameter ensemble of the Pine Island Glacier catchment, under Pliocene forcing. This ensemble highlights the importance of a basal friction coefficient in rate of retreat in the Pine Island Glacier. Following this, uncertainties in climate model forcing and modern initial condition uncertainty are explored for five climate models and two initial ice sheet and bedrock conditions in simulations of the full Antarctic ice sheet. A scoping study of the influence of surface mass balance parameters is also carried out, with a 9 member one-at-a-time sensitivity study. This shows the strong influence of precipitation lapse rate on sea level contribution under Pliocene climate. It also shows that perturbing surface mass balance parameters can have a comparable effect with choice of climate model, when surface mass balance parameters are not perturbed.

Finally, simulations of the AIS during the warm Pliocene are presented that use the modelling approach developed across the rest of the thesis. This section explores a range of climate and ice sheet modelling choices, and compares results to reconstructions of Pliocene ice sheet and sea level change. Uncertainty in model parameters and climate is explored in a 120-member perturbed parameter ensemble. Uncertainty in choice of model initial condition is explored in a 30-member ensemble. Parameter uncertainty under a modern climate is explored in a 30-member ensemble. This work shows a broad range of simulated Pliocene ice sheets driving an overall sea level fall (up to 15.89 m) to large sea level rise (up to 28.27 m), with strong sensitivity to a basal sliding parameter and the initial ice sheet state. It shows strong sensitivity of simulated sea level contribution to parameter perturbations in the control ensemble, compared with sea level contribution relative to a single control simulation. A subset of simulations are able to reproduce sea level change compatible with Pliocene reconstructions, and a smaller subset show a regional retreat in the Wilkes basin indicated in geological records of AIS margin in the Pliocene.

Across this thesis, we show the vulnerability of the West Antarctic ice sheet to ocean melt-driven mass loss under warm $21^{st}$ century and Pliocene forcing. However, we also find that warming-driven increases in accumulation in the interior can offset sea level fall, when sensitivity to ocean warming is low. Under some modelling scenarios, this can drive an overall sea level fall both over the $21^{st}$ century and with millennium-scale Pliocene warming.

# Table of contents

# List of figures

# List of tables

# List of Acronyms

**ARC** Advance Research Computing at the University of Leeds.

**ASB** Aurora Subglacial Basin.

**BISICLES** the Berkeley Ice Sheet Initiative for Climate at Extreme Scales ice sheet model.

**CCSM4** Community Climate System Model 4.

**CCSM4-UofT** University of Toronto version of CCSM4.

**CCSM4-Utr** Institute for Marine and Atmospheric Research Utrecht CCSM4.

**CMIP6** Coupled Model Intercomparison Project for the IPCC sixth assessment report.

**COSMOS** Alfred Wegener Institute COmmunity earth System MOdelS.

**d** day.

**ELRA** Elastic Lithosphere Relaxing Asthenosphere.

**FLIP** the Ferrar Large Igneous Province.

**GCM** General Circulation Model.

**GIA** Glacial-isostatic adjustment.

**GrIS** Greenland Ice Sheet.

**HadCM3** Met Office Hadley Centre Model.

**HPC** High Performance Computing.

**IRD** Iceberg Rafted Debris.

**ISMIP6** Ice Sheet Model.

**Ma** Million years ago.

**MIROC4m** Model for Interdisciplinary Research on Climate.

**mPWP** mid-Pliocene Warm Period.

**NERSC** National Energy Research Scientific Computing centre.

**PDD** Positive Degree Day model.

**PLISMIP** PLiocene Ice Sheet Model Intercomparison Project.

**PRISM** Pliocene Research, Interpretation and Synoptic Mapping project.

**SIA** Shallow Ice Approximation.

**SLC** Sea level Contribution.

**SLE** Sea Level Equivalent.

**SMB** Surface Mass Balance.

**SSA** Shallow Shelf Approximation.

**VAF** Ice sheet Volume Above Floatation.

**w.e.** fresh water equivalent.

**yr** year.

# Nomenclature

### Parameters

| | |
|---|---|
| $\gamma_0$ | Ice shelf basal melting coefficient (m $s^{-1}$) |
| $C$ | Weertman friction coefficient, *WeertC* |
| $LMV$ | Lower mantle viscosity (Pa s) |
| $LRP$ | Lapse rate precipitation - precipitation scaling with temperature |
| $LRT$ | Lapse rate temperature (°C $km^{-1}$) |
| $mTWD$ | Maximum till water depth (m) |
| $PDDi$ | Positive degree day factor for ice (mm w.e. $d^{-1}$ °C) |
| $PDDi$ | Positive degree day factor for snow (mm w.e. $d^{-1}$ °C) |
| $UMV$ | Upper mantle viscosity (Pa s) |

### Constants

| | | |
|---|---|---|
| $g$ | Acceleration due to gravity | $9.81\,\mathrm{m\,s^{-2}}$ |
| $\rho_i$ | Density of ice | $918\,\mathrm{kg\,m^{-3}}$ |
| $\rho_{sw}$ | Density of sea water | $1028\,\mathrm{kg\,m^{-3}}$ |
| $C_{pw}$ | Specific heat of sea water | $3974\,\mathrm{J\,kg\,K}$ |
| $L_f$ | Fusion latent heat of ice | $3.3 \times 10^5\,\mathrm{J\,kg}$ |

# Chapter 1

# Introduction and background

*Sections of this chapter are adapted from work submitted for the upgrade to PhD*

## 1.1 Climate change and sea level

Sea level change (SLC) poses one of the most significant challenges of anthropogenic climate change. With the population of the low elevation coastal zone - the hydrologically connected, coastal regions of the Earth less than 10 m elevation above sea level - predicted to surpass 1.4 billion by 2060 under highest growth scenarios (Neumann et al., 2015), population exposure to hazards associated with rising oceans is increasing. Rising sea levels act as a hazard multiplier for associated phenomena including storm surges, tsunamis and tidal flooding. Exposure of populations and infrastructure to SLC, in global terms, is highly regionalized - with Asia accounting for 73% of global population exposure in the year 2000 (Neumann et al., 2015), whilst in 2005 New York, New Orleans and Miami accounted for 31% of aggregate economic losses due to coastal flooding for the world's 136 largest coastal cities (Hallegatte et al., 2013).

SLC is also highly regionalised. Sea surface height can vary spatially due to ocean surface wind stress effects (McGregor et al., 2012) and changes to Earth's gravity field as ice melts and mass is redistributed (Woodward, 1886, Mitrovica et al., 2011). Several processes also affect local land surface elevation, such as post-glacial rebound, tectonism and subsidence due to groundwater or hydrocarbon abstraction (Schmidt, 2015), which can add to or counteract the ocean changes. This means that local sea level will not increase uniformly with global mean SLC.

Changes in local sea level are superimposed on changes in global mean sea level (GMSL), and to understand the former requires characterisation of the latter. GMSL rise is caused by thermal expansion, mass loss from mountain glaciers and the major ice sheets in Greenland and Antarctica, and groundwater storage changes. Between 1901 and 2018, thermal expansion and glacier loss accounted for 38% and 41% of GMSL rise respectively, whilst land water storage changes drove -7.8% of observed GMSL rise (Fox-Kemper et al., 2021). However, polar ice sheets are likely to become the largest component of GMSL rise under future warming. The IPCC Sixth Assessment Report (AR6) projects that the Greenland ice sheet will *likely* (66% probability) contribute 0.01-0.1 m to sea level by 2100 under a low emissions scenario (SSP1-2.6), and 0.09-0.18 m under a very high emissions scenario (SSP5-8.5) (Fox-Kemper et al., 2021). For the Antarctic ice sheet, the equivalent likely projected ranges are 0.03 to 0.27 m under the low emissions scenario and 0.03-0.34 m for the high emissions scenario (Fox-Kemper et al., 2021). Mountain glaciers are projected to contribute 0.07-0.11 m to sea level under SSP1-2.6, and 0.15-0.21 m under SSP5-8.5. Whilst thermal expansion has dominated sea level rise over the previous century, this is projected to contribute 0.11-0.18 m under SSP1-2.6 and 0.24-0.36 m under SSP5-8.5 (Fox-Kemper et al., 2021).

## 1.2 Antarctic contribution to sea level

### 1.2.1 Geographical setting

The Antarctic continent is covered over 98% of its surface by the Antarctic Ice Sheet. The Antarctic Ice Sheets mass accumulation is primarily derived from the 5.5 mm sea-level-equivalent precipitation (averaged over the ice sheet) it receives per year (Gardner et al., 2018), which has been increasing since the 19$^{th}$ century (Thomas et al., 2017). The Antarctic Ice Sheet can be characterised as a collection of drainage basins through which ice flows under gravity (Mouginot et al., 2019) with lowest ice flow velocities at ice divides (Gardner et al., 2018). Ice migrates from the interior ice fields of the continent in glaciers and ice streams. These can terminate as ice cliffs on land, terminate directly into the ocean as tidewater glaciers or feed into ice shelves (Bindschadler et al., 2011). Ice streams are regions where flow speed is orders of magnitude faster than in the surrounding ice sheet, bounded by basal topography or slower moving ice, and account for 90% of ice discharge from the Antarctic Ice Sheet (Bennett, 2003, Winsborrow et al., 2010). Where the ice sheet meets the surrounding ocean and becomes buoyant, it transitions into ice shelves. This transition from marine based ice sheet, in contact with bedrock, to floating ice shelves, is called the grounding line (GL) (Weertman, 1974, Schoof, 2007b). Ice shelves extend


Fig. 1.1 Antarctic reference map showing major geographical features of the continent. White regions are the ice sheet. Brown regions show open ground. Grey regions show ice shelves. Blue contours show ice sheet surface elevation at 500 m intervals. Map created to accompany the Landsat Image Mosaic of Antarctica (LIMA) (https://lima.usgs.gov).

seaward from 74% of Antarctica's coastline (Hogg and Gudmundsson, 2017), and whilst not directly contributing to SLC, play an integral role in regulating upstream glacier flow (Weertman, 1974, Rignot et al., 2013, Shepherd et al., 2010, Scambos et al., 2004).

The Antarctic Ice Sheet is composed of three distinct parts - the West Antarctic Ice Sheet and the East Antarctic Ice Sheet (referred to here as the WAIS and EAIS), and the Antarctic Peninsula ice sheet (PEN) adjoining the WAIS. Separated by the Transantarctic Mountains, the WAIS and EAIS have different glacial histories, physical characteristics and vulnerabilities to climate forcing.

The WAIS is 'marine based'- grounded largely below sea-level (maximum depth 2555 m.b.s.l) (Fretwell et al., 2013), west of the Transantarctic Mountains. The WAIS bed geometry has motivated much study as a region for future ice sheet mass loss, driven by ocean melting (Mercer, 1978), and a source of SLC. There is evidence that WAIS contribution to sea level rise is increasing (Favier et al., 2019, Gardner et al., 2018, The IMBIE Team, 2021), with 22% of its GL in retreat compared with 3% in the EAIS (Konrad et al., 2018). Constraining how and when the WAIS may retreat further has become a central question in studies of the Antarctic ice sheet (Hulbe, 2017), with the WAIS having the potential to raise eustatic sea levels by 3.3-4.3 m (Fretwell et al., 2013).

The EAIS has a volume of 53 m sea level equivalent (SLE) (Fretwell et al., 2013). Unlike the WAIS, the EAIS is grounded largely above sea level, with considerable variation in bedrock topography (Fretwell et al., 2013). The ice sheet has a mean surface elevation >2200 m, driving the continental interior's cold dry climate (Thomas et al., 2017). Whilst the majority of the EAIS is grounded above sea level, some large regions are not - and could therefore become vulnerable to ocean melting in response to climate forcing.

The PEN is a mountainous region extending northwards from WAIS into the southern ocean (Fig. 1.3). It has an average elevation of ~1500 m. Extending into lower latitudes than other regions of the Antarctic continental landmass, the Peninsula has been regarded as more vulnerable to warming climate. Whilst a warming trend is observed in Antarctic Peninsula air temperatures between 1979 and 1999 (0.32 °C / decade), this reversed between 1999 and 2014 (-0.47 °C / decade) (Turner et al., 2016) - reflecting natural climate variability for the region.

The Antarctic Ice Sheet lost 7.4 (5.0 - 9.8) mm SLE of ice between 1992 and 2020 (The IMBIE Team, 2021). The ice sheet loses mass through basal melting of ice shelves, accounting for 1516 ±106 Gt $yr^{-1}$ from 2005-2011, and iceberg calving, which accounted for 755 ±24 Gt $yr^{-1}$ across the same period (Liu et al., 2015). Factors governing iceberg calving are not fully constrained; however, glacier geometry, ice thinning, valley topog-

raphy and hence lateral shear stress all exert a control on mass loss from ice sheet outlet glaciers and ice shelves.

### 1.2.2 Marine Ice Sheet Instability (MISI)

One mechanism for deterioration of marine ice sheets over sub-millennial timescales, including the WAIS, is marine ice sheet instability (MISI) (Mercer, 1978)(Figure 1.2). Since the late 1970's, it has become increasingly accepted that the WAIS is vulnerable to collapse as a result of ocean warming (Mercer, 1978). The fundamental concept of MISI was first put forward by Weertman (1974), and expanded by Schoof (2007b). MISI occurs when ice sheets grounded on beds that deepen inland undergo an initial retreat, driven by ice shelf thinning or collapse. As the grounding line retreats and bed deepens, ice thickness increases. Grounding line thickness controls flux across it (Joughin and Alley, 2011), such that flux increases with ice thickness above the grounding line (Weertman, 1974, Schoof, 2007b). In over-deepened beds, this leads to further retreat in a self-sustaining feedback, until the bed slope reverses and the grounding line can re-stabilise. If the bed surface slopes inland over a prolonged distance, as is the case in much of the WAIS (Fretwell et al., 2013), with no ridges on which the grounding line can stabilise, sustained mass loss can result. A further component of MISI theory is unstable advance of grounding lines (Weertman, 1974, Schoof, 2007a, 2012). For ice grounded on reverse sloping bedrock, or where bed slope in the flow direction is too shallow, increased accumulation over the ice sheet may not be balanced by ice flux through the grounding line (Schoof, 2012). This can cause the grounding line to advance. If the bedrock slope in the advanced position cannot accommodate grounding line thickness, and therefore mass flux, sufficient to balance the increased accumulation, the grounding line may continue to advance until a stable bed topography and steady state is reached (Schoof, 2012).

Beyond its theoretical basis as described by Weertman and Schoof, there is support from numerical models for MISI (Pattyn et al., 2012, Durand et al., 2009), including for WAIS in the last interglacial (Clark et al., 2020) and for palaeo ice sheets in the northern hemisphere during other periods of warmth in the Quaternary (Gandy et al., 2018, Pico et al., 2019). Whilst MISI theory suggests that grounding lines re-stabilise only when the grounding line reaches upward sloping bedrock, other work has shown that grounding lines can stabilise on downward sloping bedrock if ice shelves provide buttressing (Cornford et al., 2020, Sergienko and Wingham, 2019). More generally, Sergienko (Sergienko, 2022) suggests that local feedbacks such as elevation-accumulation feedbacks or GIA can alter stability of the grounding line, such that stability cannot be assessed solely based on consideration of bedrock elevation. Observational evidence for MISI is inconclusive, with the IPCC

AR6 stating with *medium confidence* that: "the observed evolution of Amundsen Sea Embayment glaciers is compatible with, but not unequivocally indicating an ongoing MISI " (Fox-Kemper et al., 2021)

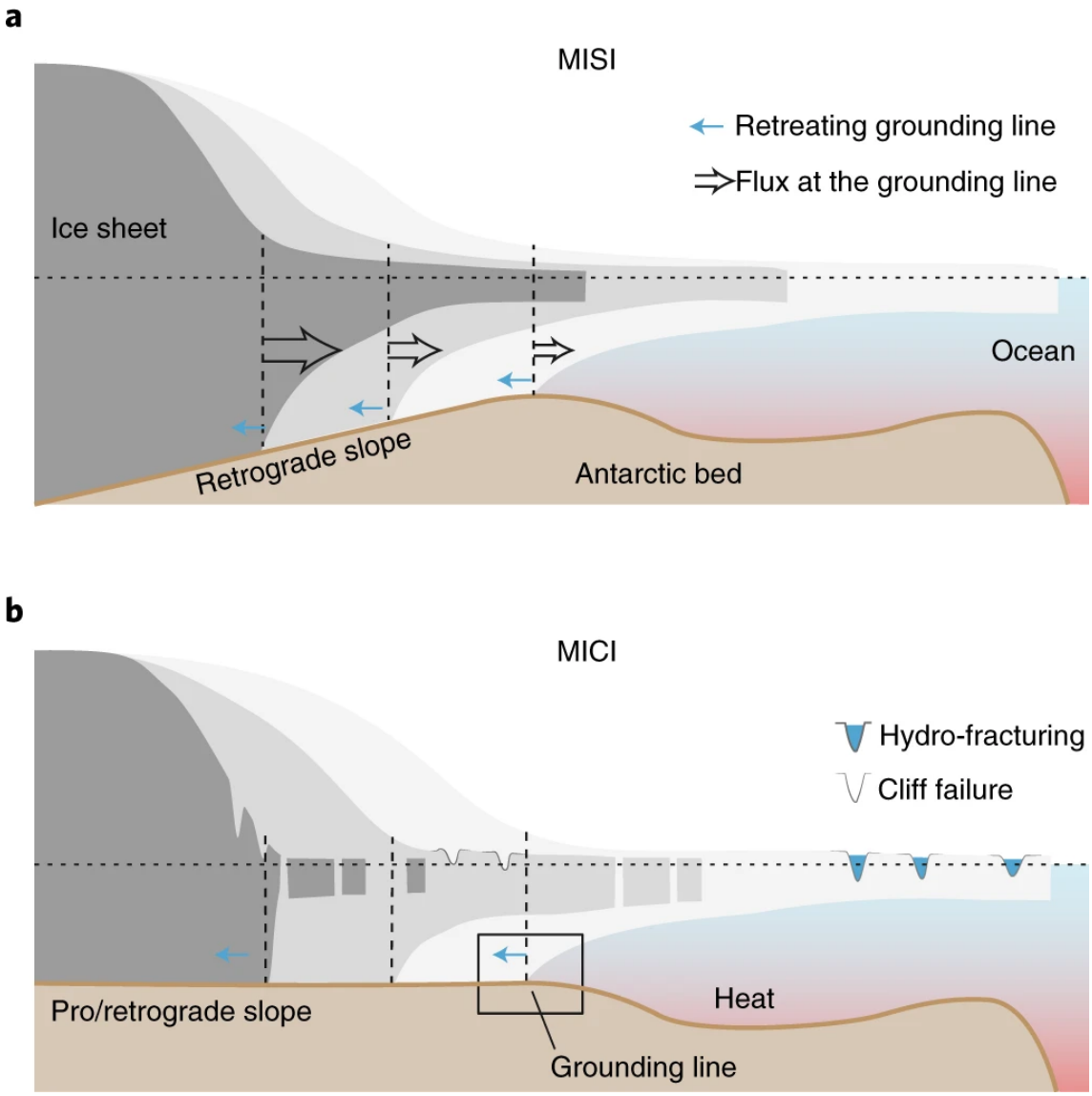


Fig. 1.2 Mechanisms of ice sheet instability discussed in the main text. Figure **a** illustrates the Marine Ice sheet instability (MISI). Where the grounding line retreats into deeper bedrock with thicker ice, this increases flux across the grounding line. Increased flux causes further thinning and grounding line retreat into deeper bedrock. Figure b is driven by sudden removal of buttressing ice shelves through hydro-fracture, followed by collapse of exposed ice cliffs through brittle failure. Figure from Pattyn et al. (2018).

Ice shelves play an important role in modulating upstream flow (Scambos et al., 2004, Rignot et al., 2013, Shepherd et al., 2010). Buttressing exerted by ice shelves is partially determined by valley shape. Sidewalls can contribute to buttressing by exerting transverse

shear stresses on the glacier or ice sheet (Goldberg et al., 2009), with length and shape of confining valley geometry controlling transverse velocity profiles (Pegler, 2016). Ice sheets with no lateral confinement exert minimal buttressing compared with confined geometries such as Pine Island Glacier (PIG) (Gudmundsson, 2013) in the Amundsen Sea Embayment of West Antarctica.

Around 87% of Antarctica's shelf ice buttresses upstream ice flow (Fürst et al., 2016), and therefore modulates glacier discharge. However, precise characterisation of how loss of shelf ice will affect glacier discharge is challenging, with buttressing of ice shelf controlling ice flow hundreds of kilometres upstream (Reese et al., 2018a). Speed up and increased ice discharge from some tributary glaciers, immediately following the breakup of Larsen B in 2002 (Wuite et al., 2015), is indicative of ice sheet sensitivity to loss of the ice shelf. Ice shelf response to climate forcing, and thus change in buttressing effect and glacier discharge, is therefore a key uncertainty in projections of the Antarctic ice sheet contribution to SLC.

Sub-ice-shelf bathymetry affects ice flow dynamics and buttressing through the influence of pinning points - topographic highs which protrude into or through the ice shelf (Favier et al., 2016). The importance of pinning points to ice shelf stability has become increasingly recognised as models able to capture GL dynamics have become more widespread (e.g. Goldberg et al. 2009). On sub-millennial timescales, the omission or inclusion of pinning points from ice shelf/ sheet models can alter rates of ice mass loss and corresponding SLC, as well as ice sheet advance (Favier et al., 2016). Adequate characterisation of sub-shelf bathymetry, along with higher model resolution to adequately resolve back stress across the grounding line can better capture pinning point contribution to ice shelf buttressing (Matsuoka et al., 2015).

### 1.2.3 Marine Ice Cliff Instability (MICI)

Whilst MISI is well established, another instability has recently been proposed that models suggest could increase sea level contribution from marine ice sheets (DeConto and Pollard, 2016, DeConto et al., 2021) - the marine ice cliff instability (MICI) (Bassis and Walker, 2012)(Fig. 1.2). As with MISI, MICI is sensitive to bedrock topography and ice sheet thickness at the grounding line (Bassis and Walker, 2012). However, whilst MISI is related to flow of ice through the grounding line, MICI is driven by brittle failure at the calving front (Bassis and Walker, 2012). In addition, MICI can proceed on prograde slopes if cliff height upstream remains above the stability threshold.

Longitudinal stretching, associated with velocity gradients in the glacier exert a primary control on ice berg calving - with steeper velocity gradients promoting deeper crevassing (Benn et al., 2007). Where velocity gradients are high, and crevasses penetrate to the water line, the glaciers are likely to calve when they reach buoyancy (Benn et al., 2007). In the case of tidewater glaciers, calving style is typified by frequent detachment of ice bergs of length-scale close to or less than the ice thickness at the glacier front. Where rifts in ice shelves can propagate over many years, far from the ice edge, rifts in tidewater glaciers form within a few ice thicknesses from the calving front where the ice approaches buoyancy (Walter et al., 2010). Calving will then proceed within weeks, meaning that few large-scale, long lived rifts are observed (Walter et al., 2010). Correlations between calving rate and variables such as ice thickness, water depth and height above buoyancy have been observed, and form the basis for heuristic calving laws (Bassis and Walker, 2012, Nick et al., 2010, 2009, van der Veen, 2002, Veen, 1996, Meier and Post, 1987). These correlations however, have limited applicability, and when incorporated into ice sheet models, fail to anticipate configurations observed in the field (Ma et al., 2017), such as floating ice tongues (Bassis and Walker, 2012, Giles, 2017). Height-above-buoyancy calving laws are therefore not universally applicable. For empirical calving laws, underlying relationships are not well constrained by observations, and may not hold outside those glacier systems on which they are based (Pattyn and Morlighem, 2020). At present, no general calving law exists.

At exposed marine ice cliffs, longitudinal stresses in the ice flow direction are countered by hydrostatic pressure exerted by ocean water at the terminus. Highest horizontal velocities in tidewater glaciers are found in a zone around the water line, and are associated with a zone of maximum tensile stress and bulging at the glacier front (Crawford et al., 2021, Hanson and Hooke, 2003, 2000). With a component of longitudinal stress due to cryostatic pressure that increases with depth, taller ice cliffs promote larger maxima in longitudinal deviatoric stress (Hanson and Hooke, 2003). When local stresses at the calving front surpass ice strength, pervasive crevassing may weaken the ice front (Hanson and Hooke, 2003), driving brittle failure through a range of mechanisms (Crawford et al., 2021, Parizek et al., 2019).

The Marine ice cliff instability (MICI) hypothesis posits that, based on the mechanical strength of ice, sub-aerial ice cliffs above a threshold height are inherently unstable and prone to failure (Bassis and Walker, 2012). Where the ice sheet thickens upstream of the grounding line, for example where ice is grounded on inland sloping bedrock, retreat into thicker ice will expose ice cliffs above the stability threshold. Failure of these ice cliffs then drives further retreat in a positive feedback, destabilising the ice sheet until a stable configuration (thinning upstream) is reached. This cliff-failure driven, positive mass-loss feedback is the marine ice cliff instability. MICI (Bassis and Walker, 2012)

has garnered significant interest as a mechanism for abrupt, catastrophic ice sheet failure on sub-centennial timescales (Pollard et al., 2015, DeConto and Pollard, 2016, DeConto et al., 2021).

Bassis and Walker (2012) derived upper and lower bounds for the glacier thickness stability threshold based on considerations of ice mechanical properties. To derive an upper bound on stable cliff height, Bassis and Walker (2012) model failure of ice neglecting lateral shear stresses. They test three models for the cohesive strengths of ice, with the weakest model assuming a yield strength of ice of 1 MPa. Ice strength is grain size and temperature dependent (Currier and Schulson, 1982) and challenging to infer for glaciers and ice sheets. Earlier field-observation-based assessments of glacier tensile strength (Vaughan, 1993) suggest that value of 1 MPa may be conservative. However, it is broadly consistent with more recent estimates for glacier ice deduced from the collapse of an ice cap in Iceland (Ultee et al., 2020).

For an ice yield strength of 1 MPa, Bassis and Walker infer a maximum stable cliff height of ~220 m for dry terminating uncrevassed ice (Bassis and Walker, 2012). Including crevasses through 50 % of the ice thickness decreases the maximum stable cliff height to ~110 m (Bassis and Walker, 2012). Where the ice is above flotation thickness, increasing water depth provides stability to the ice front and increases the stable thickness. For marine terminating ice, Bassis and Walker find a maximum stable terminus thickness of to ~900 m with crevasses to ~1100 m without crevasses (Bassis and Walker, 2012). This upper bound is computed for their plastic model for ice strength. This model, and the inferred upper bounds, are broadly consistent with thickest marine terminating glacier geometries observed in the field (Bassis and Walker, 2012). A further implication of this upper bound is that, where grounding line thickness for an ice tongue or ice shelf providing negligible back-stress exceeds ~900-1100 m, it may fail catastrophically (Bassis and Walker, 2012).

Marine terminating glaciers can lose mass through buoyant calving (Benn et al., 2007, 2017, Crawford et al., 2021). Buoyant calving can occur when the glacier terminus is in hydrostatic disequilibrium. This occurs when ice flows rapidly into water depth greater than the floatation depth, or as a result of thinning of the glacier such that buoyant forces exceed the ice overburden pressure (Benn et al., 2007). Concentration of stress at the base of the ice then promotes basal crevassing, which propagates up through the glacier until an iceberg detaches (Benn et al., 2007, 2017). Basal melting of floating or grounded marine terminating glaciers can also promote failure of the remaining ice overhang (Benn et al., 2017). Parizek et al. (2019) observe retreat of the Helheim glacier front consistent with combined cliff failure and buoyancy driven detachment of ice below the waterline, promoting full thickness calving. They observe failure of subaerial ice cliffs along faults

propagating to the waterline, followed by upward rotation of the submarine foot of the ice cliff (Parizek et al., 2019).

More recent model-based analysis of ice cliff mechanics, accounting for ductile deformation of ice, suggests that the transition to brittle failure and ice cliff collapse may be sensitive to timescale of ice shelf removal (Clerc et al., 2019). Clerc et al. 2019 suggest that over reasonable timescales of ice shelf removal (>~1 day), stresses are accommodated through ductile deformation as opposed to brittle failure. This suggests that a critical failure threshold of ~90 m (Bassis and Walker, 2012), which forms the basis of MICI parameterizations in previous projection models (DeConto and Pollard, 2016), may lead to overly large sea level projections if timescale of ice shelf removal is not taken into account. For undamaged ice, a ~90 m critical cliff height for brittle failure would require ice shelf removal on timescales of < 1 hour (Clerc et al., 2019), faster than previously observed fastest (~2 weeks) ice shelf break up - the break up of the Larsen B ice shelf (Rack and Rott, 2004, Sergienko and Macayeal, 2005). The rapid break-up of Larsen B was likely precipitated by an anomalous increase in meltwater production driving simultaneous localised melt-driven shelf failures, as opposed to interacting melt ponds causing widespread collapse (Robel and Banwell, 2019). In contrast, other previously observed ice shelf collapse events have typically proceeded over years (Cook and Vaughan, 2010). Whilst recent studies have suggested a role for ductile deformation and mélange back-stress in stabilising ice cliffs (Clerc et al., 2019, Bassis et al., 2021, Crawford et al., 2021, Parizek et al., 2019), increasing stable cliff height above that originally proposed in Bassis and Walker (2012), accounting for ice damage in these models reduces ice strength and stable cliff height (Crawford et al., 2021, Clerc et al., 2019, Bassis et al., 2021). For heavily damaged ice, stable cliff height may be as low as ~60 m (Clerc et al., 2019).

The role of mélange in slowing or stopping MICI, a process not accounted for in previous MICI-based projections of Antarctic retreat (DeConto and Pollard, 2016, DeConto et al., 2021)), remains under-explored. Previous work has suggested that, in the wide embayments of West Antarctica, mélange may provide only a negligible restraint on MICI (Pollard et al., 2018). West Antarctic scale simulations (Schlemm et al., 2022), incorporating MICI and mélange processes (Schlemm and Levermann, 2019, 2021), find that changing embayment geometry and mélange processes may slow MICI. Moreover, mélange processes may provide sufficient buttressing for an ice shelf to reform and halt MICI (Schlemm et al., 2022). Observations for the Jakobshavn Isbrae Glacier in Greenland support the stabilising effect of ice mélange in ice front retreat, with persistent rigid mélange associated with greater terminus advance in two winters (Joughin et al., 2020). Whilst significant progress has been made in understanding the suite of processes that influence and limit MICI (Bassis et al., 2021, Crawford et al., 2021, Clerc et al., 2019, Robel and Banwell, 2019,

Schlemm et al., 2022, Pollard et al., 2018), it remains a key uncertainty in continental scale Antarctic ice sheet simulations.

There is evidence of possible MICI-driven collapse of PIG from 12,300 to 11,200 years before present (Wise et al., 2017). Crucially for understanding AIS stability and contribution to SLC, the rate at which MICI can proceed once initiated is unknown. Whilst initial incorporation of MICI in an ice sheet modelling study suggested >1m AIS contribution by 2100 (DeConto and Pollard, 2016), subsequent work has shown that these estimates are sensitive to modelling choices (Edwards et al., 2019). Inclusion of MICI processes in the IPCC Sixth Assessment Report increases the *likely* range of 2100 sea level contribution to 0.19 m - 0.53 m from Antarctica under the highest emissions scenario (SSP5-8.5) (Fox-Kemper et al., 2021), incorporating revised MICI-based projections with an improved representation of surface melt 2021.

As outlined in this section, the Antarctic ice sheet contribution to sea level depends on complex, sparsely observed processes and dynamic instabilities. Alongside observations of modern ice sheet dynamics and reconstructions ice sheets in the past, ice sheet models are an important tool in characterising ice sheet response to climate change. They are discussed below.

## 1.3 Ice Sheet Modelling

### 1.3.1 Hierarchy of models

Numerical ice sheet models are the primary tool for making quantitative predictions of ice sheets under past or future conditions. Throughout this thesis, we use the term ice sheet model to refer to computer code that finds an approximate solution to a set of equations describing ice sheet physics.

The overarching mathematical model approximating flow in an ice sheet is the Stokes equations. The Stokes equations are a special case of the Navier-Stokes equations for fluid flow. Models based on the full Stokes equations (Full Stokes models) provide the closest approximation of ice sheet flow. However, they are computationally expensive, and prohibitively so for large domains, long integration times and high resolution. To overcome these constraints, ice sheet models solve simplified systems of equations that neglect components of the stress balance solved in the Stokes equations. As more simplifying assumptions are made, ice sheet models become less computationally expensive. Ice sheet

model equations generally fall into a hierarchy, based on how many components of the force balance they retain from the full Stokes model.

Below Full Stokes models in this hierarchy are Higher order models. Higher order models provide a 3 dimensional representation of the stress balance in ice, retaining longitudinal stress gradients. To improve computational efficiency, they exploit the scale relationships in the ice sheet stress balance, solving a simplified set of model equations (Blatter, 1995, Pattyn, 2003).

One of the simplest 3D models of ice sheet flow is the Shallow Shelf Approximation (SSA). The SSA makes the same simplifying assumptions as higher order models, but assumes that vertical shear stress is confined to a base layer, represented by a basal friction law. Within the ice sheet, the SSA does not account for vertical gradients in velocity. Where basal friction is low, such as in ice streams or ice shelves, this assumption is largely valid. However, in the slow flowing interior of the ice sheet or where the ice sheet is frozen to the bed, ice flow is dominated by internal deformation. The SSA can not therefore accurately model ice dynamics in these regions.

The simplest approximation of ice flow is the Shallow Ice Approximation (SIA). The SIA neglects membrane stresses, assuming that basal shear stress is balanced by gravitational driving stress (Greve and Blatter, 2009). By neglecting membrane stress, the stress balance in the SIA is localised and does not account for lateral margins or slower moving ice. The SIA is valid in contrasting settings to those successfully modelled by the SSA: i.e. in the ice sheet interior where deformation dominates ice sheet velocity, and basal sliding is negligible (Hutter, 1983, Huybrechts and Wolde, 1999).

To capture ice dynamics whilst retaining the computational efficiency of the SIA and SSA, the two approximations can be combined into hybrid SIA-SSA models (Winkelmann et al., 2011, Bueler and Brown, 2009). In hybrid models, velocities from the SIA and SSA can be linearly combined to simulate ice sheet evolution across the whole domain (Bueler and Brown, 2009). Hybrid models have been used to model ice sheet evolution over long timescales under future emissions (Lowry et al., 2021) and for periods in the past (Golledge et al., 2017b). Hybrid models can successfully reproduce observed ice flow (Winkelmann et al., 2011, Quiquet et al., 2018, Martin et al., 2011). However, their proficiency in resolving the transition between SIA and SSA regimes is unclear (Robinson et al., 2022)

An intermediary between the SIA/SSA and higher order models are L1L2 models. The L1L2 model uses depth-integrated effective viscosity to solve the momentum balance of ice in two dimensions. L1L2 models approximate depth integrated horizontal velocity, and provide a continuous treatment of the ice sheet interior, ice streams and shelves.

### 1.3.2 BISICLES

This study will use the BISICLES ice sheet model (Cornford et al., 2013). BISICLES is based on an approximation of the Stokes model, grounded in the theory of Schoof and Hindmarsh (Schoof and Hindmarsh, 2010). It implements the L1L2 model on a block structured grid with adaptive mesh refinement (AMR). This allows BISICLES to deploy fine grid resolution where it is needed, such as at the grounding line, whilst maintaining low resolution in slow moving regions of the domain. BISICLES L1L2 physics and AMR allow it to explore key grounding line processes whilst maintaining reasonable computational efficiency for ensemble experiments. Moreover, it retains enough complexity to give a close approximation of the full Stokes equations (Pattyn and Durand, 2013). BISICLES has been applied to a millennium-scale study of the Antarctic ice sheet under idealised forcing (Martin et al., 2019), and to century scale simulations of the ice sheet (Cornford et al., 2015, 2016). It has not been used to simulate the Pliocene Antarctic ice sheet, the focus of this study.

BISICLES assumes that ice is in hydrostatic equilibrium, such that given bedrock elevation $b$, and ice thickness $h$, the surface elevation of the ice sheet $s$, is given by:

$$s = \max\left[h+b, \left(1-\frac{\rho_i}{\rho_w}\right)h\right], \tag{1.1}$$

where $\rho_i$ is the density of ice and $\rho_w$ is the density of sea water (Cornford et al., 2015).

Horizontal velocity $\vec{u}$ and thickness ($h$) satisfy a mass conservation equation for depth-integrated transport of an incompressible material:

$$\frac{\delta h}{\delta t} + \nabla \cdot [\vec{u}h] = M_s - M_b, \tag{1.2}$$

where $M_s$ is the meteoric accumulation rate i.e. due to surface mass balance processes, and $M_b$ is the basal melt rate applied to the underside of ice shelves in cells with a centre at floatation. Incompressible (shear-thinning) flow of ice under gravity satisfies a stress balance equation:

$$\nabla \cdot [\phi h \mu (2\dot{\varepsilon} + 2tr(\dot{\varepsilon})\mathbf{I}] + \vec{\tau}_b = \rho_i g h \nabla s, \tag{1.3}$$

where $\mathbf{I}$ is the identity tensor and $g$ is acceleration due to gravity, and $tr(\dot{\varepsilon})$ indicates the trace of $\dot{\varepsilon}$. The strain rate tensor, $\dot{\varepsilon}$, is given by:

$$\dot{\varepsilon} = \frac{1}{2}[\nabla\vec{u} + (\nabla\vec{u})^T]. \tag{1.4}$$

The term $\phi h\mu$ in Equation 1.3 is the vertically-integrated effective viscosity. $\phi$ is a stiffening factor, which represents changes to ice viscosity due to factors such as temperature and crevasse weakening. For modern ice sheet studies, $\phi$ is found by inversion and tuned to match observations (e.g. Cornford et al. 2015). The effect of vertical shear strain is retained through viscosity, $\mu$, which satisfies the below equation when the exponent n=3 in Glen's flow law (see Cornford et al. (2015)):

$$2\mu A(T)(4\mu^2\dot{\varepsilon}^2 + |\rho_i g(s-z)\nabla s|^2) = 1, \tag{1.5}$$

where $A(T)$ is a rate factor that depends on temperature through the Arrhenius Law described by Hooke (1981), $s$ is the surface and $z$ is depth in the ice sheet. We note that n, with n=3 commonly used in ice sheet modelling studies and used here, can take a plausible range from 2 to 4 (Cuffey and Paterson, 2010).

### 1.3.3 Basal sliding

Sliding of the ice sheet over the bedrock, or basal slip, is represented in ice sheet models through basal friction laws. The original theory of basal sliding was formulated for an idealised temperate ice sheet sliding over a rigid bedrock, lubricated by a thin film of water such that the ice is separated from the bed. Whilst this thin film provides no local scale resistance to flow, on glacier to ice sheet scale bed roughness exerts mean resistance to flow or basal drag ($\tau_b$). The Weertman sliding law (1957) was formulated to relate basal velocity to basal drag in such a setting:

$$\tau_b = C\vec{u}_b^m, \tag{1.6}$$

where $C$ is a local friction parameter or Weertman friction coefficient, $u_b$ is basal velocity and $m$ is a positive constant, which usually takes the value 1/3 for hard bed rocks based on the creep exponent in Glen's flow law (Weertman, 1974, Schoof, 2007a, Gudmundsson et al., 2012, Pattyn et al., 2013, 2012). It can however take different values to approximate different bed conditions, tending to zero where deformable sediments at the bed exert resistance to flow independent of basal velocity (the plastic case).

A second family of bed friction laws, Coulomb-type laws, adapt velocity-independent plastic friction laws to account for the presence of water at the bed:

$$\tau_b = C_f N \tag{1.7}$$

where $C_f$ is the local Coulomb friction coefficient, and N is the effective pressure - the difference between ice overburden pressure and water pressure. Basal hydrology models of varying complexity can be used to simulate the water pressure component of Coulomb sliding.

The Tsai friction law (Tsai et al., 2015) incorporates the two basal friction laws outlined previously into a two component formulation of basal sliding:

$$\tau_b = min[C(\vec{u}_b)^{(\frac{1}{m})}, C_f N] \tag{1.8}$$

The two component basal sliding law facilitates Coulomb type sliding where saturated till at the base of the ice sheet, or water filled cavities, enable plastic sliding. For hard beds under the Tsai friction law, Weertman sliding is used.

### 1.3.4 Bedrock topography

A significant source of uncertainty in projections of the Antarctic ice sheet contribution to SLC is poor characterisation of conditions at the base of the ice sheet. This is particularly challenging for modelling ice streams, which account for more than 90% of ice discharge from Antarctica (Bingham et al., 2017, Durand et al., 2011). Basal traction, determined by subglacial topography and basal friction, exerts a primary control on ice flow. Subglacial topography contributes to form drag - resistive stress on glacier flow exerted by roughness in the glacier bed (Bingham et al., 2017, Cuffey and Paterson, 2010).

To fully resolve forces at the ice-bed interface and their effect on glacier flow, comprehensive representation of bed shape is needed, and at sufficient resolution. Along marine ice sheet margins, ice sheet stability can be dictated by the effect of bedrock channels and fine scale roughness on basal sliding and ice flow (Ritz et al., 2015), and resolution finer than 1km may be necessary (Goff et al., 2014). In practice however, bed topography is often smoothed to conform with model resolution. More importantly, large regions of the Antarctic bedrock are unmapped. A widely used continental-scale bed topography is the Bedmap2 dataset (Fretwell et al., 2013), which interpolates bed topography between observations onto a 5km grid, and therefore smooths the bed. In regional modelling studies,

it has been shown that this smoothing results in the omission of topographical features, which influence ice dynamics (Bingham et al., 2017, Wernecke et al., 2022). A study using an ensemble of BISICLES simulations of the Amundsen Sea Embayment (Nias et al., 2016) demonstrates that failure to account for bed roughness leads to over-prediction of the current rate of SLC as a rough bed slows ice discharge.

This thesis uses an ice sheet model (Section 1.3.2) with a minimum resolution of 1 km for decadal-scale continental simulations (Chapter 2) and regional millennium-scale simulations (Chapter 3), and 4 km for millennial-scale continental simulations (Chapters 4 to 5), therefore resolving bed features at these scales. Chapter 4 also explores the impact of bedrock topography uncertainty by using two alternative datasets: a version of Bedmap2 (Fretwell et al., 2013) modified following Nias et al. (2016) as used in (Cornford et al., 2016), and the more recent BedMachine dataset (Morlighem et al., 2020)

## 1.4 Warm Pliocene climate

### 1.4.1 Introduction

The warm Pliocene refers to the period 3.3Ma-3Ma when global mean air temperatures were 2.5-4°C higher than 1850-1900, atmospheric $CO_2$ concentrations were comparable to modern (~400 ppm), and sea level was higher than modern by ~tens of meters (Gulev et al., 2021). With similar continental configuration and periods of comparable solar forcing to modern, the warm Pliocene provides insights into the climate state at equilibrium with modern atmospheric $CO_2$ concentrations. The primary influence of $CO_2$ in warm Pliocene climate is supported in modelling studies (Lunt et al., 2012). This interval is referred to as the mid-Pliocene Warm Period (mPWP) or mid Piacenzian, and is the focus of this thesis.

Historically the Pliocene Epoch included the Zanclean, Piacenzian and Gelasian stages. However, the Pliocene-Pleistocene transition was moved to the base of the Gelasian (2.588 Ma) in 2009 (Gibbard et al., 2010, Dowsett et al., 2016). Following this change in stratigraphic boundary, the Piancezian spans the end of the Pliocene, i.e. up to the boundary with the Pleistocene. In the literature, mid-Pliocene and mid-Piacenzian are used interchangeably but generally refer to the same time interval as defined by Dowsett and Poore (1991), and revised by Dowsett et al. (2010), of 3.26 to 3.025 Ma. Within the mid-Piacenzian, the KM5c interglacial period (3.212–3.187 Ma) has increasingly become the focus of proxy data reconstructions (Dowsett et al., 2016) and modelling efforts (Haywood et al., 2016b). This focus on KM5c is due to its comparable orbital configuration and therefore insolation to present day (Haywood et al., 2016a) - facilitating

assessment of a relatively high $CO_2$ concentration world with fewer confounding variables (Haywood et al., 2016b).

The mPWP is widely studied as an analogue for Earth's future under climate change, with similar temperatures to those projected under an intermediate emissions scenario (SSP2-4.5) by 2300 [2.3-4.6 °C] (Gulev et al., 2021). Reflecting its salience, a concerted effort to reconstruct palaeo-climate for this interval has been underway since Dowsett et al. (2007). The Pliocene Research, Interpretation and Synoptic Mapping (PRISM) project (Dowsett, 2007) is now on its fourth iteration (PRISM4) (Dowsett et al., 2016). PRISM4 compiles sea surface temperature (Dowsett and Robinson, 2009, Dowsett et al., 2013), palaeo-geography (Rowley et al., 2013), soils and lakes (Pound et al., 2014), terrestrial biomes (Salzmann et al., 2013, 2008), land ice including ice sheet elevation (Hill, 2009, Dolan et al., 2015, Koenig et al., 2015) and sea ice distribution from proxy data and models. The PRISM4 project provides boundary conditions and data model comparison constraints for the Pliocene Model Intercomparison Project Phase 2 (PlioMIP2) (Haywood et al., 2016b)(Chapter 4).

The climates of the Pliocene were warmer and wetter than today (Figure 1.3 **a**), with expanded zones of shrubland, savannah and woodland outside the tropical rainforest belt (Salzmann et al., 2011, Leroy and Dupont, 1994, Dodson and Macphail, 2004)(Figure 1.3 **b**). Arid zones of North Africa saw increased vegetation cover with increased mid Piacenzian precipitation (Salzmann et al., 2011). In the continental subtropics, increased mid-Piacenzian precipitation is evident in the palaeo-botanic record (Thompson, 1991, Thompson and Fleming, 1996) and large lakes persisted across western North America (Machette et al., 2013, Forester, 1991, Knott et al., 2018, Smith, 1984). In temperate regions, Pliocene warming was accompanied by expansion and diversification of forest cover (Salzmann et al., 2011) (Figure 1.3 **b**). Type and distribution of species recorded in European proxy data indicate 3-6 °C average air temperature warming and an increase in mean annual precipitation of 400 mm in the northern Mediterranean and 230 mm in western Europe during peak Pliocene warmth (Fauquette et al., 1999, Utescher et al., 2000). Boreal forest cover extended northwards in the warm Pliocene, consistent with higher mean winter and summer temperatures (Mai, 1995). In the high northern latitudes, tundra was replaced with taiga vegetation (Bennike and Böcher, 1990, deVernal and Mudie, 1989), Arctic summer temperatures were > 8 °C and as high as 19 °C above modern in the high Canadian Arctic (Ballantyne et al., 2010, Salzmann et al., 2011, Brigham-Grette et al., 2013).

In the ocean, combined proxy data suggest SSTs were on average 2.3 °C warmer than modern for the KM5c interglacial of the mid-Piacenzian and meridional SST gradients

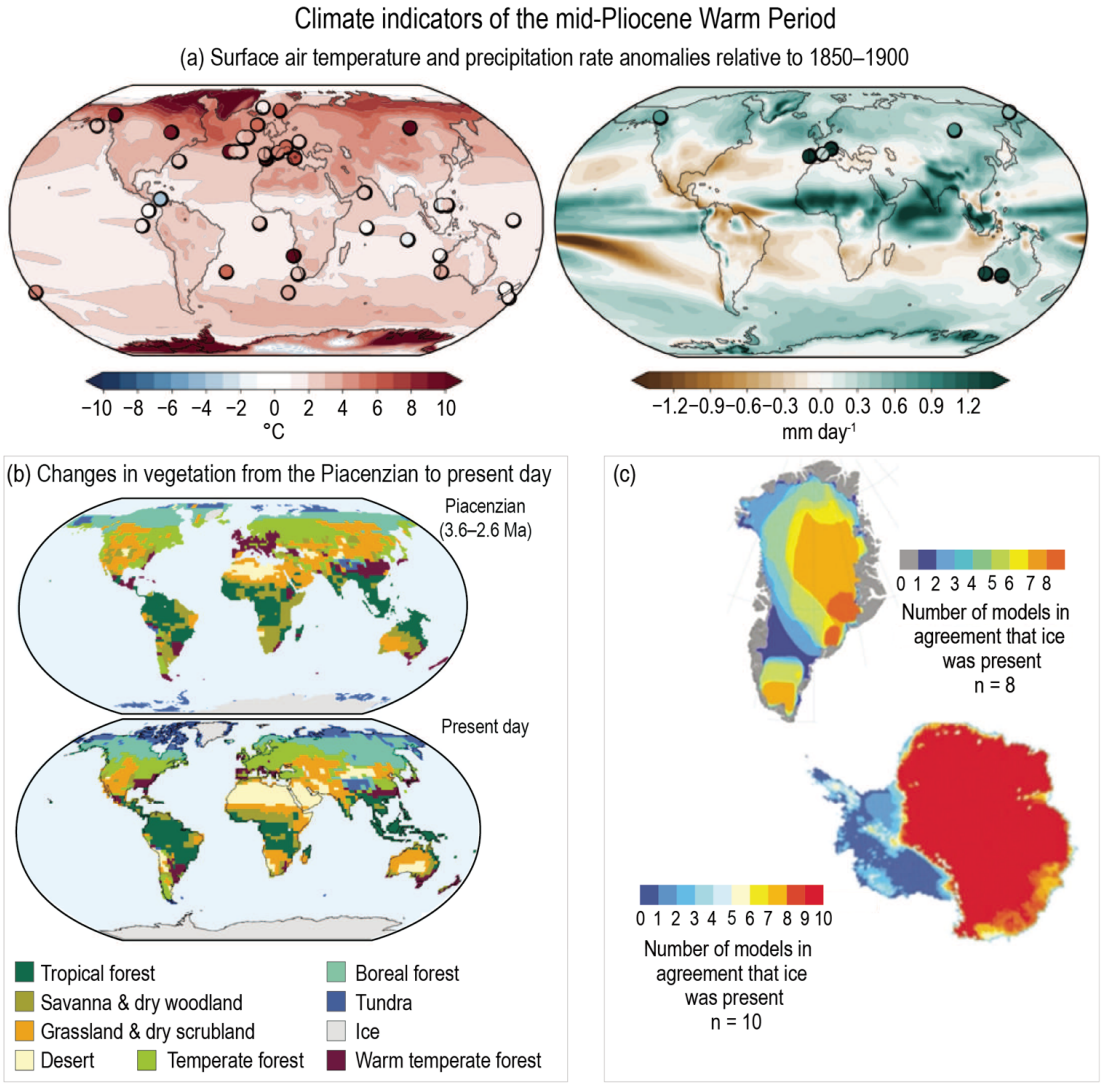


Fig. 1.3 Multi-model mean simulated surface air temperature anomaly (**a** left) and precipitation (**a** right) from the 16 climate models in the Pliocene Ice Sheet Model Intercomparison Project phase 2 (PlioMIP2). Markers show site-level proxy-based estimates of the precipitation rate for the mPWP, sea-surface temperature for KM5c and terrestrial surface temperature. Figure **c** shows the distribution of terrestrial biomes in the Piacenzian (3.6-2.6 Ma)(upper) and present-day (lower). Pliocene biomes are based on 208 sites, with the BIOME4 model predicted biomes used to fill spatial gaps. For present-day, the model is adjusted for $CO_2$ concentrations of 324 ppm. Figure **c** shows model predicted Pliocene ice sheet presence or absence for Antarctica (n = 10 total) and Greenland (n = 8 total) (Gulev et al., 2021)

were reduced by 2.6 °C (McClymont et al., 2020). It has previously been suggested that the east to west equatorial SST gradient was nearly eliminated in the mPWP, resulting in permanent El Niño conditions in the Pacific ocean (Fedorov et al., 2006, Wara et al., 2005), though a recent proxy data compilation and model comparison finds more moderate reduction in SST gradients than those associated with a permanent El Niño (Tierney et al., 2019).

### 1.4.2 Antarctica in the Pliocene

With limited proxy samples for Antarctic terrestrial climate, and challenges associated with interpreting available data (Salzmann et al., 2011, Wilson et al., 2002, Stroeven et al., 1996), the mid-Piacenzian is less well characterized in Antarctica than for more northerly regions. The most relevant departure in Pliocene climate from modern, in the context of the work presented here, is reduced ice sheet extent and volume inferred from proxy records (Section 1.4.2) (Naish et al., 2009, Cook et al., 2013, Patterson et al., 2014)

Two main approaches are established for reconstructing global mean sea level through the geological record. The first of these relies on interpreting and dating indicators of shoreline in the geological record (Miller et al., 2020), such as coral reefs or wave cut platforms, that give an indication of shoreline position in the past. These palaeo-shoreline indicators can be outcropping on land or below modern sea level. The second main approach to reconstructing sea level in the past uses geochemical proxy records from deep sea sediments. The isotopic signature of material incorporated into the shells of calcifying marine organisms, such as oxygen incorporated into calcium carbonate shells, is an indicator of ocean isotopic composition when the organism was alive. In turn, isotopic composition of the ocean reflects climate state including ice sheet volume (see below). Analysis and dating of these geochemical proxies provides another approach to reconstructing sea level in the past.

Palaeo-shoreline reconstructions have been used extensively to reconstruct warm Pliocene sea level (Raymo et al., 2018, Dowsett and Cronin, 1990, Wardlaw and Quinn, 1991, Krantz, 1991, Naish et al., 2009, Miller et al., 2012, Rovere et al., 2014, Dutton et al., 2015, Rovere et al., 2015, Kemp et al., 2015, Grant et al., 2019, Dumitru et al., 2019). Early palaeo-shoreline and sequence stratigraphy-based reconstructions of mid Piacanzian GMSL yielded estimates of a ~35 ±18 m above modern (Dowsett and Cronin, 1990). More recent reconstructions imply a lower range (Dumitru et al., 2019, Winnick and Caves, 2015, Miller et al., 2012, Grant et al., 2019, Florindo et al., 2021).

Variability in palaeo-shoreline reconstructions is a function of changes to shoreline elevation arising from local tectonic effects, as well as subsidence driven by sedimentary loading (Krantz, 1991); both need to be corrected for when constraining palaeo-shoreline estimates. More pronounced still, glacial-isostatic adjustment (GIA)-induced changes in local land surface elevation in response to loading and unloading of ice (Peltier, 1998, Rovere et al., 2014), and dynamic topography - adjustment of the Earth's crust in response to mantle driven convection (Austermann et al., 2015, Rovere et al., 2014), exert a significant control on surface elevation, and can therefore be a challenge for interpretation of sea level from palaeo-shoreline indicators. Driven by the response of the lithosphere to mantle convection, dynamic topography typically operates on >=100 ka timescales (Whitehouse, 2018, Rowley et al., 2013, Austermann et al., 2017). Whilst this is beyond the timescales for which we can simulate Antarctica in the present study, it has important implications for reconstructions of sea level in the Pliocene (Rowley et al., 2013, Austermann et al., 2015), as well as glacial dynamics in Antarctica where dynamic topography drives changes in bed elevation (Austermann et al., 2015). Both of these processes are a significant source of error in mPWP sea level estimates (Rowley et al., 2013, Rovere et al., 2014), and are generally not well reconciled in studies of the AIS in this period (Raymo et al., 2018). It has been shown that GIA can affect palaeo-shoreline estimates of relative sea level by 10m (Raymo et al., 2011), with rates of GIA varying based on regional loading history (see Chapter 3, GIA). Some of the early high palaeo-shoreline estimates of warm Pliocene sea level (e.g. Dowsett and Cronin 1990) were from the south east coast of the USA. Pliocene shoreline reconstructions from this region are particularly impacted by solid earth changes to land surface elevation (Rovere et al., 2014). Rovere et al. (2014) find that, accounting for solid earth processes, Pliocene mean sea level of <20 m above modern is most consistent with palaeo-shoreline data. Taken together, shoreline-based reconstructions imply 15 to 28 m sea level rise above modern (Dumitru et al., 2019, Dwyer and Chandler, 2009, Miller et al., 2012, 2020, Florindo et al., 2021).

Geochemical proxy sea level reconstructions are primarily based on $\delta^{18}$O and Mg/Ca analysis. The ratio of stable oxygen of relative isotopic mass 18 ($^{18}$O) to 16 ($^{16}$O), $\delta^{18}$O, recorded in calcite foraminifera shells captures a range of climatic processes ( Epstein et al. 1953, Lisiecki and Raymo 2005, Shackleton 1967, Emiliani 1955. Lighter $^{16}$O is preferentially evaporated from ocean water compared with $^{18}$O. As ice sheets grow through accumulation and compaction of snow into ice, they sequester $^{16}$O such that the oceans become relatively enriched in heavier $^{18}$O. This means that in colder climates (e.g. glacial periods), the isotopic mass fractionation of oxygen is enhanced: ocean water becomes more enriched in $^{18}$O. In warm (e.g. interglacial) periods, melting from ice sheets transfers $^{16}$O stored in glacial ice back to the oceans, leading to relative depletion of $^{18}$O in the

water and therefore more negative values of $\delta^{18}$O. The $\delta^{18}$O ratio in foraminifera ($CaCO_3$) shells is proportional to $\delta^{18}$O in the ocean water from which they precipitate.

Analysis of foraminifera $\delta^{18}$O in ocean sediments can provide a record of ice sheet volume, temperature and salinity at their time of deposition ( Epstein et al. 1953, Lisiecki and Raymo 2005, Shackleton 1967, Emiliani, 1955). Exploiting the relative stability of bottom waters, sea floor dwelling benthic foraminifera have long been recognised as a $\delta^{18}$O record that is less sensitive to large sea surface fluctuations in temperature and salinity, with a stronger ice volume signal (Shackleton, 1967). However, warm Pliocene sea level reconstructions based on $\delta^{18}$O alone would imply sea level 30 m above modern, with uncertainties of ~15 m (Raymo et al., 2018). To further isolate the ice sheet volume signal from the temperature signal, geochemical temperature proxies such as Mg/Ca can be analysed alongside $\delta^{18}$O to construct an independent record of bottom water temperature and salinity.

In the context of the warm Pliocene, paired $\delta^{18}$O Mg/Ca analyses have been used to reconstruct sea level high stands above modern. However, the utility of paired Mg/Ca and $\delta^{18}$O records as indicators of past sea level can be undermined by post-depositional mineral alteration (diagenesis) (Brown and Elderfield, 1996, Sexton et al., 2006, Kozdon et al., 2013, Regenberg et al., 2007), dissolution of carbonate tests (Regenberg et al., 2014, Rosenthal et al., 2000), changes in salinity (Dissard et al., 2010) and carbonate ion saturation/ carbonate compensation depth (Elderfield et al., 2006, Rosenthal et al., 2006). Paired $\delta^{18}$O Mg/Ca records have been used to reconstruct Pliocene peak sea level of 21 ± 10 m above modern (Woodward et al. 2014). Miller et al. (2012) used a multi-proxy approach, combining paired $\delta^{18}$O Mg/Ca records, palaeo-shoreline proxies and coral records to estimate Pliocene sea level of 22 ± 10m.

A more recent $\delta^{18}$O based study revised down previous reconstructions (Miller et al., 2012) of Pliocene peak sea level range to 9 to 13.5 m above modern (Winnick and Caves, 2015). Winnick and Caves (2015) account for different isotopic $\delta^{18}$O signatures for the Greenland, West and East Antarctic ice sheets. They also consider higher $\delta^{18}$O for the Pliocene Antarctic ice sheet due to surface warming, which would increase its $\delta^{18}$O (Winnick and Caves, 2015, Dansgaard, 1964). For the isotopically lighter East Antarctic ice sheet, less mass loss is required to explain observed $\delta^{18}$O changes (Winnick and Caves, 2015). Winnick and Caves (2015) also account for the fact that a proportion of mass loss from Antarctica will not impact global sea levels, as some of this ice is grounded below sea level (Fretwell et al., 2013, Winnick and Caves, 2015).

Whilst a multi-proxy approach (e.g Naish et al. 2009, Miller et al. 2012, 2020) can reconcile some errors in sea level reconstructions, Raymo et al. (2018) state that no

consensus estimate based on paired $\delta^{18}$O Mg/Ca exists due to post depositional and seawater chemistry alterations that drive uncertainty in estimates based on this approach.

Independent of $\delta^{18}$O, Grant and Naish (2019) use the theoretical relationship between sediment grain size and water depth to reconstruct Pliocene sea level variability from outcrops in the Whanagnui basin, New Zealand (PlioSeaNZ, Grant et al. 2019). The PlioSeaNZ record reconstructs Pliocene sea level variability with ± 5 m precision (Grant and Naish, 2019). Combining the PlioSeaNZ record, far field reconstructions and reconstructions of the Antarctic margin (discussed below), Grant and Naish (2021) suggest that peak warm Pliocene GMSL was between 4.1 m and 20.7 m above modern, with a median of 10.7 m. This is based on the assumption that PlioSeaNZ variability is greater than modern (Grant and Naish, 2021).

A key caveat for constraining Antarctic contribution to warm Pliocene sea level is the role of northern hemisphere ice sheets. Thiede et al. (2011) find limited evidence for ice sheets outside Greenland in the Pliocene. In terms of the Greenland ice sheet itself, ice sheet model reconstructions limit the ice sheet extent to high elevation regions in the south and east of Greenland (De Schepper et al., 2014, Yan et al., 2014, Koenig et al., 2015, Dowsett et al., 2016, Berends et al., 2019).

### Proximal Evidence of Antarctic configuration in the Pliocene

The alternative method of inferring the Antarctic ice sheet configuration in the Pliocene is from reconstruction of its margins. Whilst geological records from the Antarctic continental margin are relatively rare, largely inaccessible due to coverage by ice and ocean (Escutia et al., 2019), what records are available have can inform reconstructions of AIS dynamics in the Pliocene. The ANDRILL programme extracted sediment cores from the Ross ice shelf, finding evidence of periodic, ~40 ka obliquity paced WAIS collapse throughout the Pliocene (Naish et al., 2009) and open water conditions (McKay et al. 2012). Naish et al. (2009) infer open seaway conditions in the Ross sea, with diatomaceous sediment components indicating high productivity, air temperatures above freezing and minimal summer sea ice. In addition to drill core records, evidence for a highly dynamic WAIS in the warm Pliocene has been inferred from seismically correlated stratigraphic units in the Amundsen Sea (Gohl et al., 2021). These suggest advance of grounding lines seaward of their modern position during cool intervals in the Pliocene, as well as collapse during warm intervals (Gohl et al., 2021).

In contrast to WAIS, evidence for retreat of the EAIS varies by region. Cook et al. (2013) find evidence for retreat into the Wilkes basin of East Antarctica in the Pliocene. Using

geochemical provenance analysis of sediments from off-shore of the Wilkes basin, they find neodymium and strontium isotope ratios that correspond to an erosive source within the Wilkes basin (Cook et al., 2013). With maximum erosion at the grounding line (Alley et al., 1997), this geochemical signature is indicative of mPWP grounding line retreat into the Wilkes basin compatible with ~3 - 10 m EAIS sea level contribution (Cook et al., 2013). Building on Cook et al. (2013), Bertram et al. (2018) combine geochemical provenance, iceberg rafted (IRD) debris records and productivity indicators to reconstruct mPWP retreat into the Wilkes basin. On timescales of a few thousand years, Bertram et al. 2018 posit that large scale iceberg calving at the terminus of ice streams precedes more widespread grounding line retreat into the Wilkes subglacial basin (fig. 1.4), driving an increase in marine productivity. This is consistent with previous IRD evidence for iceberg production from the margin of the Wilkes basin (Patterson et al., 2014).

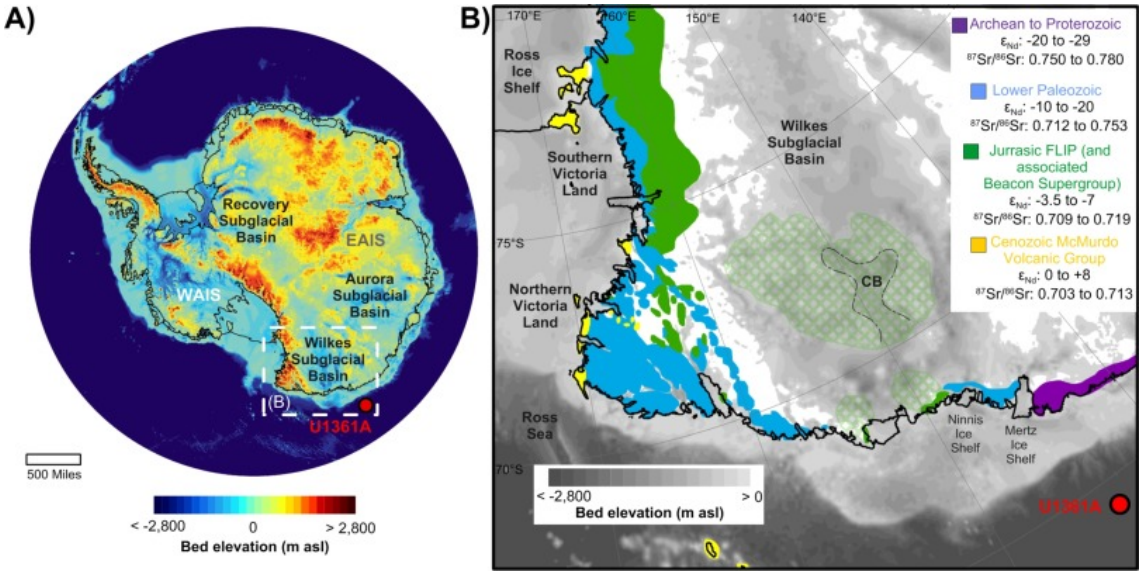


Fig. 1.4 Figure showing main East Antarctic subglacial basins and bedrock elevation (**a**), white dashed box is the region shown in **b**. Figure **b** shows the Wilkes subglacial basin and its central basin (CB), and source regions with characteristic geochemical signature found in sediments drilled at the site indicated by the red marker. Figure from Bertram et al. 2018.

The Aurora subglacial basin, extending inland from the terminus of Totten glacier, is another extensive region of the EAIS below sea level in the modern (Fig. 1.4). Aitken et al. (2016) combine airborne geophysical surveys and modelling to reconstruct grounding line retreat into the submarine basins in the Totten catchment. They find evidence for retreat of the Totten glacier into the Sabrina subglacial basin, which could contribute 2.18-2.89 m to sea level, and possibly into the Aurora basin, which would indicate ice sheet mass loss equivalent to 4.29 m of sea level rise (Aitken et al., 2016). However, the timing of this record in relation to the KM5c interval is not well constrained, so retreat into these

basins remains speculative. Conversely, Gulick et al. (2017) suggest a muted grounding line retreat in response to Pliocene warmth based on seismic survey data.

Evidence for retreat onto supra-marine bedrock in the EAIS is limited, with cosmogenic nuclide analysis of ANDRILL sediments suggesting very limited exposure of source material to subaerial conditions over the previous ~8 Ma (Shakun et al., 2018)). Given the source catchment in East Antarctica for sediments deposited at the ANDRILL site, this is interpreted as evidence for persistent glaciation for this region through the Pliocene into the modern. It is therefore incompatible with the retreat of EAIS grounding lines onto land-based regions of the ice sheet (Shakun et al., 2018).

Taken together, far field records of Pliocene sea level can provide estimates of overall ice sheet volume whilst ice proximal geological records can be be used to infer palaeo ice sheet margin position. These records of past ice sheet change, potentially equating to multi-metre sea level contributions and substantially different margin position (Section 5.2.6), can be used to constrain ice sheet model simulations and assess the plausibility of model parameter space.

## 1.5 Modelling the Pliocene Antarctic ice sheet

#### Comparable modelling studies of warm Pliocene

Since the SIA-only simulations of Hill (2009), efforts to simulate the Antarctic ice sheet in the warm Pliocene, along with the Greenland ice sheet, have incorporated an increasing range of uncertainties (Dolan et al., 2018, 2011, de Boer et al., 2015, Austermann et al., 2015, DeConto and Pollard, 2016, Golledge et al., 2017b, Yan et al., 2016). We refer the reader to Florindo et al. (2021) for a more complete summary of Pliocene ice sheet modelling studies to date, but highlight work of most relevance to the present study in the following.

Dolan et al. (2011) simulate sensitivity of both the Antarctic ice sheet and Greenland Ice Sheet (GrIS) to variations in Pliocene orbital configuration in the BASISM SIA model with 20 km horizontal resolution. Ice sheet model forcing is based on HadCM3 model simulations integrating proxy-based Pliocene initial conditions (Dowsett, 2007, Haywood et al., 2000), and insolation corresponding to the different extremes in Pliocene orbital configuration based on the astronomical solution of Laskar et al. (2004). Three experiments representing time points for Northern hemisphere summer insolation maxima, Northern hemisphere summer insolation minima and Southern hemisphere austral summer insolation minima (the maxima is equivalent to Pliocene Northern hemisphere minimum), as well as

average Pliocene and modern orbital insolation (Dolan et al., 2011). They simulate a range in Pliocene ice sheet volume, driven by orbital variations, of 25 m sea level equivalent (SLE) (Dolan et al., 2011). The GrIS shrinks under even the coldest Pliocene orbital configuration (loss of 35% of its modern mass). Conversely, Dolan et al. (2011) simulate EAIS volume changes from 20% loss compared with modern to 10% volume gain. As well as reconstructing a range of orbitally induced Pliocene sea level variability, Dolan et al. (2011) find that EAIS and GrIS sea level contribution can be anti-phased.

The largest concerted effort to understand ice sheet contributions to warm Pliocene sea level is the Pliocene Ice Sheet Model Intercomparison Project (PLISMIP) (Dolan et al., 2018, 2012, de Boer et al., 2015, Koenig et al., 2015). For the Antarctic component of PLISMIP, de Boer et al. (2015) explore the equilibrium response of six SIA-SSA ice sheet models to Pliocene climates derived again from HadCM3 with a range of elevation boundary conditions, with GIA represented in all models with an elastic lithosphere relaxing asthenosphere (ELRA) model (Meur and Huybrechts, 1996). They find dependence of modelled Pliocene ice sheet volume on ISM, climate and choice of initial condition.

Pliocene initial condition, ice sheet model, and additionally climate model uncertainty is further highlighted within the PLISMIP framework by Dolan et al. (2018). They simulate the Antarctic ice sheet with 3 ice sheet models, forced with a range of PlioMIP1 GCMs. These are HadCM3, COSMOS, CCSM4, IPSLCM5A, NorESM-L, MIROC4m and MRI-CGCM2.3 – though the modern climate forcings from the latter two GCMs result in ice sheets that do not agree with the modern configuration, and so are excluded (Dolan et al., 2018). Exploring sensitivity to choice of PlioMIP1 GCM for three ice sheet models, they find a ~12 m range in Antarctic contribution to Pliocene sea level.

Both De Boer et al. (2015), and Dolan et al. (2018) find strong sensitivity to choice of modern or reduced Pliocene (PRISM) initial condition. With six SIA-SSA ice sheet models under HadCM3 climate, mean sea level change is -1.89 ± 4.93 m SLE when initialised from modern, but increases to +9.76 ± 2.13 m SLE for simulations with a reduced initial ice sheet (de Boer et al., 2015). Across five PlioMIP1 GCMs and three ISMs, sea level contribution is +2.43 ± 3.53 m SLE with modern intial condition, and increases to +7.79 ± 4.06 m with a Pliocene initial condition (Dolan et al., 2018). Both studies find no retreat into East Antarctic submarine basins for modern initialised simulations. Moreover, a strong dependence of EAIS submarine basin deglaciation on GCM and ice sheet model is evident for PRISM initialised simulations. The SIA model used in Dolan et al. (2018) is a clear exception – simulating glaciated EAIS submarine basins for all initial conditions and GCM boundary conditions (Dolan et al., 2018).

Another approach to simulating Pliocene sea level contribution is the use of oxygen isotope enabled ice sheet models (Berends et al., 2019, Gasson et al., 2016) . These use the $\delta O^{18}$ record to reconstruct ice sheet volume compatible with oxygen isotope records. Using a $\delta O^{18}$ based approach, Berends et al. (2019)) reconstruct Antarctic and Greenland ice sheet volume through the last 5 Ma, finding sea level stands of 8-14 m above modern sourced from both Greenland and Antarctic ice sheets under Pliocene warmth. However, $\delta O^{18}$ based modelling approaches are sensitive to uncertainties in the oxygen isotope record which is uncertain (Raymo et al., 2018).

Some ice sheet modelling studies have sought to use the Pliocene as a constraint on future projections of sea level contribution. Higher end reconstructions of Pliocene sea level contribution have motivated the inclusion of a new parameterisation of ice sheet collapse, the Marine Ice Cliff Instability (MICI)(Section 1.2.3), in one ice sheet model (DeConto and Pollard, 2016, DeConto et al., 2021, Pollard et al., 2015). Using an early version of this model, DeConto and Pollard (2016) simulate a Pliocene sea level range from 3.52 m SLE (low ocean melt, MICI off) to 12.41 m SLE (high melt, MICI on). With a sea level calibration that rules out ensemble members that contribute < 10 m to Pliocene sea level, they project > 1 m SLE (0.64-1.05 m range) contribution from Antarctica by 2100 under a high emissions scenario, and > 15 m SLE in the next 500 years. However, the lower end of the Pliocene sea level reconstruction range can be reproduced in this model without the inclusion of MICI (Edwards et al., 2019). A subsequent study with an updated version of the same model, implementing MICI and calibrated against a Pliocene sea level range of 11 to 21 m, revised the estimate of 2100 Antarctic sea level contribution down, with a median of 0.34 m SLE (DeConto et al., 2021). For their Pliocene simulations, they simulated ice sheet contributions from 3.07 m SLE to 20.85 m SLE.

Another exploration of Pliocene AIS sea level contribution is that of Yan et al. (2016), who use bias-corrected PlioMIP1 NorESM climate simulations to force a PISM ice sheet model perturbed parameter ensemble. Yan et al. (2016) simulate a sea level contribution range from -4.2 m to 6.6 m, varying parameters related to ice sheet flow and surface mass balance calculations. They use an initial ice sheet configuration close to modern, and find that significant retreat into EAIS submarine basins only occurs if an additional warming of 8 °C is added to their Antarctic Pliocene climate (Yan et al., 2016).

## 1.6 Knowledge Gaps and study approach

This thesis will explore uncertainties in modelling the Antarctic ice sheet during the warm Pliocene and 21st century. Chapter 2 makes projections of the sea level contribution by

2100 using the BISICLES ice sheet model, under low and very high emissions scenarios, with a range of climate and ice sheet modelling choices. Chapters 3 and 4 develop BISICLES for simulating the Antarctic ice sheet during the warm Pliocene, by adding and testing various aspects of model setup needed for multi-millennial palaeo-ice sheet simulations, and exploring their associated uncertainties. Chapter 5 simulates the Antarctic ice sheet during the warm Pliocene with this new model setup, under a range of climate and ice sheet modelling choices, and compares the results with reconstructions of Pliocene ice sheet and sea level change. Chapter 6 summarises the findings across chapters.

The aim of the thesis is to demonstrate the impact of multiple modelling uncertainties on the Antarctic contribution to sea level rise during the 21st century and warm Pliocene, and constraints on the latter from palaeodata, to highlight priorities for reducing modelling uncertainties in both eras. Each chapter is described in more detail in the following sections.

### 1.6.1 Chapter 2: Century scale projections of Antarctic contribution to Sea level

Chapter 2 makes projections of the Antarctic contribution to sea level by 2100 using the BISICLES ice sheet model. These simulations were performed for the ISMIP6 (Ice Sheet Model Intercomparison Project for CMIP6, the Coupled Model Intercomparison Project Phase 6) for AR6 (Fox-Kemper et al., 2021), and were published in the synthesis by Edwards et al (2021). The chapter explores sensitivity of the projections to: future emissions scenarios, climate model, sensitivity of basal melting to ocean forcing, and ice shelf collapse. The aim of this chapter is to determine the importance of these uncertainties, and interactions between them, for the BISICLES contribution to ISMIP6 and probabilistic projections of the land ice contribution to 21st century sea level (Edwards et al., 2021).

The control simulation and seven of the experiments were carried out by D.F. Martin and C. Shafer. The remaining eleven simulations, along with analysis of all experiments, were carried out by this author on the National Energy Research Scientific Computing centre (NERSC) high performance computer (HPC) facility.

### 1.6.2 Chapter 3: Uncertainties at the base of the ice sheet

Chapter 3 focuses on developments in BISICLES for simulating the Antarctic ice sheet in the Pliocene, and exploring uncertainties related to processes at the base of the ice sheet. Interactions between the bedrock and the ice sheet are an important component

of ice sheet evolution across timescales (Section 3.2.1) (Whitehouse, 2018, Larour et al., 2019). In order to explore bedrock-ice sheet interactions, we use a recently developed BISICLES GIA implementation (GIANT-BISICLES) (Kachuck et al., 2020)(Section 3.2.2). Another important source of uncertainty in ice sheet modelling are interactions between the ice sheet and its bed, and ice stream evolution. We use the hydrology coupled basal sliding implementation (BISICLES_hydro) (Gandy et al., 2019)(Section 3.2.3), which has previously been applied to the British and Irish and Fennoscandian ice sheets, in order to represent hydrology coupled ice stream evolution. We implement an elevation dependent bed friction parameterisation to overcome challenges associated with simulating ice streams resting on over deepened West Antarctic bedrock.

We used this new BISICLES version incorporating the GIA component of GIANT-BISICLES and basal hydrology coupled BISICLES_hydro, to perform an ensemble of simulations for the Pine Island Glacier catchment of West Antarctica. This modelling framework allows us to explore the question: To what extent do uncertainties in:

- sensitivity of the bed to changing surface load
- ice stream evolution as a function of bed hydrology
- bed conditions in slow flowing regions of the domain
- sensitivity of basal melting to ocean forcing

impact the evolution of the Pine Island Glacier under Pliocene climate? We simulate this catchment at high resolution (1 km) in order to capture important processes, such as grounding line migration and interactions with small scale bed features.

This 30 member perturbed parameter ensemble was carried out by this author on the ARC4 HPC facility at the University of Leeds.

### 1.6.3 Chapter 4: Uncertainties in Pliocene climate

In Chapter 4, we present two sets of simulations that aim to address the question: How much of the variation in simulated Pliocene Antarctic mass loss can be attributed to:

- different modern initial conditions
- choice of climate forcing
- uncertainty in surface mass balance processes

Previous studies have explored ice sheet model sensitivity to multiple climate models (Dolan et al., 2018), initial conditions (de Boer et al., 2015, Dolan et al., 2018) and

perturbed surface mass balance processes (Yan et al., 2016). Dolan et al. (2018)(PLISMIP) use outputs from PlioMIP1 (Haywood et al., 2010) to force three ice sheet models initialised from modern and reduced ice sheets. Our work builds on that study by using outputs from the latest phase of the Pliocene Modelling Intercomparison Project (PlioMIP2)(Section 4.1.1) (Haywood et al., 2016b). An additional innovation of the work is the use of BISICLES. This has two key advantages. Firstly, BISICLES is a more physically comprehensive L1L2 model, whereas Dolan et al. (2018) use SIA and hybrid models. BISICLES can therefore more accurately capture important processes at the grounding line (Section 1.3.2). Secondly, BISICLES adaptive mesh refinement (Section 1.3.2) allows us to simulate ice sheet evolution over millennium time scales, at higher resolution (4 km) compared with 40 km resolution in Dolan et al. (2018).

Chapter 4 also assesses the role of initial conditions, and of uncertain parameters in the model that converts Pliocene temperature and precipitation to thickness change at the surface of the ice sheet - the surface mass balance scheme.

All simulations presented in this chapter were carried out by this author on the ARC4 HPC at University of Leeds.

### 1.6.4 Chapter 5: Perturbed Parameter Ensemble of the Antarctic ice sheet in the Pliocene

Chapter 5 uses the new model setup from the previous two chapters: new combinations of model components (Chapter 3; and here the GIANT-BISICLES GIA component is used for the whole ice sheet for the first time) and PlioMIP2 Pliocene climate forcing (Chapter 4). This model setup is used to address the following questions:

- What range of Pliocene Antarctic ice sheets do we simulate when incorporating known uncertainties in climate and ice sheet modelling?
- How do these simulated ice sheets compare with reconstructions of Pliocene Sea level, and the grounding line position in a key East Antarctic submarine basin?

To explore the first question we run a perturbed parameter ensemble of 120 BISICLES simulations. Using results from Chapters 3 and 4, we perturb parameters that drive the most uncertainty in:

- processes at the base of the ice sheet (ice shelf melting, basal sliding, bedrock ice sheet interactions)
- processes at the surface of the ice sheet (surface mass balance)

We also explore the sensitivity to a subset of PlioMIP2 models based on the results of Chapter 4.

Previous studies (DeConto and Pollard, 2016, DeConto et al., 2021) have invoked new processes to explain the largest Pliocene AIS sea level contributions. We aim to assess whether our BISICLES modelling framework can reproduce high end Pliocene sea level without MICI.

The importance of initial conditions in simulated warm Pliocene Antarctic ice sheet configuration has been shown in de Boer et al. (2015) and Dolan et al. (2018). We undertake a partial exploration of the impact of this uncertainty. To achieve this, we run 30 ensemble members from our main ensemble initialised from a reduced Pliocene ice sheet.

We also run the same subset of 30 ensemble members under modern climate to explore the impact of the parameter uncertainties under modern climate.

Finally, we compare our ensemble results to reconstructions of Pliocene sea level and reconstructions of the ice sheet margin. This allows us to explore some final questions:

- How compatible are our simulated ice sheets with available data?
- Can reconstructions indicate the most successful parameter values or Pliocene climate forcing in our modelling approach?

This section of the thesis will explore Pliocene ice sheet dynamics with a more physically comprehensive model than those used in previous studies of the AIS (Dolan et al., 2018, de Boer et al., 2015, DeConto and Pollard, 2016). It will also simulate the ice sheet at higher resolution than has been achieved for previous Pliocene studies (Dolan et al., 2018, de Boer et al., 2015, DeConto and Pollard, 2016). This will help capture important grounding line processes and bed topographic influences on ice sheet flow.

All simulations (120 main ensemble, 30 Pliocene initialisation, and 30 control) were carried out on ARC3 and ARC4 HPC facilities at the University of Leeds.

# Chapter 2

# Century scale projections of Antarctic contribution to Sea level

## 2.1 Introduction

The Antarctic and Greenland ice sheets are the third largest contributor to global mean sea level behind thermosteric changes (Palerme et al., 2017, Horwath et al., 2022). In recent decades, ice sheet mass loss has made up a growing proportion of sea level rise, which averaged 3.64 ± 0.26 mm $yr^{-1}$ between 2003 and 2016 (Horwath et al., 2022). From 1997 to 2007, the Antarctic ice sheet contributed 7.6 mm to global mean sea level rise (Shepherd et al., 2018). Although Antarctica was a smaller source of GMSL between 1993 and 2016 than other land ice sources and land water storage (Horwath et al., 2022), evidence of past volume and dynamics suggest that the ice sheet could become a significant source of GMSL in a warming climate (DeConto et al., 2021, Lowry et al., 2021, Edwards et al., 2019). To date, mass loss in Antarctica has been dominated by warm ocean currents eroding ice shelves in the Amundsen sea sector (Shepherd et al., 2018, Rignot et al., 2019), with reorganisation of ocean currents linked to anthropogenic warming driven changes to wind regimes (Holland et al., 2019). Around 32% of all of Earth's ice mass losses between 1997 and 2017 were accounted for by ice sheet discharge and ice shelf melt driven by ocean warming (Slater et al., 2021). Along with some East Antarctic basins, the West Antarctic ice sheet is vulnerable to ocean driven instabilities as grounding lines retreat into over-deepened subglacial basins (Schoof, 2012, Weertman, 1974, Thomas, 1979). At present, around 23m of sea level equivalent ice rests on bedrock below sea level (Morlighem et al., 2020).

Under anthropogenic warming, destabilisation of marine grounded ice could drive accelerating Antarctic GMSL contribution to 2100 and beyond (Schlegel et al., 2018, Bulthuis et al., 2019, Lowry et al., 2021, Edwards et al., 2019, DeConto and Pollard, 2016, Golledge et al., 2015, Ritz et al., 2015). Moreover, dynamic instabilities amplify uncertainty in future sea level projections (Robel et al., 2019). Alongside ocean driven retreat under anthropogenic warming, increased Antarctic surface mass balance has the potential to mitigate the ice sheet's sea level rise contribution. Warmer air temperatures over the Antarctic can increase precipitation, driving increased surface mass balance under the cold, low melt conditions of the ice sheet (Frieler et al., 2015, Palerme et al., 2017). Over the course of the 20th century, increased precipitation offset 10 mm of AIS sourced GMSL (Medley and Thomas, 2019).

Ice sheet models have developed to represent a greater range of interactions and dynamic processes at higher resolution than ever before (Pattyn et al., 2017)(see Chapter 1). However, differences in process scale representation, model physics, spatial discretisation and initialisation (Seroussi et al., 2019) mean that different ice sheet models project different AIS responses to the same climate boundary conditions (Edwards et al., 2014a, Bindschadler et al., 2013). The Ice Sheet Model Intercomparison Project for the Coupled Modelled Intercomparison Projects Phase 6 (CMIP6), ISMIP6 (Nowicki et al., 2016), builds on previous multi-model ensemble efforts (e.g. Edwards et al. 2014a, Bindschadler et al. 2013) to better characterise uncertainty in projected future GMSL from Greenland and Antarctic ice sheet model and global climate model uncertainty (Nowicki et al., 2016).

To explore the role of ice sheet models that differ in approximations of ice physics, basal sliding, model resolution and initialisation approaches, ISMIP6 provides consistent boundary conditions and suggests an ice shelf basal melt parameterisation for projection experiments (Nowicki et al., 2016). Flexibility in the ISMIP6 approach recognises the challenges associated with using the same initialisation procedure across ice sheet models, which is explored in Seroussi et al. (2019), as well as challenges in implementing new ice shelf basal melt parameterisations in ice sheet models. By including a range of ice sheet models with the same boundary conditions, with participating modelling group using a comparable set up to those used in other projection studies with the same models, ISMIP6 quantifies range of modelled sea level projections due to ice sheet model choice.

Results of ISMIP6 Antarctic ice sheet experiments forced with Coupled Model Intercomparison Project Phase 5 (CMIP5) climate models alongside the role of ice shelf collapse are explored in Seroussi et al. (2020), who find a range of -7.8 cm to 30.0 cm sea level equivalent (SLE) contribution from Antarctica from 2015 to 2100, under a very high emissions scenario (RCP8.5). Under a low emissions scenario (RCP2.6) with two CMIP5

models, an average additional mass loss of 0 to 3 cm is found (Seroussi et al., 2020). Comparing Antarctic projections using CMIP5 and CMIP6 climate forcings, Payne et al. (2021) find a limited difference between projections grouped by generation of CMIP climate model. This is attributed to the complexity of interactions between the AIS and the climate system (Payne et al., 2021). With the exception of InitMIP (Seroussi et al., 2019), BISICLES ISMIP6 Antarctic experiments have not yet been presented in detail, only used in the ISMIP6 synthesis and sensitivity tests of Edwards et al. (2021).

We present a set of 19 simulations (18 projections and a control) run with the BISICLES ice sheet model following the ISMIP6 protocol for future projections of the Antarctic ice sheet. Our simulations follow the design for Tier 1,2 and 3 experiments (see below) and we also explored the relationship between ocean melt and ice shelf collapse through additional sensitivity experiments. The Tier 1-3 experiments contribute to the ISMIP6 effort by adding another Antarctic ice sheet model to the ensemble, while the additional sensitivity experiments target uncertainties in the synthesis by Edwards et al. (2021): for example, by testing for interactions between uncertain parameters.

The control run along with the seven experiments 5-12 in Table 2.2 were carried out by Dan Martin and Courtney Schafer. The eleven experiments 13-B7 in Table 2.2 were carried out by this author.

ISMIP6 has tiers of experiments to indicate experiment priority to participating modelling groups. Experiments 5-13 are ISMIP6 Tier 1 experiments, the highest priority Tier and mandatory for inclusion in ISMIP6 (Nowicki et al., 2016). Tier 1 experiments explore the range of climate uncertainty for high skill GCMs representing the range of models in CMIP5 (Barthel et al., 2020), under two future emissions scenarios, and the impact of ice shelf fracture and sensitivity of basal melting to ocean forcing (Nowicki et al., 2016).

Tier 2 ISMIP6 experiments (Nowicki et al., 2016) explore ice sheet model sensitivity to the wider set of GCMs selected in Barthel et al. (2020) from the CMIP5 ensemble, as well as CMIP6 models based on availability. We present results for two Tier 2 simulations. In addition to Tier 1 and Tier 2 experiments, we also present results from ISMIP6 Tier 3 experiments. Tier 3 experiments provide a more in-depth exploration of the role of ocean sensitivity in modelled AIS evolution to complement Tier 1 (Nowicki et al., 2016). Tier 3 experiments are D52-D58 in Table 2.2.

Alongside ISMIP6 experiments from Tiers 1 to 3, we present results from some experiments outside the original ISMIP6 protocol. These simulations (T71, T73, TD58) support a more detailed exploration of basal melt sensitivity and ice shelf fracture in Edwards et al. (2021). Experiments T71 and T73 explore high basal melt sensitivity under a low

emissions scenario. TD58 is an experiment with high basal melt sensitivity and ice shelf collapse under very high emissions.

## 2.2 Methods

### 2.2.1 BISICLES

BISICLES is a block structured, finite volume, L1L2 physics ice sheet model with adaptive mesh refinement (Cornford et al., 2013, 2016, 2015)(Section 1.3.2). For these simulations, we use the BISICLES_B version as in (Seroussi et al., 2019). All simulations are run with a base resolution of 8km with 3 levels of refinement to give a finest mesh resolution of 1km. The model domain at the coarsest level covers a grid of 768 x 768 cells. We use the subgrid friction interpolation scheme described in Cornford et al. (2016), which allows for finest resolution of 1 km at the grounding line and in regions of fast flowing ice.

Basal traction is calculated using a pressure limited Weertman-Coulomb type law (Tsai et al., 2015)(Section 1.3.3) with m=1/3 and a Coulomb friction coefficient of 0.5. Basal traction coefficients and effective viscosity are estimated using an inversion approach to minimize the mismatch between observed and modelled ice speed (Cornford et al., 2015), and are held constant throughout the simulations. Ice temperature is from Pattyn et al. (2010), who simulated ice sheet temperature with a 3D thermo-mechanical ice sheet model, and is fixed throughout the simulations. All simulations are initialised from a short relaxation run as in previous BISICLES studies (Cornford et al., 2016), and simulate the period 2010-2100.

Ice sheet contribution to sea level is a function of change in volume above floatation (VAF). Volume Above Floatation is the volume of ice sheet that is not below sea level or hydrostatic equilibrium, and is therefore not already displacing ocean water. To calculate sea level contribution, or change in VAF in metres sea level equivalent (m SLE) for the modern ocean, we distribute sea level equivalent change in VAF over ocean area of $3.625 \times 10^{14}$ $m^2$ (Gregory et al., 2019) with ocean density of 1028 kg $m^{-3}$ and ice density 918 kg $m^{-3}$.

### 2.2.2 Ocean and atmosphere forcing

In order to facilitate a consistent approach across participating modelling groups, ISMIP6 provide surface mass balance and ocean thermal forcing data from a subset of CMIP5 and CMIP6 climate models. The selection process for core experiment model forcing is

outlined in Barthel et al. (2020). Core experiments use CMIP5 model outputs to provide boundary conditions, which are chosen based on skill in simulating atmospheric and ocean variables compared with observations (Barthel et al., 2020) whilst sampling a diverse subset of models in terms of simulated climate. The selection process for CMIP6 boundary condition models was more pragmatic, and based on availability. We sample one CMIP6 model in our simulations - CNRM-CM6-1.

To promote a consistent approach to basal melt forcing across ice sheet models most participating groups used a prescribed basal melt parameterisation (Jourdain et al., 2020), which describes the relationship between basal melting, $m$, and ocean thermal forcing, $TF$. BISICLES implements the "non-local" basal melt rate parameterisation. The non-local basal melt parameterisation captures the melt-induced cavity scale circulation changes that drive shelf melt (Jourdain et al., 2017), as well as the local influence of stratification, and compares favourably to coupled ice sheet ocean models in idealized experiments (Favier et al., 2019). A more comprehensive summary of the ISMIP6 non-local approach to calculating basal melt can be found in (Jourdain et al., 2020). It is restated here:

$$\begin{aligned} m(x,y) = \gamma_0 \times & \left(\frac{\rho_{sw} C_{pw}}{\rho_i L_f}\right)^2 \\ & \times (TF(x,y,z_{draft}) + \delta T_{sector}) \\ & \times |\langle TF \rangle_{draft \in sector} + \delta T_{sector}|, \end{aligned} \tag{2.1}$$

where $\rho_{sw}$ and $\rho_i$ are the densities of ice (918 kg m$^{-3}$) and sea water (1028 kg m$^{-3}$) respectively; $L_f$ is fusion latent heat of ice ($3.3 \times 10^5$ J kg$^{-1}$); and $C_{pw}$ is specific heat of sea water (3974 J kg$^{-1}$ K$^{-1}$). The first $TF$ is calculated at the ice-ocean interface, and the second is averaged over each of 16 sectors.

The basal melt parameter, $\gamma_0$, is calibrated against two sets of observations to span a range of possible sensitivities of the ice shelves to basal melt. For both calibration approaches, the temperature corrections $\delta T_{sector}$ are initially set to zero, and $\gamma_0$ is tuned to match one of the two observational constraints. In the first approach, $\gamma_0$ is tuned to reproduce total Antarctic melt rate sampled equally from normal distributions of two estimates of total Antarctic basal melt (Depoorter et al., 2013, Rignot et al., 2013). By repeat sampling melt estimates and error in thermal forcing, a distribution for $\gamma_0$ is generated (Jourdain et al., 2020). The $5^{th}$, median and $95^{th}$ percentiles are taken from this distribution and corresponding distributions of temperature corrections $\delta T_{sector}$ are generated for each $\gamma_0$ percentile value based on sector integrated melt rates. Median $\delta T_{sector}$ values for each of the three $\gamma_0$ percentile values are used in the experiments. As in Jourdain et al. (2020), we refer to this as the *MeanAnt* calibration, and specify the $\gamma_0$ percentile used.

The second calibration method follows a similar two stage approach. However, where the *MeanAnt* calibration approach uses estimates of total Antarctic melt, the second calibration approach samples the ten grid points with the highest melt rates and associated thermal forcing at the grounding line of the Pine Island Glacier (Jourdain et al., 2020). The calibration to Pine Island grounding line melt rates reflects the possibility that, in a warmer climate, dynamics at this deep West Antarctic grounding line may be more indicative of grounding line dynamics across the ice sheet as a whole (Reese et al., 2018b). As with the *MeanAnt* calibration, $5^{th}$, median and $95^{th}$ percentiles of $\gamma_0$ and associated median $\delta T_{sector}$ are provided. Again we follow Jourdain et al. (2020) and refer to these as PIGL simulations. In all, six values of $\gamma_0$ are provided (Table 2.1), of which five are sampled in the simulations presented here - we did not run a simulation with $PIGL_{5th}$. Average surface ocean (500 m) thermal forcing from 2015 to 2100 for the GCMs used here is shown in Figure 2.1.

| Calibration | $5^{th}$ | Median | $95^{th}$ |
|---|---|---|---|
| *MeanAnt* | 9,620 | 14,500 | 21,000 |
| *PIGL* | 88,000 | 159,000 | 471,000 |

Table 2.1 Calibrated $\gamma_0$ values used in m yr$^{-1}$

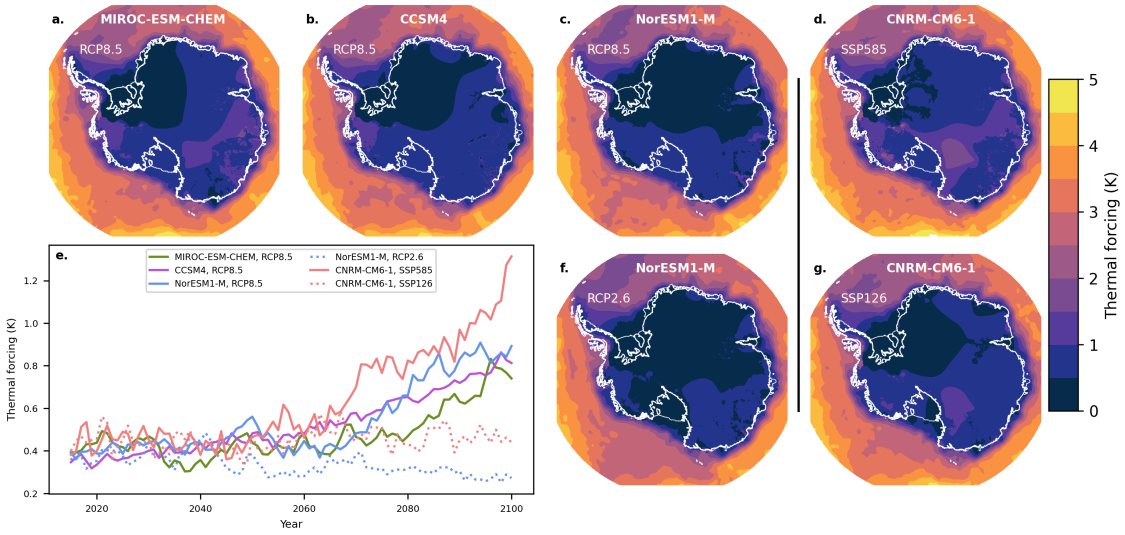


Fig. 2.1 Average thermal forcing ($TF$) in the upper ocean (500 m) (**a**,**b**,**c**,**d**, **f**,**g**), averaged from 2015 to 2100 for each of the climate models and emissions scenarios used. Subplot **e** shows mean annual upper (500m) ocean thermal forcing from 2015 to 2100 for each of the models and scenarios used. Black vertical line separates CMIP5 models forced with RCP scenarios from the CMIP6 model, SSP scenario climate fields.

For the surface boundary condition, surface mass balance anomalies were provided directly from GCMs relative to a January 1995 to December 2014 reference period (Nowicki et al.,

2016). The anomaly was added to a baseline surface mass balance taken from Arthern et al. (2006). This approach does not account for the evolving topography of Antarctica over the simulation period. Average surface mass balance anomaly for 2015 to 2100 is shown in Figure 2.2.

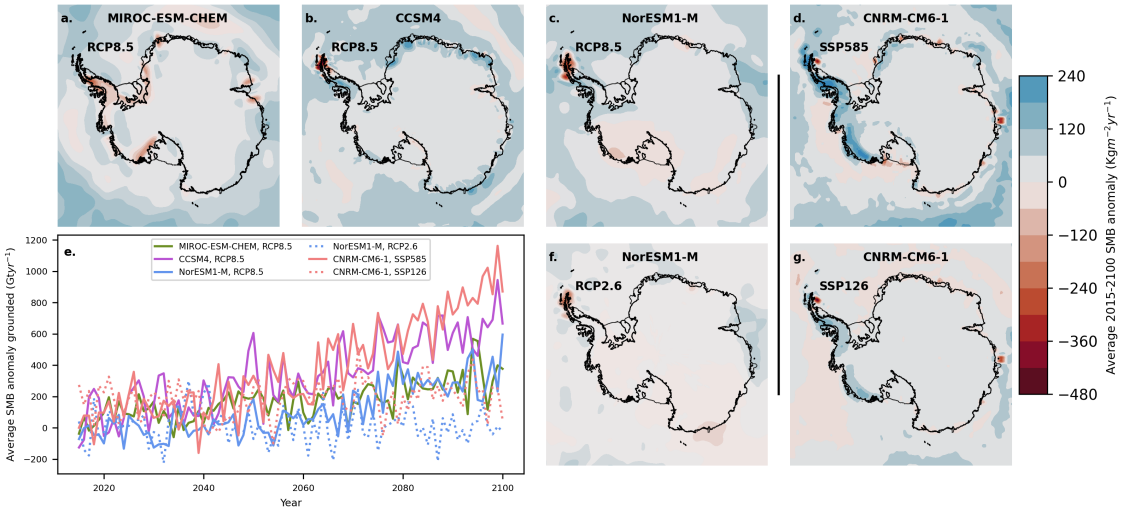


Fig. 2.2 Average surface mass balance anomaly from 2015 to 2100 (subplots **a**,**b**,**c**,**d**, **f**,**g**). Subplot **e** shows mean annual surface mass balance anomaly relative to 1995-2014 over the ice sheet. Black vertical line separates CMIP5 models forced with RCP scenarios from the CMIP6 model, SSP scenario climate fields.

Inclusion of melt driven hydrofracture and subsequent shelf collapse is a relatively recent innovation in ice sheet models (Pollard et al., 2015), and is not directly implemented in those participating in ISMIP6. Surface melt driven availability of water can enhance propagation of crevasses in the ice shelf, driving weakening and eventual collapse (Scambos et al., 2009), though shelf disintegration has also been observed under lower surface melt conditions (Scambos et al., 2009). In order to capture surface melt enhanced shelf disintegration, ISMIP6 provide time dependent masks of ice shelf collapse. These are derived from atmospheric forcing data sets such that if surface air temperature driven melt of 725 mm$a^{-1}$ water equivalent persists for 10 years, ice shelf is removed (Trusel et al., 2015).

We explore the impact of shelf collapse with two sets of experiments (Table 2.2). Both sets of collapse simulations use the same climate forcing and therefore shelf collapse mask. In 'collapse on' experiments, the shelf collapse progresses southward through time, from the Antarctic Peninsula towards the South pole.

### 2.2.3 Control Simulation

ISMIP6 require a control simulation to subtract from projection simulations, to remove model drift (Nowicki et al., 2016). Our control simulation uses the modern surface mass balance field from Arthern et al 2006, which the anomaly is applied to in projection simulations. For the control simulation, basal melting is applied such that localised thickening as a result of ice advection or surface mass balance is removed. Basal melt due to ocean thermal forcing is not applied, and accumulation onto the lower surface is not permitted in this BISICLES version (BISICLES version B in Seroussi et al. (2019)). Whilst shelves can thin locally due to advection of ice out of grid cells, this holds the ice shelves close to to their initial geometry.

## 2.3 Results

### 2.3.1 Control Simulation

From 2015 to 2100, the control simulation lost 50,149 Gt of total mass, 19,220 Gt of mass above sea level and had an overall loss of $6.9 \times 10^3$ km$^2$ in total areal extent, whilst floating area grew by $64.6 \times 10^3$ km$^2$. In total, the control run contributes 60 mm to sea level between 2015 and 2100 (Fig. 2.3).

Thinning occurs over large regions of the Amundsen sea sector, with some grounding line retreat at Thwaites glacier (Fig. 2.3). Major ice shelves (Ross, Ronne-Filchner and Amery) also thin, along with their tributary ice streams. However, thinning of Lambert Glacier is less pronounced than in some ice streams on the Siple coast or those feeding the Ronne-Filchner shelf, consistent with a limited response of this catchment to shelf thinning in previous studies (Gong et al., 2014). In East Antarctica, ice streams at the margins of Victoria Land, Wilkes Land and Queen Maud land all undergo thinning in the control experiment, as do ice shelves in the Peninsula along with grounded ice abutting the George VI ice shelf.

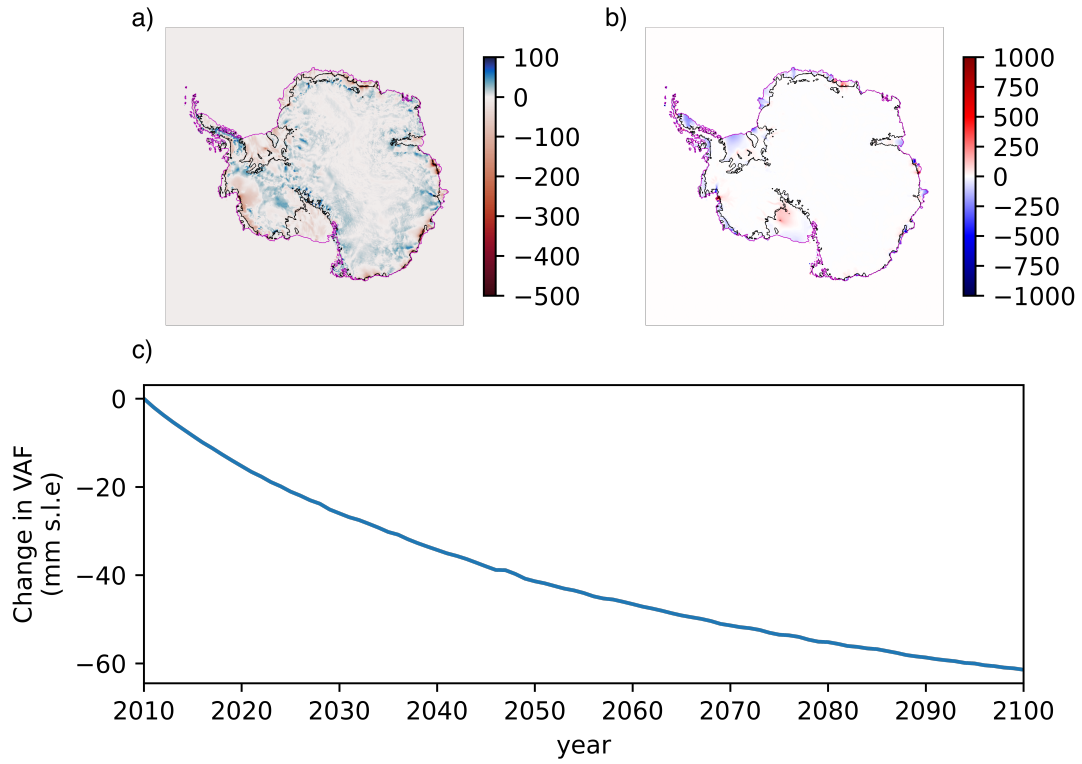


Fig. 2.3 Control run simulation output. Subplot **a** shows thickness change in metres. Subplot **b** shows the increase in ice speed from the start of the simulation to 2100 in m $yr^{-1}$. Subplot **c** shows the change in volume above floatation (VAF) for the control run from 2010 to 2100.

The most pronounced ice stream speed up in the control simulation occurs in the Thwaites glacier and its ice shelf (Fig. 2.3), consistent with grounding line retreat. By contrast, Pine Island glacier slows down between 2015 and 2100 in the control run. Along the Siple coast, Whillans ice stream (Ice Stream B) accelerates between 2015 and 2100, with grounding lines in this sector undergoing modest retreat (Fig. 2.3). Overall, outer edges of major ice shelves slow down over the simulation period, with the exception of some ice shelves on the Dronning Maud Land and the West Ice shelf. In these sectors, localised grounding line retreat is associated with speed up of ice across the grounding line and out to the shelf edge.

### 2.3.2 Projections

| Experiment | Scenario | GCM | $\gamma_0$ (m a$^{-1}$) | $\gamma_0$ percentile | Collapse | ΔVAF (mm SLE) |
|---|---|---|---|---|---|---|
| 5 | RCP8.5 | NorESM1-M | 14,477 | $MeanAnt_{50}$ | OFF | -31 |
| 6 | RCP8.5 | MIROC-ESM | 14,477 | $MeanAnt_{50}$ | OFF | 2 |
| 7 | RCP2.6 | NorESM1-M | 14,477 | $MeanAnt_{50}$ | OFF | -38 |
| 8 | RCP8.5 | CCSM4 | 14,477 | $MeanAnt_{50}$ | OFF | 45 |
| 9 | RCP8.5 | NorESM1-M | 21,005 | $MeanAnt_{95}$ | OFF | -39 |
| 10 | RCP8.5 | NorESM1-M | 9,619 | $MeanAnt_{5}$ | OFF | -23 |
| 12 | RCP8.5 | CCSM4 | 14,477 | $MeanAnt_{50}$ | ON | 20 |
| 13 | RCP8.5 | NorESM1-M | 159,188 | $PIGL_{50}$ | OFF | -82 |
| D52 | RCP8.5 | NorESM1-M | 471,264 | $PIGL_{95}$ | OFF | -91 |
| D53 | RCP8.5 | MIROC-ESM | 159,188 | $PIGL_{50}$ | OFF | -71 |
| D55 | RCP8.5 | MIROC-ESM | 471,264 | $PIGL_{95}$ | OFF | -121 |
| D56 | RCP8.5 | CCSM4 | 159,188 | $PIGL_{50}$ | OFF | -31 |
| D58 | RCP8.5 | CCSM4 | 471,264 | $PIGL_{95}$ | OFF | -102 |
| T71 | RCP2.6 | NorESM1-M | 159,188 | $PIGL_{50}$ | OFF | -62 |
| T73 | RCP2.6 | NorESM1-M | 471,264 | $PIGL_{95}$ | OFF | -57 |
| TD58 | RCP8.5 | CCSM4 | 471,264 | $PIGL_{95}$ | ON | -125 |
| B6 | SSP5-8.5 | CNRM-CM6-1 | 14,477 | $MeanAnt_{50}$ | OFF | 53 |
| B7 | SSP1-2.6 | CNRM-CM6-1 | 14,477 | $MeanAnt_{50}$ | OFF | 17 |

Table 2.2 Experiment list along with projected change in volume above floatation (VAF) relative to the control simulation from 2015 to 2100.

The range of projected changes in volume above floatation at 2100, relative to the control simulation, is 53 mm sea level equivalent (SLE) mass gain (-53 mm SLE SLC) of the Antarctic ice sheet to -125 mm SLE mass loss (125 mm SLE SLC) (Table 2.2; Figure 2.4). The majority of projections show net mass loss (negative VAF changes) over the 21$^{st}$ century. Of the 18 projections presented here, five show net mass gain i.e. they gain more mass through accumulation than they lose through basal melt and dynamic contribution, driving a sea level fall. All five are for very high emissions scenarios (RCP8.5/SSP5-8.5), and are forced by two GCMs: CCSM4 from CMIP5 (under *MeanAnt* basal melt parameterisation) and CNRM-CM6-1 from CMIP6.

### 2.3.3 Change in ice area

Grounded ice sheet area through time is shown in Figure 2.5, grouped by GCM forcing. With the exception of NorESM1-M RCP2.6 under $PIGL_{95}$, all simulations lose grounded area by 2100, though under $PIGL_{50}$ and $PIGL_{95}$ this decrease is not monotonic. Perhaps

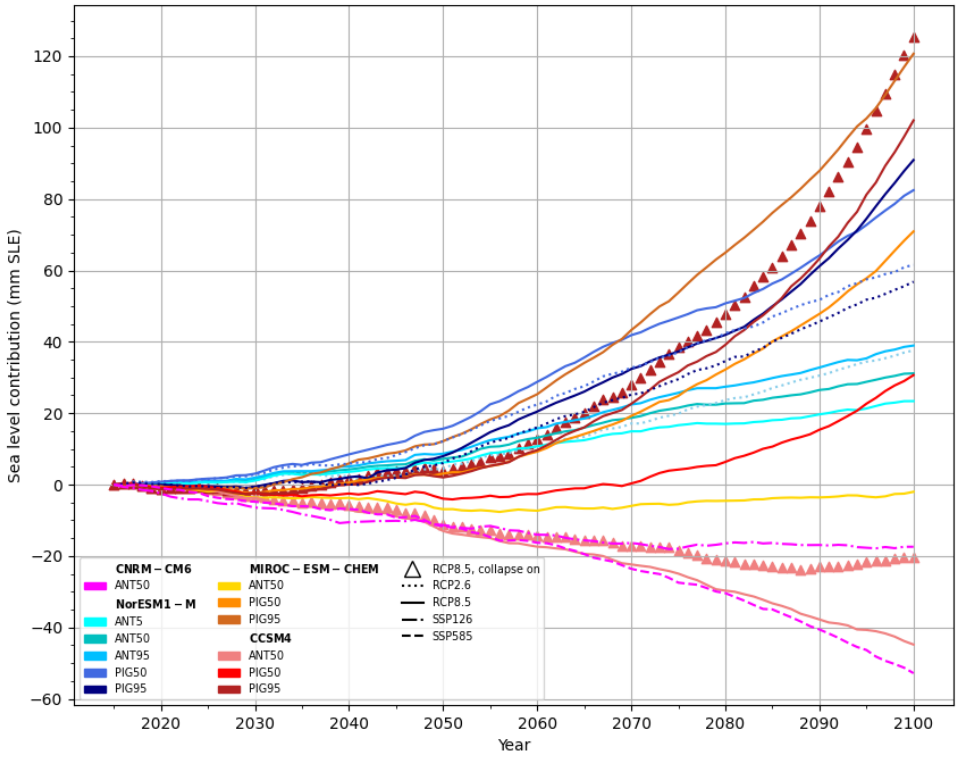


Fig. 2.4 Sea level contribution (mm) for all projections relative to control from 2015 to 2100.

counter-intuitively, initial grounded area increases with greater basal melt sensitivity to thermal forcing (i.e. higher values of $\gamma_0$: from lighter to darker colours in Figure 2.5). The differences in experiments between *MeanAnt* percentiles are small because the $\gamma_0$ values are similar (Table 2.1). However, high basal melt sensitivity (*PIGL*) experiments decrease in grounded area much more quickly, generally to smaller final values than the *MeanAnt* experiments despite their larger areas in 2015.

In contrast, floating ice sheet area is larger at 2100 compared with 2015 for all experiments with the exception of ice shelf collapse simulations (CCSM4: triangles in Figure 2.6) and NorESM1-M RCP2.6 under the highest Pine island basal melt sensitivity ($PIGL_{95}$). The overall pattern of reduced grounded ice sheet area alongside an increased floating area is consistent with grounding line retreat and loss of volume above floatation.

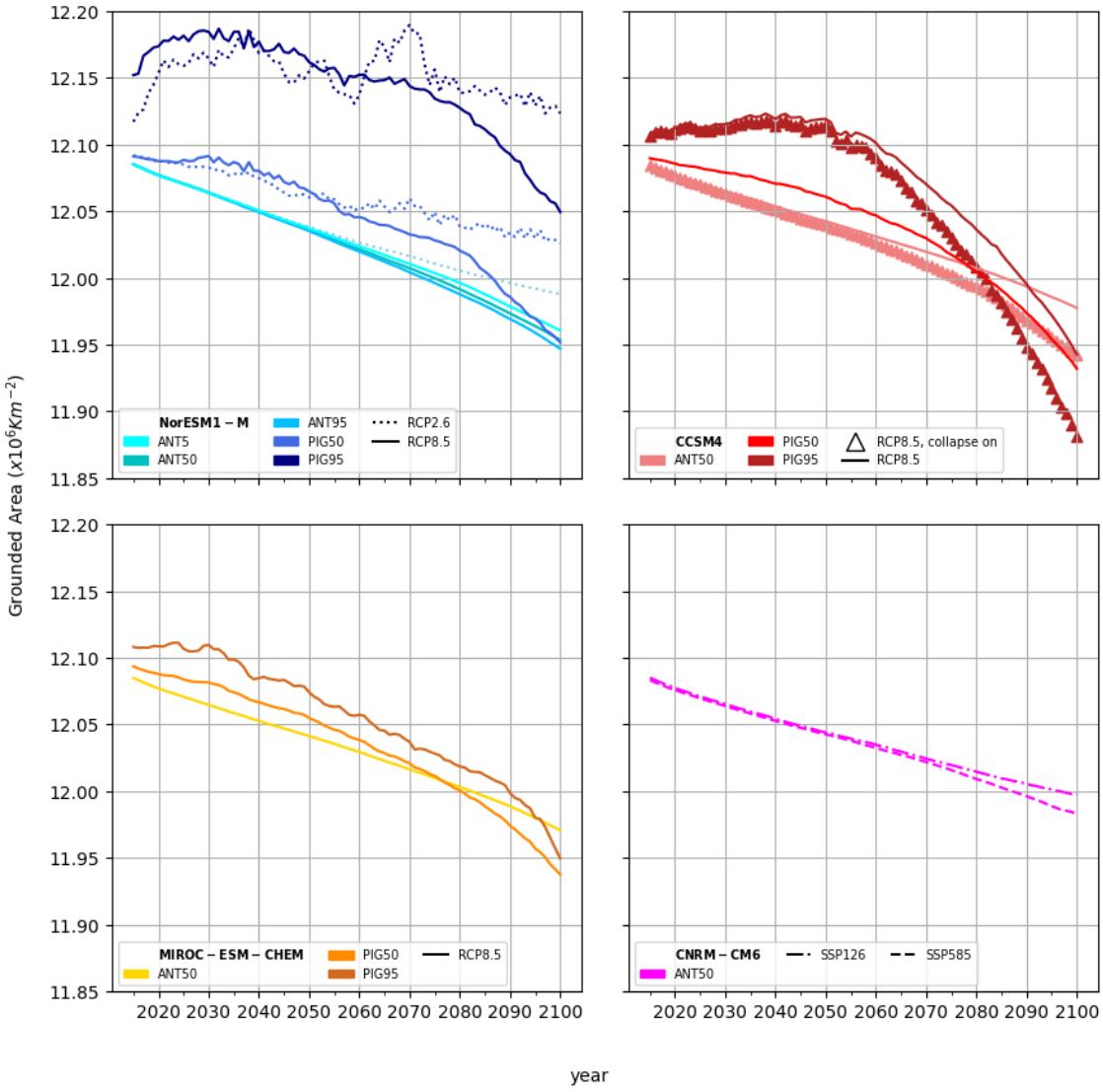


Fig. 2.5 Grounded ice sheet area for all simulations from 2015 to 2100.

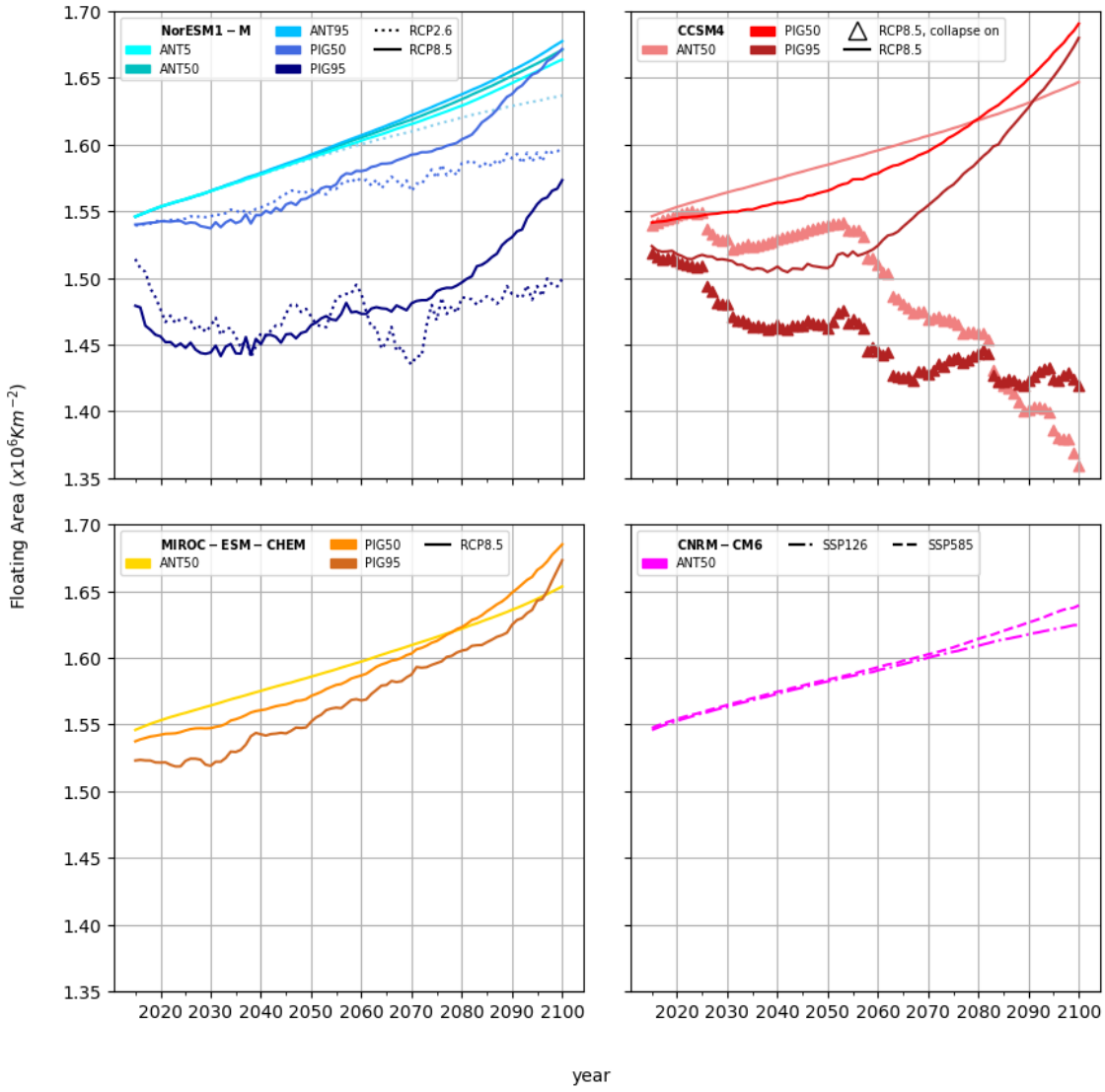


Fig. 2.6 Floating ice sheet area for all simulations from 2015 to 2100.

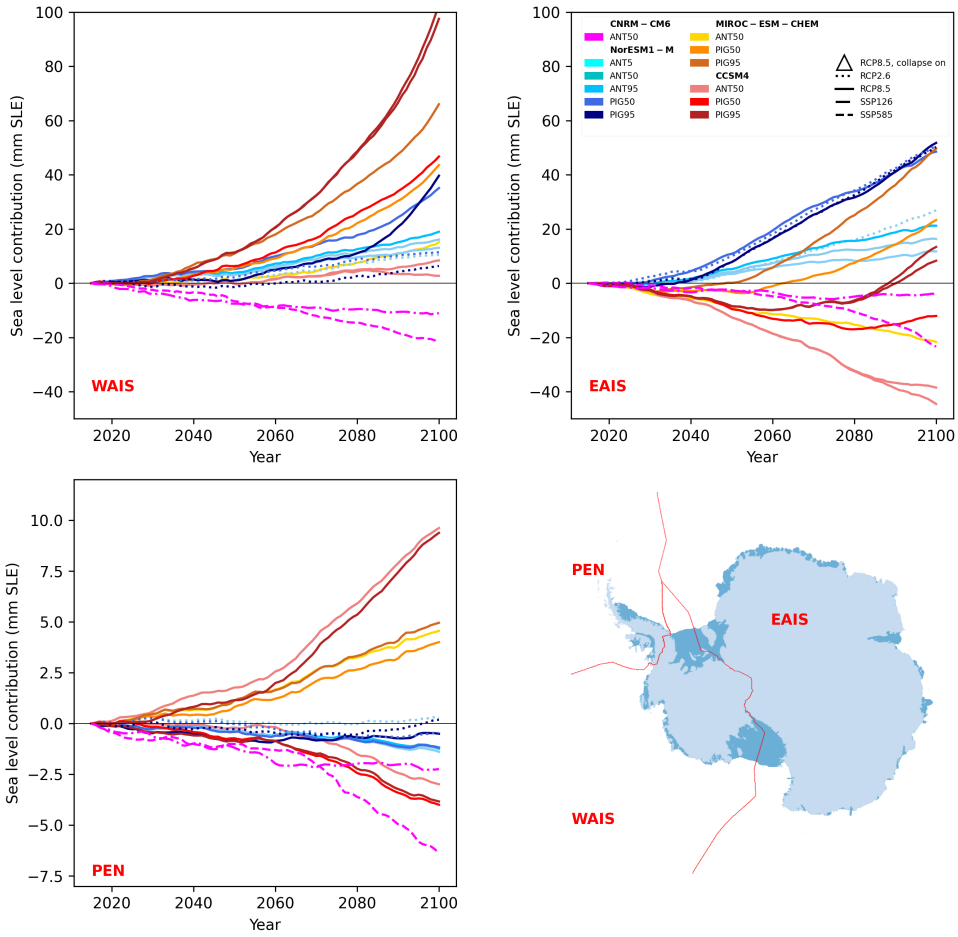


Fig. 2.7 Sea level contribution (loss of volume above floatation) (mm SLE) for East Antarctic (EAIS), West Antarctic (WAIS) and Peninsula (PEN) ice sheets from 2015 to 2100. Inset plot shows mask boundaries used to calculate regional change in volume above floatation

### 2.3.4 Regional contributions

To explore the distinct responses of West Antarctic, East Antarctic and Peninsula ice sheets to perturbed boundary conditions and basal melt sensitivity, we partition sea level equivalent mass change for these three regions. For WAIS, sea level contribution ranges from 103 mm SLE (-103 mm SLE change in VAF) to -22 mm SLE (it gains 22 mm SLE VAF). All but two experiments project a WAIS contribution to sea level rise at 2100. Projected sea level contribution for the EAIS ranges from 52 mm SLE rise (a VAF change of -52 mm SLE) to a sea level fall of 45 mm SLE (it gains 45 mm SLE VAF). Volume above floatation increases to 2100 for the EAIS in more experiments compared with WAIS – with 6 projections of sea level fall at 2100. Projections of Antarctic Peninsula change in VAF range from -9 mm SLE to +6 mm SLE. For this region, 10 experiments project increased volume above floatation relative to control. We note that the CMIP6 CNRM-CM6-1 forced simulations result in sea level fall for both scenarios and all regions.

To further partition SLE ice sheet mass change, results are presented for 16 drainage basins. Following the ice sheet mass balance inter-comparison exercise (IMBIE) assessment (Shepherd et al., 2018), Antarctica is divided into 18 sectors - with each of the major ice shelves (Ross and Filchner-Ronne) bisected by a sector boundary. To reflect the connectivity of water masses under the major ice shelves and avoid unphysical melt discontinuities imposed by sector boundaries within cavities, the two sectors feeding the Ross Ronne-Filchner ice shelves are merged to give 16 basins in total (Jourdain et al., 2020). The basins are used to derive basin scale parameters in the basal melt parameterisation, and to extrapolate under ice shelves in the ocean data preparation (Jourdain et al., 2020).

In terms of sectoral sea level contribution, the Totten sector (4) has the largest sea level contribution of any sector for the most runs (n=9) (Fig. 2.8). All but one simulation contribute to sea level, with SLE change in VAF ranging from +1 mm to -40 mm, with a mean sea level contribution of 21 mm. The Amundsen Sea Embayment sector (9) contributes to sea level rise in all but the two CNRM-CM6-1 forced projections. For four experiments, the ASE is the sector with the largest projected contribution to sea level rise. Sea level contributions in the ASE range from 5 mm sea level fall to 36 mm sea level rise, with mean loss of 12 mm SLE VAF.

In the Filchner-Ronne sector (14), nine simulations increase their VAF up to 13 mm SLE – the largest mass gain in any sector and experiment. The Filchner-Ronne has a large area over which to accumulate mass. However, for two simulations with highest basal melt sensitivity under CCSM4 RCP8.5, the Filchner-Ronne sector undergoes loss of VAF equivalent to a 46 mm sea level rise. This is the largest contribution to sea level rise of any sector and gives Filchner-Ronne the largest projected range. The projected range in

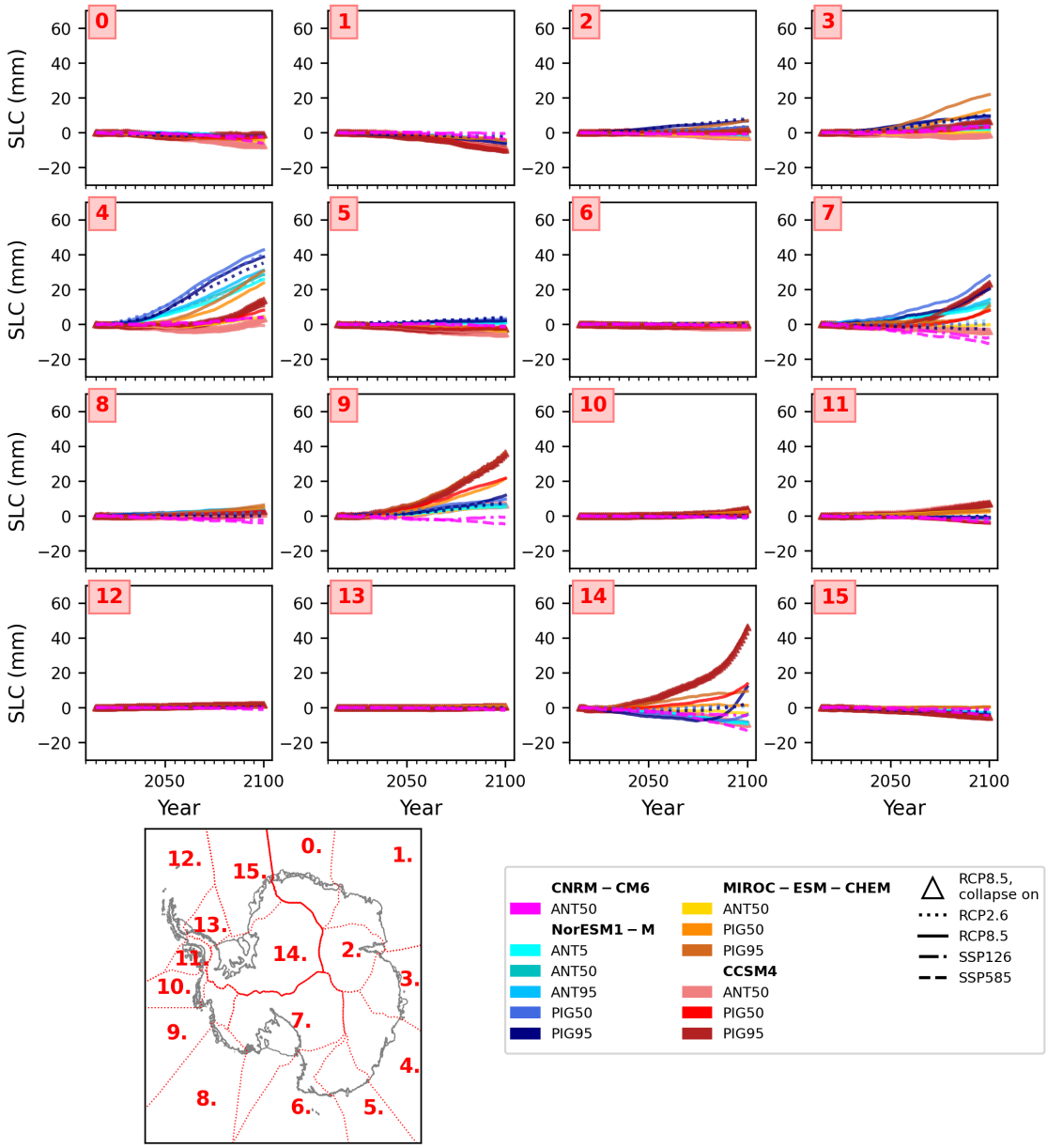


Fig. 2.8 Sea level contribution by sector for all simulations. Basins are numbered are as follows: 0: Dronning Maud Land; 1: Enderby Land; 2: Lambert Glacier catchment; 3: Wilhelm II land; 4: Totten Sector; 5: George V Land; 6: Oates Land; 7: Ross Ice Shelf; 8: Getz ice shelf sector; 9: Amundsen Sea Embayment sector; 10: Abbott ice shelf sector; 11: George VI ice shelf sector; 12: Larsen sector; 13: Palmer Land; 14: Filchner-Ronne sector; 15: Brunt ice shelf sector.

this sector illustrates the competing processes of increased accumulation under warming on the one hand (Payne et al., 2021) and increased mass loss due to basal melting on the other. When sensitivity to ocean melt is low, increased accumulation dominates ocean melt driven mass loss. Conversely, under higher ocean melt sensitivity, ocean melt driven mass loss counteracts the warming driven negative surface mass balance (SMB) feedback. Under highest basal melt sensitivity, loss of VAF is 55 mm greater than under equivalent lower ocean sensitivity scenarios with the same forcing in the Filchner-Ronne sector.

The other sector with a major ice shelf, the Ross Sea sector (7), contributes to sea level in eleven simulations, although it too has mass gain up to 11 mm SLE for lower ocean melt sensitivity experiments. The largest projected sea level contribution from the Ross sector is 24 mm for the same two experiments that lose 46 mm SLE VAF in the Filchner-Ronne sector.

For the ASE, the control simulation contributes 30 mm to sea level (loses 30mm SLE VAF). Whilst subtracting the control can account for model drift, it may also in this instance be removing the sea level signal from the ASE due to instability initiated before 2015. Evidence for marine ice sheet instability in the ASE is equivocal, with the IPCC AR6 stating that observed flow regimes in the ASE are compatible with but not incontrovertible evidence of MISI (Fox-Kemper et al., 2021). In contrast both the Ross Sea and Filchner-Ronne sectors steadily increase in VAF throughout the control simulation.

### 2.3.5 Patterns of thickness change

Across all simulations, the Thwaites and Pine Island catchments undergo thinning, as do the Totten glacier, Queen Mary Land glaciers and George V Land glaciers (Fig. 2.9). Across the majority of simulations with the exception of NorESM1-M RCP2.6 *PIGL* simulations, the Ross and Filchner-Ronne ice shelves thin. Similarly, Larson, Amery, Shackleton and Dronning Maud Land ice shelves thin in the majority of simulations (NorESM1-M RCP2.6 *PIGL* simulations again excepted).

NorESM1-M RCP2.6 *PIGL* simulations undergo thickening along the outer edge of the Ronne ice shelf, the majority of the Ross ice shelf, the Larsen ice shelf and those along the Weddell sector of Dronning-Maud Land (i.e. Brunt sector ice shelves)(Fig. 2.9 **k** and **l**).

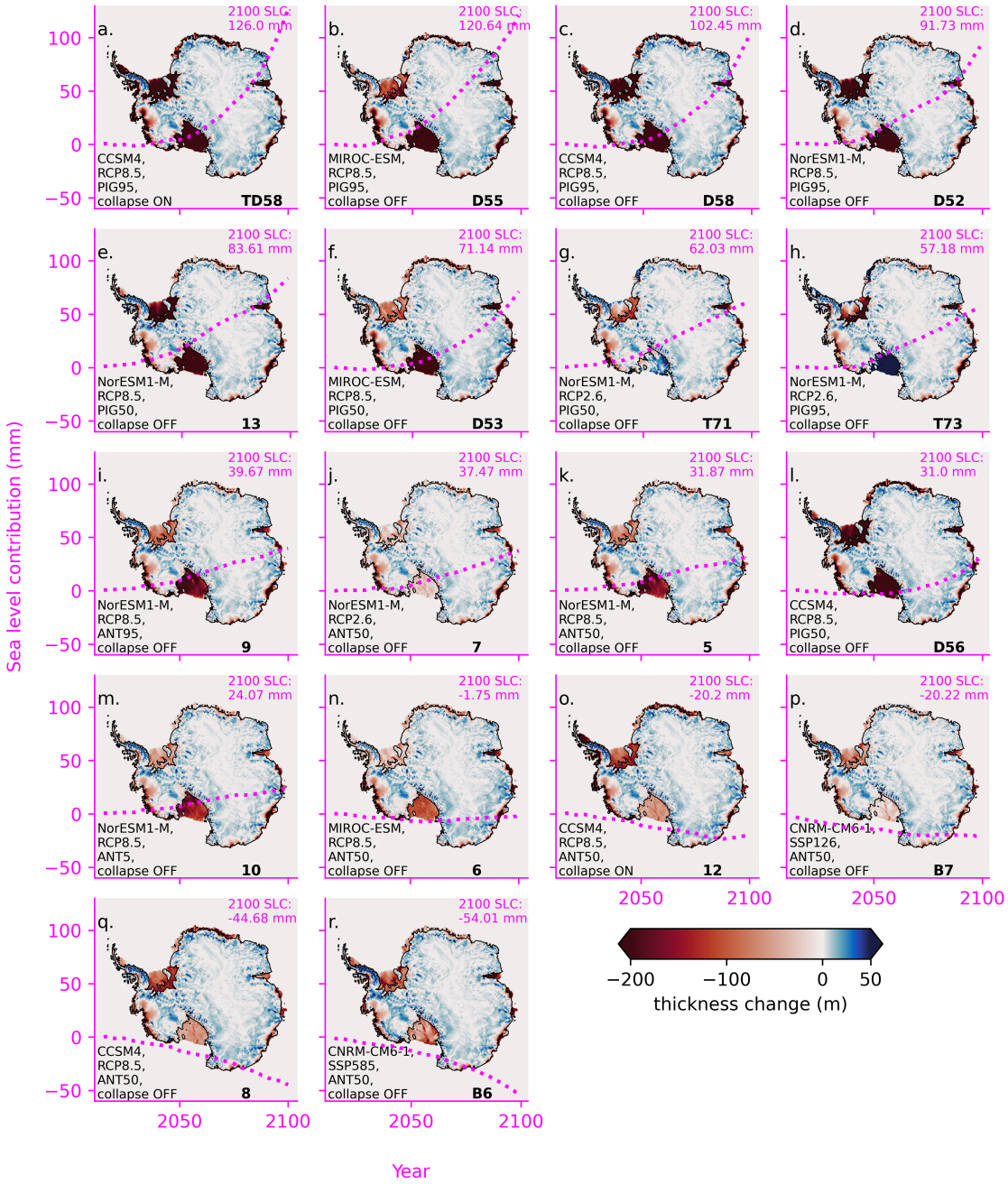


Fig. 2.9 Thickness change at 2100 relative to 2015 for all experiments, ordered by sea level contribution (SLC). Pink dashed line shows corresponding sea level contribution through time from 2015 to 2100 for each simulation.

## 2.4 Discussion

The results are discussed by the dependence on each modelling uncertainty or choice: GCM, emissions scenario, ice shelf collapse and basal melt sensitivity. The last sections compare the BISICLES projections with those from other models in ISMIP6, and summarise the contribution of these projections to the synthesis by Edwards et al. (2021).

### 2.4.1 Dependence on GCM forcing

GCM dependence is driven by differences in magnitude and distribution of thermal forcing in the ocean driving basal melt (Fig. 2.11), and the magnitude and distribution of surface mass balance over the ice sheet (Fig. 2.10).

To explore GCM dependence, we can compare simulations with the same ice shelf basal melt sensitivity under the same emissions scenario. Under the $MeanAnt_{50}$ tuning and RCP8.5, the NorESM1-M forced simulation loses 31 mm SLE VAF, MIROC-ESM drives a mass gain of 2 mm SLE VAF and CCSM4 drives a mass gain 45 mm SLE VAF. The GCM dependence for these experiments reflects surface mass balance. The CCSM4 RCP8.5 surface mass balance is positive over large regions of the ice sheet (Fig. 2.10), and MIROC-ESM is largely positive over the EAIS and interior WAIS (Fig. 2.10). Conversely, NorESM-1M surface mass balance is negative over much of WAIS and the margins of EAIS (Fig. 2.10). Mass gain in EAIS compensates WAIS mass loss, driving an overall sea level fall for CCSM4 and MIROC-ESM forced simulations under $MeanAnt_{50}$ (Fig. 2.7: pink (CCSM4) and yellow (MIROC-ESM) solid lines). Conversely, the NorESM1-M forced simulation loses mass from EAIS as well as WAIS (Fig. 2.7: blue solid line). This reflects the smaller response in NorESM1-M atmosphere to RCP8.5 warming compared with other CMIP5 models (Barthel et al., 2020), which limits warming-driven increases in surface mass balance to compensate ocean driven losses. Under NorESM1-M, larger mass loss from EAIS compared with other GCMs is largely driven by grounding line retreat and greater loss of VAF in the Totten glacier catchment (Fig. 2.8, sector 4).

With higher basal melt sensitivity ($PIGL_{50}$) under the same emissions scenario, NorESM1-M again has the largest sea level contribution at 82 mm SLE. The MIROC-ESM forced simulation increases its sea level contribution to 71 mm SLE, with CCSM4 also undergoing mass loss, with a sea level contribution of 31 mm SLE. Under the highest basal melt sensitivity ($PIGL_{95}$), MIROC-ESM drives the largest mass loss - a sea level contribution of 121 mm. The next largest sea level contribution is from the CCSM4 forced simulation, with a sea level contribution of 102 mm SLE, with NorESM1-M driving the smallest sea

level rise at 91 mm SLE. With the same surface mass balance forcing for each GCM but increased ice shelf basal melt sensitivity, model dependence becomes more influenced by differences in thermal forcing. Increased sea level contribution for MIROC-ESM is partly driven by increases in EAIS mass loss (e.g sectors 3 (Queen Mary Land) and 4 (Totten sector) in Figure 2.8) where thermal forcing is high (Fig. 2.1). Both CCSM4 and MIROC-ESM forced simulations have larger ASE sea level contribution under his higher basal melt sensitivity (sector 9 in 2.8), whilst NorESM1-M has lower thermal forcing and undergoes a smaller increase in sea level contribution with higher $\gamma_0$ in this sector.

For high basal melt sensitivity runs forced with the MIROC-ESM model, high basal melt is simulated under the Shackleton ice shelf in East Antarctica and drives higher sea level contribution for this sector compared with lower $\gamma_0$ simulations. However, the contribution does not scale directly with shelf melt. This reflects the relatively limited buttressing effect of this shelf. It illustrates the way that unconstrained ice shelves can undergo significant melt with a limited impact on sea level contribution (Fürst et al., 2016). Moreover, it illustrates how GCM dependence is partially dependent on $\gamma_0$

Alongside exploring GCM dependence amongst CMIP5 models, we also ran two simulations forced with a CMIP6 model. CNRM-CM6-1 has an equilibirum climate sensitivity of 4.8°C (Meehl et al., 2020), similar to the upper end of CMIP5 models sampled in MIROC-ESM-CHEM (4.7°C), but higher than the remaining CMIP5 models which have ECS of 2.9°C (CCSM4) and 2.9°C (NorESM1-M) (Flato et al., 2013). This drove larger surface mass balance, and therefore greater accumulation (Fig. 2.2), offsetting dynamical losses as a result of ocean melt driven retreat. Under both scenarios in CNRM-CM6-1 (SSP1-2.6 and SSP5-8.5), Antarctica contributes sea level fall. It should however be noted that we only sample the *MeanAnt* basal melt contribution, and could expect a larger contribution for CNRM-CM6-1 with greater melt sensitivity to the thermal forcing at the base of the ice shelves. Under low basal melt parameterisation, CCSM4 gains mass - this is consistent with the large continent-wide increase in surface mass balance (SMB) in this model (Nowicki et al., 2016).

### 2.4.2 Dependence on emissions scenario

The higher warming simulations (RCP8.5 for CMIP5 models and SSP5-8.5 for CMIP6) generally had higher surface mass balance over the continent (Fig. 2.10), consistent with larger precipitation flux under warming (Payne et al., 2021, Palerme et al., 2017, Frieler et al., 2015). The scenario dependence was the modulated by the value used for basal melt sensitivity.

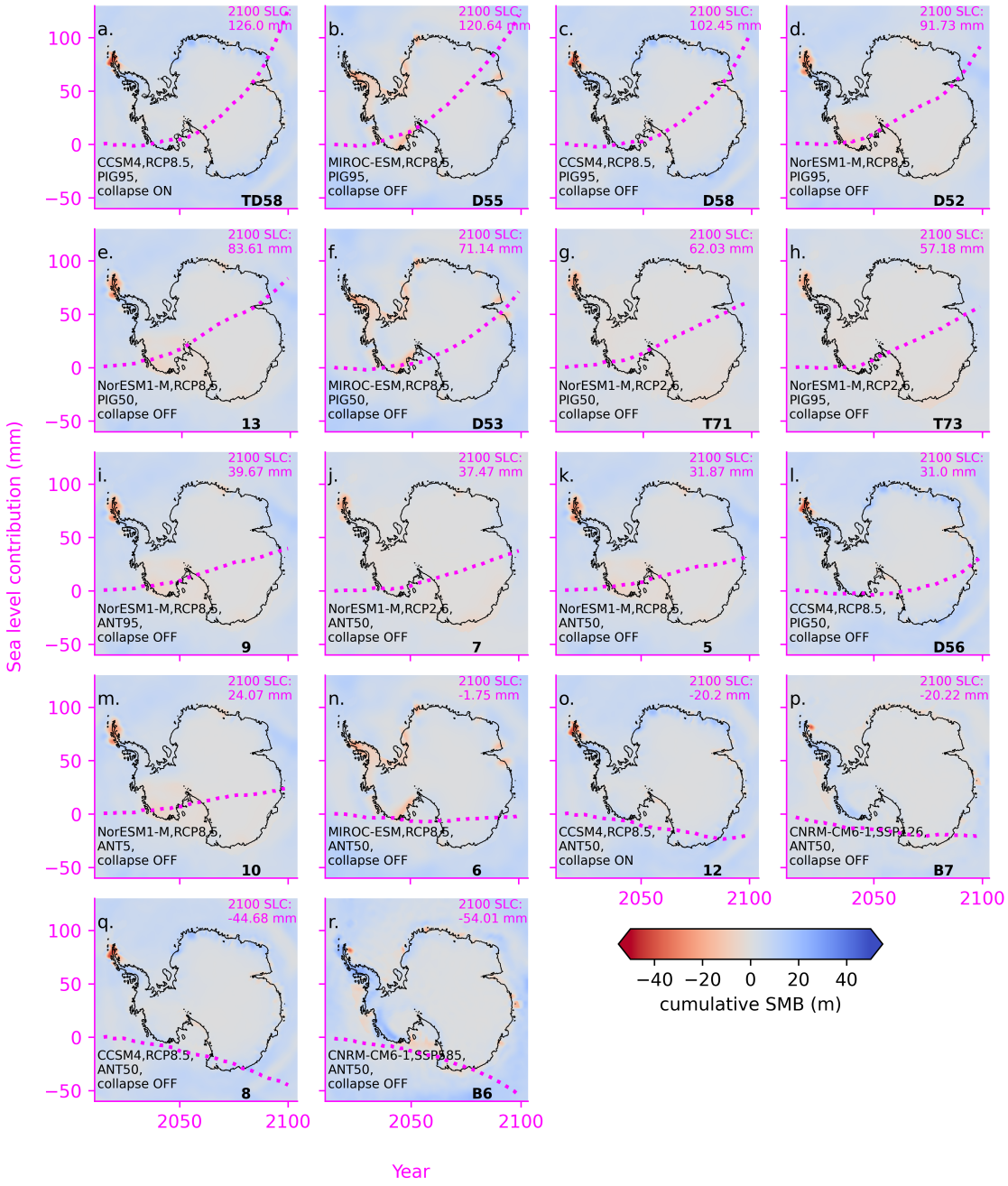


Fig. 2.10 Cumulative surface mass balance for all projections, ordered by sea level contribution (SLC). Pink dashed line shows corresponding sea level contribution through time from 2015 to 2100 for each simulation.

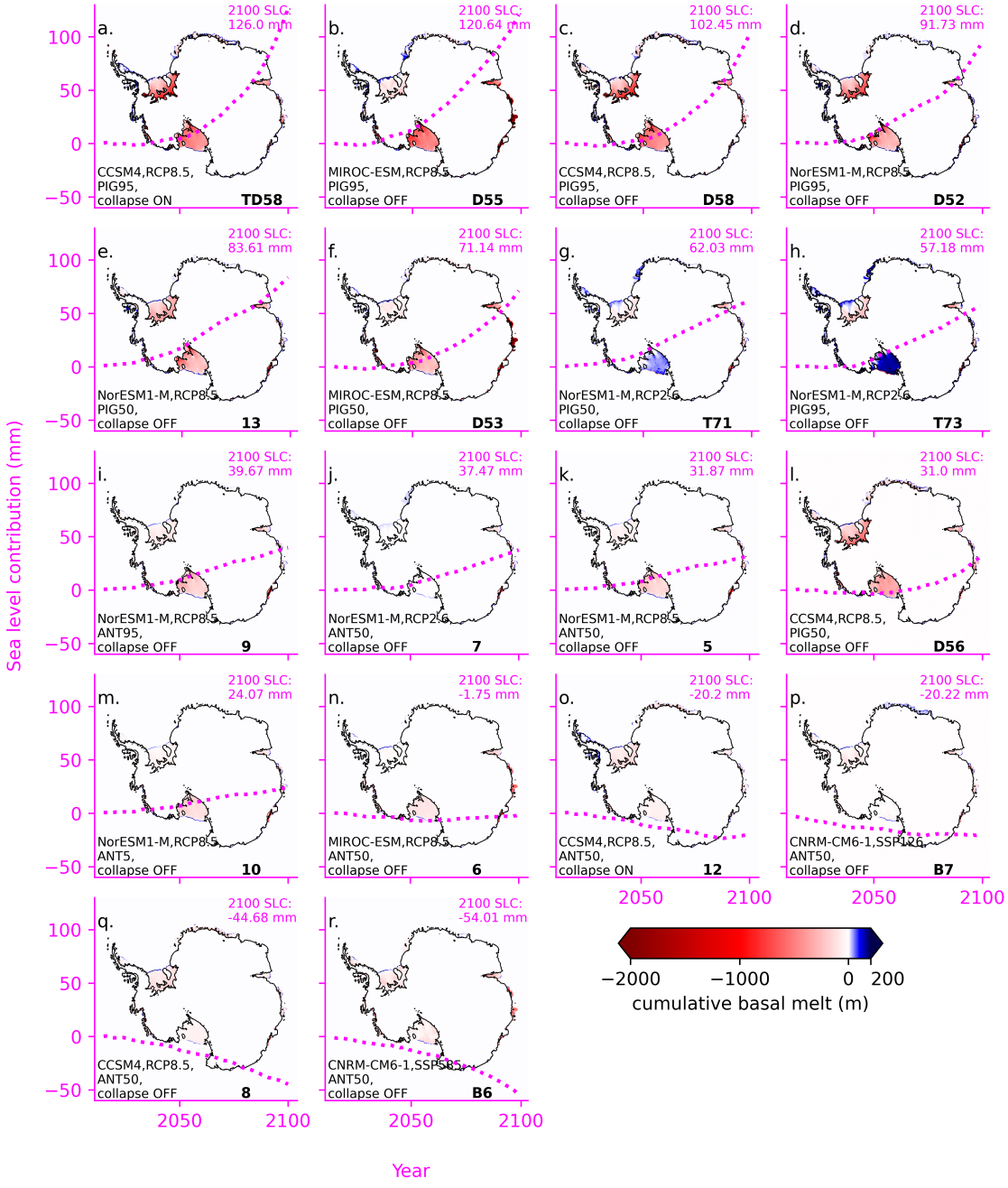


Fig. 2.11 Cumulative basal melt for all simulations, ordered by sea level contribution (SLC). Note that the color scale is inverted, so negative values indicate thinning. MIROC forced runs have large cumulative thinning of the Shackleton ice shelf. Pink dashed line shows corresponding sea level contribution through time from 2015 to 2100 for each simulation.

Scenario dependence was assessed in the two GCMs used to make projections under the low emissions scenarios (RCP2.6/SSP1-2.6): NorESM1-M from CMIP5 and CNRM-CM6-1 for CMIP6, calibrated to mean Antarctic melt rates. For the NorESM1-M simulations, the low emissions scenario leads to greater mass loss: -38 mm SLE under RCP2.6, compared with -31 mm SLE under RCP8.5. This varies regionally: WAIS mass loss, for example, was smaller under RCP2.6 than RCP8.5 (-10 mm vs -16 mm). Basal melting under RCP8.5 is greater than under RCP2.6 (Fig. 2.11 **h** vs **i**). Over the Ross shelf and WAIS, SMB is more negative under the higher emissions scenario (Fig. 2.10 **h** vs **i**). These factors together drive the higher mass loss in WAIS loss under RCP8.5 compared with RCP2.6 - consistent with other ISMIP6 ice sheet models forced by NorESM1-M, where mass loss is greater under RCP8.5 than RCP2.6 (Fig. 4(a) in Edwards et al(2021) where mass loss dominates (Fig. 4 (Edwards et al., 2021)). For the EAIS and the majority of the Peninsula, the SMB scenario dependence is reversed: SMB is higher under RCP8.5 compared with RCP2.6. This drives a smaller net mass loss in EAIS under RCP8.5 (-16 mm vs -27 mm), and a net mass gain in the Peninsula compared with RCP2.6 (1 mm vs 0 mm) which is also consistent with most other ISMIP6 models (Fig. 4(c, d) in Edwards et al. Edwards et al. 2021).

In contrast to CMIP5, the CMIP6 CNRM-CM6-1 forced simulations project net mass gain under both emissions scenarios. Under SSP5-8.5, the VAF change is +53 mm compared with +17 mm SLE under SSP1-2.6. WAIS, EAIS and PEN all have larger volume increase under SSP5-8.5 compared with SSP1-2.6. Unlike NorESM-1M, CNRM-CM6-1 consistently has higher SMB under the higher emissions scenario across the majority of the ice sheet (Fig. 2.10 **a** vs **c**). Basal melt is higher under the higher emissions scenario for CNRM-CM6-1 (Fig. 2.11 **a** vs **c**), though not by enough to counteract the SMB increases, so VAF increases for all sectors (WAIS: 22 mm vs 11 mm SLE, EAIS: 23 mm vs 4 mm SLE, PEN: 6 mm vs 2 mm SLE). This is consistent the other ISMIP6 projections forced with this model, where accumulation under higher emissions dominates melt driven mass loss (Fig. 4 Edwards et al. 2021).

Two of the three additional simulations beyond the ISMIP6 protocol (T71 and T73) provide insight into the modulation of RCP and SSP dependence by basal melt sensitivity. These were also run with NorESM1-M using $PIGL_{50}$ and $PIGL_{95}$. For the median Pine island calibration ($PIGL_{50}$), high emissions lead to greater mass loss: -82 mm SLE for RCP8.5 (experiment 13), compared with -62 mm SLE for RCP2.6 (experiment T71). This again varies regionally. WAIS losses follow the overall scenario dependence, with more mass loss under RCP8.5 compared with RCP2.6 (-35 mm SLE vs -11 mm SLE). EAIS losses again show the opposite pattern with slightly more mass loss under RCP2.6 than RCP8.5

(-51 mm SLE vs -49 mm SLE). The Peninsula gains mass under both scenarios, with change in VAF the same for both scenarios at 1 mm.

For $PIGL_{95}$, high emissions also lead to greater mass loss: -91 mm SLE for RCP8.5 (experiment D52), compared with -57 mm SLE for RCP2.6 (experiment T73). The regional scenario dependence differs from the $PIGL_{50}$ simulations. This time, both WAIS and EAIS losses follow the overall pattern of larger mass loss under RCP8.5 compared with RCP2.6 (WAIS: -40 mm SLE vs -7 mm SLE; EAIS: -52 mm SLE vs -50 mm SLE). The Peninsula shows opposite sign contributions: the region loses mass under RCP2.6, but gains mass under RCP8.5.

The projections for T71 and T73 are not shown for the ISMIP6 ensemble by Edwards et al. (2021), because they were only shown by one other ice sheet model than BISICLES. However, these experiments informed the assessment of potential interactions between scenario and basal melt sensitivity (see Contributions to Edwards et al. (2021) below).

### 2.4.3 Dependence on ice shelf collapse

Two pairs of simulations explore the impact of shelf collapse on sea level contribution. All are forced with CCSM4 under RCP8.5. The first pair have ice shelf collapse on and off, with the $MeanAnt_{50}$ basal melt parameter value (experiment 12 and 8 respectively). The second pair are the same but with the $PIGL_{95}$ parameter value (experiment TD58 and D58), to explore the interactions between the basal melt parameter and shelf collapse. Experiment TD58 was beyond the ISMIP6 protocol, and was performed to inform the synthesis by Edwards et al. (2021)

Including shelf collapse decreases the Antarctic volume above floatation by 25 mm SLE relative to 'no collapse' in in both pairs of experiments (Peninsula: 13 mm; EAIS: 5-6 mm; WAIS 4-6 mm). However, the no collapse baseline is very different in the two basal melt parameterisations: for the $PIGL_{95}$ experiments, including shelf collapse increases the net mass loss; for the $MeanAnt_{50}$ experiments, it decreases the net mass gain. Again, only one other model in ISMIP6 performed TD58. These two sets of projections informed the assessment of potential interactions between ice shelf collapse and basal melt sensitivity (see Contributions to Edwards et al. (2021) below).

### 2.4.4 Dependence on basal melt sensitivity

To understand dependence of the projections on the basal melt parameter, experiments with the same GCM forcing and different $\gamma_0$ can be compared. Here all simulations have

ice shelf collapse off. The most comprehensively sampled GCM/ scenario combination is NorESM1-M under RCP8.5, for which simulations were carried out for $MeanAnt_5$, $MeanAnt_{50}$, $MeanAnt_{95}$, $PIGL_{50}$ and $PIGL_{95}$. Three simulations were carried out for NorESM1-M RCP2.6 for $MeanAnt_{50}$, $PIGL_{50}$ and $PIGL_{95}$. Three simulations were also carried out for MIROC-ESM under RCP8.5 for the same $\gamma_0$ values, as well as CCSM4 under RCP8.5. The overall $\gamma_0$ dependence for the majority of GCMs is one of increased sea level contribution under higher $\gamma_0$, though the nature of this relationship varies by model and region (Fig. 2.12). The Antarctic Peninsula is fairly insensitive to increases in $\gamma_0$ (Fig. 2.12). In comparison to other ISMIP6 models, BISICLES has intermediate sensitivity to $\gamma_0$ (see Extended Data Figure 6 in Edwards et al. 2021).

In NorESM1-M under *PIGL* $\gamma_0$, increasing $\gamma_0$ from $PIGL_{50}$ to $PIGL_{95}$ does not drive as large an increase in sea level contribution as the same increase does for other GCMs (Fig. 2.12). For the NorESM1-M RCP2.6, the $PIGL_{95}$ simulation undergoes a smaller loss of VAF than the $PIGL_{50}$ simulation (Fig. 2.4: darker blue dashed lines). Whilst localised thickening occurs intermittently for all GCMs and scenarios under *PIGL* basal melt tuning (not shown), for NorESM1-M, thickening is pervasive enough to alter dependence of net mass loss on $\gamma_0$. As can be seen in Figure 2.9 subplots **k** and **l**, the Ross ice shelf thickens in both simulations, with more thickening under $PIGL_{95}$. Moreover, under RCP8.5, the $PIGL_{95}$ projects smaller contribution to sea level than the $PIGL_{50}$ projection until 2094 (Fig. 2.4: blue solid lines) for the whole ice sheet.

Previous studies using the ISMIP6 non-local basal melt parameterisation have noted ice shelf thickening as a result of refreezing under high basal melt sensitivity (Lowry et al., 2021, Lipscomb et al., 2021). Ice shelf refreezing under low thermal forcing is plausible, and present in observations and model simulations of Antarctic ice shelf cavities (Naughten et al., 2018, Adusumilli et al., 2020, Reese et al., 2018a, Stevens et al., 2020). However, in their simulations implementing the nonlocal ISMIP6 parameterisation in CISM, Lipscomb et al. (2021) modify the second term in the basal melt calculation to avoid what they suggest is spurious melting and refreezing where sector averaged thermal forcing plus the the basin correction ($\delta T_{sector}$) is < 0. Lipscomb et al. (2021) such that equation 2.1 becomes:

$$\begin{aligned} m(x,y) = \gamma_0 \times & \left(\frac{\rho_{sw} C_{pw}}{\rho_i L_f}\right)^2 \\ & \times \left(TF(x,y,z_{draft}) + \delta T_{sector}\right) \\ & \times max\left(\langle TF\rangle_{draft \in sector} + \delta T_{sector}, 0\right), \end{aligned} \tag{2.2}$$

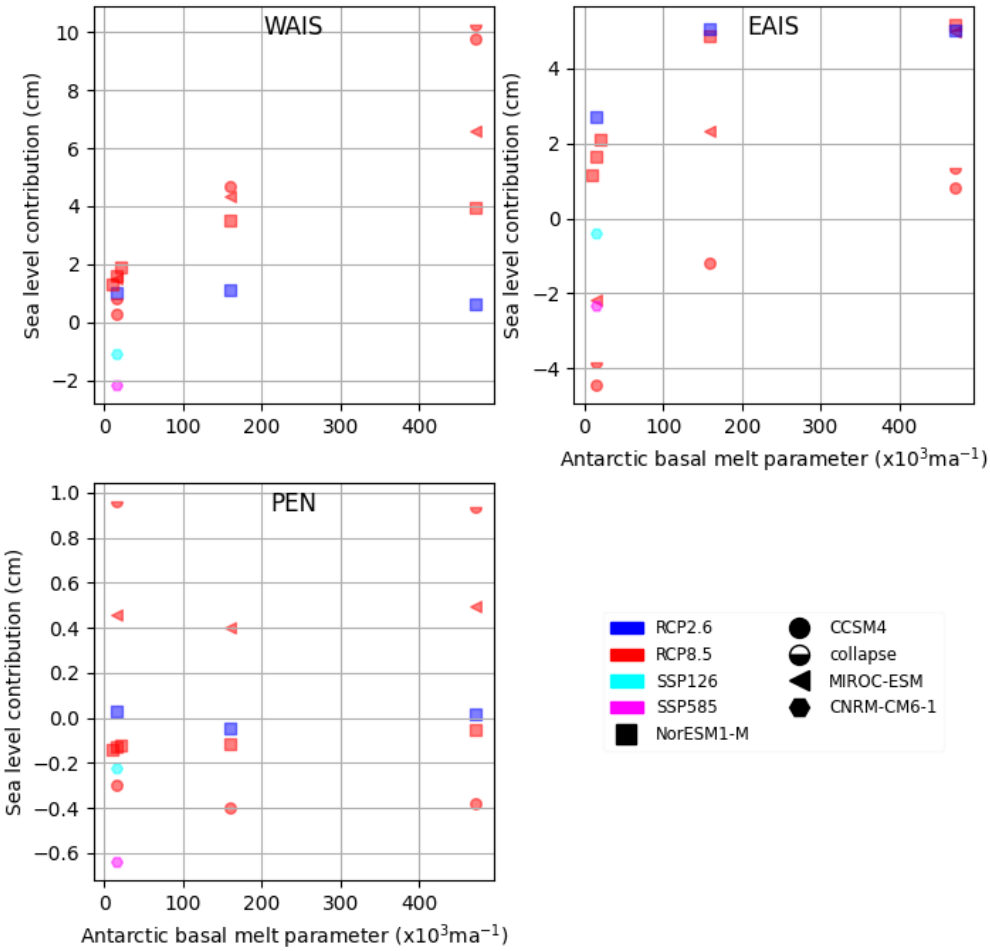


Fig. 2.12 Sea level contribution from 2015 to 2100 relative to control for all simulations as a function of basal melt sensitivity ($\gamma_0$), shown for East Antarctic (EAIS), West Antarctic (WAIS) and Peninsula (PEN) ice sheets.

By construction, this avoids negative values of m(x,y), which drive shelf thickening in the ice sheet model where $\langle TF \rangle_{draft \in sector} + \delta T_{sector}$ is negative. A previous study exploring Antarctic sensitivity to future climate and model parameters used an alternative basal melt forcing approach that also avoids refreezing of ice shelves by design (Bulthuis et al., 2019). As outlined in the methods, BISICLES version B uses the ISMIP6 non-local melt parameterisation as described in (Jourdain et al., 2020) without modification. However, thickening of ice shelves as a result of the basal melt parameterisation is not permitted in this BISICLES version. Thickening of ice shelves under highest $\gamma_0$ values could therefore be a manifestation of tributary glaciers responding to strong ice shelf thinning and removal of buttressing, and advection of ice to grounding lines as ice streams speed up. Beyond 100 year time scales, initial thickening could therefore precede a larger long term sea level response.

The Ross sector provides an example of an ice shelf and grounding line dynamic under *PIGL* $\gamma_0$ tuning, that runs counter to our expectation that higher $\gamma_0$ will increase shelf thinning and enhance grounding line retreat. For it and other sectors under NorESM1-M RCP2.6 and RCP8.5, sea level rise contribution under the highest basal melt sensitivity ($PIGL_{95}$) is lower than under the second highest ($PIGL_{50}$) basal melt sensitivity (Fig. 2.8: blue solid lines). Figure 2.13 shows a transect through the grounding line at the terminus of Whillans and ice stream A for $PIGL_{95}$ NorESM1-M RCP8.5 and $PIGL_{50}$ at three successive time slices (2015, 2050 and 2100). Also shown are the basin average thermal forcing for NorESM1-M RCP8.5. In the Ross Sea Sector, the grounding line under $PIGL_{95}$ is seaward of the equivalent $PIGL_{50}$ simulation grounding line for the duration of the run at the Whillans ice stream and ice stream A (Fig. 2.13). Ross sector ice streams drain around 40% of the West Antarctic ice sheet (Price et al., 2001), so changes to ice stream configuration along the Siple coast impact sea level contribution in the sector.

### 2.4.5 Comparison with other models

BISICLES is compared with other ISMIP6 models in Figures 2.14, 2.15, 2.16 for EAIS, WAIS and the Peninsula respectively. Whilst BISICLES generally lies within the range of other ISMIP6 models for WAIS and the Peninsula, for EAIS in some experiments it shows a systematically different response.

Compared with other ISMIP6 models, BISICLES has the largest EAIS sea level contribution under mean Antarctic $\gamma_0$ tuning for NorESM1-M RCP8.5 forced simulations (Fig. 2.14). With the largest EAIS contribution in these experiments sourced from the Totten Glacier, this could suggest that BISICLES 1 km grid resolution at the Totten grounding

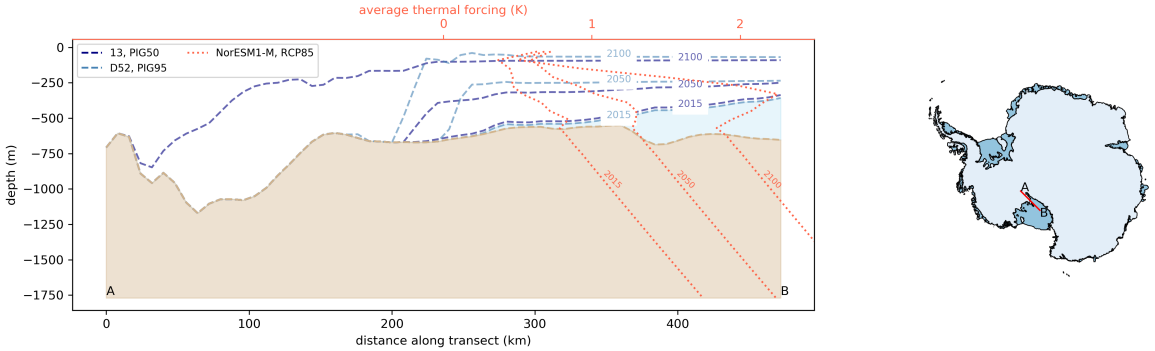


Fig. 2.13 Siple coast transect for $PIGL_{50}$ and $PIGL_{95}$ experiments under NorESM1-M RCP8.5. Blue dashed lines show ice sheet base for years indicated. Red dashed lines show average thermal forcing with depth at successive time steps. The higher basal melt sensitivity ($\gamma_0$) run undergoes more thinning in outer shelf shown in transect, but grounding line retreats further inland for lower $\gamma_0$ run - though the shelf remains thicker for the latter.

line is driving retreat not seen in lower resolution ISMIP6 models (4-20 km for fixed resolution models; minimum 2 km for variable resolution models) - though we note that Totten glacier retreats at lower resolution (< 8 km) in BISICLES (Cornford et al., 2016). BISICLES has a comparable sea level contribution to the other L1L2 physics model in the ISMIP6 ensemble for WAIS core experiments: CISM, which is run on a 4 km grid (Fig. 2.15). CISM additionally implements a sub-grid interpolation scheme to represent basal melt in partially floating cells (Lipscomb et al., 2021), which could account for its slightly larger sea level contribution under NorESM1-M RCP8.5 core experiments for WAIS (Seroussi and Morlighem, 2018). With increased basal melt sensitivity ($\gamma_0$), the CISM WAIS contribution is larger still compared with BISICLES.

For core experiments, BISICLES simulates a comparable sea level contribution to that of UCI JPL ISSM for WAIS. UCI JPL ISSM uses a variable mesh resolution, with finest resolution of 3 km near the margins, and has higher order physics (Seroussi et al., 2020). Agreement between ISSM and BISICLES for core WAIS simulations could reflect higher resolution of both models compared with other ISMIP6 models, as well as consistency between projections with higher order and L1L2 physics. We note that in the Marine Ice Sheet Model Intercomparison Project (MISMIP+), model physics had a less significant impact on simulated dynamics than basal sliding law at comparable resolution (Cornford et al., 2020).

The SICOPOLIS model projects a larger sea level contribution compared with BISICLES in the majority of experiments, whilst GRISLI consistently projects a smaller sea level contribution. As noted in (Edwards et al., 2021), SICOPOLIS shows high sensitivity to ice shelf melt, likely due to its use of a floating condition for sub shelf melt - where basal melting is applied across the entire grid cell if the midpoint is at floatation. We note that MALI also uses a floating condition at the grounding line, and has a large WAIS contribution in core experiments. Conversely, GRISLI shows low sensitivity, which is ascribed to topographical biases in the initial condition - which make the model less sensitive to ocean driven changes (Quiquet and Dumas, 2021).

### 2.4.6 Contributions to Edwards et al. (2021)

All simulations presented here were included in Edwards et al. (2021) projection of global land ice contribution to 2100 sea level, extending the ISMIP6 ensemble by an additional model compared with Seroussi et al. (2020) and Payne et al. (2021). However, as outlined in the introduction, experiments outside the main ISMIP6 protocol were conducted to provide further exploration of sensitivities and interactions.

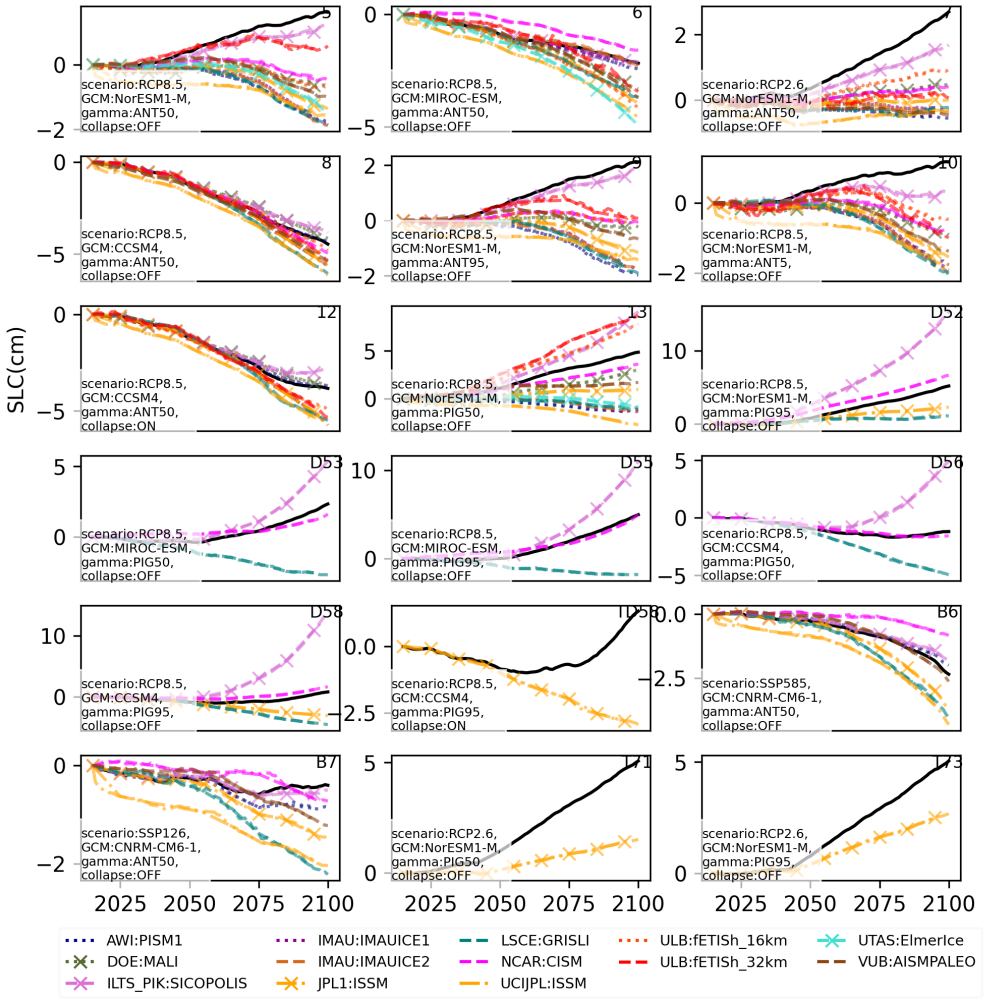


Fig. 2.14 East Antarctic Ice Sheet (EAIS) sea level contribution (SLC) comparison with other ISMIP6 simulations from 2015 to 2100. Data from Edwards et al. (2021). BISICLES shown in black solid line.

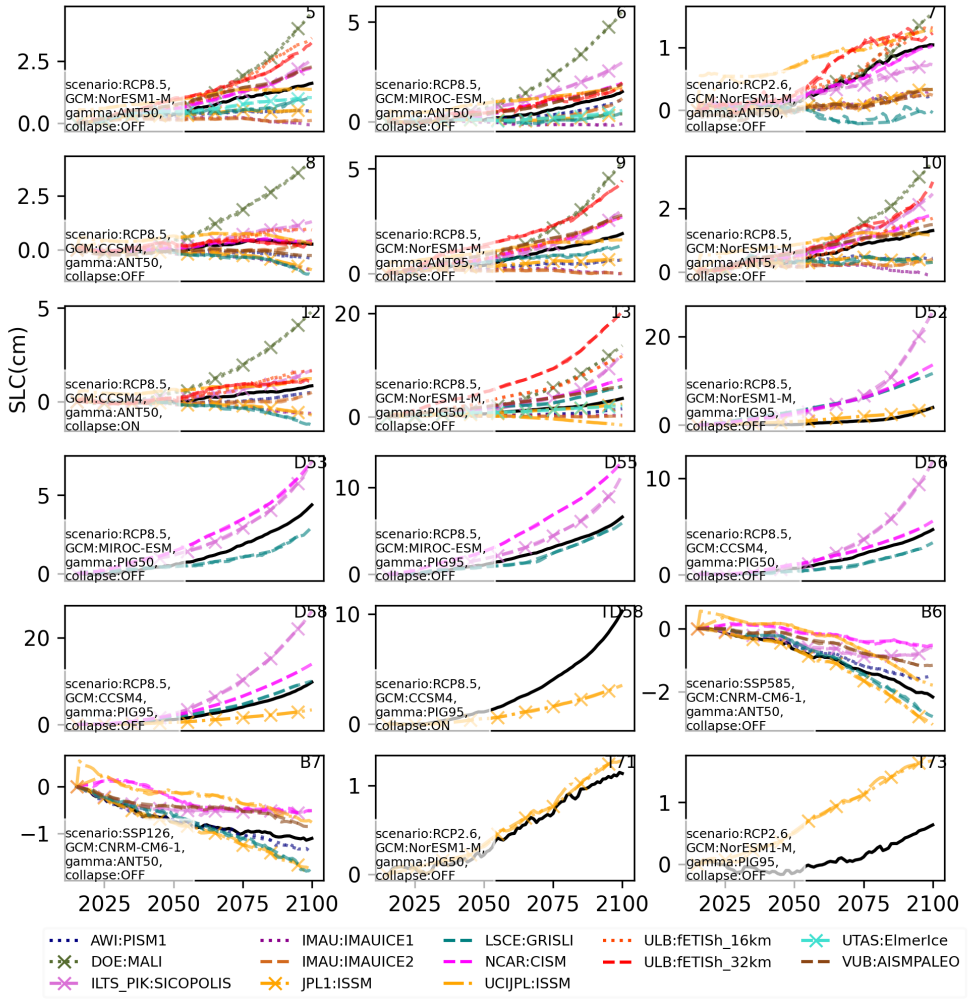


Fig. 2.15 West Antarctic Ice Sheet (WAIS) sea level contribution (SLC) comparison with other ISMIP6 simulations from 2015 to 2100. Data from Edwards et al. (2021). BISICLES shown in black solid line.

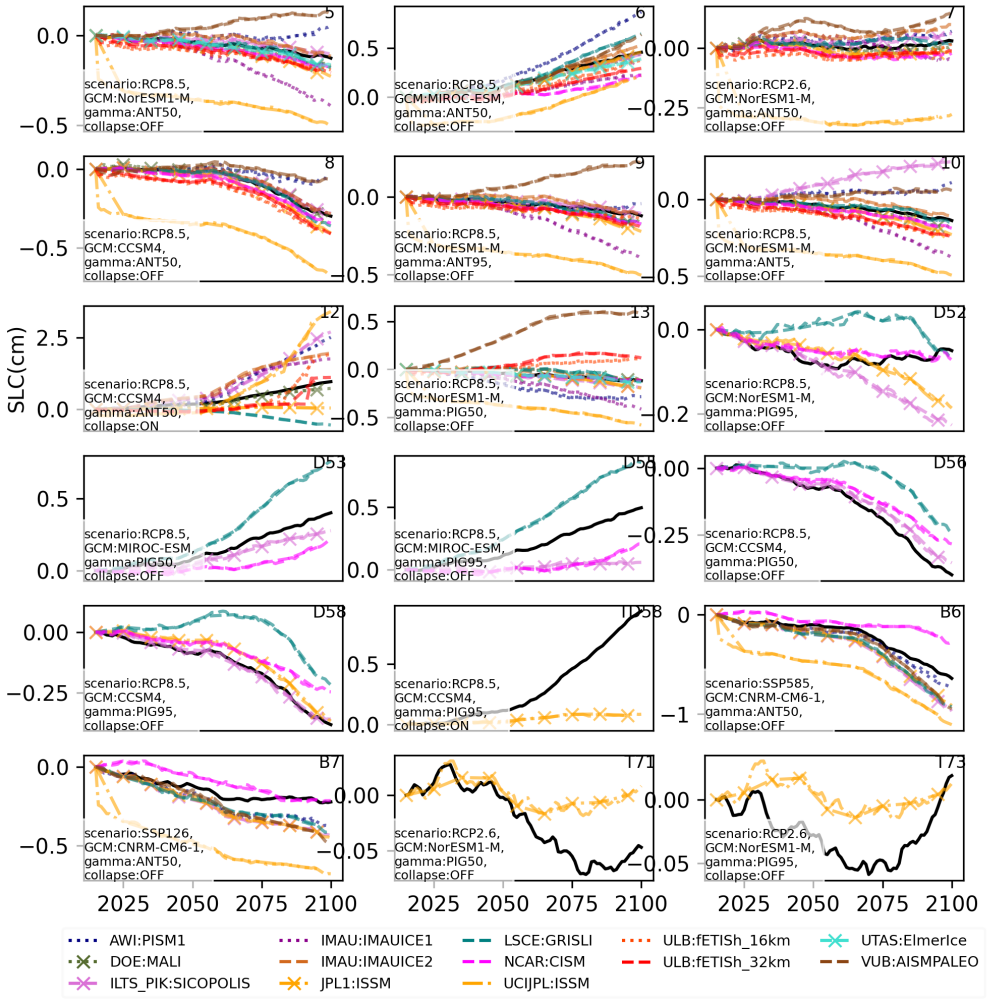


Fig. 2.16 Antarctic Peninsula (PEN) sea level contribution comparison (SLC) with other ISMIP6 simulations from 2015 to 2100. Data from Edwards et al. (2021). BISICLES shown in black solid line.

As outlined in Section 2.4.3, the increase in sea level with collapse on was almost identical for both basal melt sensitivities sampled ($MeanAnt_{50}$ and $PIGL_{95}$). Along with results from the same experiments in ISSM, this is the basis for the conclusion in Edwards et al. (2021)(section "ice shelf collapse versus basal melt" that contribution due to ice shelf collapse does not significantly increase with higher values of $\gamma_0$.

A further finding in Edwards et al. (2021) that was supported with these projections is highlighted in Section "Retreat and basal melt versus temperature" of Edwards et al(2021). Sampling *PIGL* basal melt sensitivity under RCP2.6 alongside RCP8.5 projections shows that the spread of projections is smaller under the former. This result is confirmed in complementary experiments with ISSM as presented in Edwards et al. (2021).

### 2.4.7 Limitations

Interactions between the ice sheet and the solid earth could influence Antarctic sea level contribution, including on sub-centennial time scales (Larour et al., 2019, Kachuck et al., 2020). Sea level changes resulting from mass redistribution and changes to the geoid also have the potential to stabilise sea level contribution from the ice sheet (Gomez et al., 2010). Conversely, bedrock elevation changes in response to changing ice load can impact accommodation space for ocean water, and therefore GMSL change (Pan et al., 2021, Yousefi et al., 2022). Some Antarctic ice sheet future projection studies have adopted simple models of ice-sheet bedrock interactions (DeConto and Pollard, 2016, DeConto et al., 2021, Bulthuis et al., 2019), suggesting their stabilising feedback is limited over the 21st century for slow bedrock response times that characterise most of Antarctica (Bulthuis et al., 2019) (See Chapter 3 for further discussion of Glacial Isostatic Adjustment (GIA) processes). Incorporating ice-sheet model (DeConto et al., 2021) based projections of Antarctic ice load into a 3D viscoelastic earth model (Wan et al., 2022), Yousefi et al. (2022) suggest that failing to account for the spectrum of ice-sheet, solid earth and sea level processes may underestimate future GMSL projections. However, full coupling of 3D earth models and dynamic ice sheet models remains challenging. The impacts of solid earth changes on projected ice sheet contribution to sea level are not explored for ISMIP6 (Nowicki et al., 2016). However, incorporating GIA into Antarctic scale projections of 21*st* sea level contribution would be an informative development on the work presented here. Specifically, a modelling framework capable of capturing fast responding West Antarctic bedrock and its stabilising role (Kachuck et al., 2020) would give a more detailed picture of future Antarctic sea level contribution.

For NorESM1-M RCP2.6 $PIGL_{95}$, the sea level contribution at 2100 was lower than that projected under $PIGL_{50}$. However, the trajectory of mass loss in Figure 2.4 indicates that $PIGL_{95}$ will overtake $PIGL_{50}$ beyond 2100. To confirm this, and explore longer term dynamics, extending these simulations beyond 2100 would be a worthwhile improvement on this work.

To explore modelling uncertainties further, a more comprehensive ensemble design such as a full factorial design (sampling every combination of the uncertainties), would be an improvement on this work. However, this was not done by any ISMIP6 model, and was unfeasible within the scope of this thesis. Additional GCM forcings, $\gamma_0$ values and ice shelf collapse projections were also not available, due to the pre-processing for each performed by ISMIP6.

## 2.5 Conclusions

We have presented simulations of the Antarctic ice sheet for ISMIP6 run with the BISICLES ice sheet model. Under warmer climates and lower basal melt sensitivity, Antarctica gains mass relative to the control simulation. However, scenario dependence is modulated by basal melt sensitivity ($\gamma_0$). Under RCP8.5 when $\gamma_0$ is tuned to Pine Island melt rates, strong basal melt drives dynamical loss and largest sea level contributions. With high equilibrium climate sensitivity of 4.8°C (Meehl et al., 2020) and relatively high surface mass balance (Fig. 2.2), CNRM-CM6-1 gained mass for both simulations run here. However, these were both run at $MeanAnt_{50}$, and we could expect greater mass loss and larger sea level contribution for higher $\gamma_0$ values. CCSM4 RCP8.5 also drives sea level fall under $MeanAnt_{50}$ due in part to its large surface mass balance. However, under the *PIGL* basal melt calibration with collapse on it drove the largest sea level rise. This highlights the importance of further constraining basal melt sensitivity for Antarctica under warming, as this moderates the balance between accumulation driven sea level fall on the one hand, and ocean melt driven dynamical loss on the other.

Ice shelf collapse increased sea level contribution overall, and had a comparable effect on sea level contribution for both $\gamma_0$ values tested. Increased $\gamma_0$ under the *PIGL* calibration did not uniformly increase sea level contribution for the duration of the simulation under different scenarios and models. This demonstrates the nonlinear dynamic response to large ocean melt perturbations. We expect that beyond 2100, larger *PIGL* $\gamma_0$ values would drive consistently larger sea level contribution under all scenarios.

# Chapter 3

# Uncertainties at the base of the ice sheet

## 3.1 Introduction

Century-scale model simulations allow us to explore relatively short term ice sheet response to projected 21st century warming. However, we also aim to explore the impact of processes acting over longer timescales, under climates very different to the historical period. These simulations can be compared with reconstructions from palaeodata to provide an independent evaluation of model processes and parameters. With warmer temperatures than modern at comparable atmospheric $CO_2$ concentrations, the Pliocene is an informative target for ice sheet modelling and has been explored extensively in simulation studies (Dolan et al., 2018, 2011, de Boer et al., 2015, DeConto and Pollard, 2016, DeConto et al., 2021, Yan et al., 2016, Gasson et al., 2016, Golledge et al., 2017b, Berends et al., 2019). However, previous studies of the Pliocene Antarctic ice sheet have used lower order physics compared with BISICLES, such as hybrid models (DeConto and Pollard, 2016, DeConto et al., 2021, Dolan et al., 2018, de Boer et al., 2015, Yan et al., 2016). Burke et al. (2018) project that mid-Piacenzian climate will be surpassed by 2040 under a moderate emissions scenario and sustained thereafter. Crucially, reconstructions of multi-meter sea level rise in the warm Pliocene imply that under moderate warming, global ice sheets could contribute metres to sea level rise as they equilibrate with this warmer climate over hundreds and thousands of years. Exploring mechanisms of long term Antarctic ice sheet change is the aim of the remainder of this thesis.

BISICLES (Cornford et al., 2013) (Section 1.3.2) has been used to characterise Antarctic and Greenland response to century-scale (Cornford et al., 2015, Martin et al., 2019, Seroussi et al., 2019, Goelzer et al., 2020b) and millennium-scale (Martin et al., 2019) changes in climate. However, the simulation of ice sheets under climates from the past

(here called palaeo-ice sheet modelling) presents some unique challenges. In BISICLES, Gandy et al. (2018, 2019, 2021) have addressed some of these. They apply BISICLES to the British and Irish ice sheet during the last deglaciation, successfully reproducing patterns of ice stream formation and evolution when compared with geological proxy data (Gandy et al., 2019). Typically, model-based palaeo-ice sheet studies simulate ice sheet evolution on millennium time scales to capture long-term response of ice sheets to persistent forcing. The computational demands of long model integration times mean that palaeo studies typically simulate the Antarctic ice sheet at low spatial resolution (Dolan et al., 2011, de Boer et al., 2015, Dolan et al., 2018), or sometimes over a smaller domain (Gandy et al., 2021), relative to the AIS. As described in Section 1.3.2, the adaptive mesh refinement of BISICLES reduces computational expense while still allowing fine resolution in key regions. It can therefore be used to simulate ice sheets at higher resolution than fixed resolution ice sheet models over palaeo-timescales. Alongside its more comprehensive physics compared with Hybrid models (Section 1.3), this allows BISICLES to simulate palaeo-ice sheets at relatively high resolution, capturing ice sheet physics in dynamic regions such as ice streams and at the grounding line (Matero et al., 2020, Gandy et al., 2018, 2019, 2021). However, challenges remain in applying BISICLES to the Antarctic ice sheet under past warmth, this chapter explores those challenges.

In this section we describe the challenge associated with representing bedrock-ice sheet interactions, and how we address this in BISICLES. We use the GIANT-BISICLES version developed by Kachuck et al. (2020). Secondly, we describe the basal hydrology coupled sliding approach developed by Gandy et al. (2019), used for Antarctic simulations here for the first time. We adapt the basal sliding parameterisation implemented by Gandy et al. (2019), implementing elevation-dependent bed friction outside ice streams. Elevation-dependent bed friction has previously been used in BISICLES studies of the North American ice sheet (Matero et al., 2020), however, we apply it here within the basal sliding scheme of Gandy et al. (2019). Finally, we present a perturbed parameter ensemble for the Pine Island Glacier (PIG) catchment. The aim of this ensemble is to test new aspects of our BISICLES set up, and assess the relative sensitivity of simulated ice dynamics to processes at the base of the ice sheet.

## 3.2 Background and Approach

### 3.2.1 Glacial Isostatic Adjustment (GIA)

#### GIA and ice sheet stability

Glacial isostatic adjustment (GIA) is the process describing the response of the solid earth, its gravitational field and sea level to changes in the cryosphere (Whitehouse 2018 and references therein). For the work presented in this chapter and Chapter 5, our focus is on interactions between the solid Earth and the ice sheet, and we neglect gravitational and sea level feedbacks. Bedrock elevation plays a primary role in determining ice sheet dynamics, with ocean depth determining grounding line position for marine terminating ice sheets. Height of the bedrock also influences surface elevation of grounded ice. As surface mass balance processes are sensitive to elevation, bedrock height can influence build up and decay of ice sheets through changes in accumulation and ablation (Oerlemans, 1980, Abe-Ouchi et al., 2013).

Solid Earth deformation with changing surface load is composed of an instantaneous elastic response, and a time lagged viscous response towards isostatic equilibrium. Shoaling at the grounding line as bedrock responds elastically to unloading can delay retreat for marine grounded glaciers. For the Thwaites glacier, high resolution modelling by Larour et al. (2019) suggests that inclusion of elastic rebound delays grounding line retreat by 20 years. Including other instantaneous GIA components: rotational feedbacks and gravitational changes, alongside elastic bed deformation, Larour et al. (2019) find stabilisation of grounding lines in a continent wide Antarctic ice sheet simulation after 250 years. Gomez et al. (2010) show that instantaneous GIA processes can delay or stabilise Marine Ice Sheet Instability (MISI)(Section 1.2.2) for the Antarctic ice sheet.

Slow bedrock deformation on $10^4$ year time scales has been identified as a key determinant of slow ice sheet build up and rapid decay in Northern Hemisphere glacial-interglacial cycles (Abe-Ouchi et al., 2013). Abe-Ouchi et al. (2013) find that North American ice sheet retreat, triggered by orbitally-driven increases in insolation and ablation at the low latitude ice sheet margin, is sustained in part due to slow bedrock rebound. They show that ablation-driven lowering of the ice sheet margins leads to further lowering and ice draw down. With bedrock response an order of magnitude slower than melt-driven retreat, uplift that might otherwise promote surface cooling and positive surface mass balance is ineffective. Ice sheet decay can therefore occur over $10^3$ year time scales. This dynamic accounts for the characteristic sawtooth 100 ka glacial cycles over the past 1 Ma (Abe-Ouchi et al., 2013). This is consistent with Oerlemans et al. (1980), who used a simple ice

sheet model with elevation-dependent surface mass balance to show that delayed isostatic rebound can enhance rapid decay of ice sheets. The pace of retreat is enhanced as the ice sheet retreats into the isostatic depression formed during glaciation, with rebound too slow to stabilise the ice sheet. In an Antarctic context, bedrock rebound can cause shoaling of over-deepened submarine basins on century to millennium time scales (Whitehouse et al., 2012, Adhikari et al., 2014, Peltier et al., 2015), leading to more stable bed morphologies. Decreases in grounding line depth, driven by bedrock deformation, also stabilise marine ice sheets alongside uplift of pinning points where they maintain contact with buttressing ice shelves (Matsuoka et al., 2015, Kingslake et al., 2018).

The time-lagged response of the bedrock to changing surface load is primarily driven by viscous deformation of the mantle, with response time proportional to mantle viscosity (Lingle and Clark, 1985, Bueler et al., 2007, Cathles, 2015). Viscosities close to the global upper mantle average of $10^{21}$ Pa s imply bedrock response times on millennium time scales, on the order of those in Abe-Ouchi et al. (2013). However, mantle viscosity shows three dimensional variation as function of mantle composition and temperature (Ivins and Sammis, 1995, Latychev et al., 2005, Wu et al., 2013). Antarctica shows strong spatial variation of bedrock characteristics (Heeszel et al., 2016), where the continent west of the trans-Antarctic mountains has distinctive mantle properties compared with the East (Barletta et al., 2018). Underlain by thick, stable (Nield et al., 2018) cratonic crust, East Antarctica is characterised by high mantle viscosity (Whitehouse et al., 2019). West Antarctica is underlain by thinner lithosphere and lower viscosity asthenosphere (Nield et al., 2014, Barletta et al., 2018) down to $6\times10^{17}$ Pa s beneath the Peninsula (Nield et al., 2014).

A primary tool for inferring internal mantle structure is the use of seismic tomography. Seismic wave travel times are used to construct a 3D model of seismic velocity anomalies in the Earth's interior (Whitehouse et al., 2019, Kustowski et al., 2008, Ivins and Sammis, 1995). This velocity model can be used to infer 3D viscosity variations in the mantle relative to a 1D reference Earth model (Wu et al., 2013, Ivins and Sammis, 1995), with low velocity regions generally corresponding to higher temperatures and thus lower viscosity (Whitehouse et al., 2019). In addition to seismic data, GPS based observations of uplift and gravitational data can be used to constrain the viscosity profile of the mantle (Wu et al., 2013). The lateral variability in mantle viscosity from West to East Antarctica derived using such an approach, can be seen in Figure 3.1, taken from Whitehouse et al. (2019).

When incorporating low mantle viscosity into studies of the WAIS, bedrock uplift can prevent grounding line retreat and facilitate re-advance in the Holocene (Kingslake et al., 2018). At viscosities down to $4\times10^{18}$, Pine Island Glacier sea level contribution is reduced

on century timescales through visco-elastic bedrock deformation (Kachuck et al., 2020). The presence of low viscosity mantle beneath WAIS suggests that, alongside instantaneous GIA components, larger magnitude viscous response of bedrock to surface load changes can stabilise the ice sheet on sub-century down to decadal timescales. Given that the viscous component of bedrock deformation is an order of magnitude larger than the elastic component (Nield et al., 2014, Barletta et al., 2018, Whitehouse et al., 2019), neglecting low viscosity response of WAIS mantle could lead to omission of this stabilising factor in deglacial ice sheet simulations.

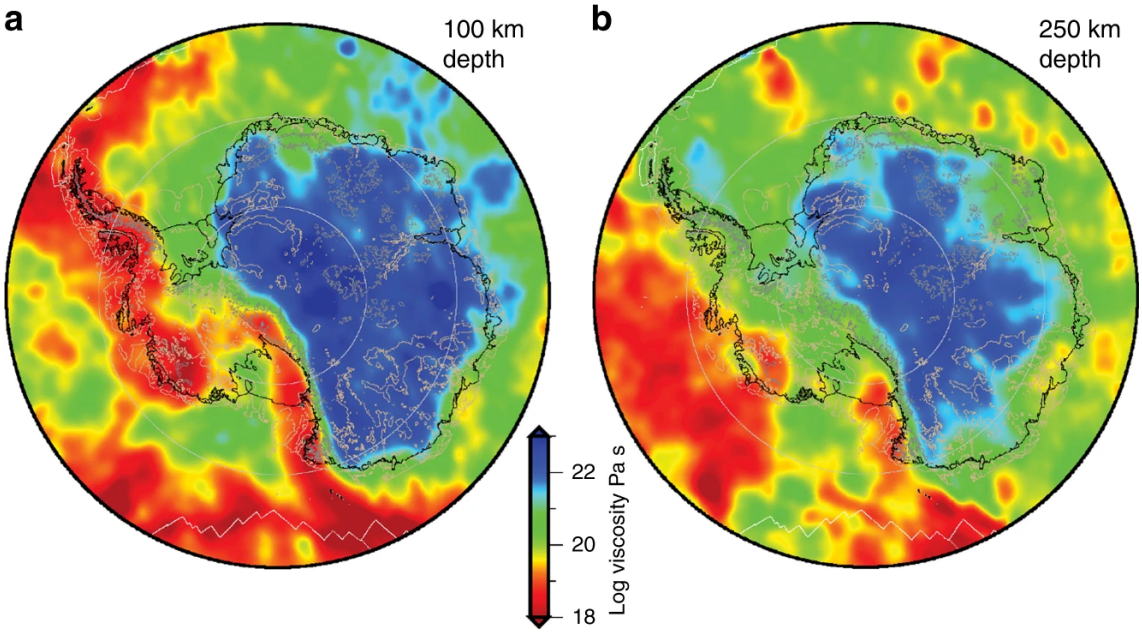


Fig. 3.1 Estimated upper mantle viscosity at 100 km mantle depth (**a**) and 250 km depth (**b**), showing spatial variability across the continent, with higher viscosity underlying EAIS compared with EAIS. Figure is from Whitehouse et al. (2019), with viscosities estimated using the method outlined in Wu et al. (2013) based on the IJ05-R2 (Ivins and James, 2005) reference viscosity model.

### GIA in Ice Sheet Models

The most complete representation of the GIA-ice sheet system couples a GIA model with 3D variations in viscoelastic Earth structure and gravitationally self-consistent global sea level to a dynamic ice sheet model (Gomez et al., 2018). Gomez et al. (2018) apply this coupled model approach to the Antarctic ice sheet since the Last Glacial Maximum (40 ka to modern), finding that the sea level contribution is relatively insensitive to inclusion of 3D Earth structure. However, based on previous simulations with an ice sheet model coupled to radially varying (1D) Earth models, Pollard et al. (2017) posit that Pliocene

sea level contribution may be more sensitive to 3D heterogeneity in Earth's structure. A number of approaches exist to deriving 3D Earth structure (e.g. Wu and van der Wal 2003, Latychev et al. 2005, van der Wal et al. 2015), all of which rely on seismic models (e.g. (Heeszel et al., 2016)). Whilst seismic models are improving with increased data availability, they are still based on sparse observations. Uncertainties remain therefore in spatial variations in lithosphere and mantle properties beneath Antarctica (Gomez et al., 2018). The procedure for coupling a 3D Earth model to a dynamic ice sheet model is complex, and increases computational cost - precluding the use of such an approach for ensemble experiments (Gomez et al., 2018).

Modelling approaches that reduce 3D structure to a radially varying (1D) representation of the solid Earth are a simplification of the approach in Gomez et al. (2018). They model gravitationally self-consistent evolution of sea level, bedrock and the ice sheet (e.g. (Gomez et al., 2012, 2013, de Boer et al., 2014, Konrad et al., 2015, Powell et al., 2021, Han et al., 2021). Using coupled 1D global Earth sea level ice sheet simulations, Pollard et al. (2017) simulate Pliocene Antarctic evolution. They find that low viscosity Earth profiles produce metres less sea level rise compared with slower responding Earth profiles (Pollard et al., 2017). Coupling an ice sheet model to a 1D global Earth model remains complex and computationally expensive (Gomez et al., 2013), with trade offs in the ice sheet component such as lower model resolution (tens of km e.g. Konrad et al. 2015, Gomez et al. 2015, 2013) and simplified ice sheet physics (e.g SSA/SIA hybrid (Pollard et al., 2017, Gomez et al., 2015, 2013)). Alongside uncertain viscoelastic Earth profiles, global Earth-sea level models use ice load histories as inputs - which are unknown for the Pliocene. In the absence of ice load history for the Pliocene, Pollard et al. (2017) initialise their simulations from a modern equilibrated initial ice sheet state (ice sheet at equilibrium with modern climate, bedrock at isostatic equilibrium with ice sheet) (Pollard et al., 2017).

A simpler approach to incorporating bedrock deformation into large ensemble modelling studies is the Elastic Lithosphere Relaxing Asthenosphere (ELRA) model. The ELRA model approximates the solid earth as a thin elastic lithosphere overlying a relaxing viscous asthenosphere (Brotchie and Silvester, 1969, Meur and Huybrechts, 1996). It accounts for bedrock response to non-local changes in surface load (e.g. forebulge) but neglects gravitationally consistent sea level and rotational effects of global GIA models. In ELRA models, the overall bedrock response to changing load combines the elastic lithosphere response and a time-lagged asthenospheric response towards isostatic equilibrium, with the asthenosphere response determined by prescribed characteristic relaxation times (Huybrechts and Wolde, 1999, Greve and Blatter, 2009, DeConto and Pollard, 2016, Pattyn, 2017, Gregoire et al., 2012). In order to capture spatial variability in GIA parameters, Coulon et al. (2021) adapt the standard ELRA model, using spatially varying flexural

rigidity and relaxation time parameters to account for differences between the EAIS and WAIS. Similarly, Bulthuis et al. (2019) use two characteristic mantle relaxation times underneath the EAIS and WAIS.

An intermediate complexity model between ELRA and 1D global Earth-ice sheet coupled models is the model of Bueler et al. (2007), which approximates spatially varying mantle flow in a viscous half space beneath an elastic plate. It is discussed in more detail below.

### 3.2.2 GIA in BISICLES

In order to represent GIA processes here, we use the model of Bueler et al. (2007) implemented in BISICLES by Kachuck et al. (2020), GIANT-BISICLES. This model has advantages over the standard ELRA model because it includes two features of more complete earth models: bed relaxation is computed from viscosity and load wavelengths, as opposed to averaging characteristic relaxation times; it also includes elastic deformation of the viscoelastic mantle (Bueler et al., 2007, Kachuck et al., 2020). This model incorporates both instantaneous elastic response of the bedrock to changing surface load and time dependent response associated with viscoelastic deformation of the mantle (Kachuck et al., 2020). Instead of using characteristic time constants for a relaxing asthenosphere, mantle layers are prescribed viscosities - with timescale of viscoelastic response proportional to mantle viscosity (Lingle and Clark, 1985, Bueler et al., 2007, Cathles, 2015). In order to represent the influence of different mantle viscosities of the EAIS and WAIS, we use two mantle layers with different viscosities - an approach that is analogous to that of Pollard et al. (2017). Setting upper mantle viscosity to a relatively low value allows for rapid bedrock response in the region of greatest retreat (WAIS) as thickness change determines rebound. We note however that this does not fully capture WAIS-EAIS mantle heterogeneity.

Simulating self-gravitation and sea level feedbacks is beyond the scope of this study. In addition, we neglect sea level rise from Greenland and its influence on the AIS, as Greenland response to Pliocene climate is also poorly constrained. However, this is a standard simplification in standalone ice sheet modelling studies (DeConto and Pollard, 2016, DeConto et al., 2021), and we expect metre scale sea level rise from Greenland to have a secondary effect on Antarctic ice sheet stability compared with direct climate forcing. Moreover, in all subsequent work we treat the ocean area as fixed - an assumption which breaks down as ice sheet volume changes. As the oceans are not bounded in all places by vertical cliffs, ocean area can increase as the sea surface migrates up sloping shorelines with sea level rise in a process called onlap (Johnston, 1993, Whitehouse, 2018). The reverse process when sea level falls is know as offlap. Furthermore, ocean area

can decrease (increase) when marine terminating glaciers advance (retreat) beyond the continental margin - displacing ocean area (Milne and Mitrovica, 1998, Mitrovica and Milne, 2003, Whitehouse, 2018).

The use of GIA-enabled BISICLES (Kachuck et al., 2020) for the whole Antarctic ice sheet over long timescales is a novel aspect of the subsequent work. It incorporates a more comprehensive representation of solid earth feedbacks than the ELRA model, and its computationally efficient implementation (Kachuck et al., 2020) means that we can simulate the Antarctic ice sheet at higher resolution and more comprehensive (L1L2) model physics than the previous studies that use hybrid or SIA models. This approach allows us to simulate Antarctica under a warm Pliocene climate, accounting for uncertain GIA processes over long timescales and at higher resolution (4 km: Chapter 5) than many previous studies. It is well suited to a perturbed parameter ensemble approach.

### 3.2.3 Conditions at the base of the ice sheet

The ice sheet bed exerts a primary control on ice sheet velocity by providing resistance to flow through basal shear stress and form drag. Key determinants of friction at the bed are geology (see below), i.e. rock type and sediment characteristics, and basal hydrology (see below), i.e. presence of water at the bed and how much it lubricates flow by exerting pressure normal to the ice sheet base. As outlined in Section 1.3, laws that determine basal friction are chosen based on assumed or inferred characteristics of the bed. Weertman friction laws (Weertman, 1957) characterise sliding of ice over hard bedrocks, with basal friction related to basal velocity through a basal friction coefficient and an exponent. As the exponent gets smaller, bed friction becomes increasingly independent of velocity at the base. Coulomb friction laws (Section 1.3) approximate velocity-independent sliding but also account for pressure exerted by water at the base through an additional parameter, and are applicable to regions with deformable sediment at the bed. In coupled ice sheet hydrology models, this parameter is determined with a model of ice sheet basal hydrology (Hewitt, 2011).

Basal sliding laws parameterise processes at the base that are not directly observable, so parameter values must be inferred from observed ice flow or bed characteristics in deglaciated regions. However, a paucity of observations of the base of ice sheets makes characterising this important boundary challenging in ice sheet models (Hewitt, 2011). In this section, we briefly outline approaches to inferring basal friction parameters from satellite observations. This approach is taken for modern ice sheets, for which satellite observations exist. We then describe approaches to inferring basal friction parameters

for palaeo-ice sheets, where direct observations are not available. Next, we describe how time-evolving basal hydrology can be represented. Finally, we discuss the two component sliding law used in this work.

### Inferring basal parameters from satellite observations

Typically in projection studies basal sliding characteristics are inverted from satellite observations. For the inversion, a basal sliding law is chosen a priori and its parameters (e.g. friction coefficients: see below) are inverted, or assimilated, by tuning to match the simulated ice sheet state to modern observations of variables such as ice sheet velocity or surface elevation change (MacAyeal et al., 1995, Gillet-Chaulet et al., 2012, Morlighem et al., 2013, Arthern et al., 2015, Cornford et al., 2015, Gong et al., 2017).

In many instances, modern bed friction parameter fields are used for palaeo-ice sheet studies (Dolan et al., 2018). However, inverting basal sliding parameters from observations promotes the formation of ice streams in regions of the ice sheet where ice streaming occurs in the modern. Moreover, inverted basal friction parameters are fixed through time. This potentially limits the evolution of ice streams, as the ice sheet responds to changing climate and GIA adjustment of bedrock beyond centennial timescales. A further consideration when prescribing ice stream positions is the feedback between surface mass balance and ice streaming (Robel and Tziperman, 2016, Gandy et al., 2021). For large ice sheets with developed ice streams, Robel and Tziperman (2016) use a numerical model to demonstrate that moderate melting and surface lowering at the margins of ice sheets increases surface gradients. This increase in surface gradient increases driving stress and discharge of a similar magnitude to the initial melt-driven mass loss (Robel and Tziperman, 2016). Moreover, surface lowering through increased discharge can increase melt at the periphery, increasing surface gradients and discharge. In this way, feedbacks between ice streaming and surface mass balance can promote deglaciation of large ice sheets (Gandy et al., 2021, Robel and Tziperman, 2016). For simulating ice sheet evolution, models should therefore accommodate ice stream evolution (Aschwanden et al., 2013).

Over long timescales, the assumption embedded in inversion-based approaches - that basal sliding regime will remain comparable to modern - also breaks down. For ice streams, which account for 90% of Antarctic discharge (Bamber et al., 2000), capturing time-evolving bed conditions over multi-centennial timescales is a key challenge in ice sheet modelling.

### Inferring basal parameters from other information

For palaeo-ice sheet modelling applications, where velocity observations are not available for carrying out the inversion, basal sliding parameter fields can be prescribed at spatially uniform values (e.g. Gandy et al. 2019), or else inferred from local bed topography and type, discussed below.

Ice streaming primarily occurs as a result of topographic focusing in the presence of a calving margin (Winsborrow et al., 2010). Ice flow through topographic confinements, i.e. troughs, causes speed up in order to maintain discharge through a restricted cross-sectional area (Winsborrow et al., 2010). Thick ice in topographic troughs promotes ice streaming through increased frictional heating and therefore basal melt water production (Paterson, 1994). Thicker ice insulates the bed - increasing basal temperatures, and allowing ice at the bed to reach the pressure melting point earlier (Winsborrow et al., 2010). Melt-water at the base of ice streams can saturate basal sediments, making them more deformable and decreasing friction at the bed - promoting ice streaming (Alley et al., 1986, Blankenship et al., 1986, Engelhardt et al., 1990). As well as increasing production of melt-water at the bed, increased basal heating reduces ice viscosity - this promotes deformation and enhances ice streaming (Clarke et al., 1977). The tendency of ice streams to form in topographic troughs can be reflected in ice sheet models through the use of spatially varying, elevation dependent basal sliding coefficients. Bed friction coefficients that vary with bedrock elevation have been used extensively in palaeo-ice sheet simulations of Antarctica (Martin et al., 2011, Seguinot et al., 2016, Blasco et al., 2021). This approach is used here (described below).

Another factor that promotes ice streaming is subglacial geology (Clark, 1994, Anandakrishnan et al., 1998, Bell et al., 1998, Blankenship et al., 2001, Studinger et al., 2001). Hard bed geology exerts frictional resistance on ice flow and is less conducive to ice streaming. Soft deformable sediments may enhance flow by reducing form drag on obstacles at the bed, and porous sediments can become saturated (Alley, 2000) - reducing pressure at the bed. In formerly glaciated regions, bed type and shape can be observed directly. In examples of this approach, geomorphological features indicating style of glacier flow, from mega-scale glacial lineations (fast flow, ice streams) (Stokes and Clark, 1999, Canals et al., 2000, Evans et al., 2008) to exposed bedrock (low flow velocity) are used to prescribe basal friction coefficients (Gandy et al., 2018). For Pliocene simulations of the Antarctic ice sheet, the latter approach is not possible due to a lack of observations of the Antarctic ice sheet bed, leading to poor characterisation of the basal geology.

### Evolving basal hydrology

The third factor in determining ice streaming is favourable basal hydrology (Nye, 1976, Hooke, 1989). Winsborrow et al. (2010) cite basal hydrology as second only to topographic focusing with a calving margin in terms of importance for ice stream formation. Basal hydrology fluctuates across timescales, from diurnal cycles driven by surface melt (van de Wal et al., 2008), to longer term (e.g. seasonal) variations as the subglacial channel system evolves (Schoof, 2010, Hewitt, 2013, Schoof et al., 2014). Where ice at the base is at the pressure melting point, or melts through frictional heating, this can promote ice streaming (Paterson, 1994). For the Antarctic ice sheet, discharge of melt water at the grounding line to the base of the ice shelf (Carter and Fricker, 2012, Le Brocq et al., 2013) is evidence of connectivity between basal hydrology networks and the ocean. Long term simulation of ice streams, and therefore ice sheet evolution, should account for basal hydrology (van der Veen, 1999).

Gandy et al. (2019) implement a new basal hydrology coupled sliding scheme in BISICLES, which enables self-generation of ice streams without the need to determine their position with a mask, or through prescribed spatially varying basal sliding coefficients. This model successfully reproduces the evolution of the British and Irish Ice Sheet during the last deglaciation, demonstrating its potential for palaeoclimate applications. This model has not yet been applied to other ice sheets or time periods.

### Two component sliding model

The basal sliding scheme in the BISICLES version used in this study is that of Gandy et al. (2019). This couples ice thermo-dynamics and the production of water at the base of the ice sheet due to frictional heating to basal sliding, through Coulomb type sliding in a two component Weertman-Coulomb sliding law (Tsai et al., 2015)(Section 1.3.3).

$$|\tau_b| = min[C_b(|u_b|)^{(1/m)}, C_f(\sigma_0 - p_w)], \tag{3.1}$$

The first term governs Weertman sliding, and the second term Coulomb sliding. Weertman sliding is proportional to the magnitude of the velocity at the base of the ice sheet ($u_b$) to the power 1/m where m is the Weertman coefficient (here m=3), multiplied by a Weertman friction coefficient ($C_b$).

Coulomb basal friction is given by effective pressure, the difference between ice overburden pressure ($\sigma_0$) and the normal force exerted by till water on the base of the ice

sheet ($p_w$), multiplied by a Coulomb friction coefficient ($C_f$). Treatment of ice thermodynamics are described in Gandy et al. (2019), and follow an enthalpy transport scheme following Aschwanden et al. (2012)(Equation 2 in Gandy et al. 2019). Basal hydrology is approximated following Van Pelt and Oerlemans (2012)(Equation 3 in Gandy et al. 2019). Time-evolving basal water pressure ($p_w$) is given by:

$$p_w = \alpha \rho_i g H \left( \frac{min(W, W_0)}{W_0} \right), \tag{3.2}$$

where $W$ is the thickness of the till-stored water layer which evolves through Equation 2 in Gandy et al. (2019). Maximum till water depth, $W_0$, is the water depth beyond which the till becomes saturated (Gandy et al., 2019). The factor $\alpha$ defines the maximum ratio of pore-water pressure to overburden pressure which is achieved in the case of till saturation (Gandy et al., 2019), and is set to 0.99 as in Gandy et al. (2019). Finally, $\rho_i$ is density of ice, $g$ is acceleration due to gravity, and $H$ is ice thickness.

### 3.2.4 Pliocene Surface Mass balance

This chapter explores the role of processes at the base of the ice sheet in the context of Pliocene climate. This section describes the surface mass balance component of this climate. We first summarise other approaches to representing surface mass balance in modelling studies, followed by an introduction to our positive degree day (PDD) approach.

The state of the art in simulating ice sheet evolution under a changing climate is the use of bidirectional, synchronously coupled GCM-ice sheet models (Earth System Models or ESMs) (e.g. Muntjewerf et al. 2021, Smith et al. 2021, Pelletier et al. 2022). In this context, coupling refers to the exchange of variables between models representing different components of the climate system, such as separate numerical models of the ice sheet and ocean. Bidirectional coupling refers to two way exchange of variables between model components. Coupled models capture ice sheet response to surface forcing and update ice sheet derived fields in the climate model, such as ice sheet surface elevation in an atmospheric model component. In this way, a coupled modelling approach can capture feedbacks between the ice sheet and its climate in a consistent manner.

Few studies have applied ESMs to millennium scale studies of ice sheets (Ziemen et al., 2019, Sommers et al., 2021). ESMs can provide insights into transient feedbacks between ice sheets and climate processes - with a more comprehensive representation of complex physics in coupled components than simpler approaches. For example, Ziemen et al. (2019) were able to capture climate-ice sheet interactions that drive the purge and recovery phases

of Heinrich events. They resolved lowering-driven precipitation changes that hastened recovery of the Laurentide ice sheet, and captured timing and magnitude of Heinrich events - achieving good agreement with reconstructions. However, ESM approaches are too complex and computationally expensive for ensemble studies (Ziemen et al., 2019, Sommers et al., 2021). Whilst asynchronous coupling of ESM components can decrease run time (Niu et al., 2021, Roberts et al., 2014), they too are unsuitable for ensemble studies. Earth system models of intermediate complexity (EMICs), with a less computationally expensive climate component, have been used more widely in studies of palaeo-ice sheets compared with ESMs (Calov and Ganopolski, 2005, Heinemann et al., 2014, , Ganopolski et al., 2010, Ganopolski and Brovkin, 2017, Stap et al., 2014, Vizcaino et al., 2015, Choudhury et al., 2020, Bahadory et al., 2021, Goelzer et al., 2016). Whilst EMICs can be run for ensemble studies (e.g. Choudhury et al. 2020), climate-ice sheet model coupling is still complex. Moreover, coupled modelling approaches can strongly amplify biases - making evaluation of climate driven uncertainty challenging. As this is a goal of subsequent chapters, a coupled modelling approach is therefore not appropriate.

To capture transient Pliocene climate, De Boer et al (2017a) use a series of HadCM3 simulations outlined in Prescott et al. (2014), with time varying insolation to reflect changing orbital configuration through the late Pliocene. In this study, transient climate is driven by time varying insolation in HadCM3, and the effects of elevation change in the ice sheet model are parameterised using lapse rate corrections for temperature and precipitation (de Boer et al., 2017a).

Another approach to simulating Pliocene Antarctic climate can be found in DeConto et al. (2016, 2021, 2015). They use output from an offline regional climate model (RegCM3), run at 40 km resolution over Antarctica with an ice-free WAIS to force Pliocene simulations (Pollard et al. 2015, supplementary information). For century scale simulations of Antarctica in Chapter 2, we use surface mass balance outputs directly from GCMs. In both cases, atmospheric fields do not respond to changes in ice sheet elevation. This will likely have a marginal impact for century-scale future simulations of Antarctica, where retreat is dominated by ocean-driven melting and elevation change is relatively limited in the interior. For future simulations of the Greenland ice sheet, elevation feedbacks can be parameterised (Edwards et al., 2014b, Goelzer et al., 2020c). However, this process is complex, and challenging for Antarctica where surface mass balance estimates are uncertain due to precipitation uncertainty (Mottram et al., 2021).

The other approach to capturing surface mass balance elevation feedbacks is to use temperature and elevation from GCMs, and parameterise the elevation feedback through lapse

rates for each. Surface mass balance can then be parameterised from temperature and precipitation (Reeh, 1991).

We adopt a simple, computationally tractable approach to calculating surface mass balance in the form of a Positive Degree Day (PDD) mass balance scheme (Reeh, 1991). Widely used in palaeo-ice sheet studies (Gregoire et al., 2015, 2016, Gandy et al., 2019, 2021), including studies of the Pliocene (de Boer et al., 2015, Yan et al., 2016, Dolan et al., 2018), PDD models calculate surface mass balance as a function of precipitation and temperature, with melt proportional to the sum of daily mean temperatures for all days with mean temperature above 0°C in a year.

We use the positive degree day (PDD) model of (Seguinot, 2013)(as used in Gandy et al. 2019, 2021) with monthly climatological mean fields of temperature and precipitation (Section 3.3.5). PDD models use constant factors to parameterise surface melting of snow (*PDDs*) and ice (*PDDi*) when temperatures are above 0 °C, which are typically prescribed values of 3 mm w.e. $^{\circ}C^{-1}d-1$ for snow and 8 mm w.e. $^{\circ}C^{-1}d-1$ (Huybrechts and Wolde, 1999), with modern values for Antarctica typically at the lower end of this range (Huybrechts and Oerlemans, 1990).

The PDD approach adopted here allows us to sample outputs from multiple Pliocene GCMs (e.g. Chapters 4 and 5), accounting for elevation-surface mass balance feedbacks and biases in GCMs (see Section 3.3.5 below). It is computationally tractable, and its simplicity allows for clearer interpretation of climate uncertainty. This makes it an ideal choice for millennium-scale ensemble studies of Antarctica in the Pliocene.

A limitation of the PDD method is the use of constant values for *PDDs* and *PDDi*. In practice, the proportion of melt at the ice sheet surface is sensitive to factors with high spatial variability across the ice sheet such as wind, humidity, cloud cover and albedo (Hock, 2003, Wake and Marshall, 2015) with the latter playing an important role in heat transfer and therefore surface melt (Wake and Marshall, 2015). Measurements of melt per degree day also show clear spatial dependence for large ice sheets. In high continental ice sheet interiors, melt occurs largely through energy intensive sublimation, leaving less residual energy for melt - reflected in low degree factors measured in the ice sheet interior (Hock, 2003). Coastal ice sheet margins typically have higher degree day factors due to latent heat of condensation and sensible heat transfer associated with high winds and high humidity.

## 3.3 Methods

The palaeo-ice sheet modelling framework described above, with the GIA model (GIANT-BISICLES, (Kachuck et al., 2020), Section 3.2.2), coupled basal hydrology sliding scheme (BISICLES_hydro, (Gandy et al., 2019), Section 3.2.3) and PDD surface mass balance scheme (pyPDD, (Seguinot, 2013), Section 3.2.4) has not been used before in BISICLES. As outlined in the previous sections, the GIA model has previously been applied to Pine Island Glacier but not the whole AIS (Chapter 5), and the basal hydrology scheme only to the British and Irish and Fennoscandian ice sheets (Gandy et al., 2019, 2021). We therefore test this setup using a small perturbed parameter ensemble to evaluate the simulations for a region of the Antarctic ice sheet, and explore the effect of their uncertain parameters.

We simulate the Amundsen Sea Embayment (ASE), a marine grounded catchment in West Antarctica, where most mass is currently being lost from the ice sheet (Fox-Kemper et al., 2021). This includes two main glaciers: the Pine Island and neighbouring Thwaites glaciers. The ASE accounts for around a third of WAIS ice discharge. With a inland sloping bedrock up to ~2.5 km depth (Morlighem et al., 2020), it is an extreme example of marine grounded geometry of ice in West and East Antarctica. The Pine Island Glacier has been the focus of a number of previous studies (Kachuck et al., 2020, Favier et al., 2014, Gladstone et al., 2012) including with BISICLES as part of the wider Antarctic ice sheet (Favier et al., 2014, Nias et al., 2016, 2019, Wernecke, 2020, Wernecke et al., 2020). It therefore represents a suitable test case for exploring sensitivity to a range of model parameters governing bedrock response to surface ice load changes (GIA: section 3.2.1), processes at the base of the ice sheet (basal sliding: section 3.2.3) and basal melt forcing in the ocean (Chapter 2)

### 3.3.1 Model description

We use BISICLES (Cornford et al., 2013) (Section 1.3.2) to simulate the ASE. The model includes the basal hydrology coupled sliding scheme of Gandy et al. (2019), where the Coulomb component of a Tsai type sliding law (2015) is coupled to basal hydrology. The GIA component of Kachuck et al. (2020) is implemented, and the pyPDD surface mass balance scheme of (Seguinot, 2013). The ISMIP6 non-local basal melt parameterisation is used as in Chapter 2. For all simulations, we use a m=1/3 for Weertman sliding.

### 3.3.2 Model Domain

Our model domain covers the ASE on a 112 by 128 grid at 8 km base resolution and 3 levels of refinement to give a maximum resolution of 1km. To isolate the ASE, we impose high bed friction outside the Thwaites and Pine Island catchment (black contour in Figure 3.2), to limit the influence of ice outside the ASE catchments on dynamic evolution within it. Within this domain, our focus is on the PIG catchment as defined by Mouginot et al. (2019) based on ice divides from Rignot et al. (2013)(red contour in Figure 3.2 **a.**). In order to use computational resources efficiently, BISICLES refines the mesh only within box-bounded areas covering the PIG catchment. We use 1 km finest resolution in the Pine Island catchment and low resolution across the rest of the domain - this is sufficiently high within the domain as we use the grounding line subgrid interpolation friction scheme (Cornford et al., 2016). This captures the relatively localised influence of bed topography and pinning points, changes to buttressing as a result of shelf removal, and high resolution variations in bed flow regime

We simulate the Thwaites glacier for stability, and do not account for changes there in our results. We found that not including Thwaites in our simulation domain produced edge effects impacting the Pine Island flow regime in test experiments (not shown). Simulating Thwaites at low resolution reduced these errors at the ice divides of the PIG catchment, whilst minimising computational overhead.

### 3.3.3 Basal sliding

We first tested constant values (~7,500 to ~62,000) for the Weertman friction coefficient ($C$). We used a Weertman exponent m=1/3, in a test ensemble of the Pine Island Glacier catchment in West Antarctica, with $C$ values encompassing the range used in Gandy et al. (2019) for the British and Irish ice sheet. However, we found that using spatially invariant $C$ values, as in Gandy et al. (2019, 2021), produced unphysical velocity patterns. An example of these velocity patterns can be seen in time snapshots for an ensemble member, shown in Figure 3.3. These errors are associated with regions of the ice sheet away from the grounding line, where the ice sheet thins below floatation - indicated by the yellow contour in Figure 3.4 **b.**. Using the hydrology coupled, two component basal sliding law, maximum till water depth is applied at the base and bed friction drops to zero when ice thins below floatation. Where this occurs in the marine grounded interior of the ice sheet, it drives the errors seen in Figure 3.4. In addition to bed friction dropping, where regions of the ice sheet thinned below the floatation thickness, ocean melt forcing was applied in these simulations. This potentially exacerbated thinning through basal melting. However, further

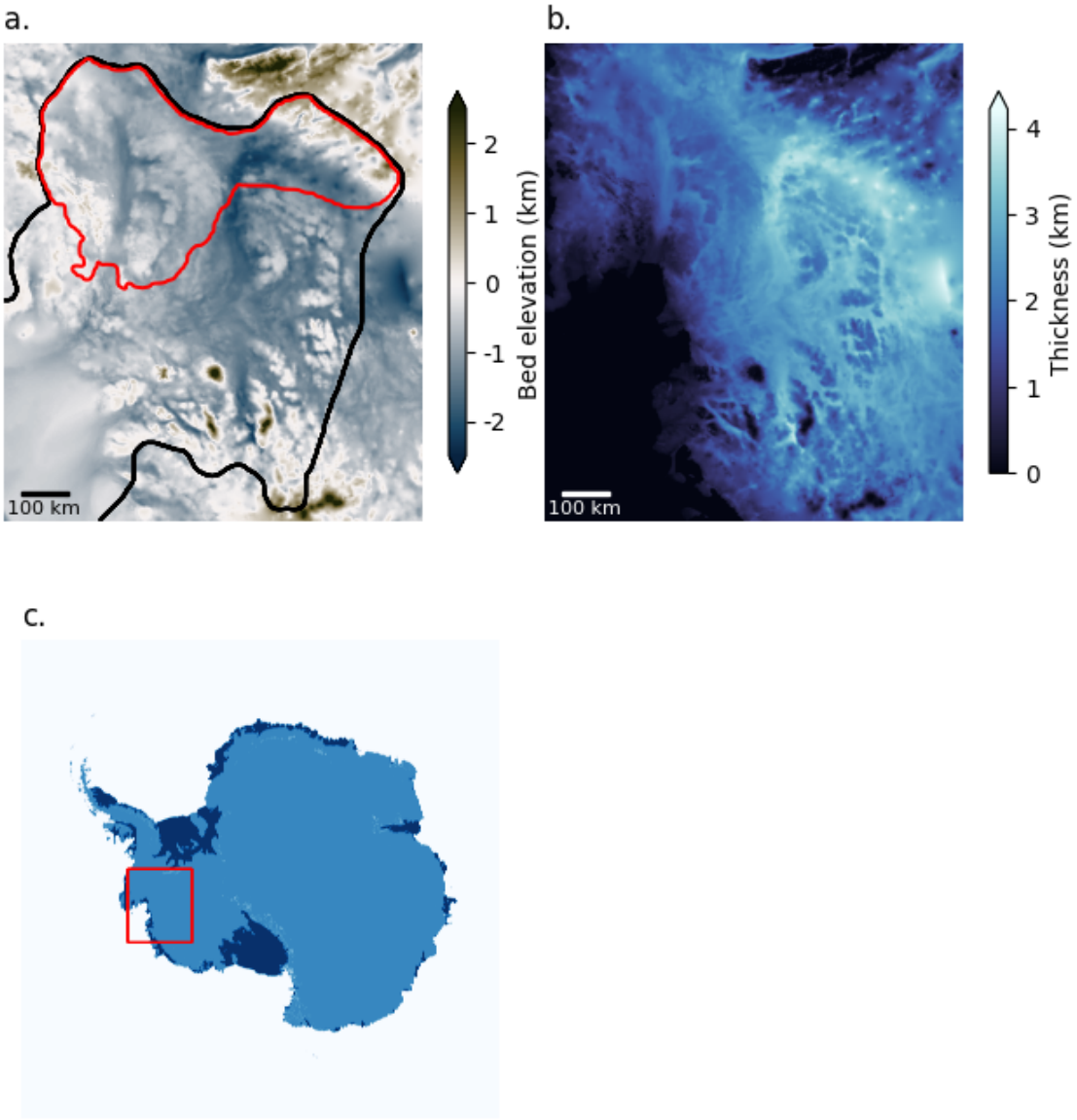


Fig. 3.2 Model domain for Pine Island Glacier catchment simulations. Initial bedrock elevation is shown in subplot **a.**. The black contour in **a.** shows the Amundsen Sea Embayment (ASE) domain. The red contour outlines the PIG catchment. Subplot **b.** shows initial ice thickness. The red box in subplot **c.** shows our model domain in the context of the Antarctic ice sheet.

test simulations, with a model version where ocean melt was not applied in "ice shelf" regions away from the grounding line (not shown), did not show a significant reduction in velocity errors. We therefore infer that the velocity errors were primarily a result of dynamic thinning to floatation, exacerbated by the use of a spatially invariant bed friction coefficient (S. Cornford, personal communication). An alternative explanation for the errors shown in Figure 3.4, is a numerical instability in the BISICLES solution. The use of a variable time step aims to maintain numerical stability. However, we note that whilst simulations with more extensive velocity errors have more refinement of the time step, they did not fail to converge to a stable solution. Previous authors have noted that whilst stability analysis of the L1L2 BISICLES solver is challenging, stability issues may arise at high resolution and with m = 3 as here (Robinson et al., 2022).

To avoid such artefacts we implement a spatially varying Weertman coefficient field ($C_b$), inferred from bedrock elevation below sea level ($z_b$). The implementation follows that of Blasco et al. (2021) and is analogous to the approach of Martin et al. (2011):

$$c_b = \begin{cases} c_{max}, & \text{if } z_b \geq 0 \\ max\left[c_{max} e^{-\frac{z_b}{z_0}}, c_{min}\right], & \text{if } z_b \leq 0, \end{cases} \tag{3.3}$$

where $C_{max}$ is the maximum value of $C_b$ across the domain and is prescribed for bedrock above sea level. In locations where the ice-bed interface is below sea level, $C_b$ decreases from $C_{max}$ to $C_{min}$ with the parameter $z_0$ controlling the e-folding depth over which friction coefficient decreases.

Blasco et al. (2021) use a linear viscous sliding law and include effective pressure in their formulation of basal sliding. The values they use for $z_0$ are therefore not applicable in the BISICLES set up here. For the simulations in this study, a suitable value for $z_0$ (-2000) was found by tuning its value in test simulations to approximately match velocity and sea level contribution in simulations using $C_b$ inverted from observations (Section 3.2.3)(inverted friction for Bedmachine Amundsen Sea Embayment domain supplied by S. Cornford and D. Martin).

Figure 3.5 shows the relationship between bed elevation and the inverted Weertman friction coefficient, with red lines indicating our elevation dependent basal friction parameterisation with $C_{max}$ set to the $5^{th}$, $50^{th}$ and $95^{th}$ percentiles of the inverted basal friction field. Visual inspection of output velocity fields shows that using an elevation dependent Weertman friction coefficient resolves the velocity errors seen in previous simulations.

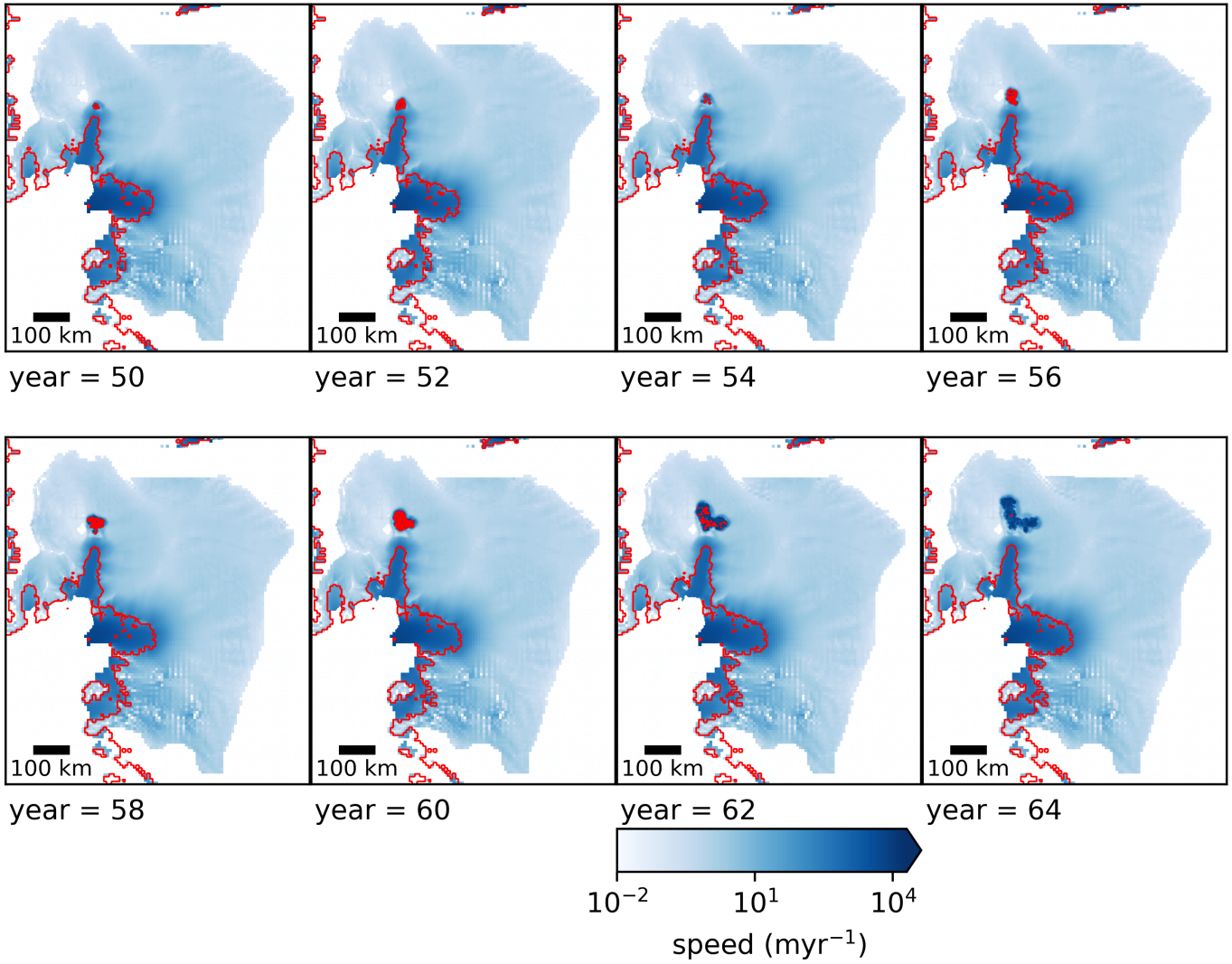


Fig. 3.3 Snapshots of speed at successive 2 year intervals, exemplifying the velocity errors discussed in the main text. Red contours show the grounding line position, including for regions in the interior ice sheet that thin to below floatation.

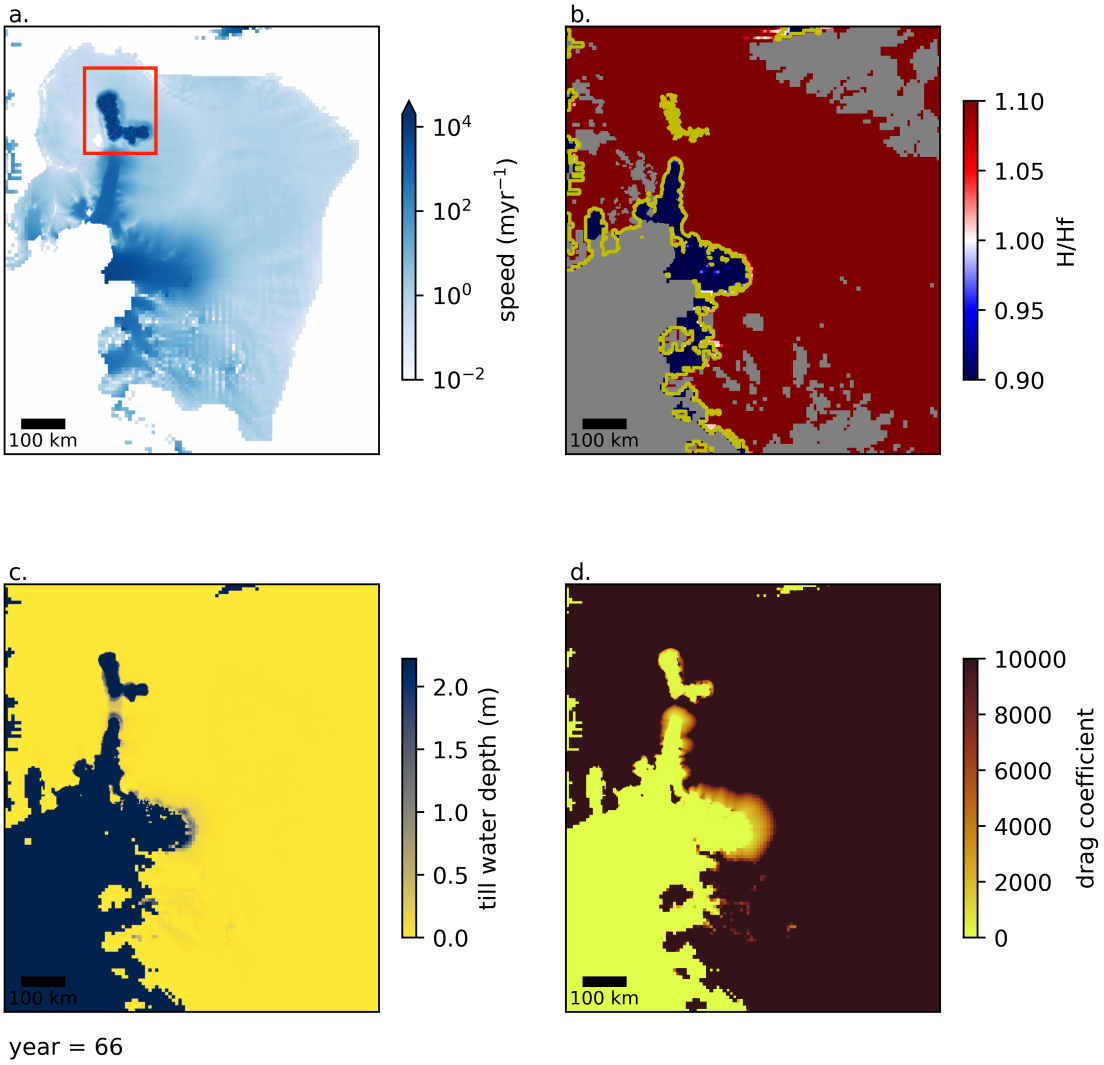


Fig. 3.4 Example plot of the error discussed in the main text showing speed (**a.**); the ratio of ice thickness to floatation thickness (H/Hf), with regions grounded above sea level or with no ice thickness are masked in grey (**b.**); till water depth (**c.**); and the drag coefficient (**d.**) for a Pine Island catchment simulation with constant Weertman friction coefficient. Where thickness/floatation thickness < 1, ice floats. Regions of unphysical velocity are highlighted by the red box in **a**. Results are from the same simulation as plotted in Figure 3.3.

We note that elevation dependent basal friction has been used for Laurentide ice sheet simulations in BISICLES (Matero et al., 2020). Matero et al. (2020) prescribe initial values of the Weertman friction coefficient based on geological data as in Gandy et al. (2018), and scale these with elevation. As noted in Section 3.2.3 however, geological evidence for conditions at the base of the Antarctic ice sheet is lacking, which is why basal friction parameters reflecting bedrock type are challenging to infer.

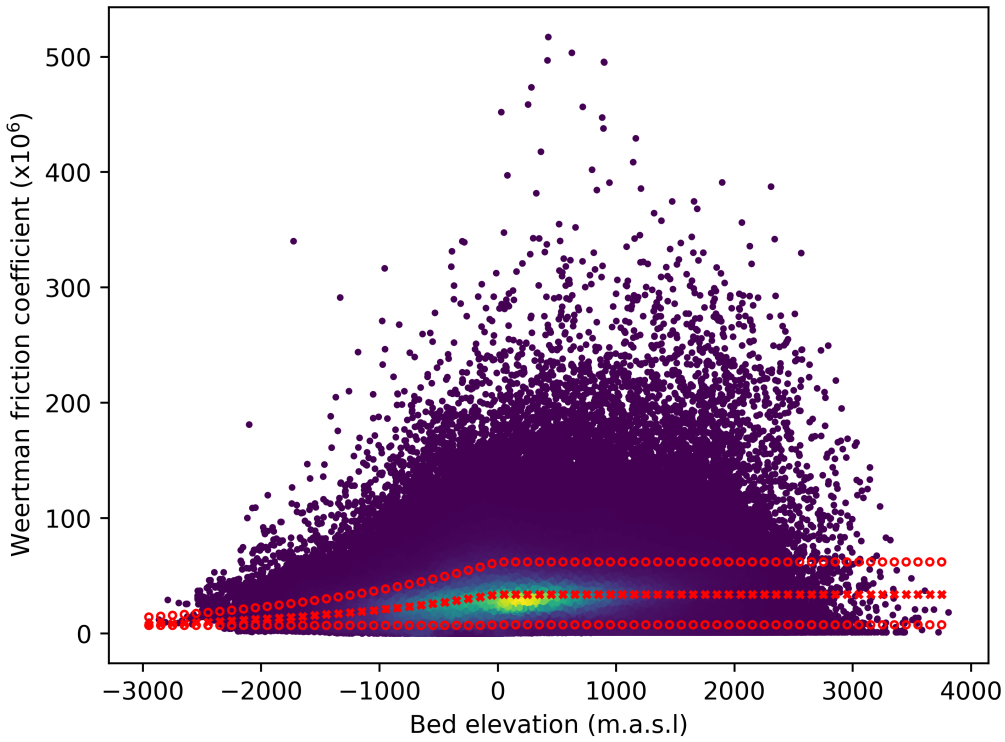


Fig. 3.5 Inverted Weertman basal friction coefficients as a function of bedrock elevation. Marker colour indicates point density, with yellow markers showing regions of higher point density. Also shown are examples of Weertman friction coefficients as a function of elevation calculated using the elevation dependent basal friction parameterisation described in the main text (red markers). Lower most line with red open circle markers is calculated with $C_{max}$ equal to the $5^{th}$ percentile of inverted Weertman friction coefficients (~7,500). Central line with red X markers is calculated with $C_{max}$ equal to the $50^{th}$ percentile of inverted Weertman friction coefficients (~34,000). Upper most line with red open circle markers is calculated with $C_{max}$ equal to the $95^{th}$ percentile of inverted Weertman friction coefficients (~62,000).

### 3.3.4 Climate forcing

To simulate Pliocene climate in this ensemble, we used outputs from the first generation of the Pliocene Model Intercomparison Project (PlioMIP1) (Haywood et al., 2010). PlioMIP1 was a climate modelling intercomparison project that compared climate model skill in modelling Pliocene climate based on comparison with proxy data (Dowsett, 2007). It is the predecessor to PlioMIP2 (Haywood et al., 2016b), which is discussed in more detail in Section 4.1.1.

We use output from the CCSM4 PlioMIP1 experiments to force this ensemble, as used in Dolan et al. (2018) as part of the Pliocene Ice Sheet Modelling Intercomparison Project (PLISMIP). Surface air temperature, precipitation and ocean temperature for Pliocene (Eoi400) and control (E280) simulations were provided by B. de Boer on 40 km polar stereographic grids. Ocean data was provided with temperature extrapolated into regions of missing data under ice shelves and in the ice sheet interior. The extrapolation used a distance weighting scheme (B de Boer, personal communication). We regridded and bilinearly interpolated surface air temperature, precipitation and ocean temperature to 8 km resolution before applying the bias-correction and downscaling outlined below.

### 3.3.5 Climate field downscaling and bias correction

To reduce biases in PlioMIP1 climate forcing, we use an anomaly approach. We calculate the difference between the Pliocene and control fields of surface air temperature and precipitation, and add these to equivalent fields from the Regional Atmospheric Climate Model (RACMO2) (Wessem et al., 2014).

RACMO2 is a regional model that has been widely applied to studies of Antarctica (Yan et al., 2016, Sutter et al., 2019). We use RACMO2 as the basis for our Pliocene atmosphere because it is run at relatively high resolution (27 km), allowing it to better simulate atmospheric processes sensitive to surface gradients and therefore resolution (van de Berg et al., 2006). RACMO2 also compares favourably to observations of surface mass balance (Wessem et al., 2014, Mottram et al., 2021). At its lateral boundaries and for the ocean, RACMO2 is forced with ERA-interim reanalysis data (Dee et al., 2011). For the baseline modern climate, we use average monthly RACMO2 precipitation and temperature between 1979-2000. We use a downscaling approach following that of Yan et al. (2016), who use RACMO2 for base temperature and precipitation and NorESM PlioMIP1 output to force a perturbed parameter ensemble.

All models used to compute Pliocene surface mass balance forcing are at lower resolution than our BISICLES lowest resolution of 8 km. To downscale atmospheric fields following bilinear interpolation, we perform an elevation correction. The procedure for calculating bias-corrected, downscaled surface mass balance fields that evolve with changes in ice sheet elevation is outlined below:

$$T_{(t)} = T_{ref(t)} + T_{plio(t)} - T_{pi(t)} \tag{3.4}$$

Where $T_{(t)}$ is elevation-corrected average monthly surface temperature, with t indicating ice sheet model time step. Subscript $ref$ is the reference climate, taken from the average RACMO2 (Wessem et al., 2014) climate. The $plio$ and $pi$ subscripts refer to the Pliocene ($Eoi400$) and pre-industrial ($E280$) climate fields respectively, averaged over the final 100 simulation years.

A lapse rate correction is applied to average monthly reference climate, Eoi400 climate and E280 climate. For example, the elevation correction is applied to monthly Eoi400 temperature as follows:

$$T_{plio(t)} = T_{plio} + LRT \times (H_{bisicles(t)} - H_{plio}) \tag{3.5}$$

Where $T_{plio}$ is the uncorrected average monthly surface temperature, $LRT$ is the temperature lapse rate (-0.008 °C m$^{-1}$), $H_{bisicles(t)}$ is the BISICLES ice sheet elevation at time step $t$, and $H_{plio}$ is Antarctic elevation in the forcing GCM Pliocene experiment. The same elevation correction is applied for $T_{ref}$ and $T_{pi}$.

As with temperature, precipitation is adjusted to account for discrepancies in ice sheet elevation in BISICLES and GCMs. Time evolving precipitation $P_{(t)}$ is:

$$P_{(t)} = P_{ref(t)} \times \frac{P_{plio(t)}}{P_{pi(t)}} \tag{3.6}$$

Where $P_{plio(t)}$ is average monthly precipitation from the Pliocene (Eoi400) GCM experiment adjusted for elevation difference between the GCM and BISICLES at time step $t$. The precipitation scaling for Pliocene precipitation is applied in the following way :

$$P_{plio(t)} = P_{plio} \times e^{LRP(H_{bisicles(t)} - H_{plio})} \tag{3.7}$$

Where $P_{plio}$ is average monthly precipitation from the Pliocene (Eoi400) GCM experiment. The LRP parameter combines temperature lapse rate and the alpha parameter used for elevation correction of precipitation in Yan et al. (2016) Pliocene experiments into a single parameter. The default value of the precipitation scaling with temperature ($LRP$) (-4$\times$10$^{-4}$) is equivalent to alpha = 0.05 (corresponding to a 5.1% increase in precipitation for every degree temperature increase) and lapse rate of -8°$Ckm^{-1}$ in Yan et al. (2016).

The approach outlined above provides steady-state Pliocene temperature and precipitation fields which evolve in time only as a function of changing ice sheet elevation through the lapse rate corrections. These bias-corrected, downscaled fields are used to drive the PDD

model of Seguinot (2013). Below 0°C, all precipitation is assumed to fall as snow with accumulation equal to precipitation. Between 0-2° the proportion of precipitation falling as rain increases to 1, with accumulation decreasing proportionally (Seguinot, 2013). Surface mass balance is recalculated every 30 years to provide elevation-corrected surface mass balance fields. For PDD parameters, we use default values of 3 mm w.e. $^{\circ}C^{-1}d^{-1}$ for snow and 8 mm w.e. $^{\circ}C^{-1}d^{-1}$ for ice. To calculate overall melt, snow is melted at a rate proportional to *PDDs*, followed by ice at a rate proportional to *PDDi*.

For the ocean, we calculate the difference between the Pliocene and control fields of ocean temperature. This anomaly is added to a modern observational data compilation (Locarnini et al., 2019, Zweng et al., 2019, Good et al., 2013b, Roquet et al., 2013) as used for ISMIP6 (Jourdain et al., 2020) (Chaper 2), averaged over 1995-2017. The resulting temperature is used to calculate thermal forcing, with modern salinity used in the absence of salinity from PlioMIP1. Thermal forcing is used to calculate ice shelf basal melt using the ISMIP6 non-local basal melt rate parameterisation (Jourdain et al. 2020, chapter 2). Atmospheric and ocean forcing for all simulations in this chapter, and throughout the remainder of this thesis, is steady state.

### 3.3.6 Experimental design

We perturb five parameters with a direct influence on the basal regime of the ice sheet, bedrock evolution and ice shelf melting. These are: upper and lower mantle viscosities ($UMV$, $LMV$) in the two mantle layer GIA model (Kachuck et al., 2020); Weertman friction coefficient ($C_b$) and maximum till water depth ($mTWD$) from the Weertman-Coulomb sliding law (Gandy et al., 2019), and basal melt sensitivity to thermal forcing ($\gamma_0$) from the ISMIP6 parameterisation (Chapter 2).

#### Mantle Viscosities

To explore sensitivity to mantle viscosity, we perturb both upper mantle ($UMV$) and lower mantle viscosity ($LMV$). Mantle viscosity affects the rate and pattern of ice sheet bed and sea floor topography change in response to changing ice load. In studies incorporating GIA, mantle viscosity is commonly set at $10^{21}$Pa s for pan-Antarctic fixed mantle viscosity simulations (Mitrovica and Forte, 1997, Ivins and James, 2005, Kingslake et al., 2018, Whitehouse et al., 2012, 2019). However, viscosity in West Antarctica's weak upper mantle can be lower by an order of magnitude (Whitehouse et al., 2019) and as low as $4x10^{18}$ Pa s for the Amundsen Sea coast (Barletta et al., 2018) and $6x10^{17}$ Pa s for the Peninsula (Nield et al., 2014). Order of magnitude variations in lower mantle viscosity have also

been derived from seismic data across Antarctica (Ivins and James, 2005, Whitehouse et al., 2019).

We perturb $UMV$ across a range from $10^{18}$Pa s to $10^{20}$Pa s for $UMV$ (Nield et al., 2014, Barletta et al., 2018, Kingslake et al., 2018). For $LMV$, our perturbation range is from $10^{19}$Pa s to $10^{22}$Pa s, within the range of global estimates (e.g. Mitrovica and Forte 1997, Lambeck 1998, Peltier 2004, Bradley et al. 2011, Steffen and Wu 2011, Whitehouse et al. 2012, Lambeck et al. 2014, Lecavalier et al. 2014, Peltier et al. 2015, Nakada and Okuno 2016, Whitehouse 2018.

A further control of bedrock response to changing surface load is flexural rigidity. Flexural rigidity is associated with the thickness of the elastic lithosphere and affects the length scale over which the bedrock responds to a changing load. We use flexural rigidity of $1.3\text{x}10^{24}$ Nm, which corresponds to an elastic lithospheric thickness of 60 km with the parameters used in GIANT-BISICLES (Kachuck et al., 2020). Studies of West Antarctica with PISM incorporating the Bueler et al. (2007) GIA model use the same order of magnitude flexural rigidity (Albrecht et al., 2020, Kingslake et al., 2018). This is at the upper end of a range of values inferred for West Antarctica by Chen et al. (2018). Although East Antarctica typically has a stronger lithosphere and therefore a higher flexural rigidity than West Antarctica, less dynamic change is expected for East Antarctica under warm Pliocene conditions (Shakun et al., 2018) and we use the same flexural rigidity value across the domain.

### Ice shelf basal melt sensitivity

To simulate melting at the base of the ice shelves, we use the ISMIP6 non-local basal melt parameterisation (Chapter 2). We perturb $\gamma_0$ across the 6 values provided by ISMIP6: the $5^{th}$, $50^{th}$ and $95^{th}$ percentiles of basal melt calibrated with estimates for the whole Antarctic ice sheet (*MeanAnt*), and the $5^{th}$, $50^{th}$ and $95^{th}$ percentiles of basal melt calibrated to the ten grid cells with highest basal melt at the grounding line of the Pine Island Glacier (*PIGL*). As in chapter 2, $\gamma_0$ takes discrete values as provided by ISMIP6. Continuous sampling of $\gamma_0$ would require repeating the sampling procedure outlined in (Jourdain et al., 2020), which is beyond the scope of this thesis.

### Basal sliding parameters

We use the elevation dependent Weertman friction coefficient fields as outlined in Section 3.3.3. To explore sensitivity to this, we sample $C_{max}$ between the $5^{th}$ and $95^{th}$ percentiles

of Weertman friction coefficient inverted from observations with modern velocity fields (Cornford et al., 2015)(Section 3.2.3), excluding regions of ice streaming in order to use Weertman coefficient values representative of non-streaming regions. This gives a range between ~7,500 to ~62,000.

To explore ice stream sensitivity to basal hydrology, we vary maximum till water depth ($mTWD$). This determines the threshold above which water at the base of the ice sheet impacts flow. Following Gandy et al. (2019), we perturb this across a range from 1-4m. Previous studies have varied till friction angle in the coulomb sliding (Gandy et al., 2019, 2021), but we found in test simulations on a smaller PIG domain (not shown) a comparable if slightly smaller influence of till friction angle compared with maximum till water depth. We therefore chose to perturb maximum till water depth over till friction angle in this study, with till friction angle set to a default value of 0.5 as in previous studies (Nias et al., 2018, Gandy et al., 2019).

### Ensemble Design

We use a 30 member 'maximin' Latin Hypercube ensemble design (Santner et al., 2003). A maximin Latin Hypercube maximises the minimum distance between points in the parameter space. For the mantle viscosities, we apply a constraint on their relative values. There is general agreement that the viscosity of Earth's lower mantle is greater than that of the upper mantle, although the magnitude of the difference in viscosity is much debated (e.g. Mitrovica and Forte 2004, Caron et al. 2017, Whitehouse 2018). In order to generate a maximin latin hypercube ensemble that evenly samples all parameters without contravening the $LMV > UMV$ relationship, we construct a constrained ensemble following Petelet et al. (2010). This ensures that no simulation has a higher upper mantle viscosity than its lower mantle viscosity, whilst preserving the efficiently space filling design.

We simulate a minimum of 1,000 years of ice sheet evolution, or until the majority of ice volume above floatation in the domain has been lost (see below).

### GIA error

After running and analysing the PIG ensemble presented in this chapter, we found that all simulations had undergone unphysical subsidence. Subsequent analysis revealed that BISICLES GIA component was interpreting initial ice sheet thickness as a load perturbation on the bedrock - contravening our initial assumption that the ice sheet and bedrock are at isostatic equilibrium. Erroneous subsidence corresponds to ice sheet thickness, such

that greater subsidence occurs away from the grounding line where the ice is thickest. Moreover, subsidence is not the same for all simulations. The impacts of this error on the ensemble, and its interpretation for later chapters, are discussed throughout and in the Conclusions (Section 3.6). The error is caused by initialising simulations from a spin up simulation where the GIA component is switched off, as in the ensemble that underwent background subsidence, or with different GIA parameters. To explore the impact of the GIA error on our interpretation of the PIG ensemble, we repeated a subset of experiments. These are discussed in Section 3.5.

## 3.4 Results and Discussion

We report results for change in volume above floatation (ice volume not displacing sea water at the start of the simulation) within the Pine Island Glacier (PIG) catchment. Grounded mostly below sea level (Fig. 3.2), once all ice has been lost from the PIG domain it no longer contributes to sea level, with no re-advance back into its submarine basin. The sea level contribution from PIG at the end of the simulation period for all runs is therefore the same at ~425 mm. We therefore explore the role of parameter perturbations, on the speed of catchment level glacier response - expressed through the time taken for the Pine Island catchment to lose 425 mm SLE VAF. Figure 3.6 shows change in volume above floatation, change in total volume, grounded area, and floating area within the PIG domain. Change in volume above floatation shows an initial drop for a subset of ensemble members. We interpret this as being an artefact of the GIA error. Where bedrock subsides at the start of the simulation, submarine grounded ice subsides with the bedrock - causing a sharp decrease in volume above floatation. The lack of a concomitant increase in floating area, on the time scale of the decrease in VAF, implies that the subsidence is not large enough to cause widespread floatation of submarine grounded ice.

Figure 3.7 shows the time taken to lose the majority of ice (425 mm SLE), as a function of each perturbed parameters. The clearest relationship is with the Weertman friction coefficient. Also shown are sensitivity to upper mantle viscosity ($UMV$), lower mantle viscosity ($LMV$), maximum till water depth ($mTWD$) and ice shelf sensitivity to basal melt ($\gamma_0$). We discuss sensitivity to model parameters further below.

The Weertman friction coefficient exerts a strong control on time taken to lose the majority of PIG VAF (Fig. 3.7), with lower Weertman friction coefficient delaying ice sheet mass loss in the PIG catchment. This is counter-intuitive, because we would expect the higher velocity seen in the interior in lower Weertman friction simulations to drive larger discharge and faster mass loss. Transect plots through the PIG trunk however, shown for

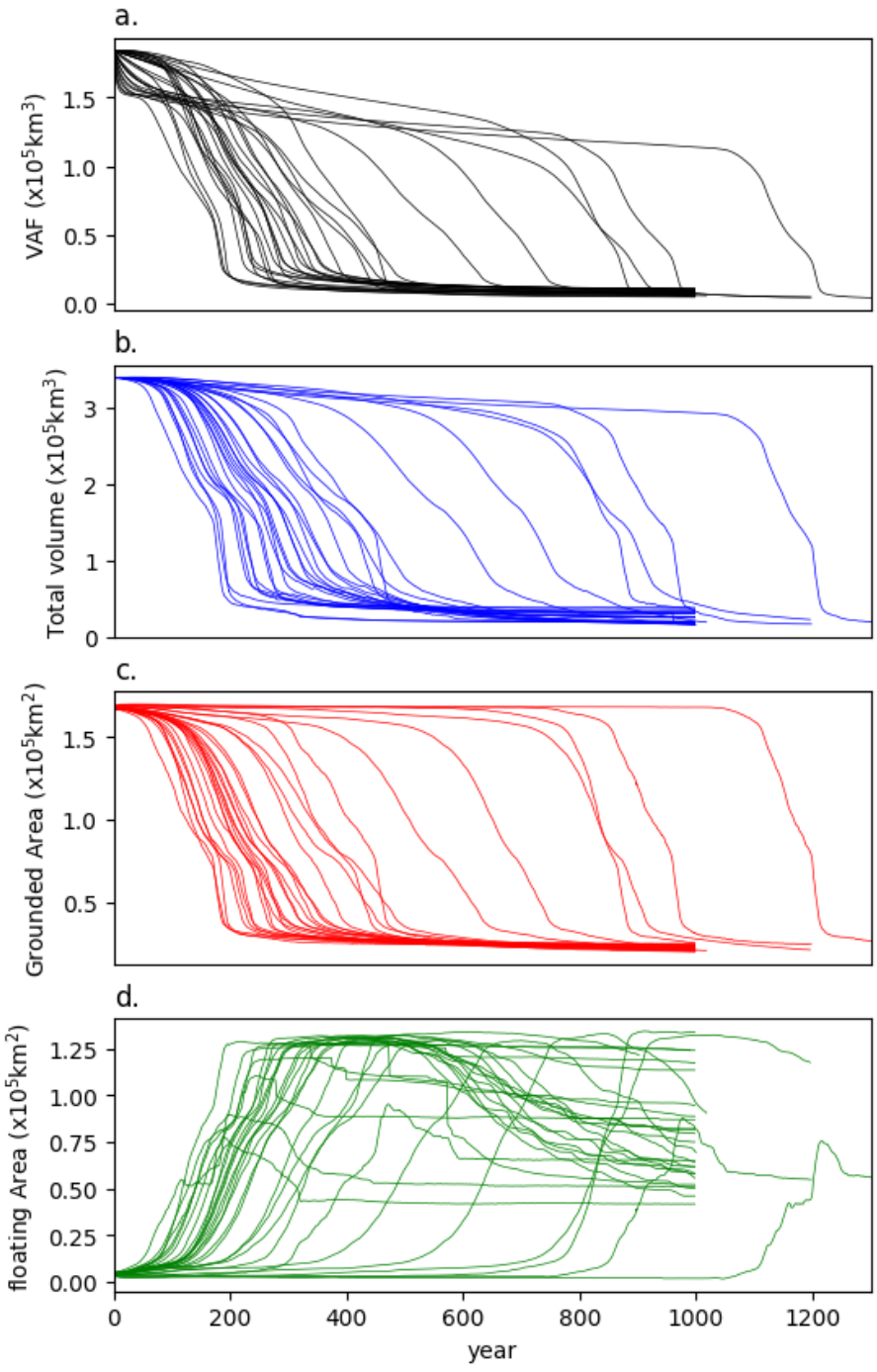


Fig. 3.6 Total volume above floatation (VAF) for Pine Island ensemble as a function of simulation year within the Pine island glacier catchment (**a.**); Total volume of ice in the domain (**b.**). Grounded area (**c.**); and Floating area (**d.**)

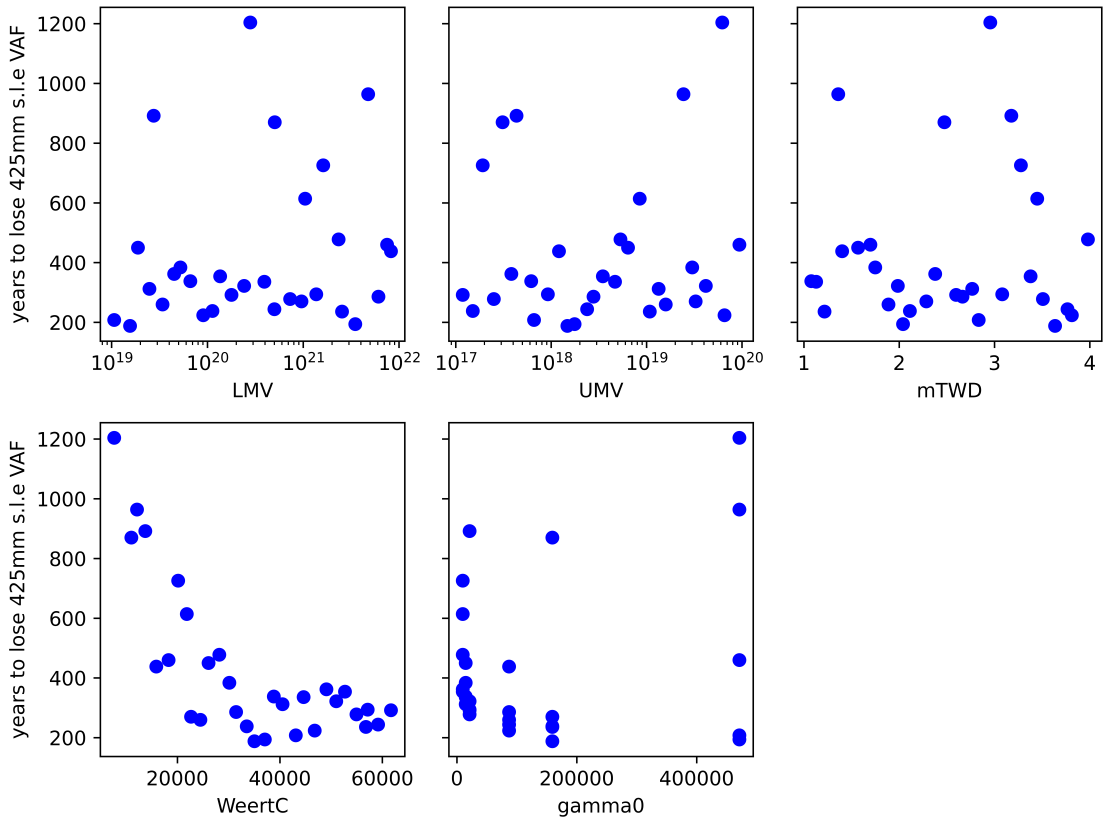


Fig. 3.7 Time taken for the domain to lose the majority of submarine ice (425mm) for the five perturbed parameters: lower mantle viscosity (*LMV*); upper mantle viscosity (*UMV*); maximum till water depth (*mTWD*); Weertman friction coefficient (*WeertC*); and ice shelf basal melt sensitivity (*gamma*0 or $\gamma_0$)

year 10 in Figure 3.8, suggest that lower Weertman coefficient simulations stabilise on the grounding ridge at the terminus of Pine Island. With positive mass balance upstream of the grounding line, grounded ice is able to thicken under increased accumulation - further stabilising the ice and limiting grounding line retreat (Fig. 3.9). This could potentially be stabilising the glacier, leading to lower Weertman friction coefficient simulations remaining stable for longer. Previous studies have found an unphysical thickening tendency at the terminus of Pine Island in simulations using the Bedmap2 bedrock geometry (Nias et al., 2018). However, we use the Bedmachine geometry in these simulations, which uses a mass conservation approach to infer bed topography (Morlighem et al., 2020). This methodology is similar to that used by Nias et al. (Nias et al., 2018), who modify Bedmap2 to reduce grounding line thickening in simulations. In practice, Bedmachine lowers the grounding line ridge at the PIG grounding line by 200 m compared with Bedmap2. Using statistical methods to generate bedrock topographies for PIG, Wernecke et al. (2022) find closer agreement between projections using their bedrock topographies and BedMachine,

compared with Bedmap2 - which is less sensitive to retreat. This supports the inference that lack of retreat in some ensemble members is not simply a product of the choice of bedrock. We therefore conclude that grounding line stabilisation and subsequent thickening seen here is unlikely to be the result of an overly high PIG grounding line ridge. However, we also note that the use of GIA enabled BISICLES allows the bedrock to deform, so direct comparisons with previous studies is challenging.

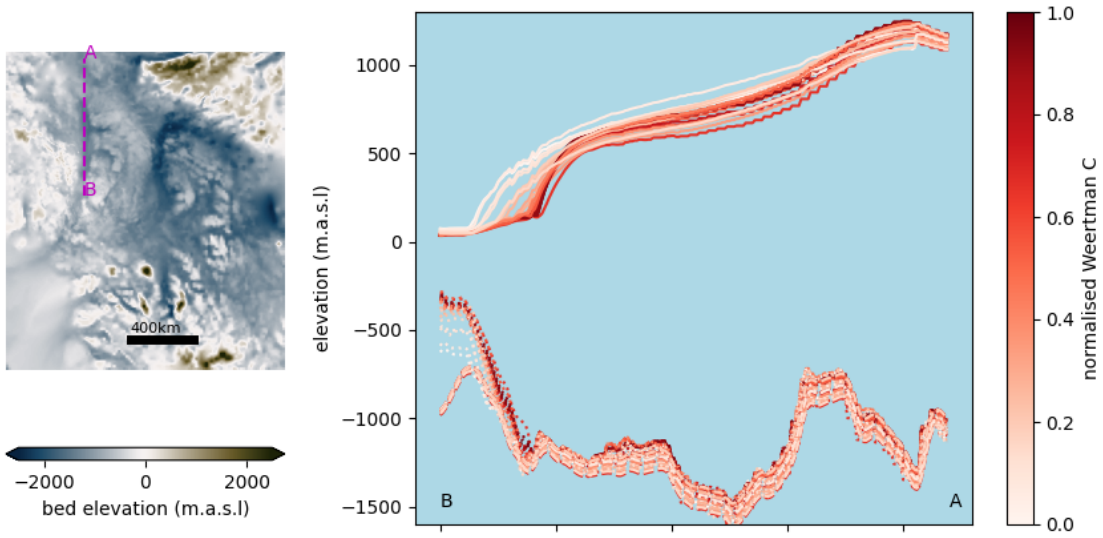


Fig. 3.8 Transect through the trunk of the Pine Island glacier after ten years of simulation time. Subplot **a** shows the bedrock elevation for the modelling domain with the transect plotted (dashed line). Subplot **b** shows transects through the bedrock, the base of the ice sheet and surface of the ice sheet. Line colors correspond to the normalised Weertman friction coefficient for the ensemble member corresponding to each surface. Darker reds show simulations with higher Weertman friction coefficient. The figure indicates that, in general, lower Weertman coefficient simulations undergo an initial thickening at the grounding line, and may remain pinned to a pinning point at the grounding line.

Overall, the PIG catchment loses ice more quickly under higher sensitivity to ice shelf basal melt ($\gamma_0$) (Fig. 3.7). Where $\gamma_0$ is higher, ice shelves thin more quickly - reducing buttressing of upstream ice. This increases discharge and drives further thinning upstream. In the over-deepened PIG bed, this can drive rapid retreat. However, high $\gamma_0$ does not drive more rapid retreat in all simulations. As shown in Figure 3.7, some ensemble members have the highest $\gamma_0$ value, but take more than 800 years to lose 425 mm SLE VAF. These simulations remain grounded on the ridge at the terminus of PIG, and therefore appear insensitive to high $\gamma_0$ and ocean driven melting. As shown in Figure 3.10, average thermal forcing in the PIG catchment increases with depth (Fig. 3.10 **b.**), with strong thermal forcing at the bedrock surface - which is shown in Figure 3.10 **a.**. Where ensemble members remain grounded at the terminus of PIG, they are less vulnerable to ocean-melt driven retreat.

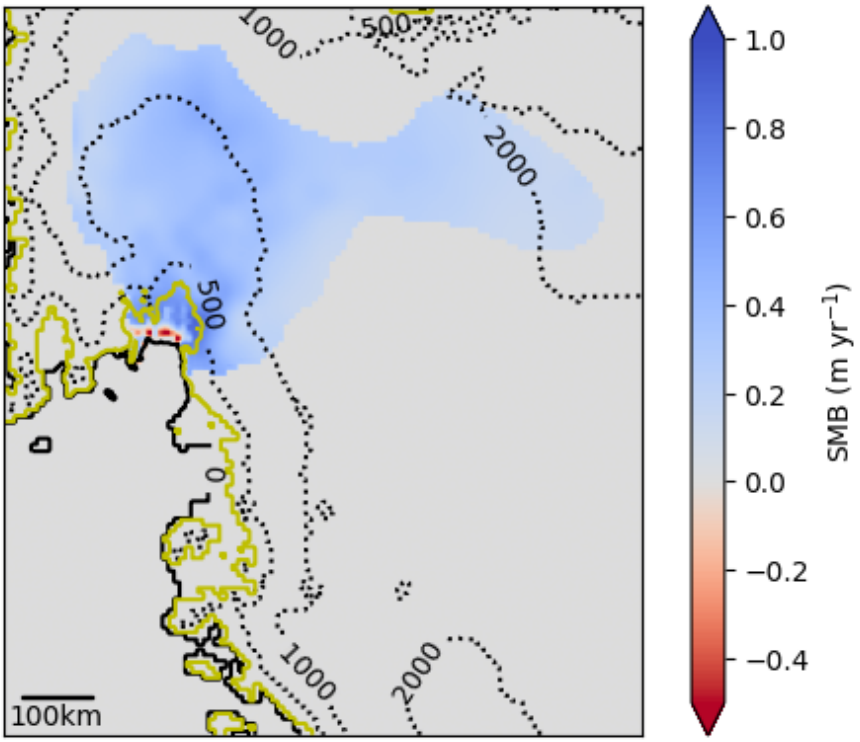


Fig. 3.9 Average surface mass balance for the Pine Island catchment, across ensemble members at the start of the simulation period (year 2). Yellow contour shows initial grounding line position. Dotted black contours show average surface elevation at the start of the simulation period.

Maximum till water depth ($mTWD$) appears to have a limited influence on the time taken for 425 mm SLE VAF to be lost from the domain. This could suggest that, under the range used for $mTWD$, high basal melt rapidly saturates the till layer at the base of ice streams. However, whilst till water depth reaches saturation near the grounding line, regions with water depth below $mTWD$ propagate upstream (not shown here). Figure 3.11 shows the maximum fraction of the domain area with water at the base that reaches saturation (equal to $mTWD$) across the duration of the simulation period for each ensemble member, as a function of maximum till water depth. Whilst lower maximum till water depth leads to a larger area at saturation (Fig. 3.11), this is generally $< 10\%$ of the area where water is present at the base. Along with patterns of till water depth evolution (not shown here), we interpret this as suggesting that the till is not saturating so rapidly as to eliminate sensitivity to $mTWD$.

As outlined in section 3.3.6, we chose not to vary the coulomb friction coefficient. Coulomb friction primarily affects velocity within ice streams (Gandy et al., 2019, Nias et al., 2018). Varying this parameter could therefore have driven faster retreat of grounding lines within

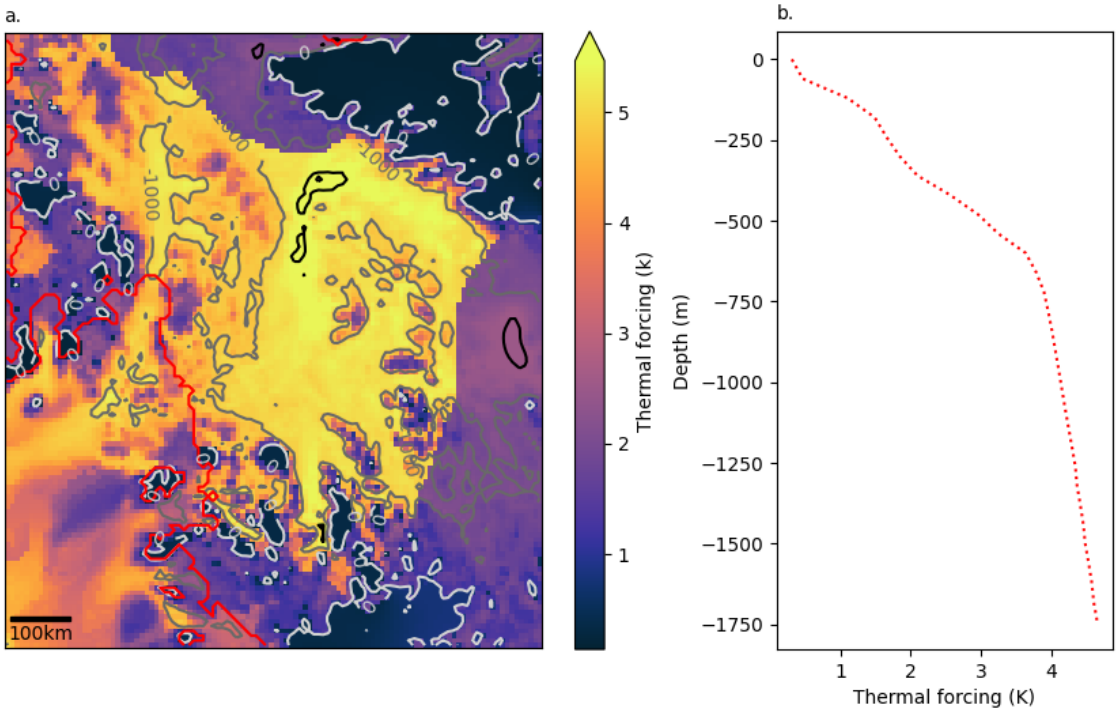


Fig. 3.10 Thermal forcing at the initial bedrock elevation, with white contour showing where bed elevation is 0, grey contour is bed elevation 1000 m below sea level and the black contour is where bed elevation is at 2000 m below sea level (subplot **a.**). The red contour in **a.** is the initial grounding line position. Also shown is the average thermal forcing gradient in the Pine Island catchment (subplot **b.**).

the PIG catchment. However, with PIG bed topography sloping inland and limited pinning points upstream of the grounding line, thinning to floatation appears to control retreat. Whilst faster ice streams would increase ice draw down, once the grounding line retreats onto retrograde slopes and basal melting causes ice shelf thinning, this drives collapse of the glacier on century time scales.

In light of errors in the GIA implementation here, we cannot be confident in our interpretation of GIA sensitivity. However, as this GIA model is yet to be used in a perturbed parameter set up, and given the importance of bedrock-ice sheet interactions on stability of the ice sheet across time scales (Kachuck et al., 2020, Larour et al., 2019, Kingslake et al., 2018, Whitehouse, 2018, Adhikari et al., 2014), we judge that perturbing one or both GIA viscosities (with the error corrected: Chapter 5) will help characterise this important uncertainty in the full Pliocene Antarctic ensemble.

Finally, clear interpretation of sensitivity to the basal melt parameter, $\gamma_0$, proves challenging. Overall, simulations appear to cluster around shorter time scales for loss of most ice at higher $\gamma_0$ values, although there are exceptions to this for some low Weertman friction

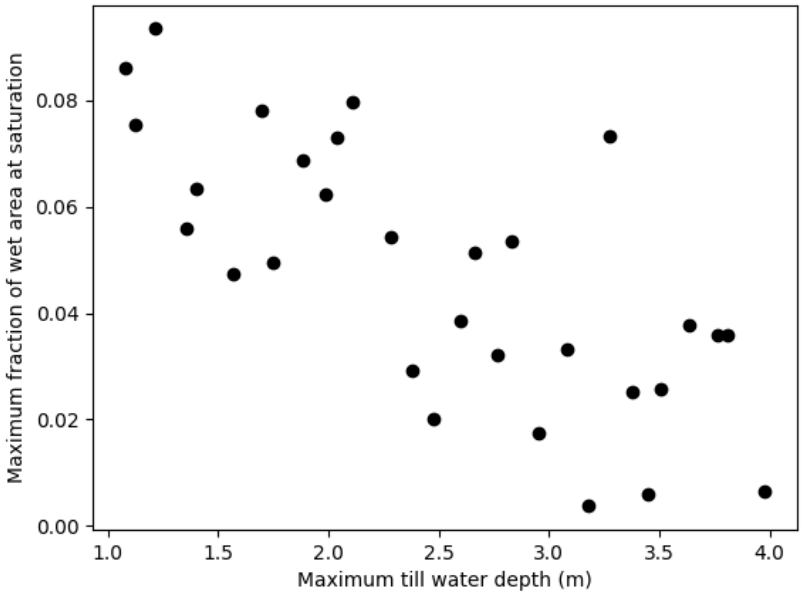


Fig. 3.11 Maximum fraction of grounded area with water at the base where till water is at saturation, for maximum till water depth used for each ensemble member.

coefficient simulations. This is largely due to stabilisation of ensemble members on the ridge at the terminus of PIG (Fig. 3.8). This allows the ice stream to maintain its stability despite ocean melt driven forcing - which does not impact the ice sheet if it remains grounded. We therefore decide to perturb basal melt sensitivity in subsequent runs.

Our main conclusion in terms of basal sliding parameters is that the Weertman coefficient appears to have a greater influence than maximum till water depth. As we want to maximise the range of uncertainties sampled, subsequent work will perturb the Weertman coefficient in future ensembles in order to characterise uncertainty in modelled ice sheet response as a result of uncertain processes at the base of the ice sheet.

## 3.5 Exploration of the GIA error

### Introduction

As outlined above, the modelling framework and run time configuration for the experiments in this chapter led to an error in the GIA component. All simulations underwent unphysical bedrock subsidence at the start of the simulation period. Subsequently, we revisited the run time configuration in order to fix the GIA error. This error arose where ice sheet

model simulations were initialised from a spin-up with GIA switched off, or different GIA parameter values to those in the subsequent model run. Initialising simulations from a spin-up with GIA on, and parameter values matching those in the main simulation, avoided unphysical subsidence. Revisiting, and devising a fix for the GIA error later in the PhD allowed us to complete GIA-enabled Antarctic ice sheet simulations presented in subsequent work (Chapter 5). To explore the influence of the GIA error on the ensemble presented in this chapter, we repeat a subset of Amundsen Sea Embayment experiments with a run time configuration that avoids the GIA error, and unphysical bedrock subsidence associated with it.

### Repeat experiments

We selected five simulations from the original ensemble to repeat, based on time taken for the simulations to lose 425 mm sea level equivalent volume above floatation. These span the original design in terms of time taken to lose 425 mm SLE VAF from fastest to slowest. We also account for amount of subsidence in the original ensemble members when selecting experiments to rerun, as we want to repeat both experiments that have significant subsidence in the original ensemble and those that do not.

For the repeat experiments, we adapt the run time configuration to avoid GIA errors. Each simulation has a short (ten year) relaxation period with perturbed GIA parameters but mass held constant, from which the perturbed simulation, with mass free to evolve, is initialised.

### Results

To illustrate the magnitude of GIA errors in experiments from the original ensemble, we can explore subsidence in the first 200 years of the simulation period. Figure 3.12 shows the subsidence from the start of the simulation, averaged over the model domain for the runs with the GIA error present (solid lines, Fig. 3.12), and for repeat simulations with the GIA error amended (dashed line, Fig. 3.12). Lines with the same colour in Figure 3.12 have the same parameter values. As can be seen in Figure 3.12, all experiments from the original ensemble (solid lines, Fig. 3.12) undergo initial subsidence. For those experiments with the most significant subsidence, rate of subsidence is far outside the range of modelled or observed bedrock deformation (Kachuck et al., 2020, Nield et al., 2014). Moreover, in the absence of significant addition of mass to the ice sheet, large-scale subsidence is physically implausible. In contrast, repeat experiments that use the updated run-time configuration (dashed lines, Fig. 3.12), undergo gradual uplift at an order-of-magnitude

rate more consistent with previous studies (Kachuck et al., 2020). This gradual uplift is more consistent with mass loss driven by warm Pliocene deglacial climate.

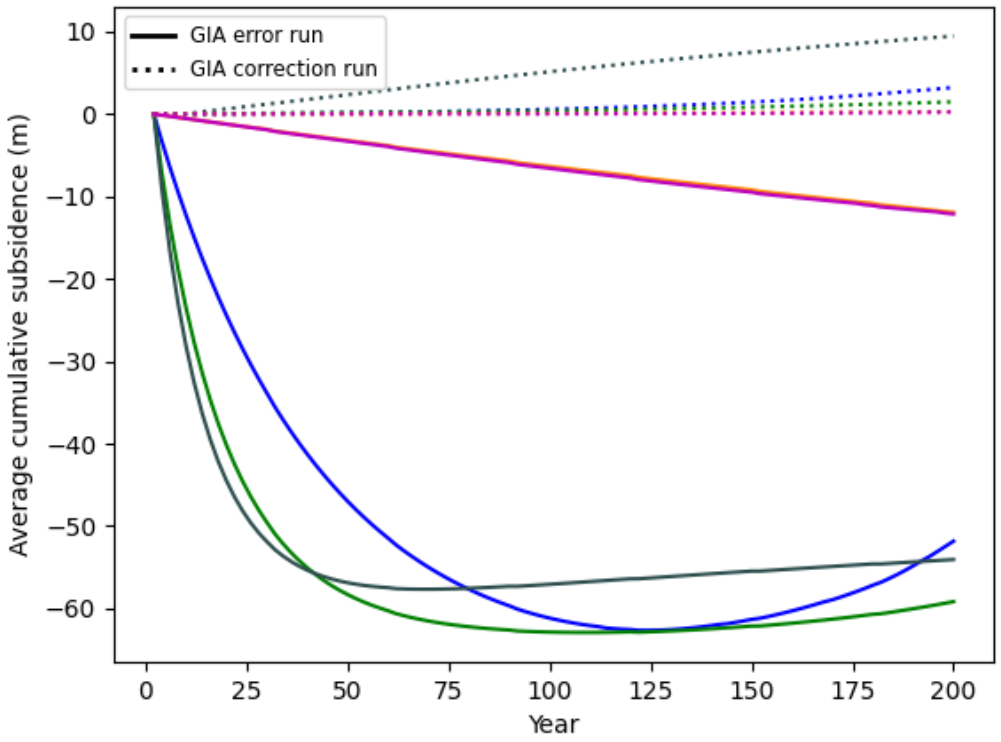


Fig. 3.12 Average cumulative bedrock elevation change over the first 200 simulation years for repeat experiments (dotted lines), along with the corresponding bedrock elevation change for corresponding simulations with the GIA error (solid lines). Line colour corresponds to ensemble member and therefore parameter values.

Figure 3.13 shows volume above floatation (VAF) (Fig. 3.13 **a.**) and total ice volume (Total volume) (Fig. 3.13 **b.**) for both GIA-error runs (solid lines), and repeat runs with the GIA error amended (dashed lines in corresponding colours). With GIA errors amended, the simulations don't show an initial drop in volume above floatation, and take longer to lose mass. Whilst the effect of resolving the GIA error is significant for individual simulations, the relationship between different ensemble members is qualitatively similar to that in the original ensemble. That is, the slowest responding ensemble members from the subset of original ensemble members (orange and grey solid lines, Fig. 3.13) are the slowest responding simulations amongst the repeated simulations (orange and grey dashed lines, Fig. 3.13). The fastest responding simulations in the subset of original experiments (blue and magenta lines in Fig. 3.13) change their ordering, however, this does not change our conclusions in terms of sensitivity as discussed below.

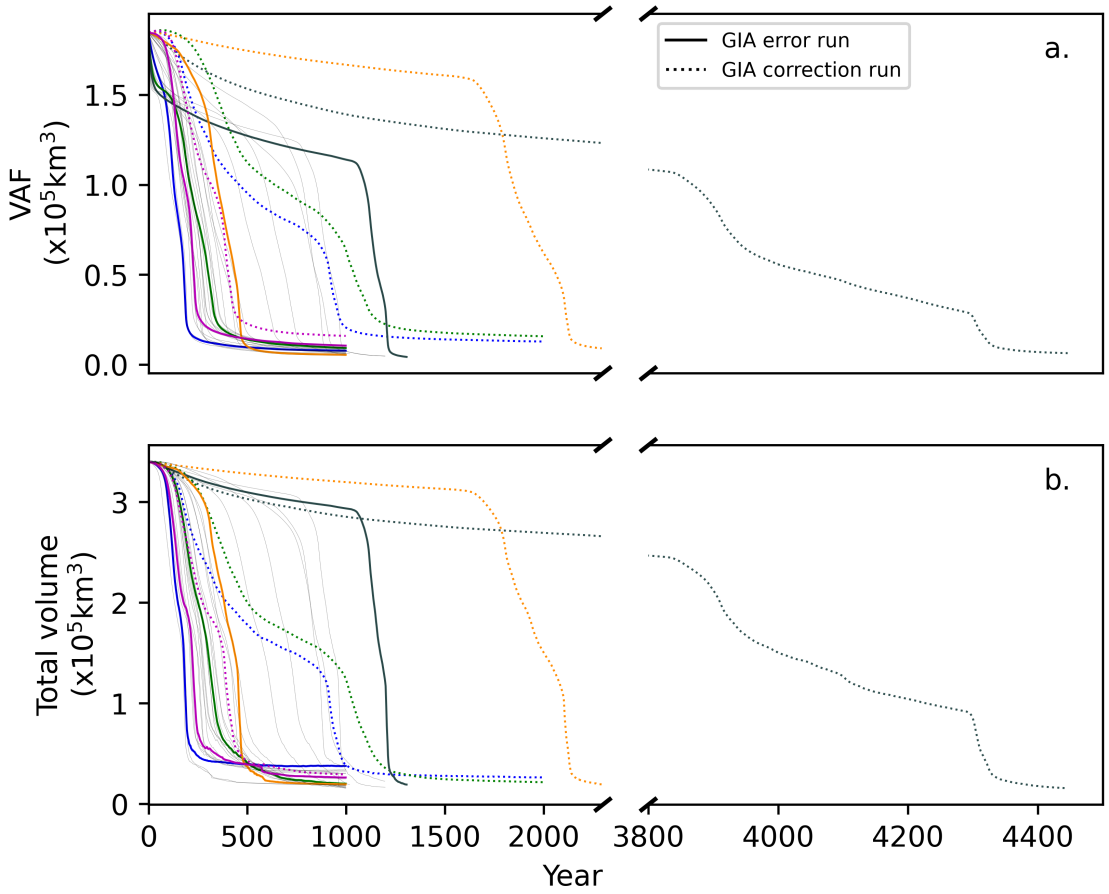


Fig. 3.13 Volume above floatation (VAF) (**a.**) and Total ice volume (**b.**). Repeat experiments are shown with dotted coloured lines, and corresponding original ensemble simulations with GIA errors are show by solid lines of the same colour. Also shown are all results from the original ensemble (faint grey lines).

As outlined in our discussion of the original 30-member ensemble (Section 3.4), we use sensitivity of time taken to lose the majority of volume above floatation (425 mm SLE VAF) to judge the relative influence of the five perturbed model parameters. In light of the GIA error affecting the ensemble, it primarily serves to show the stronger influence of the Weertman friction coefficient relative to the maximum till water depth. Figure 3.14 shows the sensitivity of time taken for the main Pine Island Glacier to lose 425 mm SLE VAF to the five perturbed model parameters. Whilst timescale of mass loss is longer for the repeat simulations (unfilled markers, Fig. 3.14) compared with corresponding simulations from the original ensemble (filled markers in corresponding colours, Fig. 3.14), overall sensitivity is broadly comparable to the original ensemble. Namely, the Weertman friction coefficient (Fig. 3.14 **e.**) appears to have the strongest influence on timescale of mass loss, and seems to have a stronger influence than maximum till water depth (Fig. 3.14 **d.**).

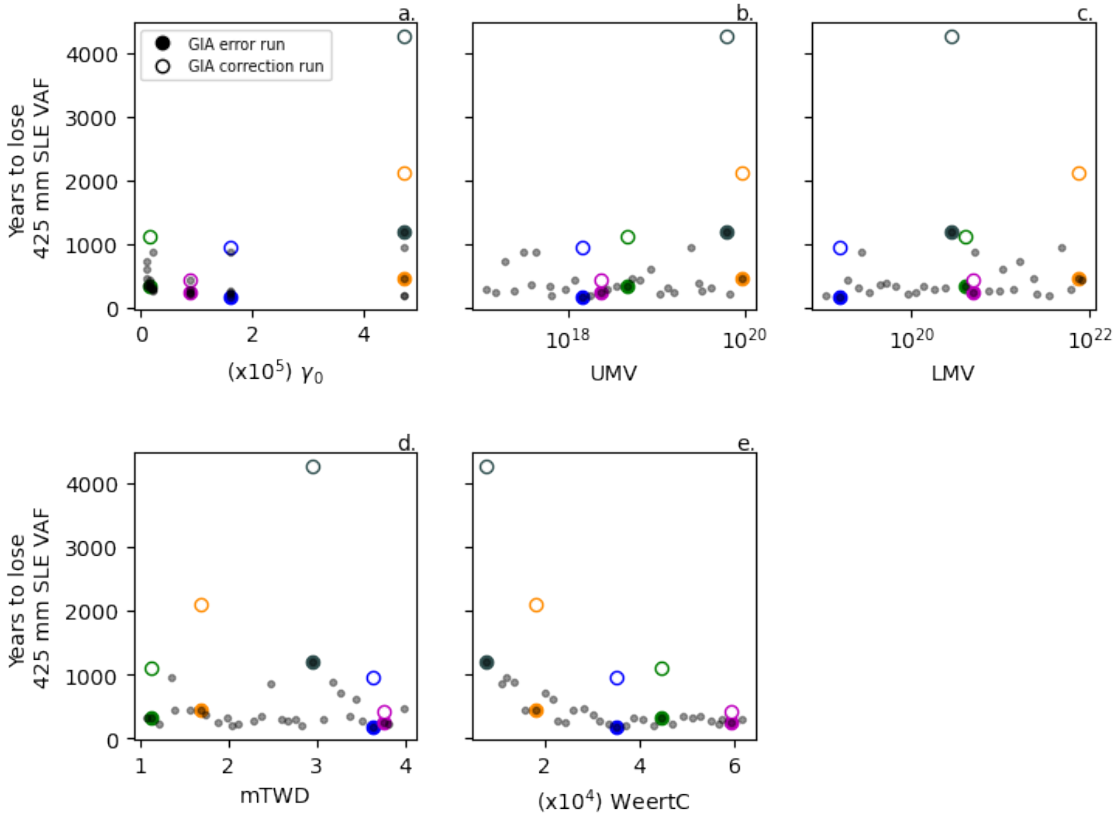


Fig. 3.14 Time taken for each simulation to lose 425 mm modern sea level equivalent (SLE) of volume above floatation (*VAF*) for the five perturbed parameters: basal melt sensitivity ($\gamma_0$), Upper mantle viscosity (*UMV*), Lower mantle viscosity (*LMV*), maximum till water depth (mTWD) and the Weertman friction coefficient (*WeertC*). Smaller circular grey markers show the original ensemble, where an error in the GIA implementation caused initial subsidence. Larger filled markers show time taken for original simulation to lose 425 mm modern sea level equivalent VAF, hollow markers with corresponding edge colors show repeat simulations with the GIA error amended.

## 3.6 Conclusions

We have presented a new BISICLES modelling framework incorporating the Glacial Isostatic Adjustment (GIA) component from GIANT-BISICLES (Kachuck et al., 2020), and the basal hydrology coupled basal sliding from $BISICLES_{hyrdo}$ (Gandy et al., 2019), with Pliocene climate forcing.

We implemented an elevation-dependent basal friction parameterisation for Weertman sliding, as constant Weertman friction values were found to produce velocity errors. To test this model set up, we simulated the Amundsen Sea Embayment region of West Antarctica, focusing on the Pine Island Glacier catchment. Alongside testing the modelling approach developed in this chapter, we also aimed to assess the relative importance of parameters

controlling processes at the base of the ice sheet under Pliocene climate. We addressed these twin aims with a perturbed parameter ensemble varying Weertman friction coefficient, maximum till water depth, ice shelf sensitivity to basal melt, upper mantle viscosity and lower mantle viscosity.

Our perturbed parameter ensemble revealed an error in the GIA implementation, which hampered interpretation of parameter sensitivities. Nonetheless, these experiments showed the importance of the Weertman friction coefficient in determining catchment scale response to Pliocene forcing. In order to explore the impact of the GIA error, we repeat a subset of five simulations from the original ensemble, using a different run time configuration to avoid unphysical subsidence at the start of the simulation period. These repeat simulations did not change our overall conclusion - that the Weertman friction coefficient exerts the strongest influence on time scale of mass loss. In terms of parameters related to basal sliding: the Weertman friction coefficient and the maximum till water depth, the former remains the most influential in our simulations with the GIA error amended. We explore a wide range of different sources of uncertainty in subsequent perturbed parameter ensembles (Chapters 4 and 5): climate forcing, surface mass balance processes, sensitivity to ocean forcing, GIA processes and basal sliding.

Chapter 2 established the importance of ice shelf basal melt sensitivity in determining how the AIS responds to century-scale warming. Overall, with faster retreat under higher basal melt sensitivity, the simulations in this chapter suggest ice shelf melt sensitivity should be explored further for the Pliocene. For GIA parameters, the error described above precludes reliable assessment of their importance in terms of PIG retreat. However, the importance of GIA in Antarctic ice sheet stability across time scales has been well established (Kachuck et al., 2020, Larour et al., 2019, Adhikari et al., 2014), as has uncertainty in Earth structure underlying the continent (Heeszel et al., 2016, Nield et al., 2018, Whitehouse et al., 2019). Identifying the GIA error paves the way for application of this model to whole Antarctic ensembles, and further exploration of the role of GIA uncertainty in ice sheet stability with perturbed parameter ensembles. In terms of basal sliding, perturbing Weertman friction had a stronger effect than perturbing maximum till water depth. Including ice streaming through coupled basal hydrology captures important processes of spontaneous ice stream formation and evolution (Aschwanden et al., 2013, Gandy et al., 2019, Robel and Tziperman, 2016, Winsborrow et al., 2010). With Weertman friction showing a stronger effect on PIG response to warming, we conclude that perturbing this parameter will simulate a broader range of AIS Pliocene dynamics compared with perturbing maximum till water depth. Our repeat simulations, where we change the run time configuration to avoid unphysical subsidence, support this conclusion and suggest that it is not impacted by the GIA error.

Having explored sensitivity to processes at the base of the ice sheet in this chapter, we next focus on uncertainties in Pliocene climate forcing and surface mass balance processes in Chapter 4.

# 3.7 Appendix

| expnum | $\gamma_0$ | $UMV$ | $LMV$ | $mTWD$ | $WeertC$ | $\Delta$V ($m^3$) |
|---|---|---|---|---|---|---|
| 1 | 4.713E+05 | 6.619E+17 | 1.065E+19 | 2.8335 | 43095 | -3.202E+14 |
| 2 | 1.592E+05 | 1.479E+18 | 1.559E+19 | 3.6359 | 35019 | -3.015E+14 |
| 3 | 1.448E+04 | 6.381E+18 | 1.883E+19 | 1.5676 | 26062 | -3.225E+14 |
| 4 | 1.448E+04 | 1.337E+19 | 2.480E+19 | 2.7654 | 40513 | -3.207E+14 |
| 5 | 2.101E+04 | 4.334E+17 | 2.749E+19 | 3.1756 | 13713 | -3.169E+14 |
| 6 | 8.698E+04 | 1.586E+19 | 3.402E+19 | 1.8872 | 24479 | -3.055E+14 |
| 7 | 9.619E+03 | 3.824E+17 | 4.492E+19 | 2.3774 | 49079 | -3.216E+14 |
| 8 | 1.448E+04 | 3.011E+19 | 5.225E+19 | 1.7480 | 30136 | -3.224E+14 |
| 9 | 1.448E+04 | 6.168E+17 | 6.627E+19 | 1.0765 | 38801 | -3.210E+14 |
| 10 | 8.698E+04 | 6.551E+19 | 9.042E+19 | 3.8116 | 46800 | -3.085E+14 |
| 11 | 1.592E+05 | 1.506E+17 | 1.130E+20 | 2.1114 | 33516 | -3.156E+14 |
| 12 | 9.619E+03 | 3.483E+18 | 1.358E+20 | 3.3787 | 52702 | -3.211E+14 |
| 13 | 2.101E+04 | 1.183E+17 | 1.780E+20 | 2.5973 | 61669 | -3.131E+14 |
| 14 | 2.101E+04 | 4.175E+19 | 2.418E+20 | 1.9845 | 50997 | -3.143E+14 |
| 15 | 4.713E+05 | 6.203E+19 | 2.799E+20 | 2.9555 | 7662 | -3.207E+14 |
| 16 | 1.448E+04 | 4.673E+18 | 3.932E+20 | 1.1271 | 44619 | -3.192E+14 |
| 17 | 8.698E+04 | 2.378E+18 | 4.998E+20 | 3.7654 | 59167 | -3.130E+14 |
| 18 | 1.592E+05 | 3.094E+17 | 5.043E+20 | 2.4740 | 11011 | -3.023E+14 |
| 19 | 2.101E+04 | 2.504E+17 | 7.304E+20 | 3.5075 | 54947 | -3.131E+14 |
| 20 | 1.592E+05 | 3.265E+19 | 9.586E+20 | 2.2840 | 22645 | -3.065E+14 |
| 21 | 9.619E+03 | 8.482E+18 | 1.046E+21 | 3.4483 | 21825 | -3.234E+14 |
| 22 | 2.101E+04 | 9.239E+17 | 1.368E+21 | 3.0811 | 57130 | -3.135E+14 |
| 23 | 9.619E+03 | 1.913E+17 | 1.616E+21 | 3.2764 | 20134 | -3.204E+14 |
| 24 | 9.619E+03 | 5.329E+18 | 2.342E+21 | 3.9802 | 28165 | -3.238E+14 |
| 25 | 1.592E+05 | 1.080E+19 | 2.541E+21 | 1.2153 | 56777 | -3.066E+14 |
| 26 | 4.713E+05 | 1.761E+18 | 3.494E+21 | 2.0400 | 37057 | -3.203E+14 |
| 27 | 4.713E+05 | 2.433E+19 | 4.756E+21 | 1.3591 | 12107 | -3.228E+14 |
| 28 | 8.698E+04 | 2.773E+18 | 6.102E+21 | 2.6639 | 31452 | -3.089E+14 |
| 29 | 4.713E+05 | 9.400E+19 | 7.490E+21 | 1.6969 | 18272 | -3.199E+14 |
| 30 | 8.698E+04 | 1.206E+18 | 8.226E+21 | 1.4010 | 15870 | -3.229E+14 |

Table 3.1 Parameter values for all simulations in the 30-member perturbed parameter Pine Island ensemble, as well as total volume change over the simulations period ($\Delta$V ($m^3$))

# Chapter 4

# Uncertainties in Pliocene climate

## 4.1 Introduction

In this chapter we focus on exploring ice sheet-climate interactions under sustained Pliocene warming. This builds on Chapter 2, which explored modelled ice sheet sensitivity to projected 21st century warming. Chapter 2 showed that to 2100, ice sheet model response is dependent on GCM and scenario, moderated by basal melt sensitivity to thermal forcing. Higher emissions scenarios generally drove a greater increase in surface mass balance, as well as ocean thermal forcing. The overall Antarctic ice sheet sea level response was largely dependent on the balance of these processes, with greater basal melt sensitivity increasing ice shelf melt, driving a larger sea level contribution under high emissions scenarios. Conversely, with low basal melt sensitivity to thermal forcing, warmer emissions scenarios drove smaller sea level rise, to a sea level fall. This underlines the importance of competing warming-driven accumulation increases and ice shelf melt-driven mass loss processes under warmer than modern climates, on century timescales. As well as sensitivity of ice shelf melt to thermal forcing, magnitude and spatial pattern of thermal forcing determined the balance between warming-driven interior thickening and ocean melt-driven changes in ice sheet discharge.

We explore Antarctic ice sheet sensitivity to GCM choice for Pliocene climate on millennium time scales, sampling the most recent generation of Pliocene climate simulations (Haywood et al., 2020). Chapter 2 simulations used an initial bedrock and ice sheet geometry derived from modified Bedmap2 as in Cornford et al. (2016). In this chapter, we explore how choice of modern initial condition influences Antarctic sensitivity to Pliocene forcing by simulating Antarctic ice sheet initialised from the BedMachine bedrock and ice sheet, alongside Bedmap2. Chapter 2 sampled low and high emissions scenarios for a

range of GCMs, with atmospheric forcing derived from GCM outputs. We introduced our approach to generating bias-corrected downscaled climates in Chapter 3. This chapter will present an initial assessment of differences in ice sheet response as a result of perturbing surface mass balance parameters across plausible ranges.

We base Pliocene climate on results from the Pliocene Model Intercomparison Project Phase 2 (PlioMIP2) (Haywood et al., 2016b). PlioMIP2 is the most comprehensive exploration of climate response to Pliocene like boundary conditions to date. The Pliocene Ice Sheet model Intercomparison Project (PLISMIP) (Dolan et al., 2012) is the first intercomparison of ice sheet models for the Pliocene. As part of this, Dolan et al. (2018) used results from the first PlioMIP phase, PlioMIP1, to force three ice sheet models with a range of PlioMIP1 models. That study provides a foundation for the work presented here. However, this study is the first to use PlioMIP2 results to force an ice sheet model. In addition to using PlioMIP2 forcing, this study builds on Dolan et al. (2018) by using an L1L2 physics model (BISICLES), rather than simpler SIA and hybrid models, and a maximum ice sheet model resolution a factor of ten higher than that used in PLISMIP.

In this chapter we first give a brief summary of the Pliocene Model Intercomparison Project Phase 2 (PlioMIP2, Haywood et al. 2016b). We then present two ensembles. The first ensemble explores the relative importance of different modern initial conditions, under a range of climate model forcings based on PlioMIP2 GCMs. The second ensemble explores uncertainty in surface mass balance processes, and identifies which surface mass balance parameters (Section 3.2.4) drive the greatest variability in projected sea level across a plausible range. This will inform our choice of parameters to perturb in Chapter 5.

### 4.1.1 Modelling warm Pliocene climate (PlioMIP2)

PlioMIP2 is the successor to the first phase of the Pliocene Ice Sheet Modelling Intercomparison Project (Haywood et al., 2010). Key improvements between PlioMIP1 and PlioMIP2 are: higher resolution boundary conditions with revised palaeo-geography; revised Greenland ice sheet boundary conditions; and the use of a time slice approach - focusing on a single interglacial to improve data model comparison (Haywood et al., 2010).

To facilitate comparison with geological proxies of warm Pliocene climate, PlioMIP2 focused on simulating an interglacial at marine isotope stage KM5c, 3.205 Ma (Haywood et al., 2016b), identified based on the orbital solution of Laskar et al. (2004). The boundary conditions used in participating models have Greenland ice sheet cover approximately $\sim 25\%$ of modern. Antarctic ice sheet elevation in PlioMIP2 is the same as that used in

PlioMIP1. The PRISM3/4 Antarctic ice sheet is based on Hill et al. (2009) and features a collapsed West Antarctic ice sheet, consistent with proxy based reconstructions (Naish et al., 2009), and retreat into the Wilkes and Aurora subglacial basins, as supported by Cook et al. (2014) and Young et al. (2011), respectively. Over the interior EAIS, surface elevation shows little change or is slightly higher than modern (Hill, 2009, Dowsett et al., 2016). In all, global ice sheet volume prescribed in the PRISM4 boundary conditions is equivalent to a GMSL < 24m above modern (Dowsett et al., 2016).

Across the PlioMIP2 ensemble, 16 models simulate a climate state under $CO_2$ concentrations of 400ppm, Pliocene orography and reduced Pliocene ice sheets (Eoi400 experiment). They also complete a control simulation with pre-industrial atmospheric $CO_2$ concentrations, and modern orography and ice sheets (E280 experiment). The global mean surface air temperature anomaly ($\Delta T$), calculated as the difference (Eoi400 - E280) across the ensemble, is $3.2^{\circ}C$ and median temperature increase of $3.0^{\circ}C$. The mean $\Delta T$ is 0.5 $^{\circ}C$ higher than for PlioMIP1, which is ascribed to the inclusion of more sensitive models in PlioMIP2 (Haywood et al., 2020).

Following the approach of the Pliocene Ice Sheet Model Intercomparison Project (de Boer et al., 2015, Dolan et al., 2018) which used outputs from the PlioMIP1 ensemble to force ice sheet model simulations, we explore BISICLES sensitivity to a subset of PlioMIP2 simulations. A subset of 5 PlioMIP2 models were selected based on data availability. These are: COSMOS (Stepanek et al., 2020), CCSM4-UofT (Chandan and Peltier, 2017), HadCM3 (Hunter et al., 2019), MIROC4m (Chan and Abe-Ouchi, 2020) and CCSM4-Utr (Baatsen et al., 2021). PlioMIP2 data were provided by modelling groups or accessed from PlioMIP2 data repository at Leeds ftp://see-gw-01.leeds.ac.uk/. We briefly describe each model and broad features of its simulated mPWP climate below.

### CCSM4-Utr

Institute for Marine and Atmospheric Research Utrecht CCSM4 (referred to here as CCSM4-Utr) (Baatsen et al., 2022) is a version of the Community Earth System Model (CESM 1.0.5) - equivalent to the most recent version of the Community Climate System Model (CCSM4; Blackmon et al. 2001, Gent et al. 2011). The atmospheric component of CCSM4-Utr is modelled with CAM4 (Neale et al., 2013), and has a nominal resolution of $1^{\circ}$ with 26 vertical layers. On land, physical, chemical and biological processes are represented with the Community Land Model (CLM4; Oleson et al. 2010, Lawrence et al. 2011).

The ocean component of CCSM4-Utr is modelled by the Los Alamos National Laboratory's (LANL) Parallel Ocean Program version 2 (POP2; Smith et al. 2010). Ocean grid resolution is nominally 1° (1.25° x 0.9°), with 60 vertical depth layers. POP2 implements a new parameterisation of overflow of density-driven currents over bathymetric ridges, which results in improved penetration depth of North Atlantic Deep Water (NADW), but biases elsewhere (Danabasoglu et al., 2010). Moreover, this overflow parameterisation is tuned to match present day overturning circulation. However, in PlioMIP2, the overflow of density-driven currents over ocean ridges and tidal mixing parameterisations are switched off (Baatsen et al., 2022). Sea ice is modelled with the LANL Community Ice Code version 4 (CICE4; Hunke et al. 2017). CCSM4-Utr simulates near sea ice free conditions for summer sea ice minima in Antarctica (Baatsen et al., 2022) under warm Pliocene boundary conditions. Vegetation is prescribed from the PRISM4 (Dowsett et al., 2016) dataset (Salzmann et al., 2008).

CCMSM4-Utr simulates an overall warming of 4.7°C for the mPWP compared with pre-industrial (Baatsen et al., 2022). Warming at the mPWP shows strong polar amplification, largely driven by surface albedo feedbacks, reduced ice sheet cover and latitudinally dependent lapse rate feedbacks (Baatsen et al., 2022). The largest temperature deviations from pre-industrial are seen over ice-free regions of Greenland and Antarctica (Baatsen et al., 2022), consistent with warming driven by reduced ice sheet elevations. In this configuration, CCSM4-Utr has an equilibrium climate sensitivity (ECS: warming in response to a doubling of atmospheric $CO_2$ from pre-industrial levels) of 3.17°C.

CCSM4-Utr uses a 'warm spin-up' for Pliocene Eoi400 experiments (Baatsen et al., 2022). The Eoi400 CCSM4-Utr simulation is initiailised with a highly idealised ocean temperature and salinity distribution (Baatsen et al., 2022), with initial ocean heat content prescribed to match simulated ocean heat content in the PlioMIP1 CCSM4 mid-Pliocene experiment (Rosenbloom et al., 2013, Baatsen et al., 2022). Baatsen et al. (2022) ascribe the enhanced Pliocene warming in their Eoi400 experiment to this warm initialisation. This initialisation approach promotes elevated Pliocene warming compared with the other CCSM4 version in PlioMIP2 - CCSM4-UofT (Chandan and Peltier, 2017)(Section 4.1.1), in which the ocean is initialised with modern temperature and salinity (Levitus and Boyer, 1994, Chandan and Peltier, 2017).

Average annual global precipitation in the Eoi400 experiment is 1180 mm compared with 1042 mm for pre-industrial (E280), and Baatsen et al. (2022) report noticeably wetter conditions over the southern ocean, and in the polar regions more generally. On average, southern ocean SSTs are 4-8°C warmer than the pre-industrial simulation.

### CCSM4-UofT

The second variant of the CCSM4 (Gent et al., 2011) model used here is the University of Toronto version (Chandan and Peltier, 2017), referred to in the following as CCSM4-UofT. CCSM4-UofT uses the same atmospheric component as CCSM4-Utr, and the same ocean model - POP2 (Smith et al., 2010). As in CCSM4-Utr, the overflow parameterisation is switched off in Pliocene simulations (Chandan and Peltier, 2017). In CCSM4-UofT, the ocean model is further modified to account for the fact that in the default CCSM4 version, spatially variable mixing includes a large contribution from tides and is tuned to modern tidal regimes (Chandan and Peltier, 2017). In order to account for Pliocene differences in bathymetry, as well as coastlines and tidal regime, CCSM4-UofT diverges from the default CCSM4 by using a simplified vertical mixing scheme (Chandan and Peltier, 2017).

Global mean surface air temperature is 3.8 °C higher at the Pliocene than pre-industrial for CCSM4-UofT. The mid-Pliocene ocean is warmer than the pre-Industrial by at least 2.5-3.5°C, with elevated SST warming at high latitudes in the southern ocean (Chandan and Peltier, 2017). Sea ice is significantly reduced in austral summer, with sea ice in the Antarctic archipelago and ice-free conditions along the rest of the Antarctic coastline (Chandan and Peltier, 2017). CCSM4-UofT has an equilibrium climate sensitivity of 3.2°C (Chandan and Peltier, 2018).

### HadCM3

The third PlioMIP2 model used is the UK Met Office Hadley Centre Model (HadCM3) (Hunter et al., 2019, Pope et al., 2000, Gordon et al., 2000, Valdes et al., 2017). HadCM3 has a horizontal atmospheric resolution of 3.75° x 2.5° with 19 layers in the atmosphere. Surface processes, including run-off and surface hydrology, are modelled with a version of MOSES2.1 (Met Office Surface Exchange Scheme; Cox et al. 1999, Essery et al. 2003), updated in line with the version used in HadGEM2 (Good et al., 2013a). The ocean in HadCM3 is modelled on a 1.25° x 1.25° grid and has a rigid lid in the Bryan-Cox lineage (Hunter et al., 2019), and sea ice is represented through a simple thermodynamic scheme based on Semtner et al. (1976) with ice drift and concentration parameterised (Hunter et al., 2019).

Global mean surface air temperature is 2.9°C above pre-industrial in the Pliocene, and equilibrium climate sensitivity is 3.5°C (Hunter et al., 2019). HadCM3 simulates warming in the poles of up to 31.3°C for global mean surface temperature, with temperature increases largest where the land sea mask prescribes ice-free conditions (Hunter et al., 2019). South of 60° S, HadCM3 simulates a mean surface air temperature warming anomaly relative

to pre-industrial of 6.3°C - over twice as much warming as global mean surface air temperature warming (Hunter et al., 2019). Precipitation change over the EAIS in the Pliocene Eoi400 simulation is minimal (< 0.1 mm $d^{-1}$) whilst a larger increase (< 1 mm $d^{-1}$) is seen over West Antarctica (Hunter et al., 2019). In the ocean, Hunter et al. (2019) simulate a mean global sea surface temperature anomaly of +1.8°C and up to +4°C for the southern ocean. Summer sea ice extent is reduced in Eoi400 HadCM3 experiments, and largely concentrated around the Ross and Amundsen seas (Hunter et al., 2019)

### COSMOS

The Alfred Wegener Institute Community earth System MOdelS (COSMOS) model (Stepanek et al., 2020, Stepanek and Lohmann, 2012) uses the ECHAM5 spectral model (Roeckner et al., 2003) to represent the atmosphere at a resolution of 3.75° x 3.75° with 19 vertical layers. ECHAM is internally coupled to the JSBACH (Raddatz et al., 2007) model, which includes land surface and carbon cycle processes (Stepanek et al., 2020). The COSMOS has a dynamic vegetation scheme (Brovkin et al., 2009), allowing it model climate vegetation feedbacks (Stepanek et al., 2020) - the only published PlioMIP2 model that does so (Stepanek et al., 2020, Haywood et al., 2020). The ocean component of COSMOS is modelled in MPI-OM (Marsland et al., 2003), which has a nominal resolution of 1.8° × 3.0° and simulates sea ice using a scheme based on Hibler (1979).

Stepanek et al. (2020) report global mean surface air +3.37°C above their pre-industrial (E280) simulation in the core Pliocene simulation (Eoi400). ECS in COSMOS is 4.7°C (Stepanek et al., 2020) Global average precipitation is 0.17mm $d^{-1}$ higher in Eoi400 compared with E280. In Antarctica, COSMOS simulates an overall increase in precipitation up to 0.5m $yr^{-1}$ and widespread warming up to >15°C (Stepanek et al., 2020). COSMOS dynamic vegetation model allows it to characterise Pliocene Antarctic vegetation, simulating southward expansion of grassland across the West Antarctic but no tree cover (Stepanek et al., 2020). Austral summer sea ice area is 2.33x$10^6$ $km^2$ in the COSMOS Eoi400 experiment compared with 7.55x$10^6$ $km^2$, and Southern Ocean SST warms by up to 2°C.

### MIROC4m

The final model is the Model for Interdisciplinary Research on Climate (MIROC4m) (Chan and Abe-Ouchi, 2020). The MIROC4m atmospheric component is described in Numaguti et al. (1997), and has a grid resolution of 2.8° with 20 vertical layers. Land surface processes are simulated in MATSURO (Takata et al., 2003). The ocean component is

the CCSR Ocean Component Model (COCO) (Hasumi and Emori, 2008), and has a nominal resolution of 1.4° at the poles with 43 ocean layers. The MIROC4m includes a component to calculate horizontal sea ice velocities, concentration and thickness (Chan and Abe-Ouchi, 2020).

South of 60°S, the Eoi400 experiment in MIROC4m simulates an average surface air temperature 6.4°C warmer than pre-industrial (E280), with the largest increases around the edge of the EAIS and across West Antarctica where ice sheets have been removed (Chan and Abe-Ouchi, 2020). MIROC4m has an ECS of 3.9°C (Haywood et al., 2020). The MIROC4m simulates large areas with increased mean annual precipitation compared with pre-industrial, up to a doubling over Antarctica (Chan and Abe-Ouchi, 2020). Southern ocean SST shows strong overall warming in the Pliocene compared with pre-industrial (Chan and Abe-Ouchi, 2020). However, in the Weddell Sea along the edge of the modern day Filchner-Ronne ice shelf warming is less pronounced, with a SST anomaly between -0.5°C and 0.5°C. Sea ice area in the Pliocene is ~30% smaller than in the control (Chan and Abe-Ouchi, 2020).

## 4.2 Methods

### 4.2.1 BISICLES

We use the same BISICLES version as in Chapter 3, with basal hydrology coupled sliding and surface mass balance simulated with pyPDD. The interval for recalculating elevation adjusted surface mass balance is 25 years. We use the two-component sliding law outlined in Section 3.2.3, with the idealised hydrology scheme coupled to Coulomb sliding (Gandy et al., 2019, 2021). Elevation dependent Weertman friction coefficients are used to calculate basal sliding, with $C_{max}$ set to 34,000 based on the average value for inverted bed friction coefficients outside ice streams in the modern. Results are presented for simulations to 5,000 model years, run with 4km finest resolution and 8km base resolution. We acknowledge that the ice sheet model does not reach equilibrium within this interval. However, other studies have simulated Pliocene sea level response for a 5,000 year interval initialised from a modern ice sheet (DeConto et al., 2021). Moreover, we expect a strong enough sea level signal to emerge within this interval to assess broad characteristics of BISICLES response to each climate.

For the simulations presented in this chapter, glacio-isostatic adjustment (GIA) processes were not included, as GIA errors outlined in chapter 3 remained unresolved. Based on the previous study with GIANT-BISICLES (Kachuck et al., 2020), we could expect that

omission of viscoelastic GIA processes may lead to an underestimation of grounded ice stability, and an overestimation of sea level contribution. For ocean melt-driven retreat of WAIS submarine basins, elastic bedrock response to unloading would likely slow the pace of retreat (Larour et al., 2019). On longer, century to millennium timescales, viscous response of the mantle could stabilise grounded ice further - with timescale of response dependent on mantle viscosity (Kachuck et al., 2020, Adhikari et al., 2014). In the absence of GIA, we therefore expect that these simulations may overestimate rate of retreat and millennium scale change in volume above floatation. However, the relative influence of different modelling choices explored (initial state, GCM forcing and PDD scheme parameters) should be sufficiently robust to draw conclusions about which uncertainties should be explored in the final ensembles in Chapter 5.

### 4.2.2 Initialisation

The initial condition describes the model state at the start of a simulation and is highly influential on ice sheet evolution (Seroussi et al., 2019, Dolan et al., 2018, de Boer et al., 2015). In the simulations presented below, we test the impact of using one of two modern-day bedrock and ice sheet thickness datasets. The first is Bedmap2 (Fretwell et al., 2013), modified to avoid thickening at the grounding line of Pine Island (Nias et al., 2016) and used in the majority of Antarctic BISICLES studies (Cornford et al., 2016, 2015, Seroussi et al., 2019). We also test the more recent BedMachine topography (Morlighem et al., 2020) which has been explored in fewer BISICLES studies (Wernecke et al., 2022). It should be noted that this does not represent a full comparison between the two bedrocks, as we do not carry out the inversion for basal sliding parameters with BedMachine. Instead, we use the same field of inverted basal friction parameters as in Cornford et al. (2016, 2015) for the relaxation simulation. However, as we use elevation-dependent bed friction parameters in perturbation runs following a short relaxation run, we expect this choice to have a limited impact on longer term sea level response. To explore the impact of ice sheet initial conditions on sea level contribution, we perform two sets of simulations for each PlioMIP2 GCM.

### 4.2.3 Ocean forcing

In order to drive the parameterisation of melt at the base of ice shelves, we use 3D fields of ocean potential temperature and salinity to construct depth-dependent thermal forcing following the approach used in ISMIP6 (Jourdain et al., 2020). GCM resolution is an order of magnitude lower than the lowest resolution (8 km) used for BISICLES

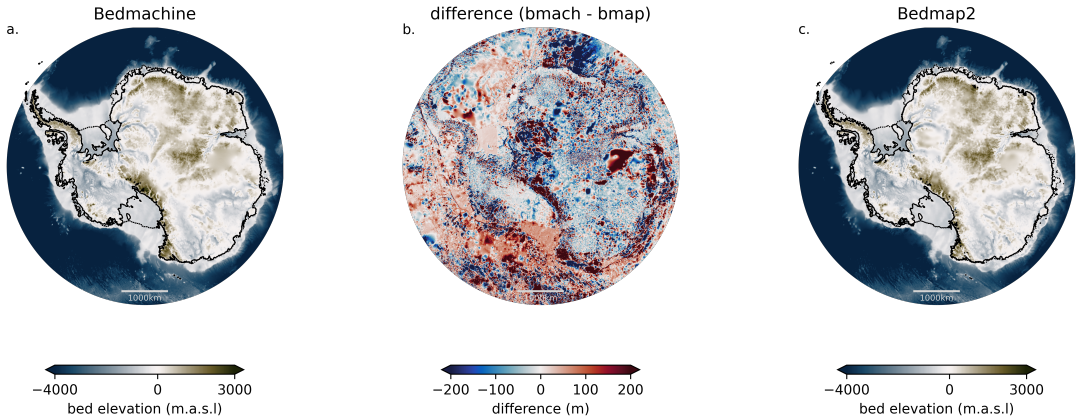


Fig. 4.1 Initial bedrock elevation for BedMachine (bmach)(**a**) and modified Bedmap2 (bmap) (**c**) used in the simulations presented here. The difference in bedrock elevation between the two (bmach - bmap) is also shown (**b**).

simulations presented here. In order to generate ocean forcing fields at the same resolution as BISICLES, we perform a process of downscaling, extrapolation and bias-correction that closely follows that of Jourdain et al. (2020). Further details of this procedure for ISMIP6 can be found in the previous reference; however, we restate our approach here.

Before generating the 3D thermal forcing we first downscale ocean variables and account for data gaps in regions not simulated by GCMs. Potential temperature is converted to in-situ temperature using the Gibbs SeaWater Oceanographic Toolbox of TEOS-10 (McDougall and Barker, 2011). We then regrid salinity and temperature fields onto a standard polar stereographic grid where we have data in the GCM, using bilinear interpolation to achieve 8km resolution. Next, temperature and salinity fields are conservatively interpolated from variable depth layer GCM grids, onto regular 20 m ocean depth layers.

PlioMIP2 models have coarse representation of the Antarctic continental shelf and do not resolve ice shelf cavities, resulting in gaps under ice shelves and in regions designated land in GCM land sea masks. To capture melting in these regions, we extrapolate into the ice sheet interior to provide ocean forcing as the ice sheet retreats. Bathymetric features exert a primary control on ocean properties in ice shelf cavities (De Rydt et al., 2014, De Rydt and Gudmundsson, 2016), with sea floor topography routing inflow of ocean water into cavities. The processing scheme devised by Jourdain et al. (2020) and used here aims to capture the flooding of shelf waters into sub-shelf cavities through topographic troughs in the sea floor. Ocean fields are extrapolated from the open ocean into ice-covered regions for each of the 16 sectors demarcated in ISMIP6 (Jourdain et al., 2020), and for each depth layer. A 3D mask of the Bedmap2 bedrock is used during the extrapolation procedure such that fields from grid cells cannot be extrapolated into regions where topographic

features would block inflow of water masses towards the ice sheet interior. Missing data values are filled iteratively until regions of missing data connected to the ocean have been filled. Salinity and temperature are copied from overlying ocean layers to infill deep ocean cavities blocked by sills. The resulting 3D fields are then conservatively interpolated to 60 m depth layers. In this way, continuous fields of salinity and in-situ temperature for each PlioMIP2 GCM are constructed. These are used to calculate thermal forcing.

Once thermal forcing has been constructed for the PlioMIP2 Pliocene (Eoi400) and pre-industrial (E280) PlioMIP2 outputs, we add the Eoi400 - E280 anomaly to the same observationally based thermal forcing field as used in ISMIP6 (Jourdain et al., 2020). This compilation of the NOAA World Ocean Atlas 2018 dataset (Locarnini et al., 2019, Zweng et al., 2019), the Met Office EN4 subsurface ocean profiles (Good et al., 2013b) and data from the Marine Mammals Exploring the Oceans from Pole to Pole (MEOP) project (Roquet et al., 2013, 2014, Treasure et al., 2017). For EN4 and WOA18, data spanning 1995-2017 is used, whilst the MEOP data covers 2004-2018 (Jourdain et al., 2020). Figure 4.2 shows bias-corrected, downscaled thermal forcing fields, averaged over the upper 500 m of ocean.

To convert thermal forcing to basal melt, we use the ISMIP6 basal melt parameterisation (Jourdain et al., 2020), and the highest values of ice shelf melt sensitivity to thermal forcing provided by ISMIP6 ($PIGL_{95}$). This value was used due to an earlier aim of this work, which was to generate a reduced Pliocene ice sheet from which subsequent perturbed parameter ensembles could be initialised. The initial state was not eventually used in the final ensemble (Chapter 5), but using the high sensitivity parameter is useful for assessing the maximum sensitivity of the ice sheet response to the other uncertainties explored here.

### 4.2.4 Atmospheric forcing

We use the methods of downscaling and bias-correction described in Section 3.3.5. For the baseline temperature and precipitation fields, we use the 1979-2000 monthly averages (Section 3.3.5) (Wessem et al., 2014). Pliocene climate fields were regridded from their native model grid to BISICLES 8km grid. To simulate surface mass balance, we use the pyPDD positive degree day model (Seguinot, 2013) of the kind described in Section 3.2.4. For the first ensemble, where simulations are forced with a subset of PlioMIP2 GCMs, we use default surface mass balance parameter and lapse rate correction values as in Section 3.3.5. For the second ensemble, exploring sensitivity to PDD parameters, we perturb these as described in Section 4.2.5. Bias-corrected, downscaled temperature and precipitation fields are show in Figure 4.3.

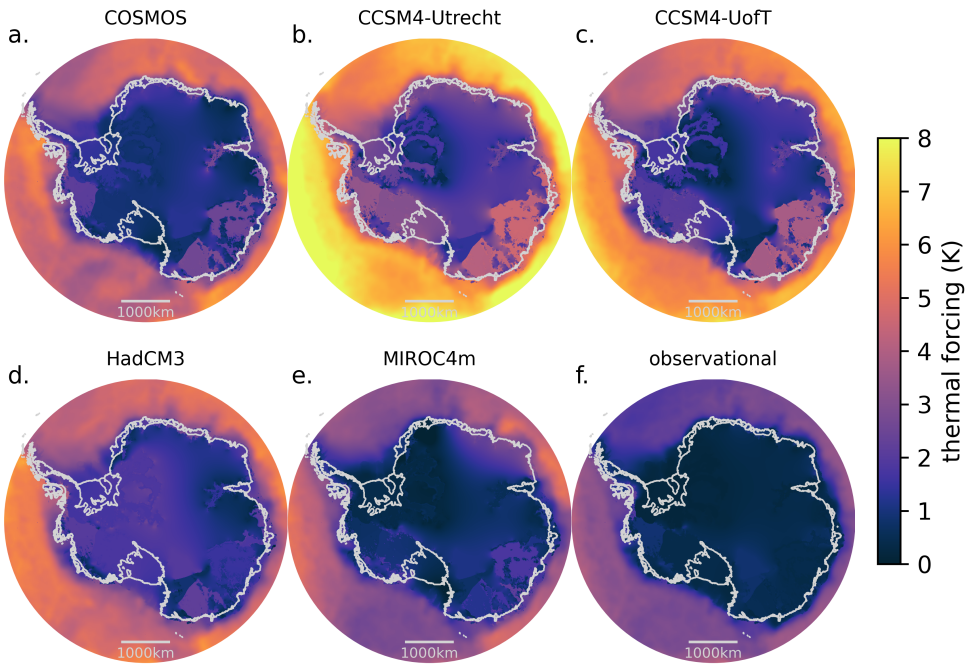


Fig. 4.2 Average upper ocean thermal forcing for PlioMIP2 GCMs sampled (a-e), as well as the observation-based thermal forcing dataset (f) (Jourdain et al., 2020) used as the baseline for bias-corrected thermal forcing.

Our downscaling approach aims to account for elevation discrepancies between our simulated ice sheet model and GCM boundary conditions. Pliocene PlioMIP2 experiments use the PRISM3 ice sheet elevation and a Pliocene land sea mask (Haywood et al., 2016b). This prescribes deglaciation of West Antarctica, and regions of East Antarctica. In addition to the elevation driven temperature changes this drives (lower GCM elevation, warmer temperatures), a component of temperature change can also be attributed to surface type changes prescribed in the boundary condition (Hill et al., 2014). Regions prescribed as land or ocean in the Pliocene land sea mask have a lower surface albedo compared with ice regions. This albedo difference at the Pliocene plays a significant role in increasing temperatures at the poles. Whilst our use of an elevation correction aims to offset elevation driven differences in surface temperature and precipitation, it does not account for temperature differences driven by surface type and associated albedo differences. For the PlioMIP1 ensemble, Hill et al. (2014) find that albedo changes due to Pliocene sea ice and ice sheet distribution are the most significant driver of elevated warming at the poles. Albedo changes are likely to play a similar role in the PlioMIP2 ensemble (Haywood

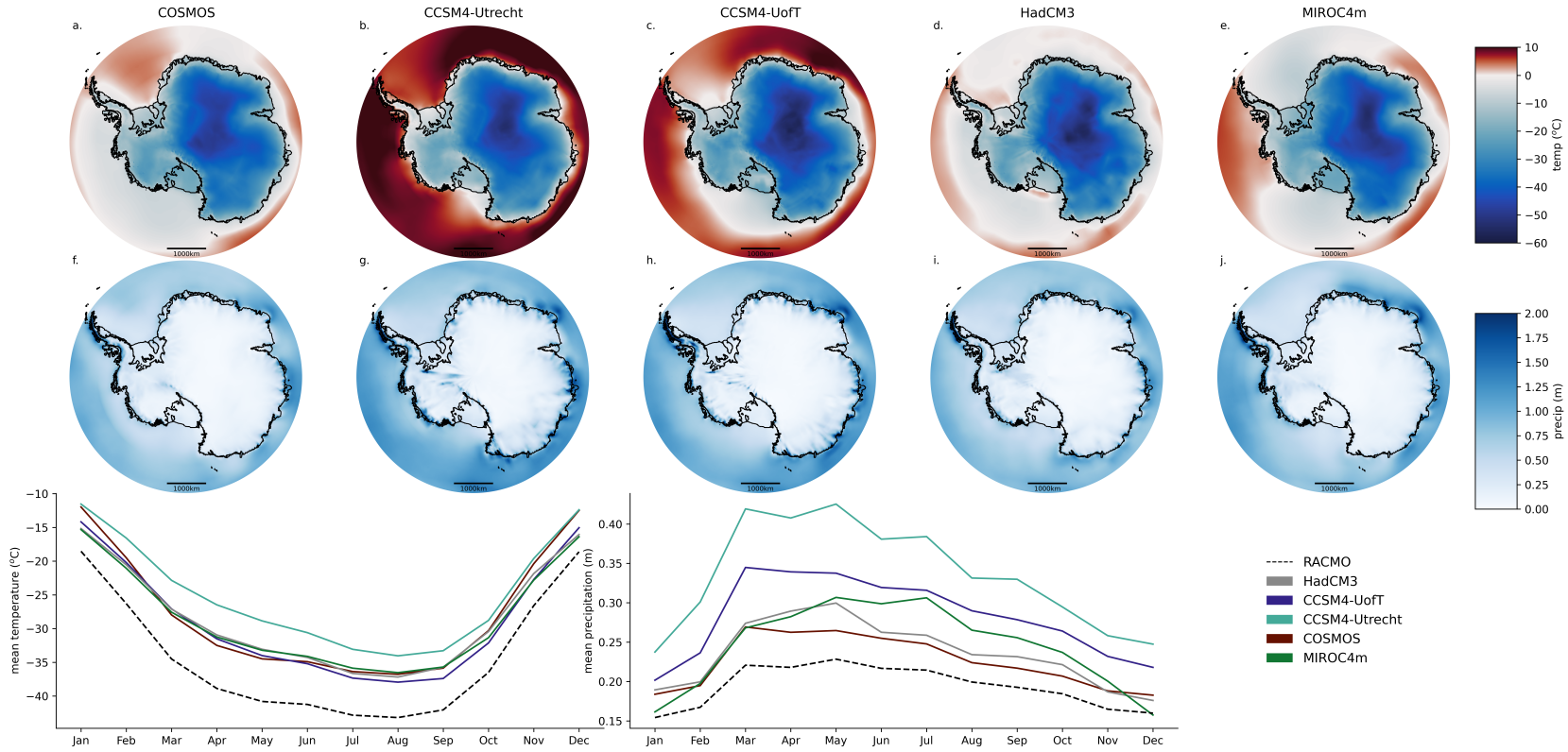


Fig. 4.3 Average annual surface air temperature for each PlioMIP2 GCM (a-e), and average annual precipitation elevation corrected to modern Bedmap2 surface elevation (f-j), added to the RACMO climate fields. Also shown are average monthly bias-corrected precipitation and temperature fields for each GCM, corrected to Bedmap2 ice sheet elevation. Elevation is comparable for both BedMachine and Bedmap2 ice sheet geometries geometries, along with the modern fields from the RACMO regional climate model used in bias correction.

et al., 2020). Similarly, individual models used in this study show a strong surface albedo component of polar amplification (Baatsen et al., 2022, Samakinwa et al., 2020, Chandan and Peltier, 2018), with increased warming in COSMOS Pliocene simulations compared with PlioMIP1 attributed to albedo changes (Samakinwa et al., 2020). Chandan and Peltier (2018) suggest that surface albedo changes are a significant component of polar amplification in CCSM4-UofT. For CCSM4-Utr, surface albedo plays a significant role in polar amplification and Antarctic warming (Baatsen et al., 2022), consistent with the findings of Hill et al. (2014) for PlioMIP1. As noted in Dolan et al. (2018), attributing changes in simulated ice sheet behaviour to climate model processes and boundary conditions is challenging. Whilst our use of temperature and precipitation lapse rate corrections aims to address Pliocene elevation changes in the PRISM3 boundary condition, changes to surface type and albedo are more challenging to account for. Where deglaciated regions are designated land or ocean, with a lower albedo, but are glaciated in our initial condition, we cannot account for this component of warming in our elevation correction approach. We acknowledge this is as a limitation of the work presented here.

### 4.2.5 Ensemble Design

#### PlioMIP2 climate forcing and initial states

As outlined above, our first ensemble aims to explore the influence of five PlioMIP2 GCMs in driving Antarctic ice sheet change under Pliocene climate, as well as comparing ice sheet evolution initialised from two different modern initial conditions. We run ten simulations, one for each of the PlioMIP2 GCMs and ice sheet initial conditions. Temperature lapse rate is set at -8°C km$^{-1}$, precipitation lapse rate -4$\times$10$^{-4}$ and PDD factors to the default values for pyPDD (3 mm w.e. d$^{-1}$ for snow, 8 mm w.e. d$^{-1}$ for ice) (Seguinot, 2013).

#### PDD parameter screening simulations

We also assess sensitivity to the surface mass balance parameters across a plausible range of values, forcing all simulations with the COSMOS GCM. Four parameters are perturbed in a 9-member 'one-at-a-time' ensemble design, where each is perturbed to its maximum or minimum value while the others are held at their default values. These are: the precipitation lapse rate (*LRP*), which determines the magnitude of the precipitation adjustment with elevation correction (Section 3.3.5); the temperature lapse rate (*LRT*), this determines the temperature adjustment with elevation correction (Section 3.3.5); positive degree day factor

for ice (*PDDi*) (Section 3.2.4); and positive degree day factor for snow (*PDDs*)(Section 3.2.4).

We choose our default value of *LRP* (-4$\times10^{-4}$) following the default range used in Yan et al. (2016) and based on Frieler et al. (2015). However, we differ from the former in perturbing *LRP* and *LRT* separately in order to isolate the impact of each parameter in this set of experiments. Whilst Yan et al. (2016) determine precipitation scaling by multiplying temperature lapse rate by a precipitation scaling parameter, our approach is equivalent to combining their precipitation scaling and temperature lapse rate parameters into a single parameter: LRP. This allows us to independently perturb *LRP* and LRT. Our *LRP* range is from precipitation lapse rate off (0) to a doubling of the *LRP* parameter (-8$\times10^{-4}$).

We use a range for *LRT* from -4°C km$^{-1}$ to -10°C km$^{-1}$, based on modern day observations (Reynolds, 1981, Magand et al., 2004) but widened by 1°C km$^{-1}$ in order to maximise coverage and account for possible differences in *LRT* for the Pliocene. Our default value of *LRT* is -7°C km$^{-1}$, the middle of this range. For the positive degree day factors, the *PDDi* range is 8 mm w.e. d$^{-1}$ °C to 20 mm w.e. d$^{-1}$ °C and $PDD_s$ uses a range from 3 mm w.e. d$^{-1}$ °C to 5 mm w.e. d$^{-1}$ °C (Stone et al., 2010). For both PDD factors, the middle of the range is used for default runs (14 mm w.e. d$^{-1}$ °C for *PDDi*, 4 mm w.e. d$^{-1}$ °C for *PDDs*).

## 4.3 Results and Discussion

### 4.3.1 PlioMIP2 climate forcing and initial states

All simulations show a reduction in grounded and floating ice sheet area, particularly over the first thousand years (Fig. 4.4). Most simulations show a decrease in volume above floatation (VAF) during this initial period, followed by a longer term increase. However, Figure 4.4 shows MIROC4m-forced simulations are distinct in their response to Pliocene climate compared with simulations forced with the remaining PlioMIP2 models. CCSM4-UofT, CCSM4-Utr, COSMOS and HadCM3 forced runs all undergo an initial mass loss of up to ~3 m SLE. By contrast, MIROC4m simulations gain mass initially and maintain a volume above floatation greater than the initial for the duration of the 5,000 years. Similarly, grounded ice area for MIROC4m-forced runs consistently exceeds grounded ice sheet area for simulations forced with CCSM4-UofT, CCSM4-Utr, COSMOS and HadCM3. Floating ice sheet area is also consistently larger for MIROC4m forced runs compared with simulations forced with other PlioMIP2 models. For the MIROC4m forced runs, floating area decrease is slower than for the remaining simulations - consistent with

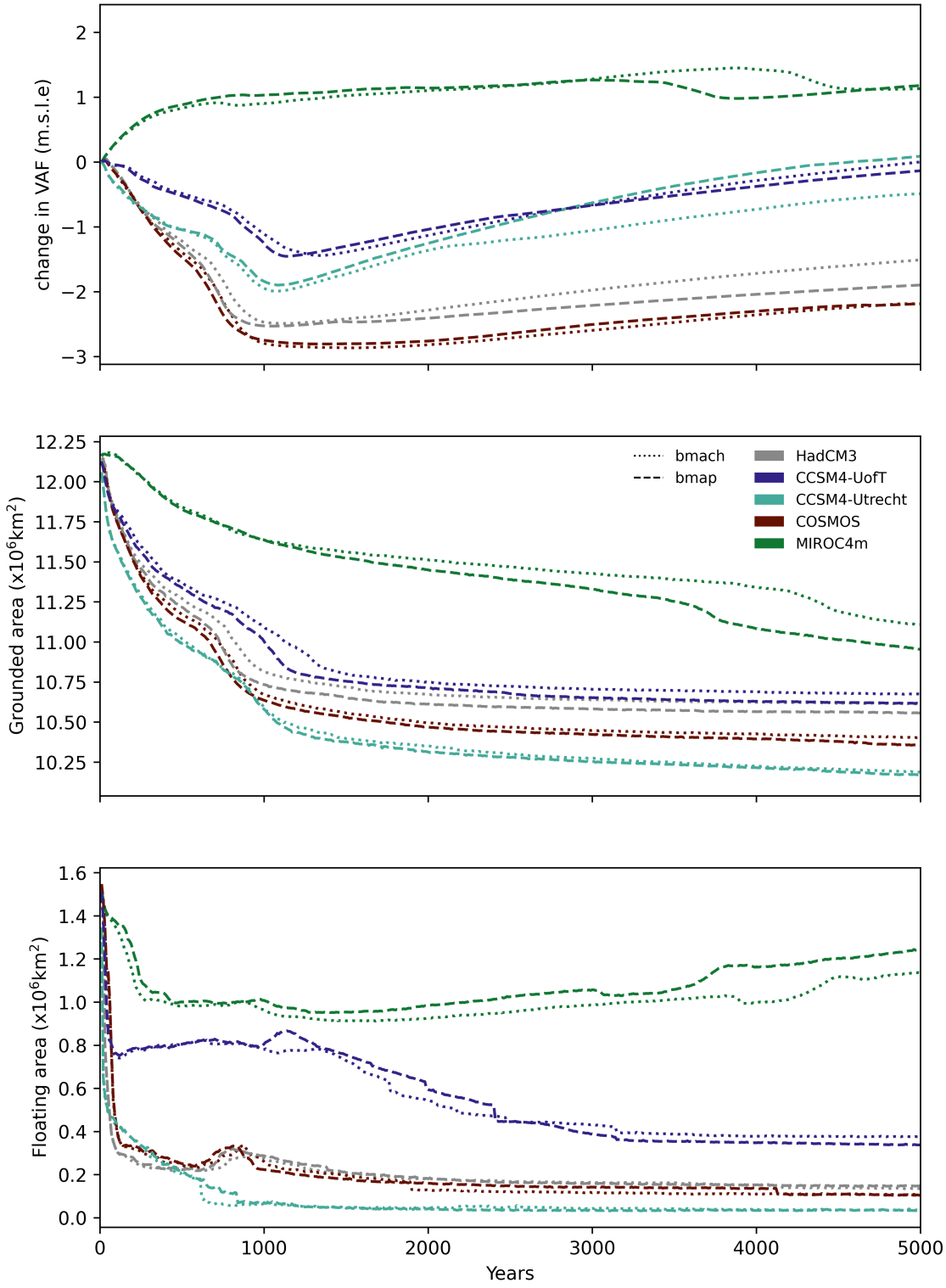


Fig. 4.4 Change in volume above floatation (top), grounded ice sheet area (middle) and floating ice sheet area (bottom) during 5,000 year simulations, using different GCM climate forcings and initial states (BedMachine and Bedmap2). Colours indicate the different climate forcings (see legend), dashed lines show Bedmap2 (bmap in legend) initialised simulations, dotted lines show BedMachine (bmach in legend) initialised simulations.

slower grounding line retreat. This shows the temporal relationship between thickening driven by warming (due to increased SMB: discussed below), and increased discharge driven by ocean melting (loss of buttressing).

In MIROC4m, lower ocean thermal forcing allows the Filchner-Ronne shelf to persist throughout the simulation period. Concomitantly, increased SMB drives thickening in the interior. With low ocean driven mass loss, increased accumulation dominates volume change for MIROC4m forced simulations, driving an overall sea level fall. For the other climate models, substantial mass loss occurs at first, so the increase in accumulation only tends to replace this mass loss over the long-term.

MIROC4m-forced simulations are punctuated by loss of volume above floatation and grounded area at ~3,500 years for Bedmap2 initialised simulations, and ~4,200 years for BedMachine initialised simulations, as well as slight increases in floating area (Fig. 4.4). This reflects the loss of grounded ice sheet area in the Amundsen Sea Embayment sector, which is destabilised by slow grounding line retreat initialised in the Ross shelf sector of WAIS (not shown).

Dolan et al. (2018) simulate the Antarctic ice sheet using PlioMIP1 boundary conditions, and reject MIROC4m based on it's representation of the Antarctic ice sheet in modern control simulations, finding a collapsed WAIS under the control climate. PlioMIP2 MIROC4m is the same model version as used in PlioMIP1 (Chan and Abe-Ouchi, 2020). Rejection of MIROC4m in Dolan et al. (2018) based on its simulation of an overly warm modern climate, and therefore small modern ice sheet, contrasts with our finding of MIROC4m-forced sea level fall. This likely reflects our use of an anomaly approach to correcting climate model bias. A warm MIROC4m control climate without a proportionally large Pliocene warming generates a smaller anomaly, which is apparent in the average thermal forcing shown in Figure 4.2 **e.**, particularly under the Filcher-Ronne ice shelf.

Across simulations, the Amundsen Sea Embayment glaciers collapse and grounding lines retreat through deep submarine basins (Fig. 4.5), with the exception of MIROC4m-forced simulations. These undergo thinning of the Thwaites glacier to floatation, but maintain grounded area in the Pine Island Glacier. Along the Siple Coast, grounding lines retreat back to the Trans Antarctic Mountains (Fig. 4.5), with an ice free sea way connecting the Amundsen Sea to the Ross sea through the formerly glaciated basin of West Antarctica. In all simulations, the Ross shelf collapses. However, whilst the majority of experiments simulate large scale thinning and collapse of the Filchner-Ronne ice shelf, this is notably absent in MIROC4m forced simulation - which has greater thickness in this region compared with the mean for all GCM runs for each initial condition. For both

Fig. 4.5 Thickness change after 5,000 simulations years for runs under Pliocene climate boundary conditions from MIROC4m, CCSM4-Utr, CCSM4-UofT, COSMOS and HadCM3 relative to the mean thickness change for all five simulations for each initial condition. Subplots **a.** - **e.** show runs initialised from modified Bedmap2 initial condition. Subplots **f.** - **j.** show runs initialised from BedMachine initial condition. Contours show shelf edge (dashed line) and grounding line (solid line) position at the start (black) and end (pink) of each simulation.

Bedmap2 and BedMachine initialised, MIROC4m-forced simulations, the Filchner-Ronne ice shelf remains in place, whilst over the Thwaites basin, a large ice shelf forms (Fig. 4.5).

In terms of initialisation with BedMachine bedrock and ice sheet thickness compared with modified Bedmap2 initialisation, the difference in sea level contribution is smaller than that for choice of PlioMIP2 forcing model. Figure 4.6 shows the average thickness change at 5,000 years across the five GCMs for each initial condition, as well as the bedrock elevation in Bedmachine (Fig. 4.6 **c.**) and Bedmap (Fig. 4.6 **d.**). Notable in thickness change plots in Figure 4.6, is the more extensive thinning in the Lambert Glacier catchment for runs initialised with BedMachine (Fig. 4.6 **a.**) compared with the equivalent Bedmap2 (Fig. 4.6 **b.**) simulations. Compared with Bedmap2, Bedmachine has deeper bedrock at the outlet of the Lambert glacier, this leads to greater instability at the grounding line, and hence smaller grounded area in this catchment (Fig. 4.7).

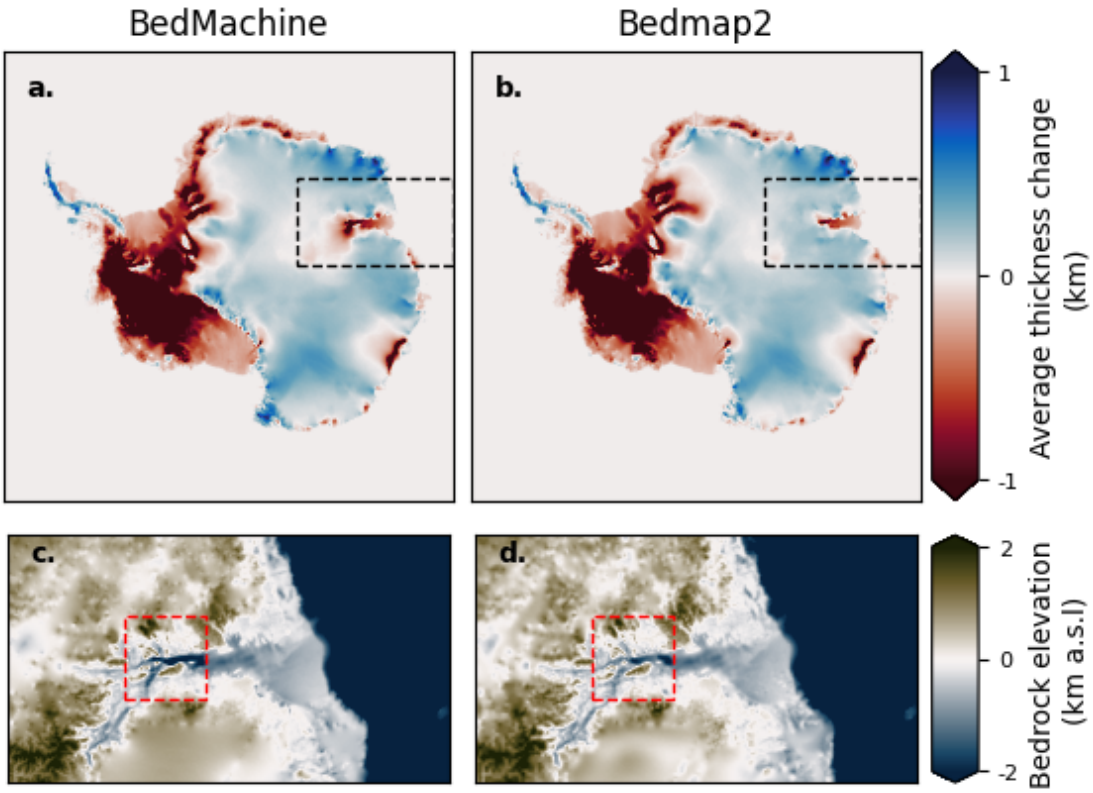


Fig. 4.6 Average thickness change at 5,000 years for all BedMachine initialised simulations (**a.**) and Bedmap2 initialised simulations (**b.**). Also shown are the bedrock elevations for BedMachine (**c.**) and Bedmap2 (**d.**), within the dashed boxes shown in **a.** and **b.**. As can been seen in **c.**, the bedrock is deeper at the outlet of the Lambert glacier (red dashed box in **c.** and **d.**)

Figure 4.7 shows grounded area change after 1,000 years (unfilled markers) and at the end of the 5,000 year simulation period (filled markers) for each of the ice sheet sectors from

Chapter 2. Overall, higher thermal forcing is associated with greater loss of grounded area, with the highest thermal forcing GCM (CCSM4-Utr) driving the largest loss of grounded area in most sectors, and the lowest thermal forcing GCM (MIROC4m) consistently driving the smallest change in grounded area. For the majority of sectors, grounded area is smaller after 5,000 years than after 1,000 years. However, in sectors with bedrock above sea level and limited ice shelf buttressing (e.g. Sectors 1, 3 and 6 in East Antarctica, and sectors 12 and 13 in the Peninsula (Fig. 4.7), grounded ice sheet area does not decrease significantly between 1,000 and 5,000 years. This suggests that, in these sectors, grounded area stabilises early in the simulation, following an initial adjustment to forcing. Grounded ice is then relatively disconnected from the ocean, and insensitive to ice shelf melt-driven retreat. In one Antarctic Peninsula catchment (Sector 12), grounded ice sheet area increases under MIROC4m forcing between 1,000 and 5,000 years. This is indicative of grounding line advance as ice thickens under sustained Pliocene surface mass balance, suggesting that accumulation driven advance from the interior Peninsula is greater than surface mass balance driven retreat, or retreat due to shelf melting.

For the Filchner-Ronne catchment (Sector 14 in Fig. 4.7), persistence of the ice shelf under MIROC4m forcing through to 5,000 years is evident in the limited grounding line retreat compared with other experiments. For the remaining simulations, grounded area loss does not increase linearly with thermal forcing. In the Ross catchment (Sector 7 in Fig. 4.7), MIROC4m-forced simulations maintain grounded area as the grounding line retreats more slowly than in the remaining simulations. However, at 5,000 years, the Ross ice shelf has collapsed in all simulations. Slow loss of the Ross shelf in MIROC4m-forced simulations, but persistence of the Filchner-Ronne shelf, is consistent with relatively low thermal forcing shown in these sectors compared with other models (Fig. 4.2), and lower thermal forcing under the Filchner-Ronne shelf compared with the Ross shelf.

As well as determining the distribution of thermal forcing under ice shelves, choice of GCM influences surface mass balance. Figure 4.8 shows the proportion of total ice sheet and exposed ground area where surface mass balance is negative for each PlioMIP2 GCM. For CCSM4-Utr, COSMOS, HadCM3 and CCM4-UofT forced simulations, ablation area as a proportion of total area undergoes an initial decrease. This reflects loss of lower elevation ice shelf, where melt is more prevalent. For MIROC4m-forced simulations, ablation area is consistently $<$~2% (Fig. 4.8). Moreover, MIROC4m ablation area slightly increases as the simulation progresses - concomitant with ice shelf area gradually increasing (Fig. 4.4). In contrast, CCSM4-Utr has a peak ablation area of 14 % of total area, and stabilises around 7 %. For HadCM3, CCM4-UofT and COSMOS forced simulations, ablation areas stabilise at 2 %, 3 % and 4 % of total area respectively. The ordering of GCMs by ablation fraction in Figure 4.8 is approximately the same as the ordering by grounded ice sheet area

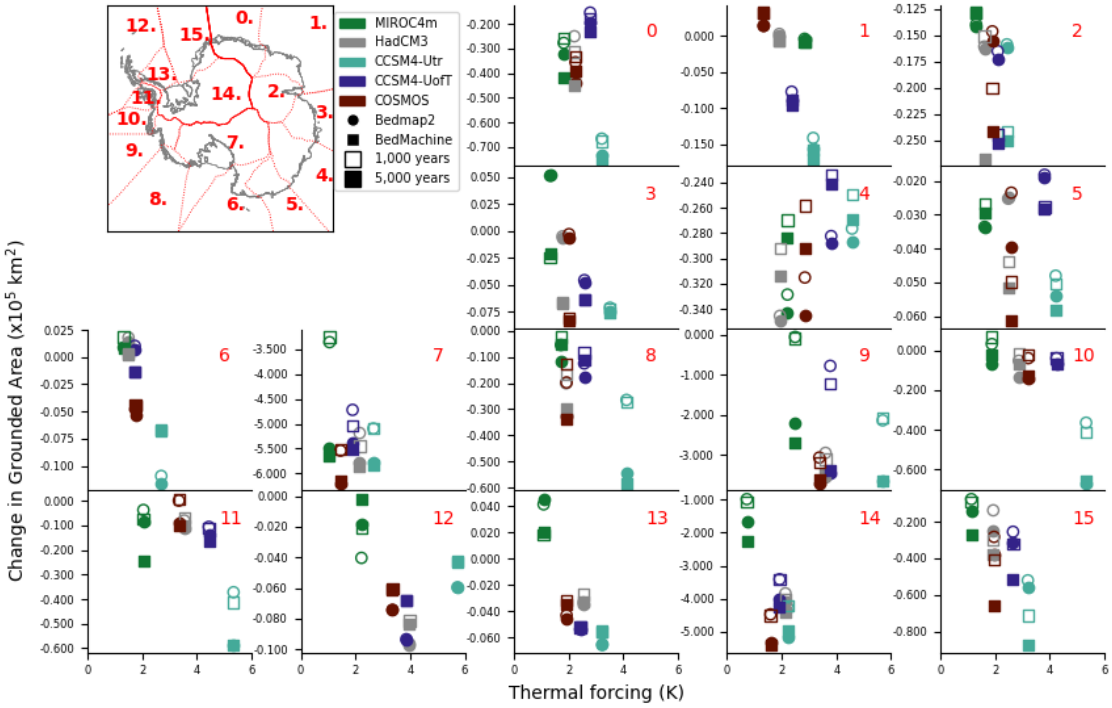


Fig. 4.7 Change in grounded ice sheet area since the start of the simulation in each sector at 1,000 years (unfilled markers), and 5,000 years (filled markers) as a function of sector averaged thermal forcing, excluding open ocean areas at the start of the run. Circular markers indicate Bedmap2 initialised simulations. Square markers indicate BedMachine initialised simulations. Red numbers in the top right corner of each scatter plot corresponds to a sector number. Inset plot shows sector boundaries and initial grounding line (solid grey line contour) and shelf edge (dashed grey contour). Sector boundaries are shown with red dotted contours, with each sector number labelled. Sector names are the same as those in Chapter 2, Figure 2.8.

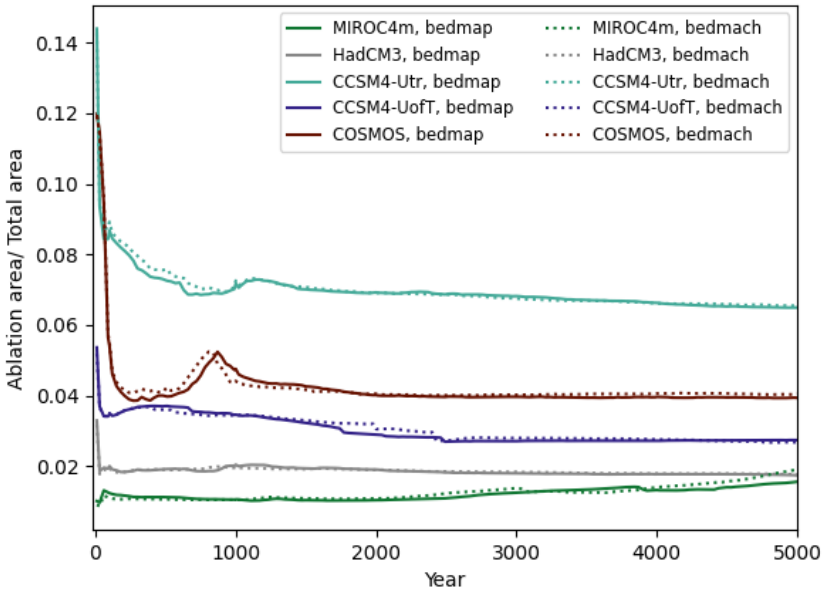


Fig. 4.8 Fraction of the total ice sheet area with negative surface mass balance i.e. where surface ablation occurs.

at the end of the simulation in Figure 4.4. In other words, greater loss of grounded area generally corresponds to higher ablation area fraction.

Distribution and magnitude of SMB are shown in Figure 4.9, for Bedmap2 initialised simulations, at three time-steps: 10 years, 210 years and 1000 years. This illustrates surface mass balance at the start of the simulation period, after century scale duration of forcing, and following loss of most ice shelves in the majority of simulations. Also shown is the mean SMB over the full 5,000 year simulation period. In all simulations, negative surface mass balance is restricted to ice shelves and the lower elevation periphery of the ice sheet (Fig. 4.9). Notable in CCSM4-Utr and CCSM4-UofT surface mass balance fields is the relatively large surface mass balance over the Wilkes Land coast of East Antarctica. This broadly coincides with the ice-free, lower elevation region in PlioMIP2 CCSM4-Utr and CCSM4-UofT GCM simulations. As the Wilkes land coast is lower elevation and warmer in PlioMIP2 GCM simulations compared with modern, it receives more precipitation. An elevation correction is applied to account for the higher, colder, dryer conditions where BISICLES elevation is above elevation in the GCM (i.e. along the Wilkes Land coast). However, CCSM4-UofT and CCSM4-Utr have higher initial precipitation compared with other PlioMIP2 models after elevation correction to the Bedmap2 initial surface (Fig. 4.3) (elevation-corrected precipitation is comparable for BedMachine initialised simulations, not shown). The increased accumulation in the EAIS

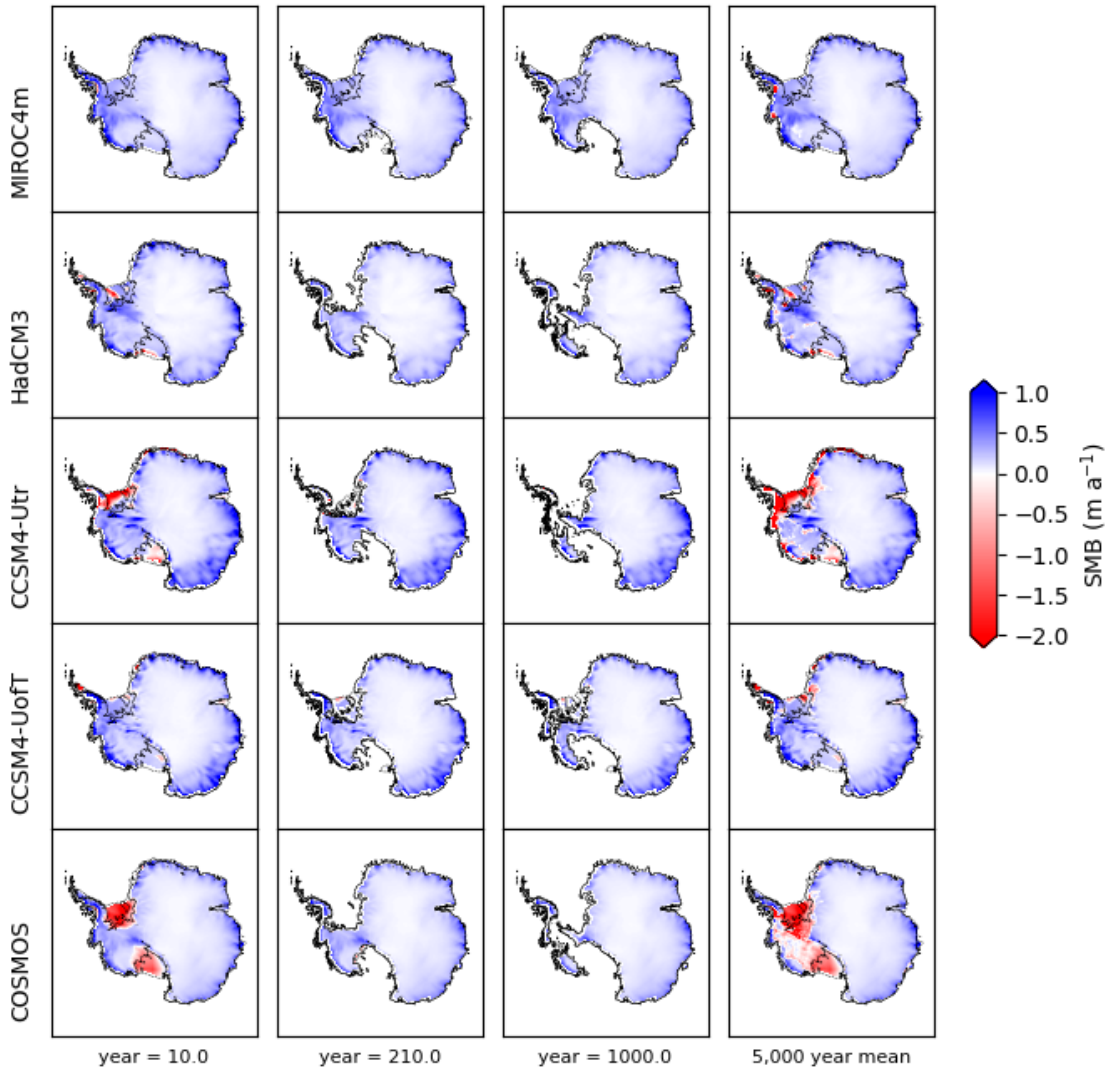


Fig. 4.9 Snapshots of surface mass balance (SMB) at 3 timesteps for simulations initialised from Bedmap2, for each PlioMIP2 GCM. Also shown is the mean surface mass balance over the 5,000 year simulation period. Black solid lines show grounding line position, with dashed line showing shelf edge for each time-step. For mean fields, contours are for initial grounding line and ice shelf boundaries.

interior offsets widespread surface ablation (Fig. 4.8) and ocean melt-driven mass losses (Fig. 4.7) such that CCSM4-Utr and CCSM4-UofT have the smallest sea level contribution after MIROC4m forced simulations for the majority of the simulation period (Fig. 4.4). In comparison, COSMOS and HadCM3 have less accumulation over the EAIS (Fig. 4.9), and have the largest sea level contributions over the simulation period (Fig. 4.4).

### 4.3.2 PDD parameter screening

| Experiment | Change in VAF (m SLE) | Grounded area ($x10^6 km^2$) | Floating area ($x10^6 km^2$) |
|---|---|---|---|
| Default | -2.45 | 10.25 | 0.1068 |
| $PDDs_{max}$ | -2.44 | 10.25 | 0.0989 |
| $PDDs_{min}$ | -2.27 | 10.29 | 0.1117 |
| $PDDi_{max}$ | -2.70 | 10.17 | 0.0874 |
| $PDDi_{min}$ | -2.06 | 10.38 | 0.1278 |
| $LRT_{max}$ | -2.83 | 10.18 | 0.09021 |
| $LRT_{min}$ | -2.64 | 10.26 | 0.08925 |
| $LRP_{max}$ | -3.46 | 10.23 | 0.09653 |
| $LRP_{min}$ | -0.46 | 10.30 | 0.1028 |

Table 4.1 Change in volume above floatation, grounded ice sheet area, and floating ice sheet area for perturbed surface mass balance ensemble.

All perturbed PDD simulations show a large initial decrease in sea level equivalent volume above floatation (VAF)(Fig.4.10, Table 4.1) as the West Antarctic ice sheet collapses - which it consistently does across all simulations. The precipitation lapse rate (*LRP*) has the largest impact: a 3 m SLE difference in VAF, similar to the difference between GCMs in the first ensemble (Fig. 4.4).

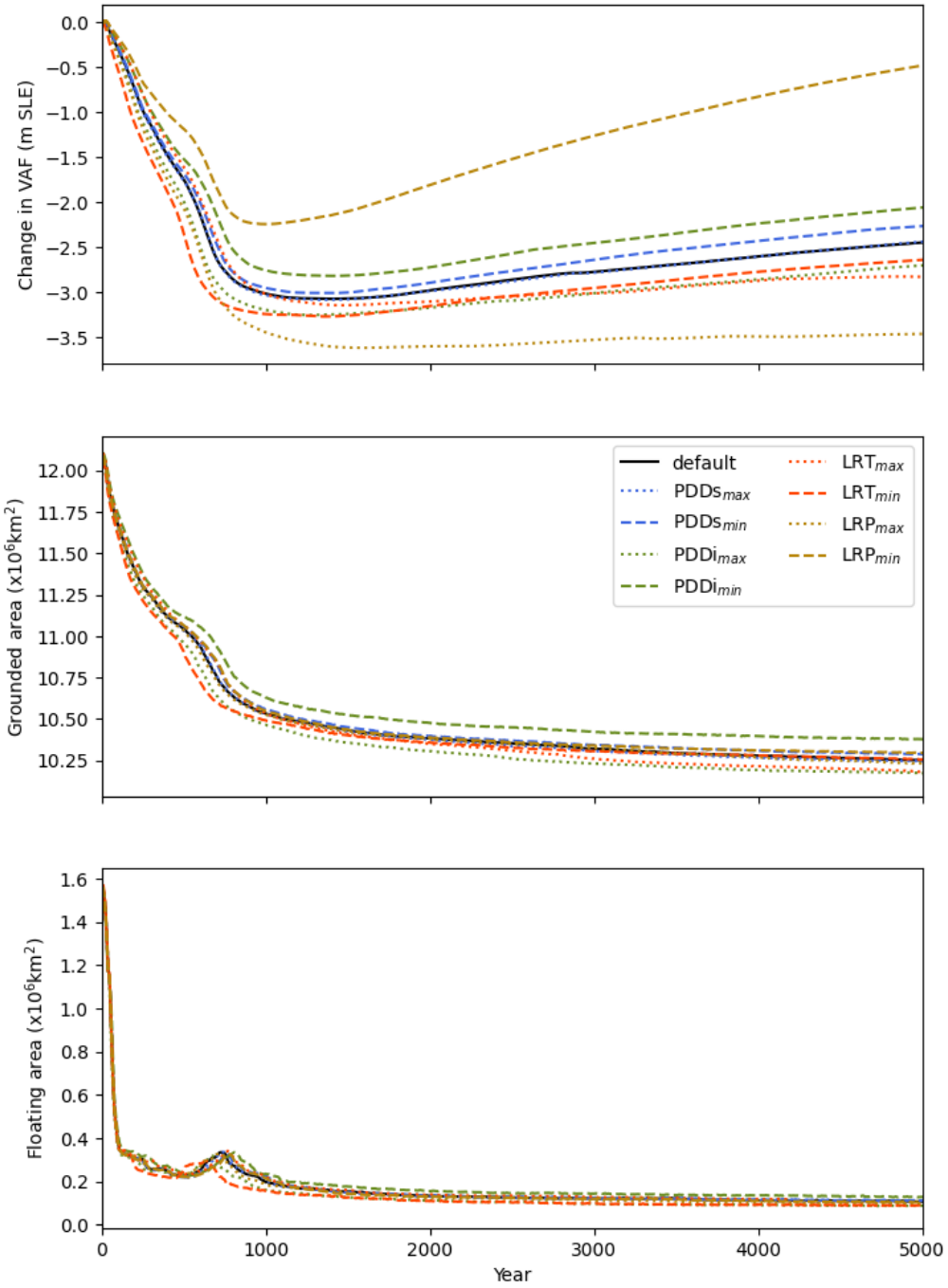


Fig. 4.10 Time series of change in volume above floatation over 5,000 years of simulation time (top). Grounded ice sheet area of simulation period (middle). Floating ice sheet area over simulation period (bottom).

When perturbing the *LRP* parameter, the greatest difference in thickness change relative to the default simulation is seen along the Wilkes Land coast margin of East Antarctica and into the interior (Fig. 4.11). The PRISM4 boundary conditions used in PlioMIP2 (Dowsett et al., 2016, Haywood et al., 2016b) feature a deglaciated Wilkes subglacial basin, with

ice sheet geometry based on Hill et al. (2009). As we initialise from a modern ice sheet elevation, this is also the region with the largest elevation correction in our simulations. With the precipitation lapse rate switched off ($LRP_{min}$ is zero), the high precipitation simulated for the deglaciated Pliocene Wilkes basin in PlioMIP2 COSMOS drives large surface mass balance over this region in BISICLES (Fig. 4.12). Conversely, more negative *LRP* decreases precipitation in this sector to reflect the higher, colder ice sheet model surface elevation.

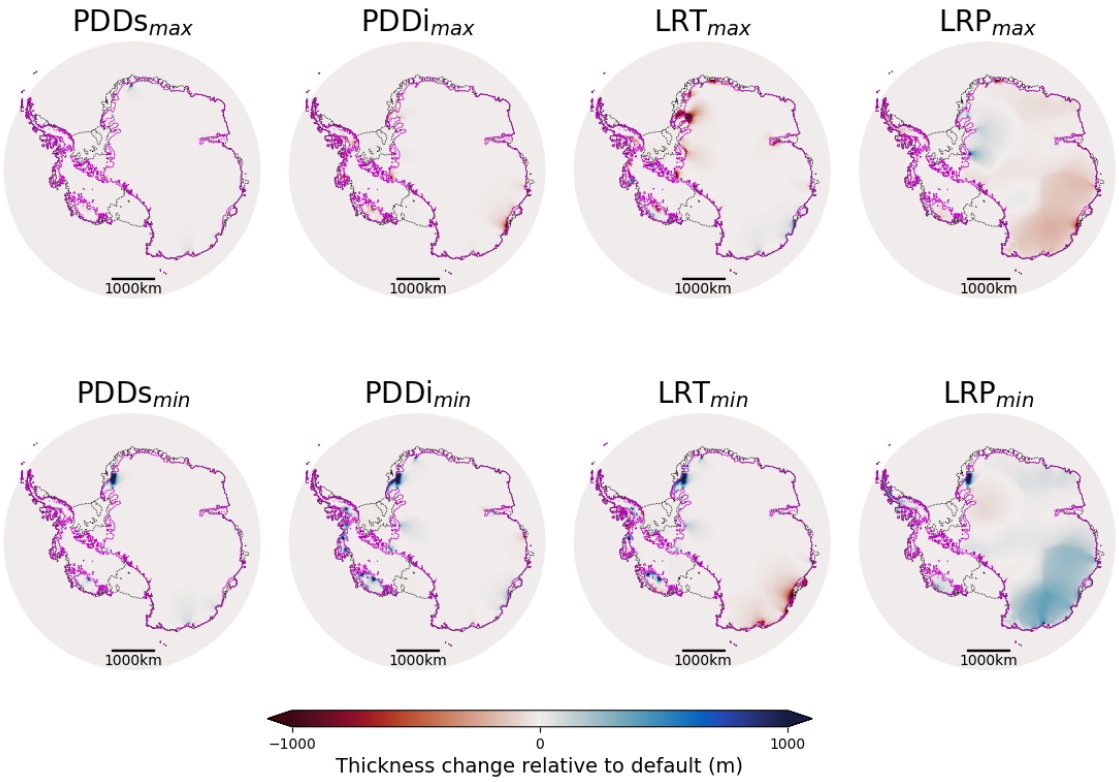


Fig. 4.11 Thickness change after 5,000 years relative to the control run simulation where parameters are at the centre of their ranges.

This *LRP* dependence is consistent with the the findings of Yan et al. (2016) - who simulate greater mass loss for more negative precipitation scaling. Dolan et al. (2018) simulate the mPWP Antarctic ice sheet under PlioMIP1 model forcing for a range of ice sheet models. They find that large positive surface mass balance over the Wilkes and Aurora basins prevent retreat into these when models are initialised from modern. On the eastern edge of the Filchner-Ronne ice shelf, the $LRP_{max}$ simulation undergoes more thickening than the $LRP_{min}$ simulations, highlighting the inverse situation: where the surface elevation of the GCM ice sheet is higher than that of the modern ice sheet, so more negative *LRP* values increase precipitation.

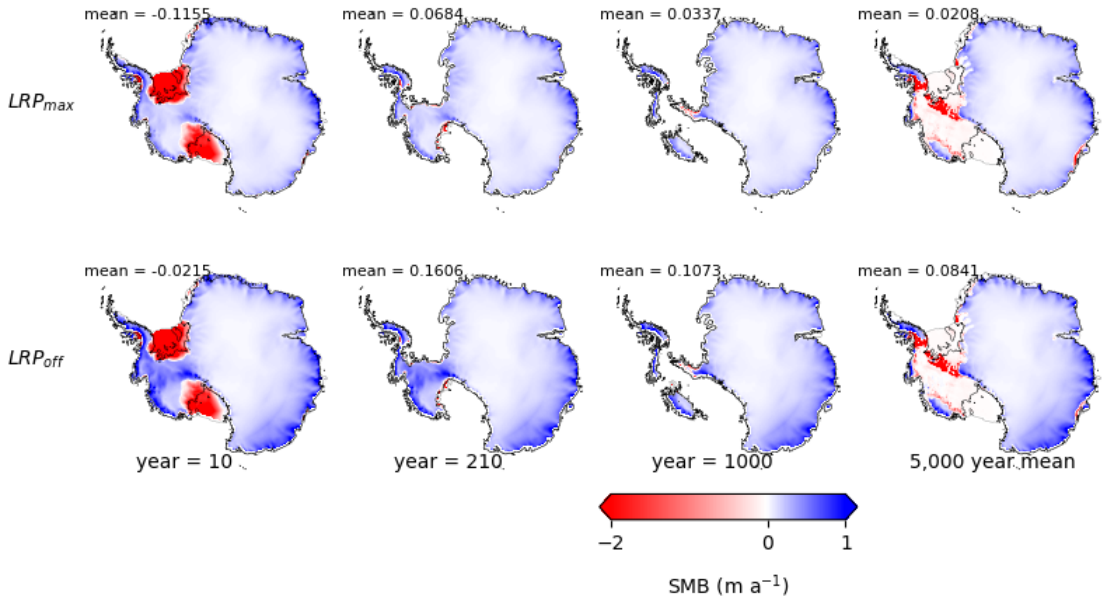


Fig. 4.12 Surface mass balance snapshots for perturbed precipitation lapse rate correction ($LRP_{max}$ and $LRP_{min}$) simulations at year 10, year 210 and year 1,000. Mean surface mass balance for each snapshot is shown in the top left of each subplot. Also shown is the 5,000 year mean surface mass balance

When perturbing the *LRT* parameter, thickness changes also show clear spatial dependence (Fig. 4.11). Under $LRT_{min}$, some of the most extensive regions of thinning overlie the Wilkes and Aurora subglacial basin. As noted for *LRP*, this region is particularly sensitive to lapse rate correction as the elevation in PlioMIP2 models is much lower than the initial ice sheet model elevation. For $LRT_{min}$, a smaller correction is applied than for $LRT_{max}$ or the default simulation. This results in more of the warming over low elevations simulated in COSMOS being retained after the elevation correction step, and a more negative surface mass balance at the margins - driving increased thinning compared with more negative *LRT* simulations. This can been in Figure 4.13, which shows snapshots of surface mass balance for $LRT_{max}$ and $LRT_{min}$ simulations during the initial retreat phase (years 10, 210 and 1,000) as well as the average SMB over the 5,000 year simulation period. More negative surface mass balance for the $LRT_{min}$ simulation compared with the $LRT_{max}$ simulation during the first 1,000 years is apparent at WAIS margins, and the Totten Glacier and George V margins (Fig. 4.13). These regions are largely deglaciated in the boundary conditions of Pliocene PlioMIP2 simulations, underlining the effect of elevation correction where ice sheet model elevation is above GCM surface elevation. Moreover, surface lowering at ice stream margins such as Totten glacier will increase driving stress and discharge, driving further lowering and surface melting. The faster rate of grounded ice retreat in $LRT_{min}$ compared with $LRT_{max}$ during the first 1,000 simulation years (Fig. 4.10), alongside more

negative surface mass balance at the margins of Totten Glacier and George V Land (Fig. 4.13) could evidence greater strength of this feedback for these regions in the $LRT_{min}$ simulation. This contributes to faster retreat for $LRT_{min}$ during the first 1,000 years.

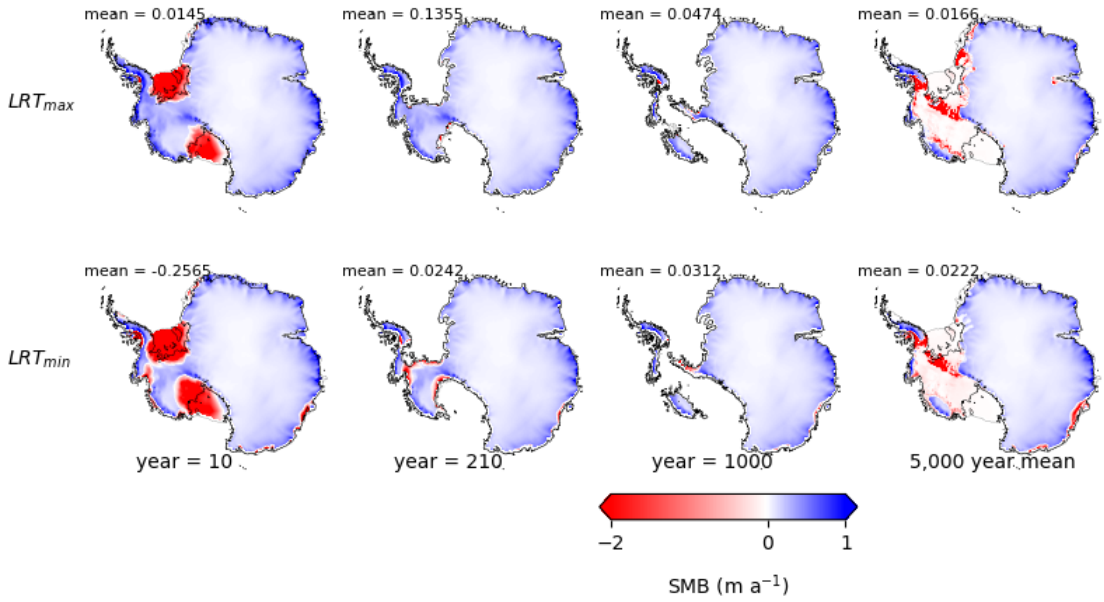


Fig. 4.13 Surface mass balance snapshots for perturbed temperature lapse rate correction ($LRT_{max}$ and $LRT_{min}$) simulations at year 10, year 210 and year 1,000. Mean surface mass balance for each snapshot is shown in the top left of each subplot. Also shown is the 5,000 year mean surface mass balance

In the Filchner-Ronne region of the Dronning Maud Land coast and in Queen Elizabeth Land, the relationship is reversed: $LRT_{max}$ shows thinning while $LRT_{min}$ thickens (Fig. 4.11). This follows the pattern seen for $LRP$, supporting the inference that elevation differences between the ice sheet model and GCM are driving this change. Again, surface mass balance feedbacks play a part in rate of thinning in regions of the EAIS drained by ice streams feeding into the Filchner-Ronne ice shelf. Where retreat of these ice streams drives surface lowering of the EAIS, the simulated ice sheet surface thins below the GCM elevation. For $LRT_{max}$ simulations, this results in a larger positive temperature correction than for $LRT_{min}$ simulations - causing more lowering, which further increases melt. This is consistent with more extensive ablation seen in this region for $LRT_{max}$ mean SMB compared with the same for $LRT_{min}$ (Fig. 4.13). Overall this process dominates: although the $LRT_{min}$ simulation begins with more ablation in some regions, as described above, the eventual melting in the Filchner-Ronne region of the $LRT_{max}$ simulation is larger. This can be seen in Figures 4.10 and 4.13, where $LRT_{max}$ initially has smaller VAF decrease and larger SMB, but these reverse over the long-term.

The compensating thickening and thinning as a result of the temperature lapse rate is further evident in sea level contribution over time (Fig. 4.10), where the difference between $LRT_{min}$ and $LRT_{max}$ at year 5,000 is smaller than the differences for *LRP* and $PDD_i$, and comparable with $PDD_s$. A more negative *LRT* drives a larger negative temperature correction and larger surface mass balance where ice sheet model elevation is higher than GCM elevation. However, it will also cause larger magnitude warming where correcting for lower surface elevation in the ice sheet model than the GCM. This compensation effect limits the net impact of the *LRT* parameter.

Figure 4.10 also shows the $LRT_{min}$ sea level contribution exceeding both $LRT_{max}$ and the default run time series - confounding a clear interpretation of *LRT* influence on ice sheet volume change. This is because the relationship between surface mass balance and temperature is non-linear - warming only increases melting if it exceeds the melting temperature. Where elevation is maintained above the equilibrium line, as over much of the EAIS, the ice sheet is relatively insensitive to changes in *LRT*. Again, this could be driven by elevation differences between BISICLES and COSMOS. For the initial retreat phase, mass loss and grounding line retreat predominantly occur in regions where BISICLES elevation is higher than in COSMOS Pliocene GCM simulations. In this setting, $LRT_{min}$ conserves more warming (imposes a less negative elevation temperature correction) from the GCM, and therefore loses more mass, than $LRT_{max}$. The default simulation lies between the two (Fig. 4.10). Once the majority of ice has been lost in WAIS, thinning predominantly takes place in glacier catchments draining into the Filchner-Ronne ice shelf. Here, the COSMOS GCM Pliocene surface elevation is higher than modern. In this setting, $LRT_{max}$ imposes a more positive temperature correction, increasing surface melt, so the trajectories of VAF in $LRT_{max}$ and $LRT_{min}$ cross over at around 2,000 years (Fig. 4.10). The default simulation is a combination of the two: initially following close to the trajectory of VAF loss in $LRT_{max}$, then increasing at a similar rate to $LRT_{min}$. This leads to a final VAF outside the range of either.

After *LRP*, *PDDi* shows the largest impact on change in VAF (Fig. 4.10 and Table 4.1). Of the four surface mass balance parameters perturbed, *PDDi* has the largest impact on grounded ice sheet area. We expect *PDDi* to have a strong influence on the narrow ablation zone around the ice sheet margins, where temperatures persist above 0°C for more of the year than in the interior. Whilst PDD factors do not change the size of this ablation zone directly (Ritz et al., 1996), they do increase the rate at which mass is lost from the surface within it. This effect is evident in the thickness change for both sets of PDD factors, where thickness differences are strongest at the margins. Moreover, average SMB for $PDDi_{max}$ is more negative or an order of magnitude smaller with greater ablation (Fig. 4.14). The direct effect of *PDDi* in increasing melt within the ablation zone under $PDDi_{max}$, is evident

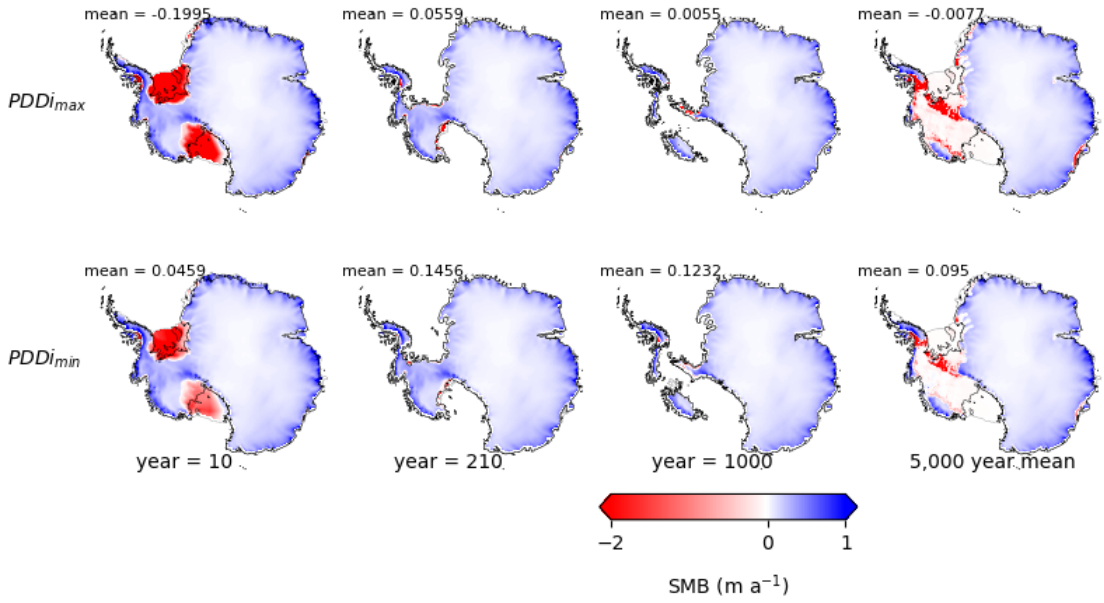


Fig. 4.14 Surface mass balance snapshots for maximum and minimum positive degree day factor for ice ($PDDi_{max}$ and $PDDi_{min}$) simulations at year 10, year 210 and year 1,000. Mean surface mass balance for each snapshot is shown in the top left of each subplot. Also shown is the 5,000 year mean surface mass balance.

in its strong effect on grounded area in Figure 4.10. This is consistent with previous studies (Stone et al., 2010, Yan et al., 2016). We note however that *PDDi* indirectly impacts ablation area, with a consistently larger ablation area as a proportion of total area for $PDDi_{max}$ compared with $PDDi_{min}$ (Fig. 4.15) .

**Conclusions**

The first aim of this chapter was to explore sensitivity to the choice of available PlioMIP2 climate in BISICLES simulations of the Antarctic ice sheet, on millennium time scales. We also sought to assess the differences in ice sheet response for two modern initial ice sheet geometries - Bedmap2 and Bedmachine. To address these aims, we simulated the Antarctic ice sheet forced with five PlioMIP2 GCMs for each initial ice sheet. We found larger differences in simulated ice sheet evolution for different GCMs, compared with initial conditions.

The choice of GCM controlled ice sheet evolution and sea level response through the magnitude and distribution of surface mass balance and ocean thermal forcings. The largest simulated sea level contributions were ~3 m for COSMOS-forced simulations, followed by HadCM3-forced simulations. Both CCSM4-Utr and CCSM4-UofT have stronger thermal forcing than COSMOS and HadCM3. However, both CCSM4 variants undergo a smaller

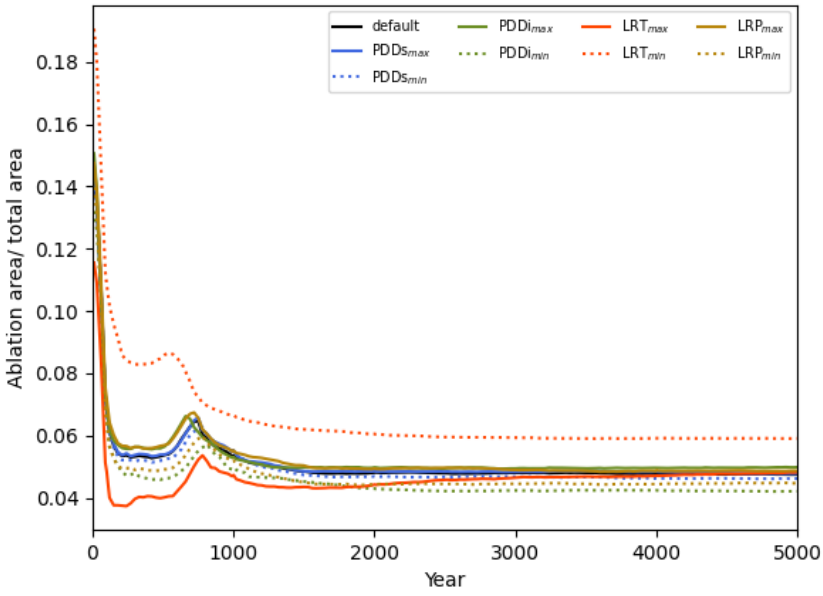


Fig. 4.15 Area with negative surface mass balance (ablation area) divided by area of the ice sheet for all PDD perturbation simulations.

loss of volume above floatation, and are approaching their initial volume after 5,000 model years. This reflects the elevated EAIS surface mass balance in both CCSM4-Utr and CCSM4-UofT compared with COSMOS and HadCM3. MIROC4m-forced simulations increased their volume above floatation over 5,000 years, and maintained their ice shelves for longer than simulations forced with the other four GCMs. This is consistent with relatively low thermal forcing in MIROC4m, particularly under the Filchner-Ronne ice shelf. MIROC4m-forced simulations also had the smallest ablation area, at < ~2% of total area throughout the simulation period. With the high basal melt sensitivity used in these simulations, we would expect strong initial ice shelf melt-driven retreat. With the aim in Chapter 5 of simulating Pliocene retreat of the Antarctic ice sheet, and comparing with reconstructions of the Pliocene ice sheet volume, we judge that MIROC4m-forced simulations may produce sea level changes that are inconsistent with records of the Pliocene. We therefore use only HadCM3, COSMOS, CCSM4-Utr and CCSM4-UofT in subsequent ensembles. A caveat to this judgement is that sea level fall in MIROC4m-forced simulations is likely to be sensitive to surface mass balance parameters, so we might expect a larger sea level contribution when these are perturbed later. Moreover, small sea level fall from Antarctica is not precluded by the low end of Pliocene sea level reconstructions, if sea level rise is dominated by melt of ice sources outside Antarctica.

The second aim of this chapter was to explore variability in simulated ice sheet evolution driven by uncertain parameters in our surface mass balance scheme. To this end, we ran 9 simulations forced with PlioMIP2 COSMOS climate, with four surface mass balance parameters perturbed one at a time to the edges of their ranges, and one simulation with all parameters at the middle of their ranges. Precipitation lapse rate (*LRP*) had a considerable influence on ice sheet volume, with the $LRP_{min}$ simulation (in which no precipitation correction was applied) losing less volume above floatation than other simulations. In terms of rate of area change and grounding line retreat however, perturbing *LRP* had a limited effect. This reflects the role of increased precipitation distributed over the high EAIS in increasing ice sheet volume above floatation, whereas retreat of grounded ice is dominated by melt of submarine ice in WAIS and surface melting. Temperature lapse rate (*LRT*) predominantly impacted melt and retreat at the margins of the ice sheet, and the size of the ablation area. During the initial retreat phase, for regions where modern ice sheet surface is above the Pliocene surface elevation in the GCM (WAIS, George V Land and Totten Glacier margin), $LRT_{min}$ conserved more warming from the Pliocene climate through the elevation correction - imposing a smaller negative temperature correction. This increased ablation area and melting area in low elevation retreat margins. Later in the simulation, near the Filchner-Ronne ice shelf where the modern ice sheet surface elevation is lower than the Pliocene, $LRT_{max}$ resulted in larger temperature correction and therefore greater melting. The net effect of *LRT* on volume above floatation change (sea level contribution) was limited. Positive degree day factor for ice (*PDDi*) had a relatively strong influence on both rate and magnitude of grounded area loss, and change in volume above floatation. Given that *PDDi* impacts rate of melting in the ablation zone, its impact on grounded area and volume reflects feedbacks between melt at the margins and ice sheet discharge. Stronger melting at the margins, under higher *PDDi*, increases lowering at the margins. This increases surface gradients, driving stress and therefore discharge at ice streams - which causes thinning upstream. With surface lowering from the margins, the ablation area can advance upstream - driving further melt. The positive degree day factor for snow (*PDDs*) drove the smallest variability in change in volume above floatation.

Based on differences in sea level contribution between parameter minimum and maximum values, we choose to focus on the positive degree day factor for ice (*PDDi*) and the precipitation lapse rate (*LRP*) in subsequent ensembles, as these had the largest magnitude difference in loss of volume above floatation. *LRP* perturbations can drive differences in sea level contribution as large as differences due to choice of GCM. *PDDi* perturbations drive the largest difference in grounded area retreat, and the second largest difference in volume above floatation changes. This allows us to explore both the volumetric impact of a warmer atmosphere distributing more SMB over the surface of the ice sheet through

*LRP*, and the ice sheet sensitivity to increased melting in the ablation zone (Ritz et al., 1996). We therefore judge that perturbing these parameters in chapter 5 ensembles, in combination with four PlioMIP2 GCMs, will generate the most diverse range of Pliocene climates.

# Chapter 5

# Perturbed Parameter Ensembles of the Antarctic Ice Sheet in the Pliocene

## 5.1 Introduction

In chapter 1, we highlighted the Pliocene as a potential analogue for future warming, with comparable atmospheric $CO_2$ concentrations to modern (~400 ppm) (de la Vega et al., 2020), moderate warming (~2-3 °C global mean air temperature anomaly), but multi-metre sea level rise (Gulev et al., 2021)(Section 1.4). It has been studied as both an exploration of Antarctic ice sheet response to warm Pliocene climate (Dolan et al., 2018, de Boer et al., 2015, Yan et al., 2016, Austermann et al., 2015, Golledge et al., 2017b, Berends et al., 2019, Gasson et al., 2016), and as a constraint on Antarctic contribution to sea level under future warming (DeConto and Pollard, 2016, DeConto et al., 2021). This chapter builds on previous work to address two questions. First, what range of Pliocene Antarctic ice sheets do we simulate when exploring known modelling uncertainties? Second, how do these compare with reconstructions of palaeo-data of Pliocene sea level and grounding line position in a key East Antarctic basin?

The model intercomparison studies of PLISMIP highlight the sensitivity of simulated ice sheets to both climate forcing model and ice sheet initial condition (Dolan et al., 2018, de Boer et al., 2015)(Section 1.5). Perturbed parameter ensemble studies (Yan et al., 2016, DeConto and Pollard, 2016, DeConto et al., 2021) have shown the importance of ice sheet model parameters. In this chapter, we aim to undertake an exploration of both sources of uncertainty with the BISICLES ice sheet model (Cornford et al., 2013). Previous studies of the Pliocene Antarctic ice sheet have used lower order physics models compared with BISICLES (SIA (Dolan et al., 2018) to hybrid (Dolan et al., 2018, DeConto and Pollard,

2016, de Boer et al., 2015, DeConto et al., 2021)), at model resolution on the order of >10 km (Dolan et al., 2018, de Boer et al., 2015, DeConto et al., 2021, DeConto and Pollard, 2016).

With its adaptive mesh refinement (Section 1.3.2), BISICLES can maintain computational efficiency whilst resolving the grounding line and ice streams at relatively high resolution. This allows us to simulate this key region at higher resolution that previous studies - down to 4 km. BISICLES L1L2 physics provides greater accuracy compared with hybrid SIA-SSA models (Pattyn et al., 2013), and does not rely on parameterizations of grounding line ice flux and migration, which can limit accuracy in short term transient simulations and in the presence of buttressing (Pattyn et al., 2013, Reese et al., 2018c). We note however that in the case of ice sheet models that apply the grounding line flux parameterization of Schoof et al. (2007, the case of rapid sliding) (DeConto and Pollard, 2016, DeConto et al., 2021), changes to this scheme in the most recent study (Pollard and DeConto, 2020b, DeConto et al., 2021) address these accuracy issues. Moreover, updating the grounding line parameterization is shown to have a limited impact for continental scale simulations when compared with the previous model version (DeConto et al., 2021). This suggests that accuracy issues in this hybrid model related to the grounding line flux paramaterization may be negligible for continental Pliocene Antarctic simulations, including in Deconto and Pollard (2016). With the modelling implementation developed in the rest of this thesis, we can simulate the Antarctic ice sheet under Pliocene climate in this chapter, including GIA processes and ice stream evolution.

We explore a range of ice sheet simulations for Antarctica, accounting for uncertainty in climate boundary conditions, ice sheet initial conditions, parameters governing sensitivity to climate and internal ice sheet model parameters. We first perform a 120-member perturbed parameter ensemble sampling: positive degree day factor for ice (*PDDi*), precipitation lapse rate (*LRP*), ice shelf sensitivity to basal melt ($\gamma_0$), upper mantle viscosity (*UMV*) and Weertman friction coefficient (*C*). This is forced with four different climate models and initialised from the modern ice sheet. Our design spans a broad range for perturbed parameters and efficiently samples the design space, making it a suitable candidate for building an emulator (e.g Edwards et al. 2019, 2021, Lowry et al. 2021, Bulthuis et al. 2019) to quantify uncertainties for simulations of the Pliocene Antarctic ice sheet.

We also perform a 30-member subset of this ensemble initialised from a PRISM-based reconstruction of the reduced Pliocene ice sheet. Finally, we begin to explore the impact of parameter uncertainty on control simulations, by performing the same 30-member subset of the ensemble under sustained modern climate. We compare the Pliocene ensembles

with reconstructions from palaeo-data, and the control ensemble with modern observations, to comment on the plausibility of different modelling choices.

## 5.2 Methods

### 5.2.1 BISICLES

We use the BISICLES version presented in Chapter 3 with GIA (Section 3.2.2), basal hydrology coupled basal sliding (Section 3.2.3) and the ISMIP6 ice shelf basal melt parameterisation (Section 2.2.2). The GIA model is the BISICLES implementation developed by Kachuck et al. (2020), based on Bueler et al. (2007). It simulates an elastic plate overlying a viscous half space; which can be composed of n layers for the viscous mantle. For the simulations presented here, we use two viscous mantle layers. The basal hydrology component (Gandy et al., 2019) couples the Coulomb component of a Tsai et al.(2015) type sliding law to a simplified representation of ice sheet basal hydrology. We use a sliding exponent of m=1/3 for Weertman sliding. Base resolution for all simulations is 16 km, with two levels of refinement to 4 km. We implement the BISICLES grounding line subgrid friction interpolation scheme, which gives comparable results to higher resolution simulations where the interpolation scheme is not applied (Cornford et al., 2016). BISICLES is free to refine grid resolution in any part of the domain, with the grid refined in ice streams and at the grounding line.

### 5.2.2 Simulation Ensembles

We present three ensembles in this chapter: a Pliocene-forced ensemble initialised from the modern ice sheet ($Plio_{modern}$); a Pliocene-forced ensemble initialised from a reduced Pliocene ice sheet ($Plio_{PRISM}$) and a Control ensemble forced with modern climate, initialised from the modern ice sheet and bedrock ($Ctrl_{modern}$) (Table 5.1). An outline of the ensembles is given in this section; details of the initialisation, climate forcings and ensemble design for each are given in the following sections.

The $Plio_{modern}$ ensemble aims to explore sensitivity of simulated Antarctic ice sheets to perturbed Pliocene climate and uncertain model parameters, initialised from a modern ice sheet configuration. We perturb two parameters related to surface mass balance processes (Section 3.2.4)(positive degree day factor for ice ($PDDi$), precipitation lapse rate ($LRP$)); ice shelf sensitivity to basal melt ($\gamma_0$)(Section 2.2.2); bedrock sensitivity to changes in ice sheet loading (upper mantle viscosity ($UMV$))(Section 3.2.2); and basal sliding outside

ice streams (Weertman friction coefficient ($C$))(Section 3.2.3). The $Plio_{modern}$ ensemble is forced with output from four PlioMIP2 GCMs (Haywood et al., 2016b). Ice sheet thickness and bedrock elevation at the start of each simulation are based on modern geometry (Morlighem et al., 2020) (Section 5.2.3). By varying the boundary condition GCM, ice sheet sensitivity to Pliocene climate, glacial isostatic adjustment processes and sliding at the base of the ice sheet, this ensemble will assess how ice sheet extent and volume respond to Pliocene forcing across a wide range of model uncertainties. This ensemble builds on the work of Dolan et al. (Dolan et al., 2018), who highlight the role of boundary condition GCM from the PlioMIP1 ensemble, in driving variability in simulated Pliocene AIS configuration. The initialisation procedure, climate forcings and ensemble design are described in Sections 5.2.3, 5.2.4 and 5.2.5, respectively.

The $Plio_{PRISM}$ ensemble aims to explore how initial ice sheet and bedrock geometry influence ice sheet evolution under Pliocene climate. To achieve this, a subset of $Plio_{modern}$ simulations are run with a bedrock and ice sheet representative of the reduced Pliocene ice sheet used as a boundary condition in the PlioMIP2 climate simulations (Haywood et al., 2010). Again, this follows the approach taken in PLISMIP (Dolan et al., 2018, de Boer et al., 2015), where a reduced Pliocene ice sheet with bedrock at isostatic equilibrium was used to initialise ice sheet modelling experiments. PRISM (Pliocene Research Interval for Synoptic Mapping) refers to the ice sheet from PRISM4 (Dowsett et al., 2016), which was used as a boundary condition in both the PlioMIP1 and PlioMIP2 GCM experiments (Haywood et al., 2010, 2016b). This ice sheet configuration is described further in Section 5.2.3.

Our third ensemble, $Control_{modern}$, aims to explore how much the control simulation is affected by perturbing the parameters. Generating equivalent control simulations to subtract for each perturbed parameter ensemble member has been done since the earliest climate ensemble studies (Murphy et al., 2004), but not for Pliocene ice sheet ensemble studies (DeConto and Pollard, 2016, DeConto et al., 2021, Yan et al., 2016). To achieve this, $Control_{modern}$ runs a subset of $Plio_{modern}$ simulations under modern climate boundary conditions, initialised from modern ice sheet and bedrock geometry. Subtracting $Control_{modern}$ simulations from the corresponding $Plio_{modern}$ and $Plio_{PRISM}$ ensemble members gives the range of Antarctic ice sheet sea level contributions forced with Pliocene climate while also accounting for how uncertain parameters affect the baseline.

| Ensemble name | Climate forcing | Initial condition | Ensemble size | Simulation Length |
|---|---|---|---|---|
| $Plio_{modern}$ | Pliocene | Modern (BedMachine) | 120 | 10,000 years |
| $Plio_{PRISM}$ | Pliocene | Pliocene (PRISM) | 30 | 10,000 years |
| $Control_{modern}$ | Modern | Modern (BedMachine) | 30 | 5,000 years |

Table 5.1 Details of the three simulation ensembles presented indicating: ensemble name as used in the main text; climate forcing; initial ice sheet thickness and bedrock condition; number of ensemble members; and full simulation period.

### 5.2.3 Initialisation

#### Modern initial states

Our main Pliocene simulation ensemble ($Plio_{modern}$) and Control ensemble ($Control_{modern}$) are initialised from BedMachine bedrock elevation and ice sheet thickness (Morlighem et al., 2020), as in Chapter 4 and described in Section 4.2.2. Each simulation has modern initial ice sheet temperature from Pattyn et al. (2010).

Every ensemble member is initialised from a short (10 year) relaxation run with inverted basal friction, modern accumulation, and idealised basal melt to maintain stable ice shelves (Cornford et al., 2016). This allows the ice sheet geometry to relax, before parameter perturbations are introduced (Section 5.2.5). The use of this relaxation run is the same as the approach in modern projection ensembles (Chapter 2), where the ice sheet is relaxed with modern initial conditions and inverted bed friction parameters. This allows all simulations to be initialised from the same starting point. The short relaxation period is due to a restriction of the GIA implementation. We found it was not possible to perturb GIA parameters partway through a simulation (i.e. after the relaxation period in a single relaxation simulation, from which other simulations could initialised as in Chapter 2). This resulted in new values not being recognised in BISICLES. We therefore perturbed the GIA parameter ($UMV$: upper mantle viscosity) at the start of the relaxation period, and the other parameters from the end. This leads to a trade-off in relaxation time: we allow the ice sheet model enough time to relax, but without evolving so much that the simulation starts with a markedly different initial ice sheet, due to the different $UMV$ values in the relaxation run. We expect that over the millennial scale of these simulations, the impact will be small. This initialisation approach is used for $Plio_{modern}$ and $Control_{modern}$ ensembles. Initial bedrock elevation and ice sheet thickness for $Plio_{modern}$ and $Control_{modern}$ ensembles are shown in Fig. 5.1.

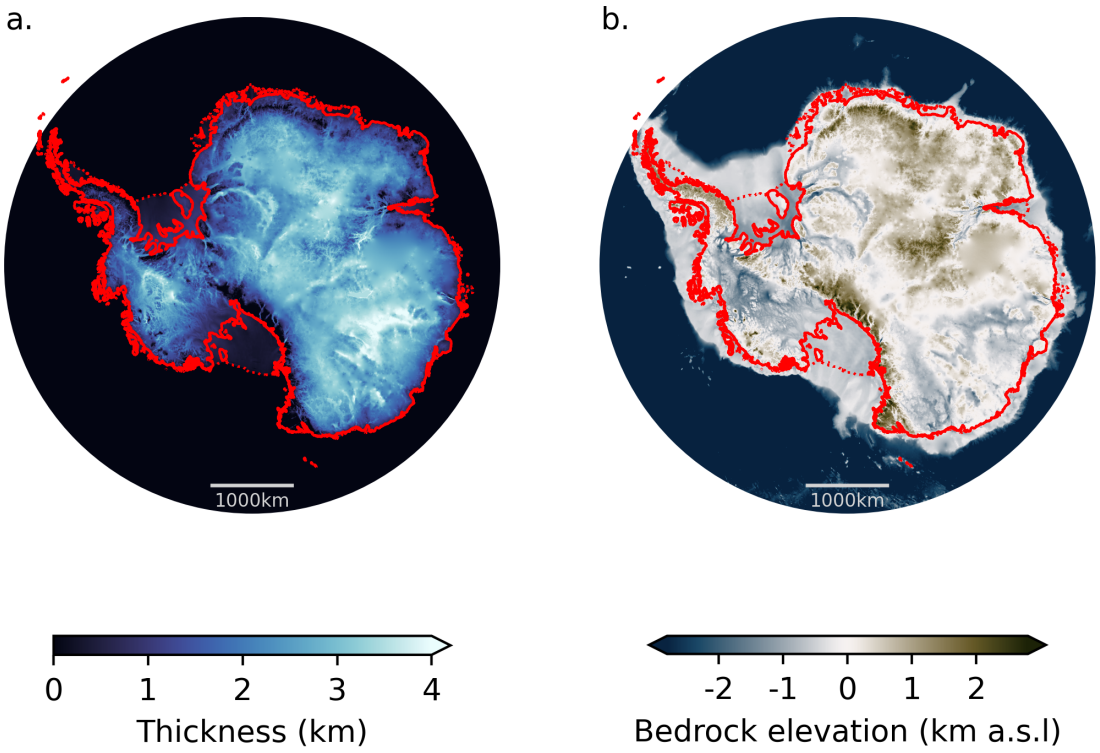


Fig. 5.1 Initial ice sheet thickness (**a**) and bedrock elevation above sea level (**b**) for ensembles initialised from modern (BedMachine) data. Red solid line in both plots shows initial grounding line position. Red dotted line shows initial position of the shelf edge.

### PRISM initial ice sheet state

We initialise the $Plio_{PRISM}$ simulations from an ice sheet derived from the PRISM Antarctic ice sheet and bedrock, as used in PLISMIP. The original PRISM3 ice sheet was generated with the BASISM ice sheet model (Hill, 2009) at a resolution of 40 km, a factor of 10 lower than BISICLES maximum resolution in the Pliocene simulations used here. The PRISM3 ice sheet and bedrock were simulated in Hill et al. (2009) with GIA until isostatic equilibrium.

In order to generate a high resolution bedrock elevation and thickness, we use an anomaly approach. We regrid and bilinearly interpolate PRISM fields of ice sheet surface, thickness and bed elevation (Dolan, personal communication) from 40 km onto a 1km polar stereographic BISICLES compatible grid. We then subtract the modern from Pliocene surface and bedrock fields, and add these to the high resolution (1 km) Bedmap2-derived modern fields ( Fretwell et al. 2013, Cornford et al. 2016 as in Chapter 4). Ice sheet thickness is taken as the difference between the two.

In order to generate self-consistent temperature fields for PRISM initialised simulations, we run a 10,000 year spin-up simulation in BISICLES with fixed PRISM geometry, initialising the temperature from Pattyn et al. (2010) and freely evolving thermodynamics. The geometry is then relaxed for 150 years to generate an initial thickness and bedrock elevation from which $Plio_{PRISM}$ simulations are initialised. This allows the ice sheet internal energy, from which 3D temperatures can be derived, to evolve towards an equilibrium within computational constraints. Ice sheet thickness and bedrock initial conditions for $Plio_{PRISM}$ are shown in Fig. 5.2.

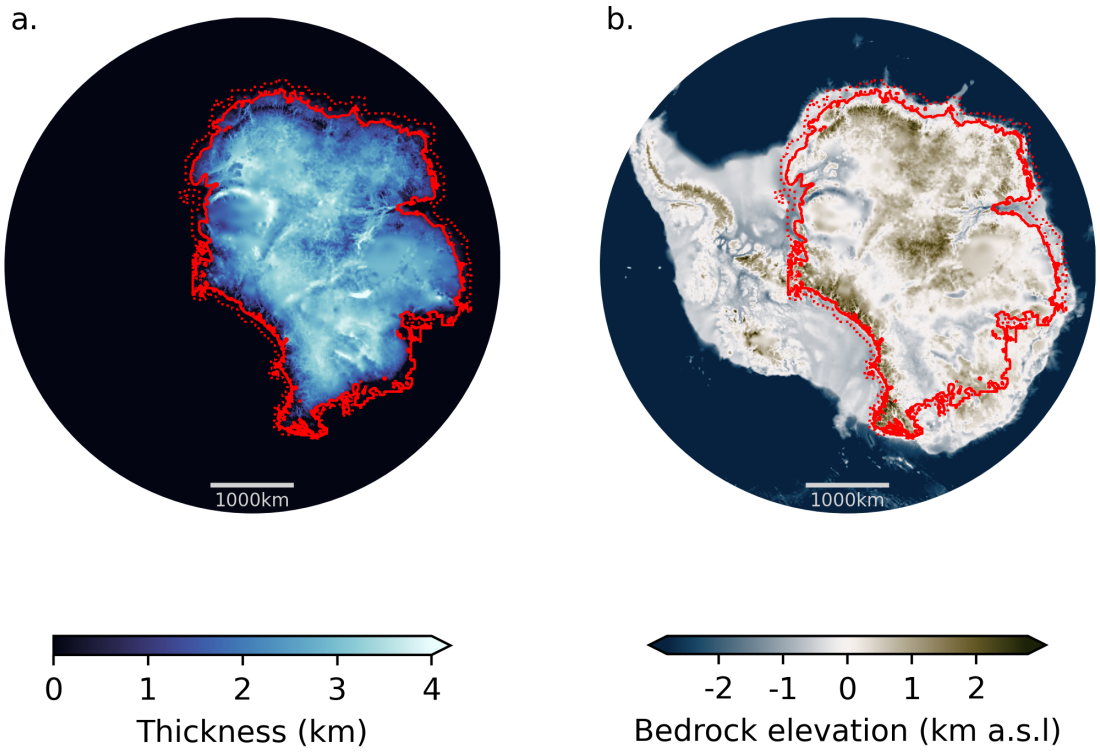


Fig. 5.2 Initial ice sheet thickness (**a**) and bedrock elevation (**b**) reduced Pliocene, PRISM-based ice sheet. Red solid line in both plots shows initial grounding line position. Red dashed line shows initial position of the shelf edge.

### 5.2.4 Climate forcings

All ensembles ($Plio_{modern}$, $Plio_{PRISM}$ and $Control_{modern}$) use the same positive degree day model (pyPDD (Seguinot, 2013), Section 3.2.4) to calculate surface mass balance from average monthly temperature and precipitation. Surface melting is proportional to the number of days with temperatures above melting in a year. We use an elevation correction

to downscale temperature and precipitation to the evolving ice sheet surface elevation (see below). The surface mass balance is recalculated at 30 year intervals.

For the ocean forcing, melting at the base of the ice shelves is calculated from ocean thermal forcing using the ISMIP6 non-local basal melt parameterisation (Jourdain et al., 2020)(Section 2.2.2). As in previous chapters, simulations are forced with steady state climate.

### Modern Climate

Modern surface mass balance fields are computed using pyPDD with temperature and precipitation from the Regional Atmospheric Climate MOdel (RACMO2) (Wessem et al., 2014), forced with ERA-interim reanalysis data (Dee et al., 2011) and averaged from 1979-2000 (Section 3.3.5). RACMO precipitation and temperature are elevation-corrected to the evolving ice sheet surface (Section 3.3.5).

Ocean thermal forcing used to drive the basal melt parameterisation is based on the ISMIP6 thermal forcing, compiled from MEOP, EN4 and WOA18 representing the 1995-2014 average (Jourdain et al., 2020)(Section 2.2.2).

### Pliocene Climate

We use four of the five PlioMIP2 GCMs used in Chapter 4: COSMOS (Stepanek et al., 2020), CCSM4-UofT (Chandan and Peltier, 2017), CCSM-Utr (Baatsen et al., 2022) and HadCM3 (Hunter et al., 2019). We calculate bias-corrected, down-scaled temperature and precipitation fields to drive pyPDD. Ocean temperature and salinity fields are used for calculating bias-corrected, down-scaled thermal forcing to drive the ISMIP6 non-local ice shelf basal melt parameterisation (Jourdain et al., 2020).

For temperature and precipitation, we add the Pliocene minus Control anomaly to the baseline modern climate, as in Section 3.3.5. For ocean thermal forcing, we add the Pliocene minus Control anomaly to the observation-based modern thermal forcing, as in Section 4.2.3.

### 5.2.5 Ensemble Design

#### Control simulation

In order to compare our Pliocene perturbation simulations ($Plio_{modern}$ and $Plio_{PRISM}$) to a single control, we run a control simulation designed to capture the trajectory of an unperturbed AIS. For this control simulation, we use inverted Weertman friction coefficients as in Cornford et al. (2016, 2015) and Chapter 2 in order to maintain ice velocity fields close to modern. The control simulation is forced with modern climate as described in Section 5.2.4. We use surface mass balance parameters at the centre of their sampled ranges: -4x$10^{-4}$ for LRP and 14 mm w.e. $d^{-1}$ for *PDDi*. For basal melt sensitivity ($\gamma_0$), we use $MeanAnt_{50}$ in order to capture an average modern-like basal melt regime.

#### $Plio_{modern}$ ensemble design

For the main 120 member Pliocene Ensemble, parameters are varied in a Latin Hypercube design that maximises the minimum distance between design points (Fig. 5.3). A Latin Hypercube design was also used for the Pliocene ice sheet perturbed parameter ensemble by Yan et al. (2016); it is a much more efficient method of sampling the parameter space than a full factorial design (DeConto and Pollard, 2016, DeConto et al., 2021).

A total of 5 model parameters were varied, along with four forcing models. Our parameter ranges are the same as those used in previous simulations – *UMV* is varied between 6x$10^{17}$Pa s and 1x$10^{21}$Pa s (Chapter 3); *PDDi* between 8 mm w.e. $d^{-1}$ °C to 20 mm w.e. $d^{-1}$ °C; *LRP* between 0 and -8x$10^{-4}$ (Chapter 4); and basal melt sensitivity ($\gamma_0$, or gamma0) takes the 6 values provided for ISMIP6 (Chapter 2). The climate models are divided evenly across the ensemble, with 30 simulations for each GCM. Remaining surface mass balance parameters are kept at their default values: $PDD_s$ is constant at 4 mm w.e. $d^{-1}$ °C, temperature lapse rate (*LRT*) is -7°C$km^{-1}$. Lower mantle viscosity is constant at 5x$10^{21}$ Pa s. Maximum till water depth is constant at 2 m.

| Parameter | Abbreviation | Min | Max | Section |
|---|---|---|---|---|
| Weertman friction coefficient | *C* | 7,600 | 62,000 | 3.2.3 |
| Upper mantle viscosity | *UMV* | 6x$10^{17}$Pa s | 1x$10^{21}$Pa s | 3.2.2 |
| Lapse rate precipitation | *LRP* | 0 | -8x$10^{-4}$ | 3.3.5 |

| Parameter | Abbreviation | Min | Max | Section |
|---|---|---|---|---|
| Positive degree day factor ice | *PDDi* | 8 mm w.e. $d^{-1}$ °C | 20 mm w.e. $d^{-1}$ °C | 3.2.4 |
| Ice shelf melt sensitivity | $\gamma_0$ | 9,620 m $yr^{-1}$ | 471,000 m $yr^{-1}$ | 2.2.2 |

Table 5.2 Perturbed parameter names, abbreviations, ranges and section for reference.

### $\mathbf{Plio_{PRISM}}$ ensemble design

Our selection of a subset of ensemble members aims to compare a sample of simulations initialised from the PRISM ice sheet with simulations initialised from BedMachine, under the same boundary conditions and model parameter values. We select a subset of 30 simulations, based on sea level contribution of $Plio_{modern}$ after 5,000 years. We select candidate members from our main ensemble by requiring that their Pliocene simulations show a reasonable initial ice flow speed in the interior (Section 5.6.1). Our aim here was to prioritise ensemble members from our main ensemble to run, assuming that the rapid ice speeds seen in the lowest Weertman friction coefficient simulations would produce an overly thin ice sheet. The sub-sampling leaves 80 ensemble members from $Plio_{modern}$, from which we select those with the 10 highest Pliocene sea level contributions after 5,000 years, the 10 lowest contributions and 10 intermediate values. This leaves 30 parameter combinations from our original ensemble. Each PRISM initialised simulation is run for 10,000 years.

### $\mathbf{Control_{modern}}$ ensemble design

The same ensemble members were run for the control ensemble as in the PRISM-initialised ensemble. The 30 ensemble members each completed 5,000 simulation years. Whilst model parameters can drive large variability under mPWP climates (e.g Yan et al. 2016), we might expect a limited range of sea level contributions over this 5,000 year simulation period, given the use of modern climate forcing. Conversely, large sea level changes could indicate overly large model parameter ranges.

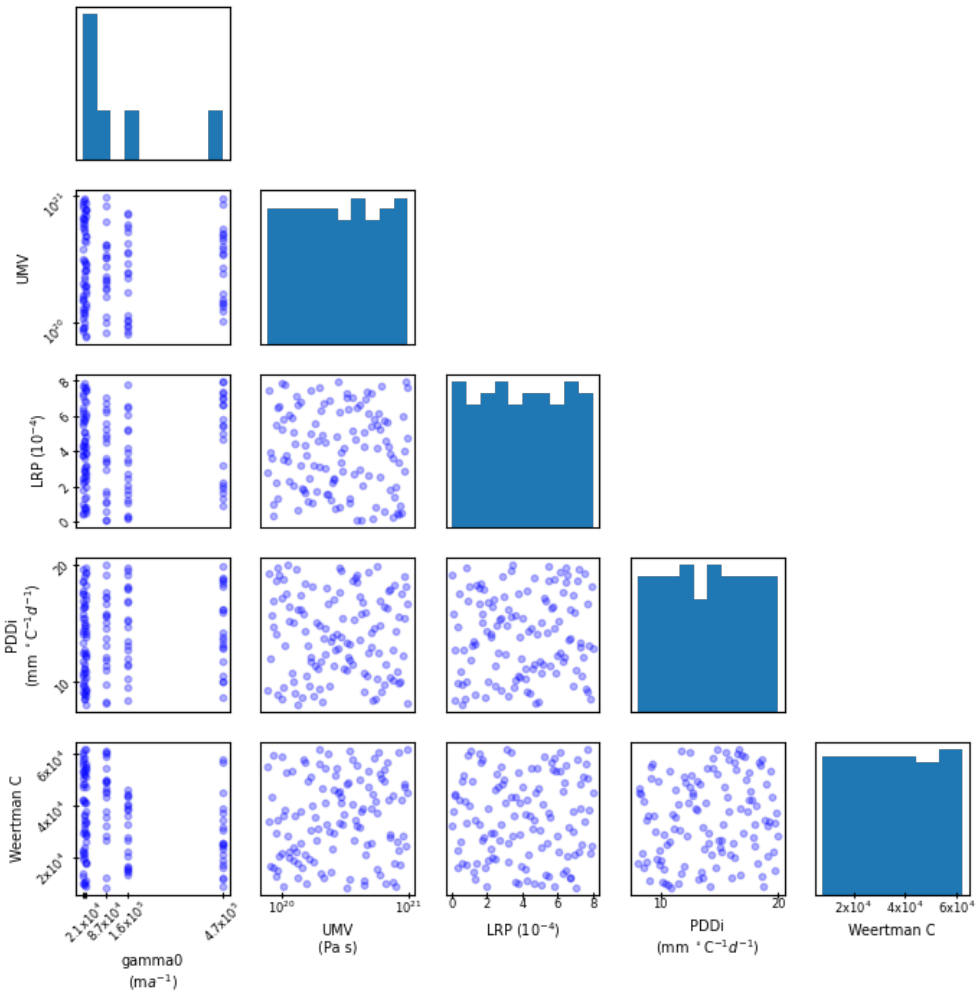


Fig. 5.3 $Plio_{modern}$ perturbed parameter ensemble design, with 5 parameters (and GCM, not shown) perturbed in a 120 member Latin Hypercube. See Table 5.2 for parameter details.

### 5.2.6 Pliocene reconstructions

We undertake comparisons with two reconstructions from palaeodata: Wilkes retreat - the retreat of the grounding line into the Wilkes subglacial basin, and reconstructed maximum sea level contribution from the Antarctic ice sheet during the warm Pliocene.

#### Wilkes retreat

We compare our Pliocene ensembles to reconstructed retreat of the grounded margin into the Wilkes subglacial basin (Section 1.4.2) based on Bertram et al. (2018) and Cook et al. (2013). A simple pass/ fail requirement is applied to the ensemble: simulations that retreat

into the Wilkes basin, which is indicated by the pink contour in Figure 5.12, are judged to have reproduced retreat consistent with evidence from palaeodata (Bertram et al., 2018, Cook et al., 2013)

#### Sea level

We also compare with a recent reconstruction of Pliocene sea level above modern (Grant and Naish, 2021). In a recent reassessment of available records, primarily based on the PlioSeaNZ record (Grant et al., 2019), Grant and Naish (2021) give a mPWP range of at least 4.1 m sea level above modern and no more than 20.7 m, with a median of 10.7 m (Grant and Naish, 2021). Of this range, a possible contribution from the Greenland ice sheet of up to its full modern sea level equivalent of 7.4 m (Morlighem et al. 2017), or a smaller contribution from Greenland and a contribution from mountain glaciers, is considered. Including 7.4 m contribution from Greenland and glaciers, the Grant and Naish (2021) range would imply an Antarctic contribution of -3.3 m to +13.3 m. Conversely, if we assume all Pliocene sea level is sourced from the Antarctic ice sheet, the range is that of Grant and Naish (2021). Combining these ranges, we can compare our main ensemble to a range of -3.3 m to +20.7 m Pliocene AIS contribution.

### 5.2.7 Calculating SLC

In simulations where bedrock is fixed, as in Chapter 4, sea level contribution is equal to change in ice sheet volume above floatation. However, isostatic adjustment of the bedrock changes ocean volume and should be accounted for in simulations of sea level in GIA-enabled models (Bamber et al., 2013, de Boer et al., 2015). We follow the method outlined in Goelzer et al. (2020a) to calculate sea level contribution accounting for: changes in ocean volume due to bedrock elevation changes in the model domain; volume above floatation; and density differences of ice, fresh water from ice melt and ocean water density.

## 5.3 Results

### 5.3.1 Control simulation

The control simulation loses mass under modern climate forcing, and equilibrates with a sea level contribution of 0.77 m SLE after around 2,000 years, of which 0.68 m SLE

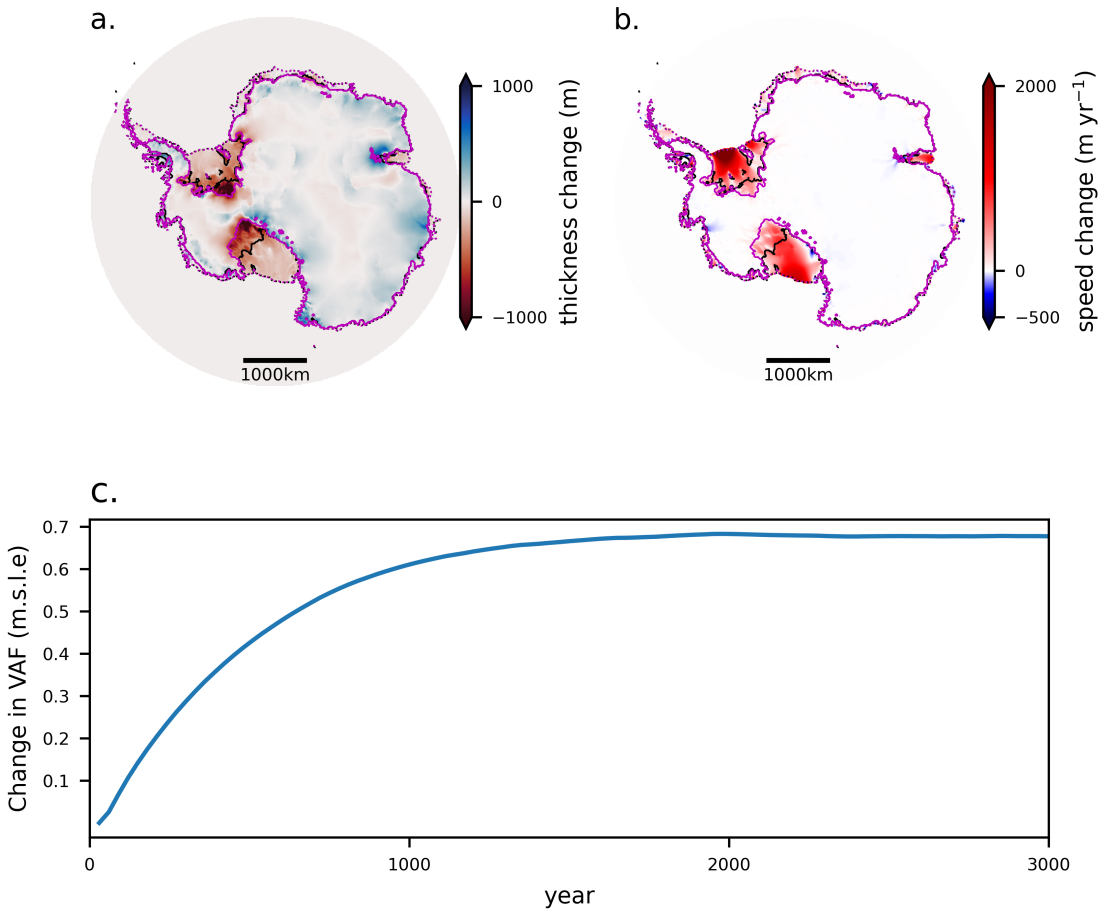


Fig. 5.4 Change in thickness from the start of control simulation to equilibrium (**a**), change in speed across the same period (**b**), change in volume above floatation (VAF) in metres sea level equivalent (**c**). Solid lines show the grounding line position at the start of the control simulation (black) and at equilibrium (pink), with dashed lines corresponding to the shelf edge position.

is accounted for by change in volume above floatation (Fig. 5.4). As it evolves to equilibrium, there is significant thinning up to ~1600 m along the Siple coast of the Ross shelf, coincident with retreat of the grounding line up to ~350 km from its initial, present day position. Similarly, along the Queen Elizabeth Land coast in the vicinity of the Filchner-Ronne ice shelf, grounding line retreat of up to ~300 km occurs alongside thinning of up to ~1100 m. At the base of the Antarctic Peninsula, south of Palmer Land, grounding line retreat of up to ~200 km is seen, with less extensive retreat southwards near the Ellsworth mountains. Tributary glaciers on the Eastern margin of the Filchner-Ronne ice shelf retreat by up to ~130 km. In all cases, surface lowering accompanies loss of grounded area in the WAIS catchments of ice streams feeding the Ross and Filchner-Ronne ice shelves (Fig. 5.4). Across higher regions of the WAIS, such as Marie-Byrd land,

the Peninsula and the summit of WAIS, the ice sheet thickens as the simulation reaches an equilibrium. Speed increases in WAIS ice shelf tributary glaciers, with the notable exception of the Thwaites glacier catchment, which slows over much of its area and by up to ~800 m $yr^{-1}$ at the edge of its shelf. We ascribe grounding line retreat along the margins of ice shelves to sustained ocean-driven melt, with low but positive surface mass balance too small to balance losses due to loss of grounded ice. Across the EAIS, the ice sheet thickens across broad regions of the continental interior, with the largest magnitude thickening, associated with grounding line advance of ~160 km at the Lambert glacier (up to ~1200 m). Slow down of an ice stream in the Queen Mary Land sector of the EAIS is associated with thickening of up to ~600 m.

### 5.3.2 $Plio_{modern}$

#### Sea level contribution after 10,000 years

We first present the results of the $Plio_{modern}$ ensemble relative to the default control simulation. Of the 120 initial ensemble members, the majority (n=110) complete 10,000 years of model simulation time (2 failed at < 4,000 years, 8 failed after). Relative to the control simulation contribution at equilibrium (i.e. after subtracting 0.77 m SLE), the largest contribution to sea level is 28.27 m SLE whilst the smallest is -15.89 m (sea level fall). Overall, mean sea level contribution across all 110 simulations is -1.85 m ± 9.28 m (SD) sea level fall, with a median contribution of 0.03m.

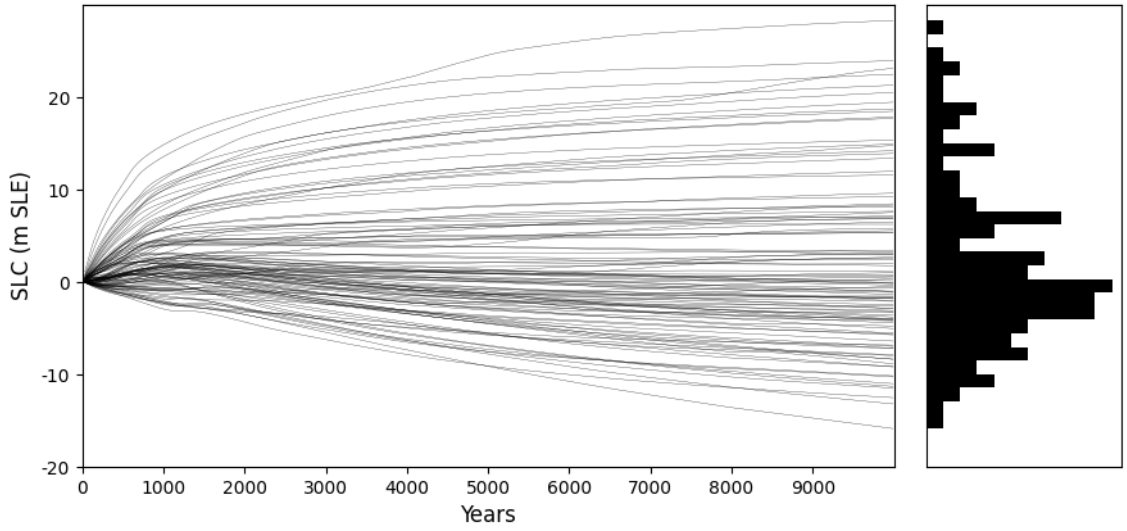


Fig. 5.5 Sea level contribution for all ensemble members over 10,000 years (n=110), relative to control (left), and values at 10,000 years (right).

Marine-based sectors of the West Antarctic ice sheet collapse in all ensemble members (Fig. 5.6) - with all ensemble members free of grounded ice (darkest blue regions = 0 in Fig. 5.6 **a**). The Marie Byrd Land dome remains glaciated in all ensemble members, and mountainous regions of the Antarctic Peninsula retain their ice cover (Fig. 5.6 **b**). Whilst most of the interior East Antarctic ice sheet retains grounded ice cover across the ensemble (whitest region = 1, Fig. 5.6**a**), values < 1 at the margins indicate retreat of some ensemble members. This is particularly the case for the Wilkes subglacial basin. The Totten glacier experiences grounding line retreat across a majority of ensemble members; however, retreat into the interior Aurora subglacial basin only occurs in < ~10 % of ensemble members. The Bailey, Slessor and Recovery ice stream undergo some retreat in all simulations, with the Recovery ice stream retreating the furthest up its trough.

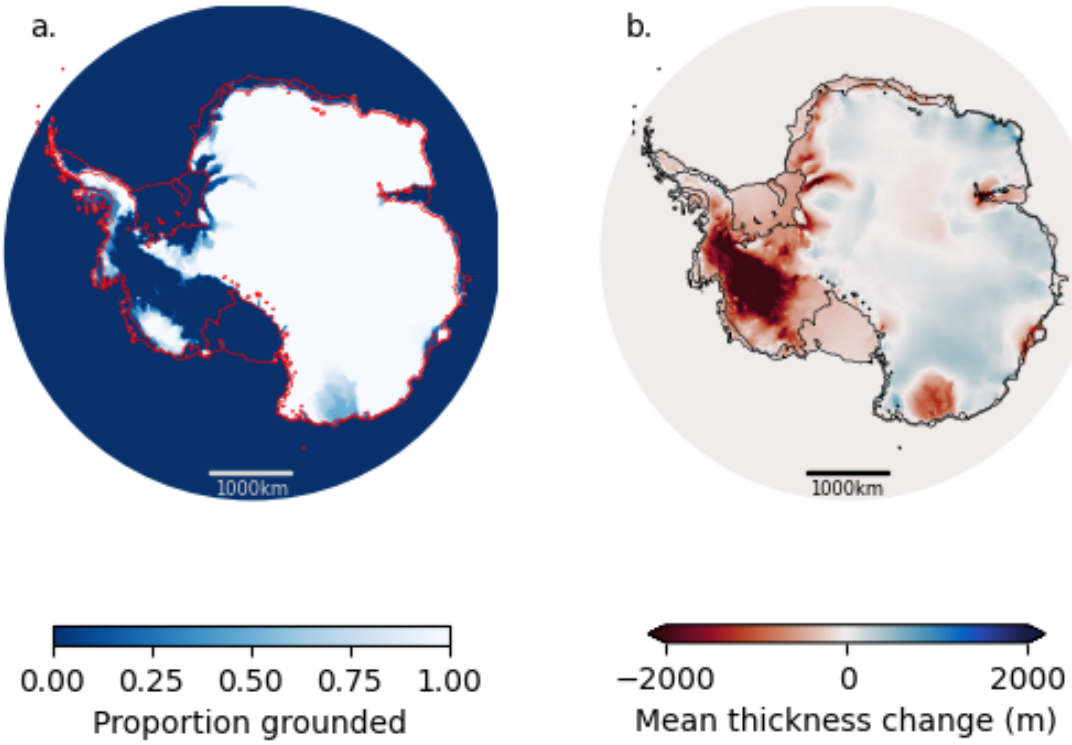


Fig. 5.6 (**a**) Fraction of ensemble members in which the ice sheet remains grounded at the year 10,000: the sum of grounded ice masks divided by the number of ensemble members. White grid regions (grounded fraction = 1) are where no ensemble members are ungrounded. Dark blue regions (grounded fraction = 0) are where all are ungrounded, and open ocean. The red contour indicates the initial, modern grounding line position. (**b**) Ensemble mean thickness change, relative to control.

Ensemble mean thickness change (Fig. 5.6 **b.**) shows the consistent pattern of WAIS collapse. This is contrasted by thickening across most regions of the EAIS, including the coastal region between Dronning Maud Land and Mac Robertson Land, and the interior of

Wilkes basin and Victoria Land. Tributary glaciers of the Filchner-Ronne ice shelf draining the EAIS, including Recovery, Slessor, Bailey and the Support Force glacier, undergo thinning and retreat in some ensemble members. The extent of inland thinning following retreat up deeply incised glacial troughs in the Recovery basin varies: some ensemble members lose contact with the bed and retreat upstream, others remain grounded closer to the present-day grounding line. The Aurora subglacial basin, drained by Totten glacier, undergoes substantial thinning.

Along the George V Coast, Figure 5.6 shows an average thinning of ice over the Wilkes subglacial basin. There is a large ensemble standard deviation for ice thickness and surface elevation in this region (Fig. 5.7). Considered alongside variations in patterns of ungrounding (Fig. 5.6 **a.**), the divergence in thickness change in the Wilkes subglacial basin makes this region a suitable target for model-data comparison to identify the most successful ensemble members (Section 5.3.2).

### Sensitivity to model parameters

We show the sensitivity of four summary outputs to the six uncertainties explored in the ensemble. The summary outputs are the 10,000 year sea level contribution, grounded ice sheet area, floating ice area, and $99^{th}$ percentile of thickness (Fig. 5.8). The six uncertainties are the five BISICLES parameters (Table 5.2) and Pliocene climate forcing. We summarise the climate forcing with Antarctic mean surface air temperature at the start of the simulation (table 5.3).

Weertman friction coefficient ($C$) exerts a strong influence on sea level contribution and $99^{th}$ percentile thickening. Simulations with lower $C$ export more ice from the interior of the ice sheet to its margin, driving larger sea level contribution and thinner ice sheets. Conversely, where $C$ is high, ice sheet velocity is lower and ice accumulated in the interior is retained - driving a sea level fall. The strong relationship between Weertman friction coefficient and sea level contribution, compared with the influence of parameters controlling climate, reflects the dominance of basal sliding in controlling ice sheet geometry. The dependence of volume on climate forcing (ocean temperature, surface mass balance) that we might expect to see, and that we found in chapter 4 is less strong.

Compared with the Weertman friction coefficient, other parameters have a less systematic effect on sea level contribution. However, climate model choice has a discernible impact on ice sheet grounded and floating area, with the warmer models leading to smaller floating and grounded area. Increasing the basal melt sensitivity parameter ($\gamma_0$) drives a reduction in floating ice sheet area. Across the ensemble, simulations are more likely to have low

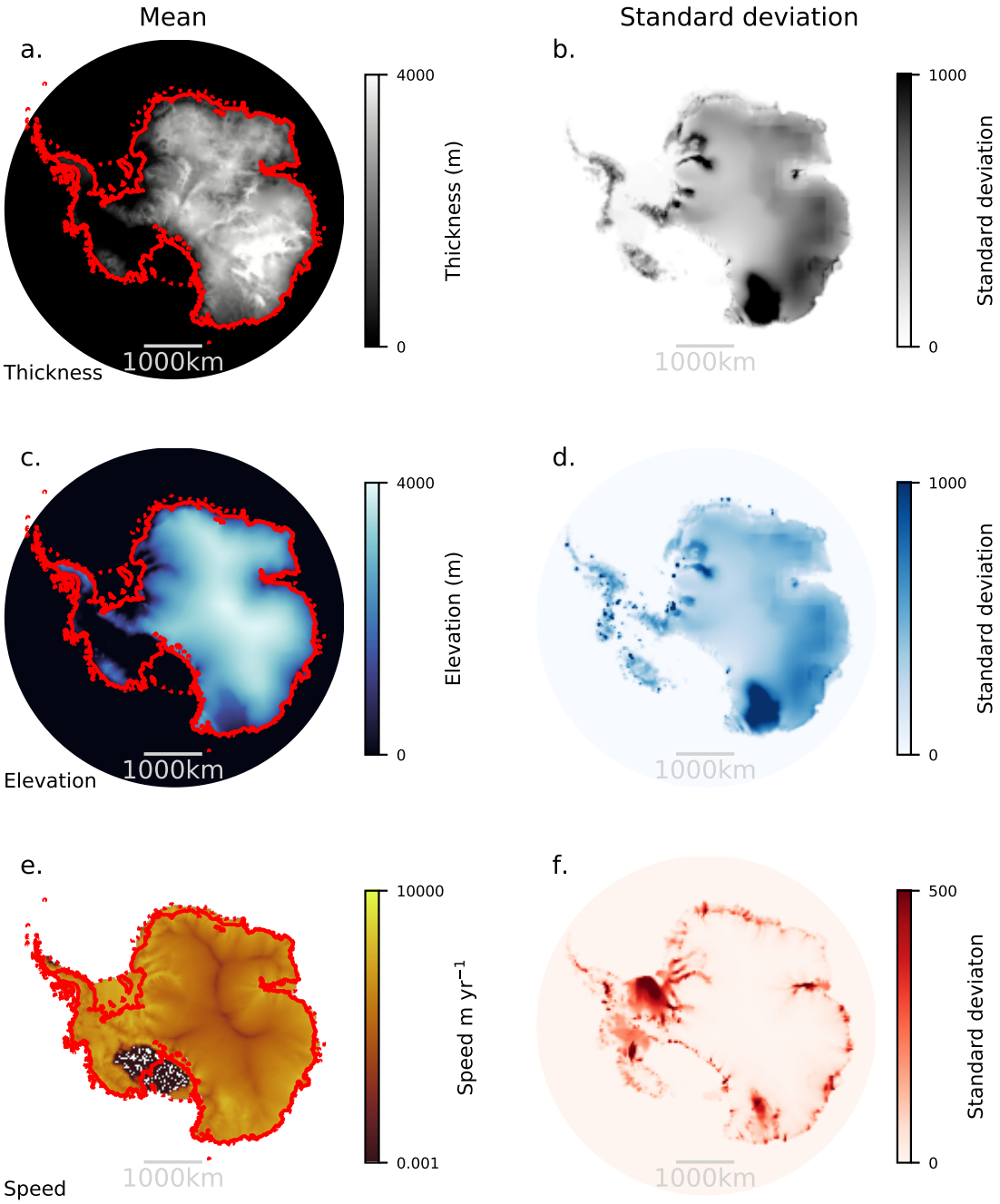


Fig. 5.7 Mean thickness (**a.**), elevation (**c.**) and speed (**e.**) for all 110 ensemble members that completed the full 10,000 year simulation period. Also shown is standard deviation across the ensemble for each field (thickness **b.**, elevation **d.**), speed **f.**).

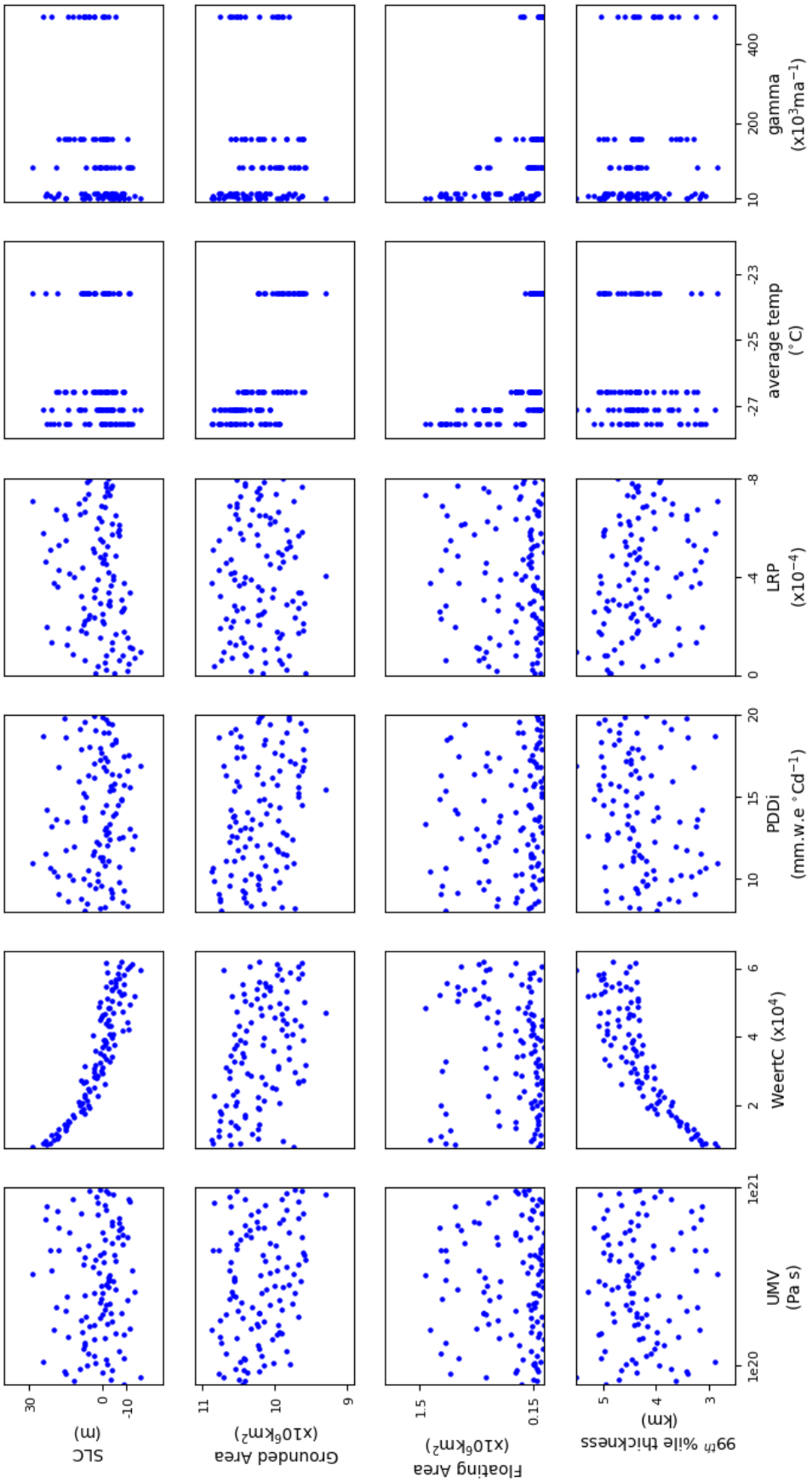


Fig. 5.8 Sensitivity of sea level contribution, grounded ice sheet area, floating ice sheet area, and $99^{th}$ percentile of thickness to uncertain inputs: Upper mantle viscosity (*UMV*), Weertman friction coefficient (*C*), Positive degree day factor for ice (*PDDi*), Precipitation lapse rate (*LRP*), GCM expressed through mean Antarctic air temperature at modern elevation (average temp) and basal melt sensitivity (%).

values of floating area, showing the strong combined effect of climate forcing and basal melt sensitivity on ice shelf area. In some simulations, this results in virtual collapse of the ice shelf area. Although the Weertman friction coefficient predominantly controls volume and therefore sea level contribution, there is a weak positive correlation between basal melt sensitivity and sea level contribution. Precipitation scaling (*LRP*) is positively correlated with sea level contribution. The positive degree day factor for ice shows a slight negative correlation with grounded ice sheet area. Similarly, Upper mantle viscosity ($UMV$) and Weertman coefficient ($C$) are slightly negatively correlated with grounded area.

| PlioMIP GCM | Average Air Temperature ($^{\circ}C$) |
|---|---|
| CCSM4-Utr | -23.6 |
| COSMOS | -26.6 |
| HadCM3 | -27.1 |
| CCSM4-UofT | -27.6 |

Table 5.3 Average surface air temperature over Antarctica for each GCM, elevation corrected to initial ice sheet surface.

### Surface Mass Balance

As discussed in section 5.3.2, sea level contribution is determined primarily by Weertman friction coefficient rather than climate forcing. However, choice of GCM determines where the ice sheet undergoes retreat. In order to explore the role of GCM choice in surface mass balance (SMB), we can compare SMB across simulations forced with each PlioMIP2 climate model. Figure 5.9 shows average SMB for simulations forced with each GCM, in the $Plio_{modern}$ ensemble, for four time snapshots. These snapshots correspond to: the start of the simulation (10 years); the initial retreat phase (210 years); after a millennium of Pliocene forcing (1,020 years); and as the simulations approach equilibrium, having lost the majority of grounded ice in WAIS (5,020 years). Highest accumulation is seen at the margins of the EAIS and over higher elevation regions of WAIS at the start of the simulation period, with a low accumulation over the high EAIS interior (Fig. 5.9), as in the modern. For CCSM-Utr and CCSM4-UofT, a region of high SMB also overlies the Wilkes subglacial basin and the Totten glacier catchment (Fig. 5.9). As outlined in previous work (Chapter 4), this region is deglaciated in PlioMIP2 climate simulations - with elevated precipitation compared with cooler, higher regions of the ice sheet. Averaging across simulations with a range of precipitation lapse rate corrections (*LRP*), with the low end of the LRP range at 0 (LRP off), high precipitation in this region drives elevated surface mass balance.

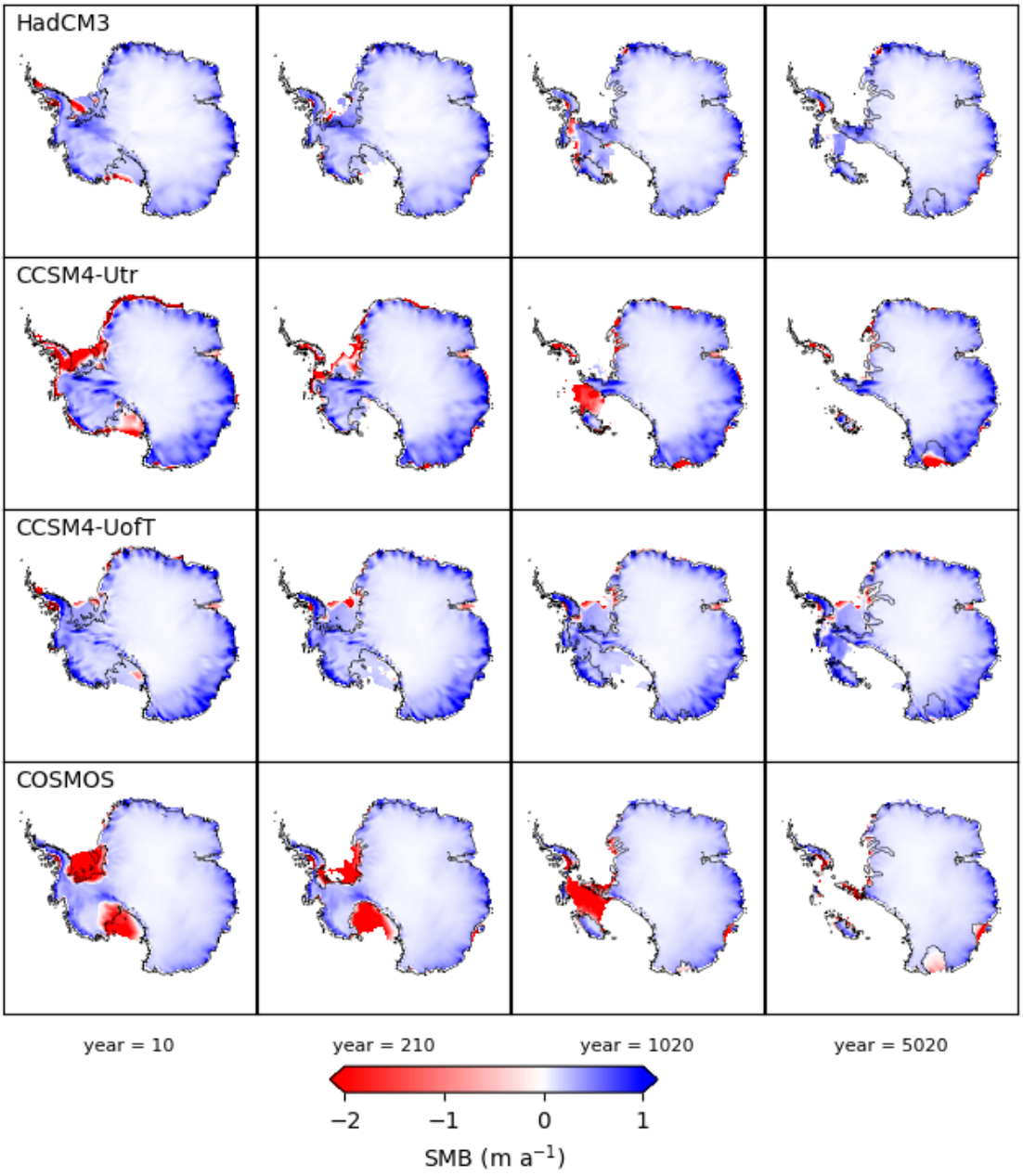


Fig. 5.9 Snapshots of surface mass balance for $Plio_{modern}$ simulations, averaged across ensemble members forced with each climate model, at three time snapshots - 10, 210, 1,020 and 5,020 years. Fields are masked over regions that are open ocean in all simulations, for each climate model. Black contours bound regions where all simulations forced with each climate model are grounded.

Across all simulations and time snapshots, ablation (negative SMB) is generally restricted to ice shelves and the margins of the ice sheet, with the high interior EAIS too cold for surface melting to occur (Fig. 5.9). An exception to this is the Antarctic Peninsula under CCSM4-Utr climate, which experiences more extensive ablation than other GCMs for all time snap shots - reflecting positive temperatures over much of this region when corrected to modern initial elevation (Fig. 4.3). With surface melt coupled to elevation change through the temperature lapse rate correction, SMB reflects temperature and precipitation, as well as elevation changes. Elevation is influenced by surface lowering through increased discharge and ocean melt, and feedbacks with SMB. Comparing SMB fields at the start of the simulation period, with the least divergence of ice sheet elevation from the initial condition, reflects variability in SMB due to precipitation and temperature with a limited influence from elevation changes. At year 10, ablation is most extensive over ice shelves (Fig. 5.9). COSMOS simulates strong surface melting over the Ross and Filchner-Ronne ice shelves, and over grounded ice regions feeding each shelf (Fig. 5.9). These regions of surface melt promote grounded ice retreat, with the contour showing the grounded ice area in all simulations at year 210 (Fig. 5.9), coinciding with the edge of the surface melt region at year 10. Ocean melt-driven thinning of ice shelves reduces buttressing in tributary glaciers, alongside SMB-driven surface melting of grounded ice. This drives surface lowering and further melt, such that ice thins to floatation or melts completely. Similarly, strong surface ablation over grounded ice, in the Southern Antarctic Peninsula for CCSM4-Utr at year 10, is associated with loss of grounded ice to year 210 (Fig. 5.9). More extensive shelf collapse (masked white regions in Fig. 5.9 indicate open ocean in all ensemble members) is seen for CCSM4-Utr than COSMOS in regions with surface melt - consistent with higher thermal forcing in CCSM4-Utr (Fig. 4.2) driving faster shelf loss.

A feature of average CCSM4-Utr SMB at year 10 is strong ablation around the periphery of the EAIS - particularly around the coast of Dronning Maud Land, and at margins of George V Land (Fig. 5.9). Surface melt at George V Land, overlying the Wilkes subglacial basin, initiates thinning and grounding line retreat at outlet glaciers in the region. Over the simulation period, CCSM4-Utr has stronger and more extensive negative surface mass balance over the Wilkes basin compared with simulations forced with other PlioMIP2 GCMs. This reflects both higher surface temperatures compared with other GCMs, and elevation-SMB feedbacks - such that CCSM4-Utr warming drives retreat in the Wilkes basin for more ensemble members, and more ensemble members have lower surface elevation and greater melting, compared with other climate models. The role of boundary condition model in Wilkes basin retreat is discussed further in Section 5.4.3.

### Comparison to Pliocene sea level reconstructions

We compare 10,000 year sea level contribution to the reconstructed mPWP sea level range, adjusted for contributions from Greenland and glaciers as described in section 5.2.6. Our range of sea level contributions for the full ensemble (-15.89 to 28.7 m SLE; Fig. 5.5) are larger than the reconstructed Pliocene range (-3.3 to 20.7 m SLE). Out of 110 simulations that completed 10,000 simulation years, 39 fall outside the Pliocene range. For simulations that fall within the Pliocene sea level range (n=71) the mean sea level contribution is 4.76 ± 6.31 m. Figure 5.10 shows the histogram of projected sea level contribution for these ensemble members, as well as the upper and lower bounds of the Pliocene sea level range.

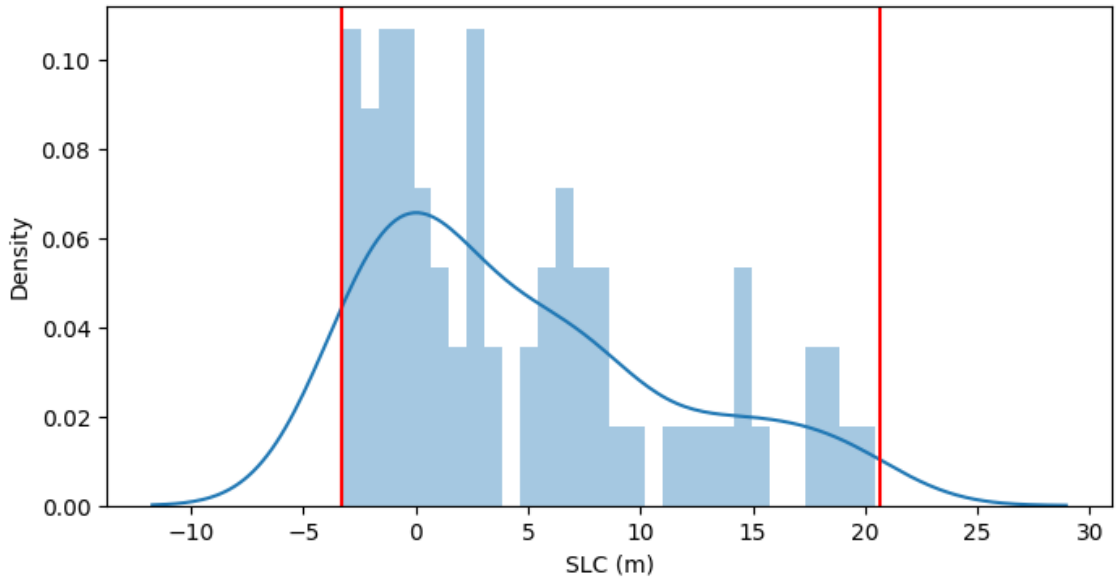


Fig. 5.10 Histogram and density estimate of Pliocene sea level contribution at 10,000 years for ensemble members that have a sea level contribution within the estimated range (red vertical lines). See text for detail.

Figure 5.11 shows sensitivity analysis of Figure 5.8 again, this time dividing ensemble members that fall within the reconstructed sea level range (blue markers) from those that do not (grey markers). Red lines indicate the bounds of the sea level range. Whilst the Pliocene sea level comparison predominantly favours lower Weertman friction coefficient runs, it does not definitively rule out high values, due to the wide range of contributions arising from parameter interactions, where other parameters increase mass loss. The very lowest values are ruled out in this ensemble.

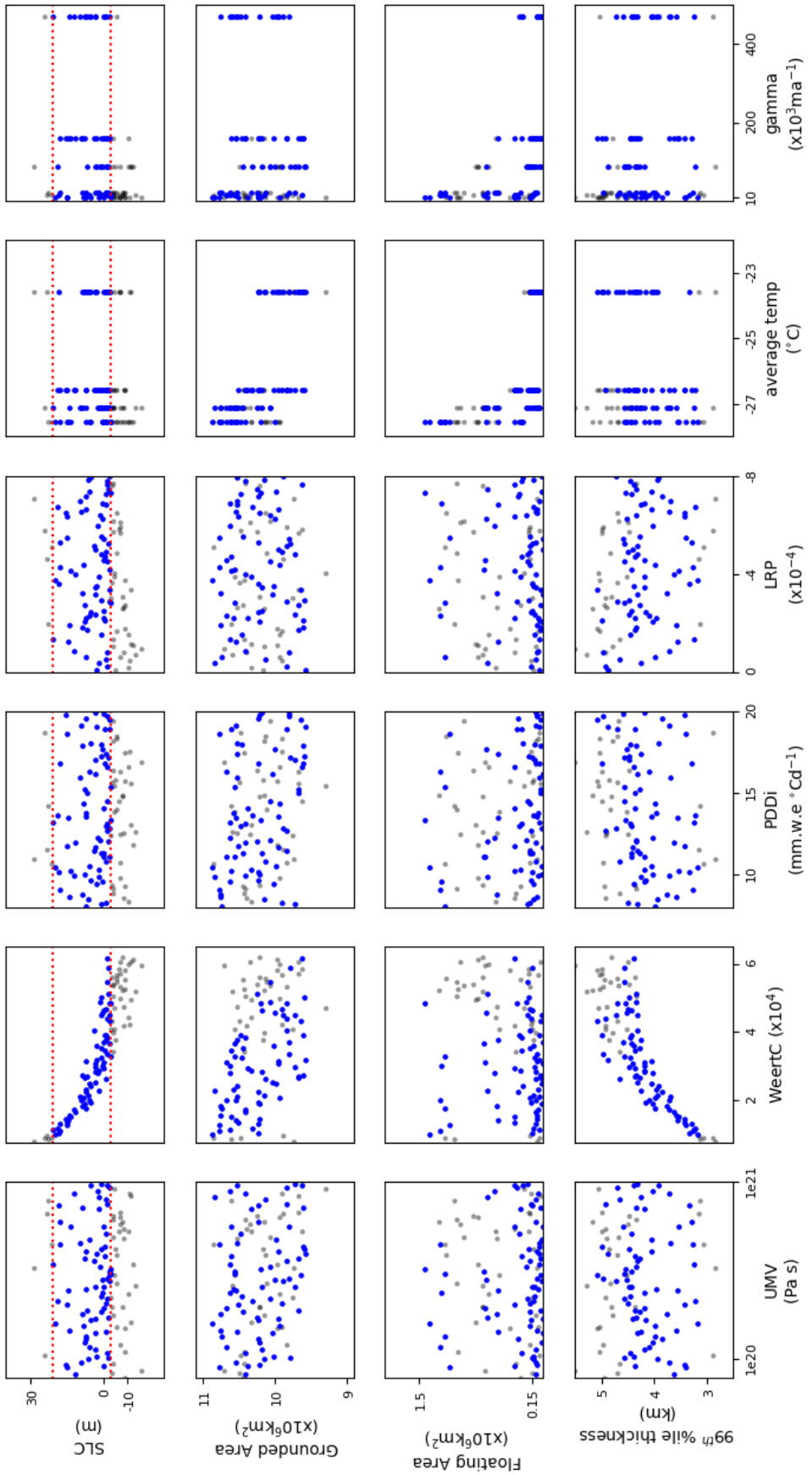


Fig. 5.11 Sensitivity of sea level contribution, area changes (floating and grounded), as for Fig. 5.8, but with blue circles indicating simulations that have a sea level contribution falling within the range (Section 5.2.6). Red lines show the bounds of this range.

### Wilkes basin grounding line retreat

To identify ensemble members compatible with Wilkes basin retreat, we examine grounded area retreat in this catchment. We use area change in the Cook glacier catchment (Fig. 5.12, red contour), and grounding line position within the boundaries of the central Wilkes subglacial basin (marked as "CB" in Fig. 1.4; pink contour in 5.12). As our first constraint we exclude those that do not retreat into the basin. The pink contour bounded region in Fig. 5.12 also includes the neighbouring Ninnis catchment. No simulation retreats into the Ninnis basin without also retreating into the Wilkes basin. For two simulations, grounding line only retreats just inside the Cook catchment, with very small changes in grounded area: we allow these to pass the data constraint.

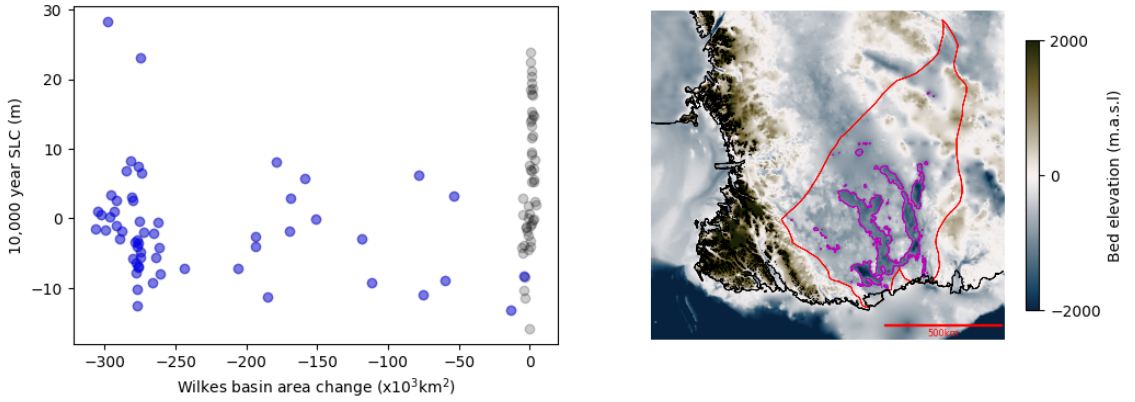


Fig. 5.12 Sea level contribution as a function of area Change ( **a.**) within the region bounded by the red contour in subplot **b**. Blue circles show ensemble members that undergo retreat into the Wilkes subglacial basin (pink contour in **b**). Grey circles are ensemble members that do not undergo retreat into the Wilkes basin.

Figure 5.12 shows the relationship between sea level contribution after 10,000 years and Wilkes grounded area retreat. The two are uncorrelated: in other words, retreat into the Wilkes subglacial basin is not associated with large sea level contributions from the ice sheet. Some ensemble members show no retreat into Wilkes (grey dots: Figure 5.12) but sea level contribution greater than 10 m; some show substantial retreat (blue dots), but negative sea level contributions. In fact, all but two of the ensemble members that retreat into the Wilkes basin have sea level contributions of less than 10 m. Decoupling of ice sheet area and volume in our ensemble results reflects the competing influences of Weertman sliding and surface mass balance, and is explored further in the discussion section.

Where retreat occurs into the Wilkes basin, but sea level contribution is small or negative, this is the result of compensatory EAIS thickening. Figure 5.13 shows a subset of ensemble

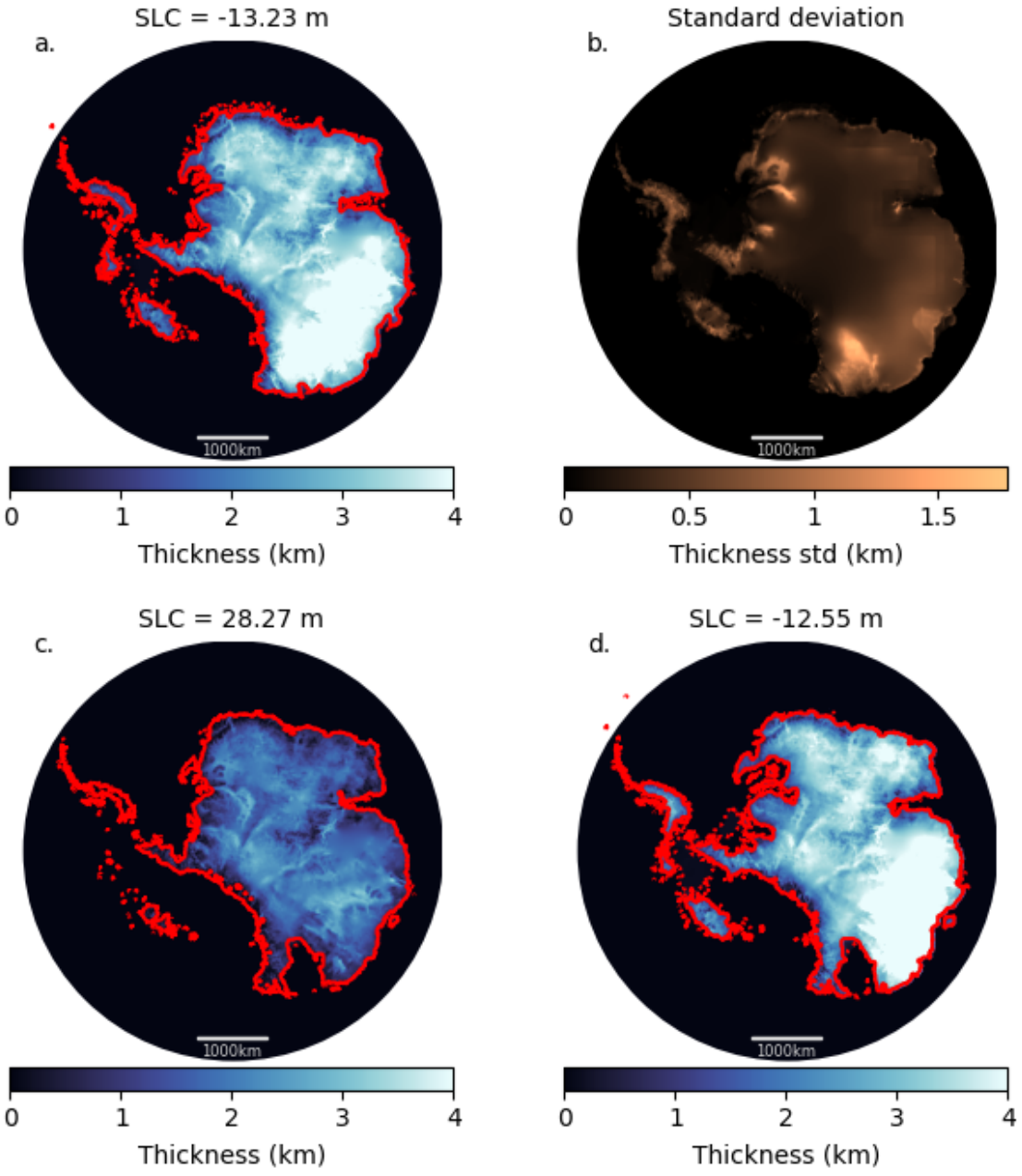


Fig. 5.13 The smallest SLC (sea level fall)(**a**), and largest SLC (**c**) thickness for simulations that retreat into the Wilkes basin, as well as standard deviation for all ensemble members that undergo retreat into the Wilkes basin (**b.**). Also shown is an ensemble which undergoes retreat into the Wilkes basin, but undergoes thickening that compensates for mass loss, driving an overall sea level fall of 12.56 m SLE. Solid red line in (**a., c., d.** is grounding line position, dotted line indicates the shelf edge. All plots are at 10,000 years.

members that pass the Wilkes basin comparison, including the ensemble member that drives the largest sea level fall (**a.**) and the ensemble member that drives the largest sea level rise (**c.**). The largest sea level fall ensemble member undergoes grounding line retreat of < 100 km into the outer Wilkes basin, and maintains large thickness over the Wilkes Land coast - driving a sea level contribution of -13.23 m. Some ensemble members undergo significant retreat into the Wilkes basin, but still maintain large enough thickness in other regions of EAIS to drive sea level fall. This is illustrated in Figure 5.13 **d.**, which has grounding line retreat of ~800 km into the Wilkes basin, but has mass loss here offset by thick ice along the Wilkes Land coast and into the interior. It drives a sea level fall of 12.56 m. Conversely, the largest sea level contribution simulation with retreat into the Wilkes basin has grounding line retreat of up to ~800 km inland. It is the largest sea level contribution simulation across the ensemble at 28.27 m. The average sea level contribution of simulations that retreat into the Wilkes basin (n=58) is -1.53 m.

Figure 5.14 shows the grounded fraction and ensemble mean thickness only for simulations that do not retreat into the Wilkes basin, but do contribute to sea level rise. These generally show widespread thinning across the EAIS, with the only region of thickening in the Wilkes basin itself. Simulations with large sea level contributions that do not undergo retreat into the Wilkes basin, predominantly at the lower end of the Weertman coefficient range (Fig. 5.15: discussed below), typically undergo widespread thinning across the EAIS without concomitant retreat into the Wilkes basin as illustrated in Fig. 5.14. This indicates that large sea level contributions in these simulations are not the result of collapse in basins other than the Wilkes, but are due to widespread thinning.

Figure 5.15 shows the sensitivity analysis of Figure 5.8 again, this time dividing ensemble members into those that undergo retreat into the Wilkes basin (blue) and those that do not (grey). With the exception of two of the simulations with the largest sea level contribution, grounding line retreat into the Wilkes basin only occurs in ensemble members with Weertman friction coefficient > $2 \times 10^4$, i.e. this data constraint suggests lower values are implausible.

The relationship with climate model mean Antarctic surface air temperature shows that more simulations forced with the warmest model (CCSM4-Utr) undergo retreat into the Wilkes subglacial basin than for the others.

To summarise: 71 of the 110 ensemble members pass the sea level constraint, and 58 pass the Wilkes basin retreat constraint. Combining the two, 38 ensemble members pass both constraints. The mean sea level contribution for these 38 simulations is 1.46 ± 3.64 m. The range is from -3.11 m to 8.29 m, i.e. corresponding to the lower half of the reconstructed sea level range.

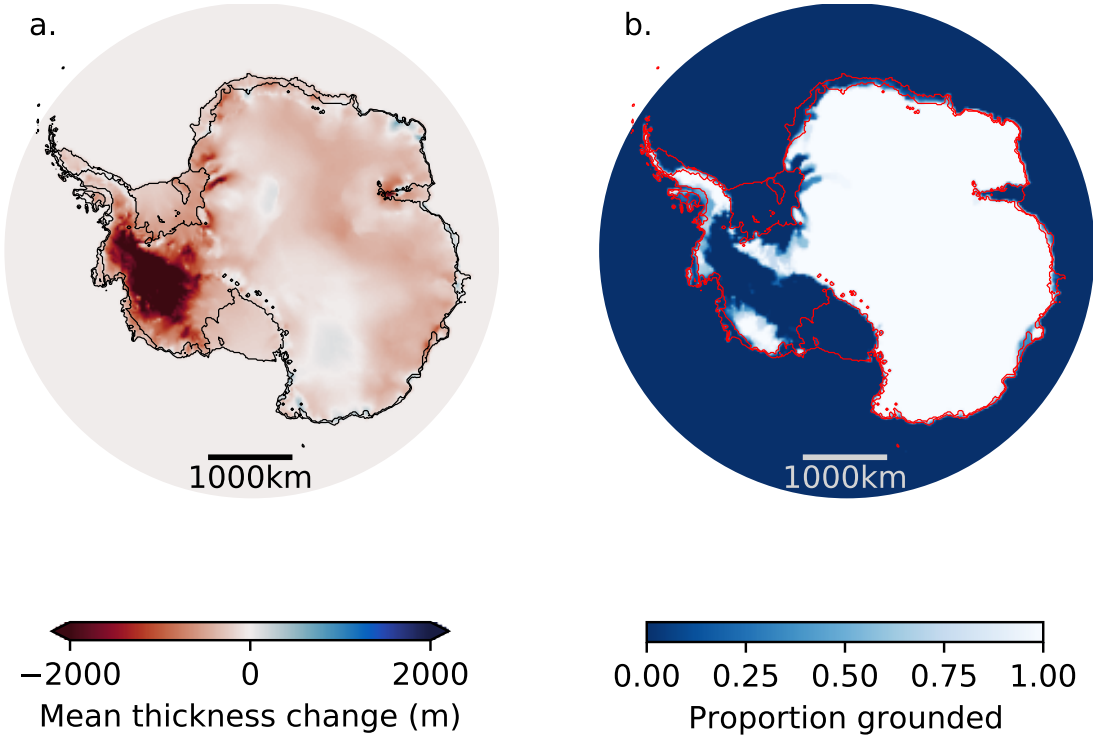


Fig. 5.14 Average thickness change for simulations that do not undergo retreat into Wilkes consistent with geochemical provenance studies (Cook et al. 2013, Bertram et al. 2018, Section 5.2.6), but do contribute to sea level rise (**a.**). Proportion of simulations that remain grounded across the domain (**b.**).

### 5.3.3 $\text{Control}_{\text{modern}}$ Ensemble

The $Control_{modern}$ ensemble explores the influence of parameters on the long-term ice sheet response to modern climate. In total, 29 of 30 ensemble members reached 5,000 simulation years. Some simulations ran for longer, up to 10,000 years.

During the 5,000 years (Fig. 5.16), some control simulations undergo significant mass gain: up to -11.30 m SLE. Moreover, these are on a trajectory of continued mass gain at 5,000 years. Fewer control simulations (n=7) show mass loss (maximum SLC = 2.40 m). The mean sea level contribution is -4.93 ± 4.65 m. The three modes of the histogram of sea level contributions in Figure 5.16 are likely the result of sampling high, medium and low members of the $Plio_{modern}$ ensemble (Section 5.2.5).

Figure 5.17 shows average fields for $Control_{modern}$ at 5,000 years. It shows ice thickness retained over East Antarctica, and persistence of marine grounded ice in the Amundsen Sea Embayment. Surface lowering coincides with grounding line retreat along the Siple coast, and around the grounding line of ice streams terminating in the Filchner-Ronne Ice

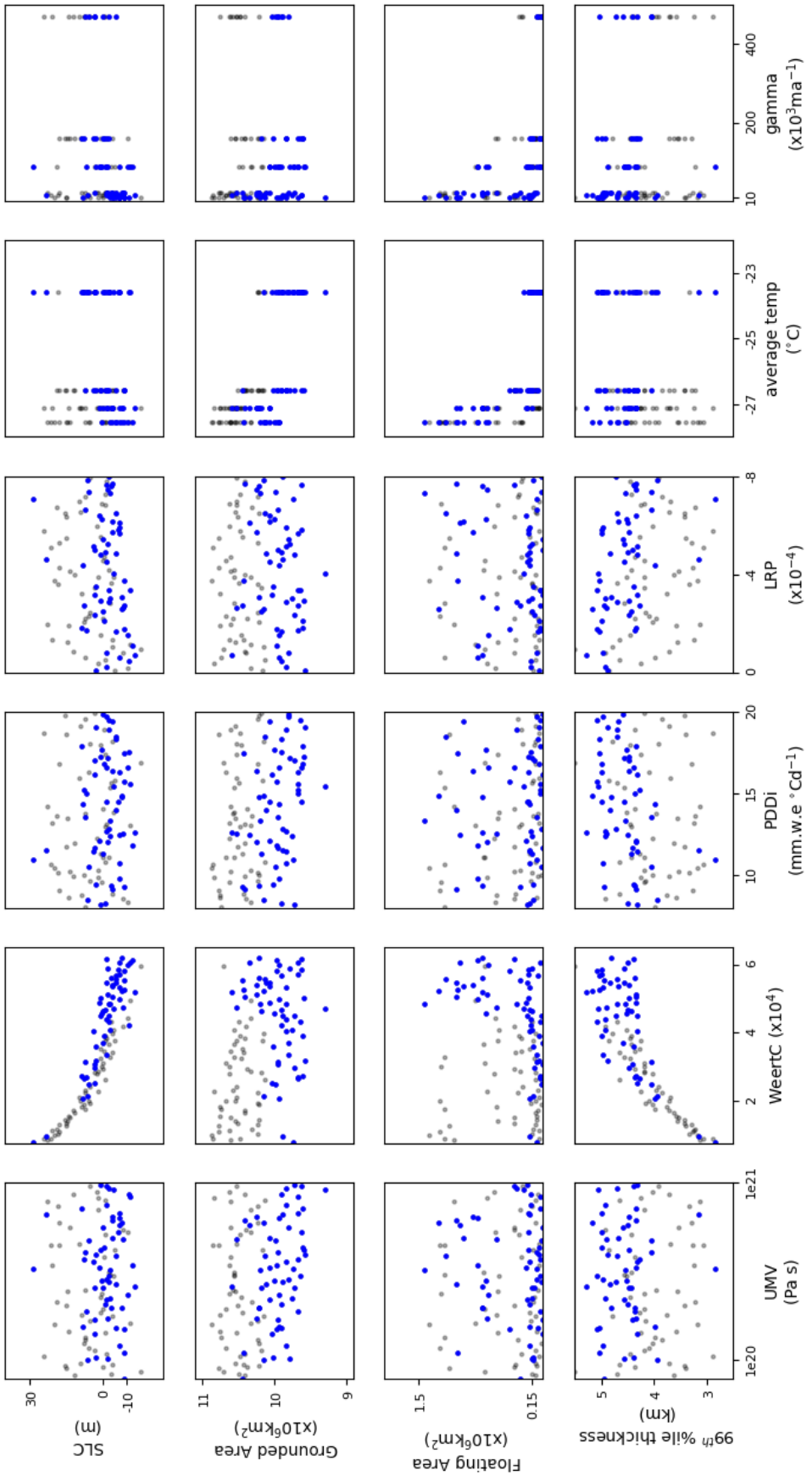


Fig. 5.15 Sensitivity of sea level contribution, area changes (floating and grounded) as in Fig. 5.8, with blue circles indicating simulations that undergo retreat into the Wilkes basin.

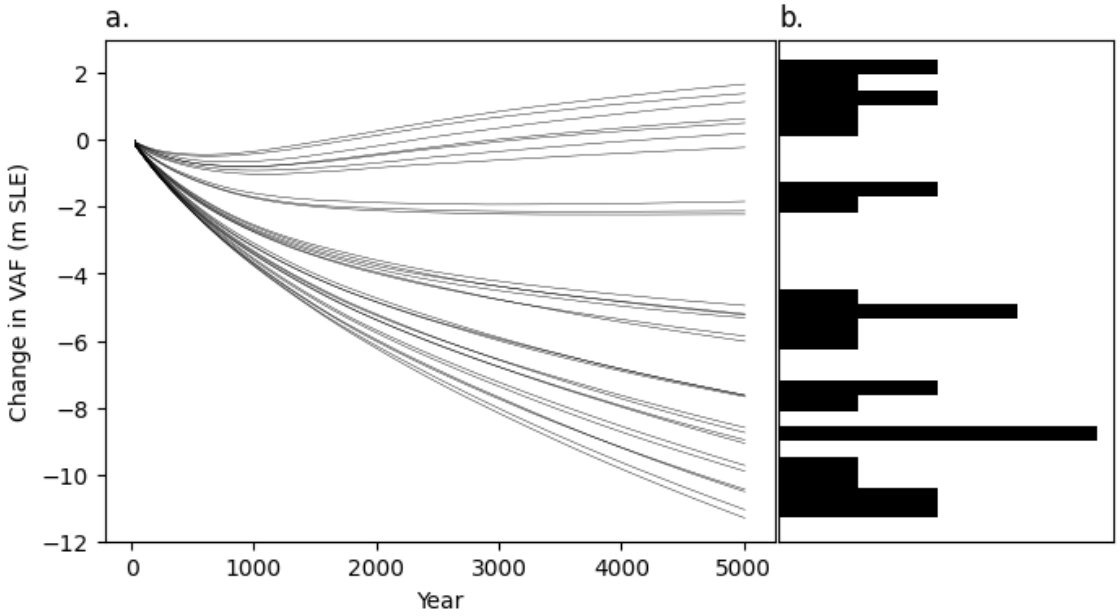


Fig. 5.16 Change in volume above floatation (**a.**) for the control simulation subset, neglecting sea level contribution from changes in bedrock volume, which average <7% of the overall sea level signal. The histogram of total sea level contribution relative to the main ensemble reference simulation is shown in (**b.**) for all control ensemble simulations.

shelf (Fig. 5.17 **c.**). Average ice speed is highest in ice shelves, with largest differences in ice speed at the shelf edges, indicated by high standard deviation. Thickening in the control ensemble is largest around the Amundsen Sea Embayment of West Antarctica, with thickening also seen around the margins of East Antarctica (Fig. 5.17). Standard deviation of ice thickness across the control ensemble (Fig. 5.17) shows that most variability is associated with regions of grounding line retreat along the Siple and Filchner-Ronne ice shelf margins. The regions of thickening around the margins of the EAIS also show relatively large variability.

Figure 5.18 compares thickness and speed in $Control_{modern}$ with equivalent modern observational fields. Compared with modern (Fig. 5.18) (Mouginot et al., 2019, Morlighem et al., 2020), ice streams are slower by more than 500m $a^{-1}$ in some regions. Regions of greatest slow down coincide with largest thickening compared with modern (Fig. 5.18), such as in the ASE and along the Wilkes Land coast.

The sensitivity of the control ensemble simulations to parameters is shown in Figure 5.19. All four variables show a very strong dependence on Weertman friction coefficient, with increasing values of $C$ leading to larger mass gains. High values of the basal melt parameter tend to lead to more mass loss, smaller floating ice area and a thinner ice sheet. This further

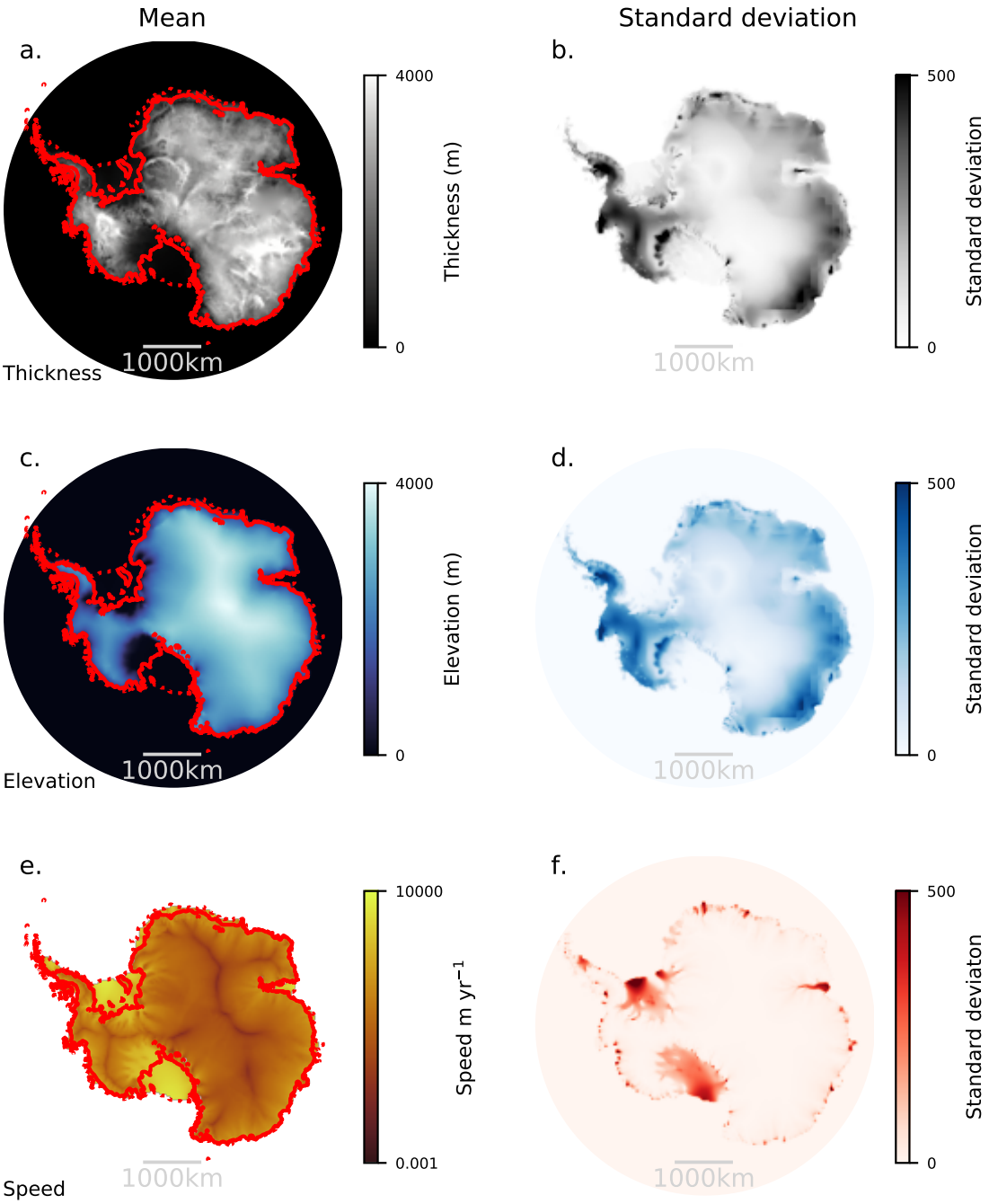


Fig. 5.17 Mean thickness (**a.**), surface elevation (**c.**) and speed (**c.**) for $Control_{modern}$ simulations. Also shown is the standard deviation for each field (**b.**: thickness, **d.**: surface elevation, **f.** speed.)

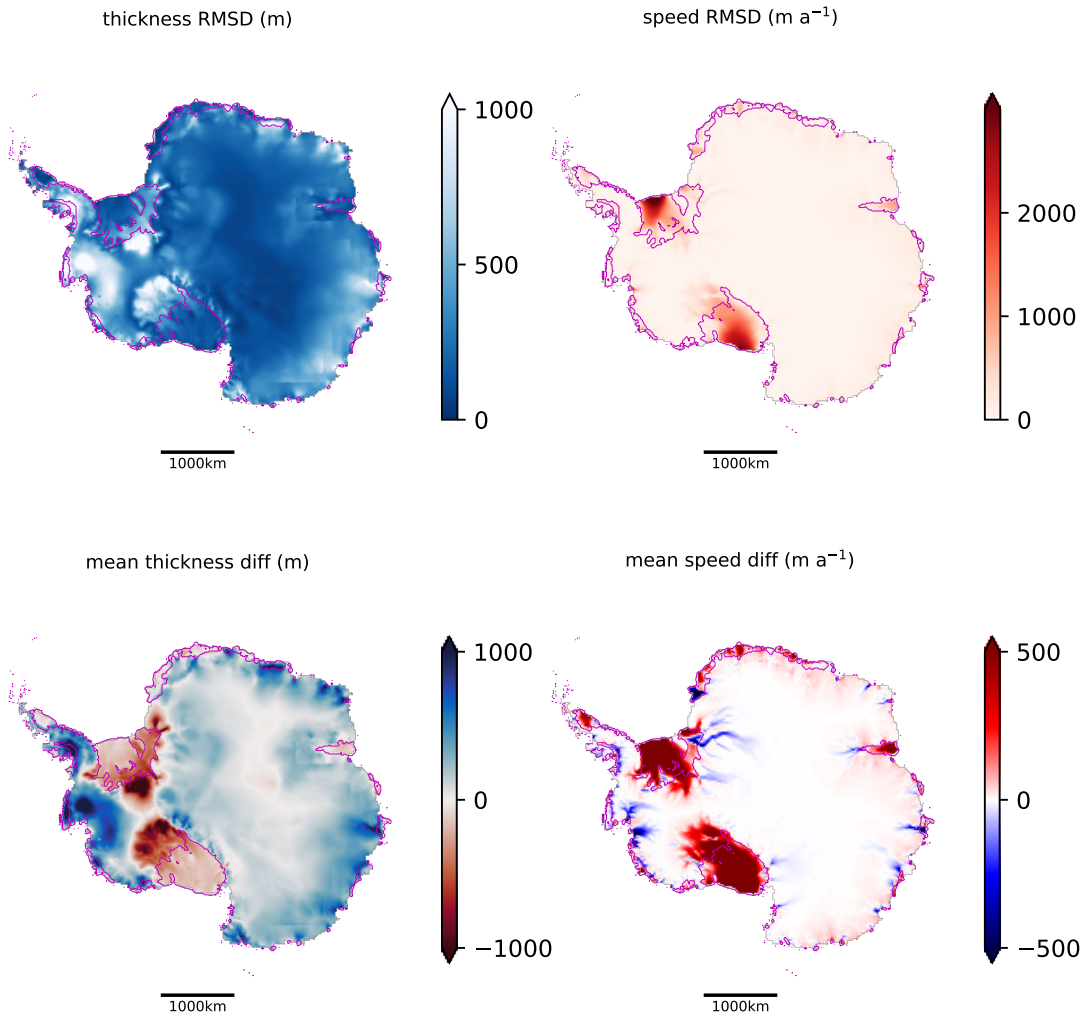


Fig. 5.18 Root mean squared deviation from modern ice sheet thickness from BedMachine (Morlighem et al., 2020) and average difference. Root mean square deviation from observations of modern velocity (Mouginot et al., 2019), as well as average difference.

demonstrates how simulations with less basal sliding and basal melting (high $C$, low $\gamma_0$) are more likely to gain mass overall, through accumulation.

#### Main Ensemble relative to Control

Here we show the impact of subtracting the perturbed ensemble of control simulations from each equivalent member of the $Plio_{modern}$ ensemble, rather than the default control simulation. We calculate this difference after 5,000 years, due to the shorter length of the control simulations; most of the $Plio_{modern}$ response has occurred during this period (Fig. 5.5, see also Table 5.4, discussed in Section 5.3.5). The sensitivity of the resulting $Plio_{modern}$ - $Control_{modern}$ ensemble sea level contributions to the parameters and climate model is shown in Figure 5.20. We find a mean Pliocene sea level contribution of 4.44 ± 2.19 m, and a range of 0.31 m to 8.41 m, compared with -0.90 ± 7.84 and a range of -9.16 to 8.23 m for the same subset of the $Plio_{modern}$ ensemble at 5,000 years, when subtracting the default control. The main impact is therefore to increase the lower end of the original range, such that most Pliocene sea level contributions are positive after 5,000 years, instead of being approximately equally divided between positive and negative contributions. This is because the ensemble members with large and negative Pliocene contributions show the same under the modern climate forcing, and when this is subtracted it gives a small net contribution. This can be seen in Figure 5.20, which shows $Plio_{modern}$ minus $Control_{modern}$, with blue circles showing sea level contribution for ensemble members that retreat into the Wilkes basin after 5,000 years in $Plio_{modern}$ and fall within the sea level constraint (red dahsed lines), and grey circles showing those that do not. The weaker dependence of sea level contribution ($Plio_{modern}$ - $Control_{modern}$) on the Weertman friction coefficient is indicative of differences driven by this parameter cancelling out across the two eras.

### 5.3.4 $Plio_{PRISM}$

As outlined in the previous section, we also undertake an initial assessment of the role of initial condition uncertainty in Antarctic ice sheet response to Pliocene climate, by running the same 30 ensemble members as in $Control_{modern}$ under Pliocene climate, initialised from a reduced PRISM-derived ice sheet as described in Section 5.2.3, following (Dolan et al., 2018). The majority of ensemble members reached 10,000 simulation years. We present results from the end of the full simulation period in the following. Figure 5.21 shows how volume above floatation evolves over 10,000 years under Pliocene climate forcing in metres of modern sea level equivalent, as well as the density plot for VAF change at 10,000 years. We note that differences in bedrock elevation at the Pliocene decrease

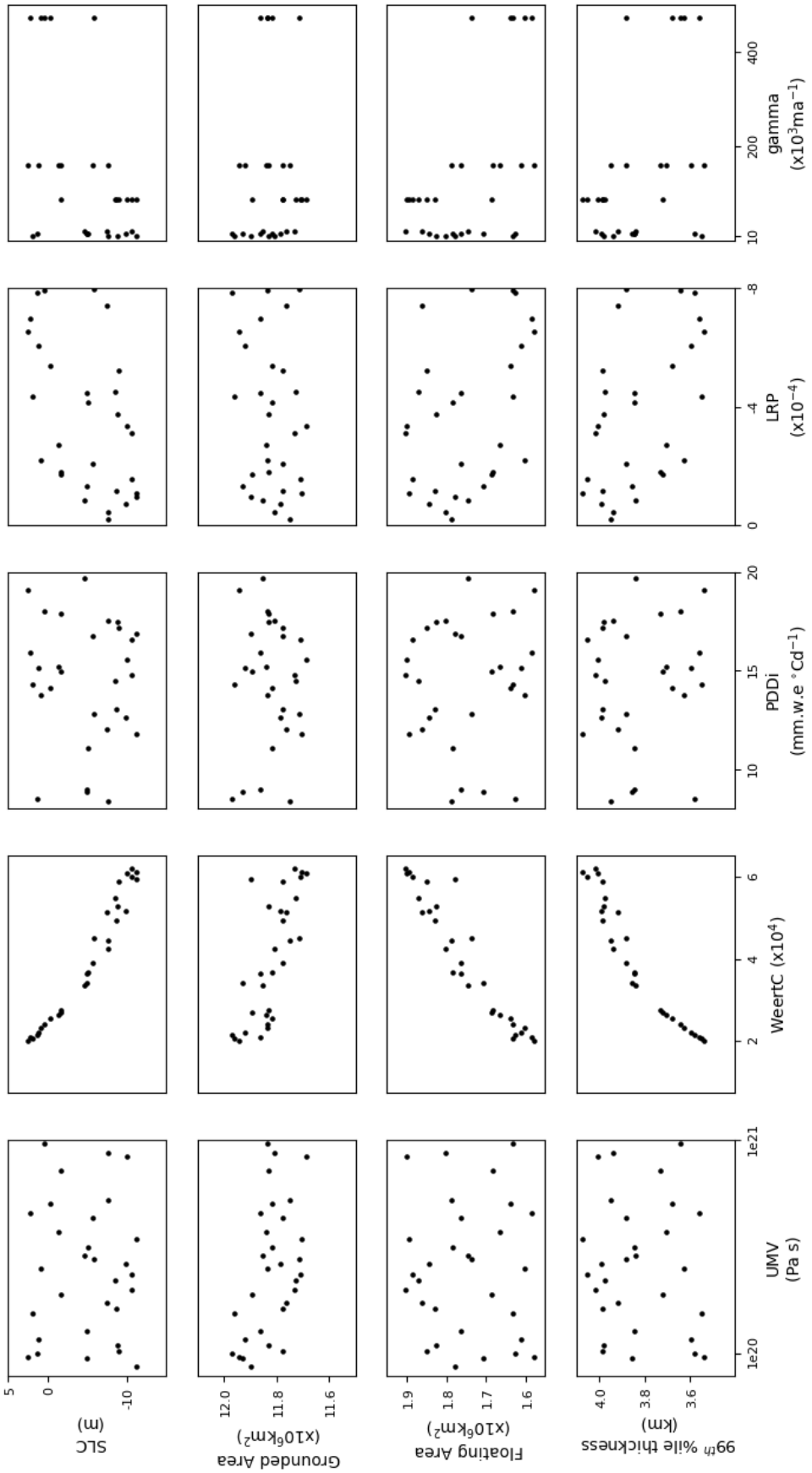


Fig. 5.19 Sensitivity of control ensemble ($Control_{modern}$) sea level contribution, area changes and thickness to perturbed model parameters.

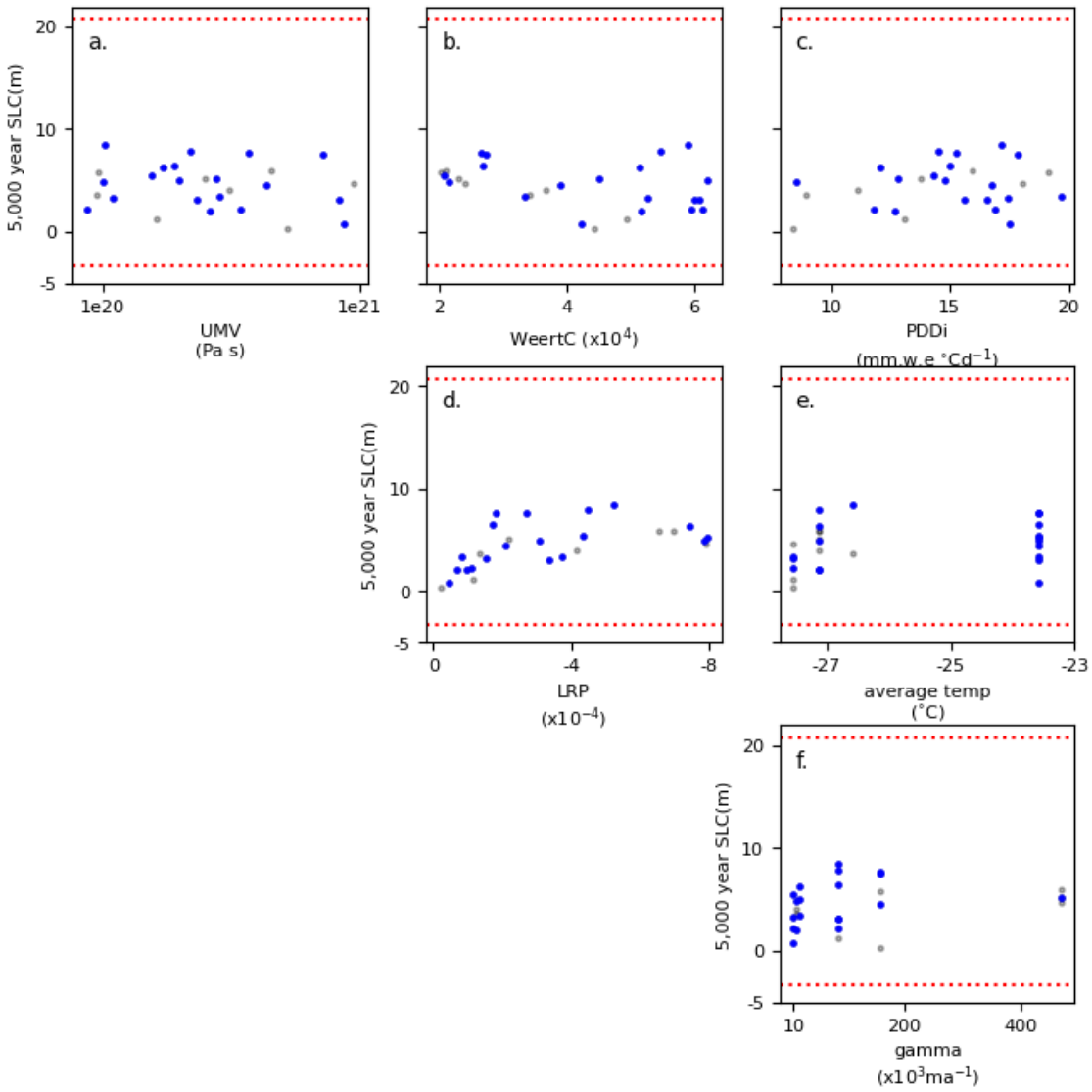


Fig. 5.20 Sensitivity of main Pliocene ensemble minus control ensemble ($Plio_{modern-control}$) after 5,000 years to perturbed parameter. Blue points show ensemble members that retreat into the Wilkes basin within 5,000 years in $Plio_{modern}$ and fall within the sea level range. Grey points show ensemble members that do not retreat into the Wilkes basin, or fall within the sea level range. Red lines show reconstructed sea level range (Section 5.2.6).

ocean volume within the domain, resulting in less accommodation space for sea water in the domain compared with modern - increasing sea level contribution. As in $Control_{modern}$, some simulations increase their volume above floatation substantially over the course of the simulation period. Using the sea level calculation approach outlined in Goelzer et al. (Goelzer et al., 2020a) accounting for differences in ocean volume in the model domain, mean sea level contribution for the $Plio_{PRISM}$ ensemble is 9.10 ± 6.74 m, with a range of -1.28 m to 19.96 m.

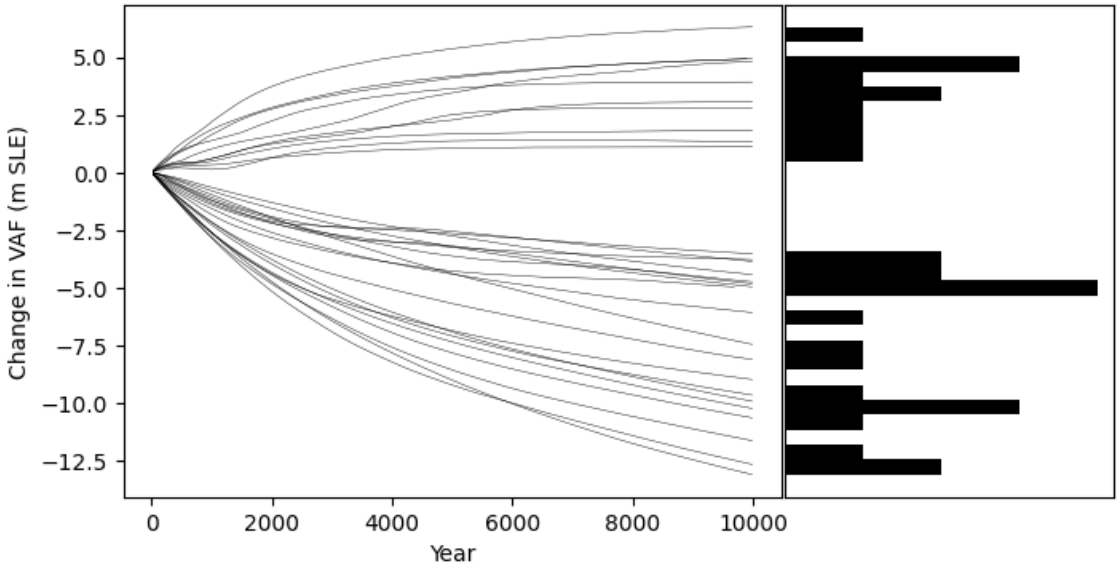


Fig. 5.21 Change in volume above floatation for $Plio_{PRISM}$ simulations (**a.**) and density plot (**b.**) in metres of modern sea level equivalent. Note that change in volume above floatation is not equivalent to sea level contribution in our GIA enabled modelling framework, as changes in bedrock elevation also contribute to sea level differences compared with modern. Moreover, initial ice sheet volume is smaller for the PRISM ice sheet by 9 m modern sea level equivalent.

Figure 5.22 shows the mean output fields for thickness, surface elevation, and ice velocity. Grounded ice is absent on the Antarctic Peninsula, Marie-Byrd land and islands remaining when ice is removed from West Antarctica (blue regions outside the red solid red contour in Fig. 5.22). The ensemble mean ice velocity field shows consistent placement of ice divides for all simulations (Fig. 5.22), with higher standard deviation in regions that become ice shelves in some simulations.

Regions of greatest thickness are along the Wilkes coast, as well as Enderby Land and the margin between Amery ice shelf and the Aurora basin. The Wilkes basin remains deglaciated in all ensemble members. Grounding line position in the Wilkes basin varies across the ensemble, but stabilises on pinning points dotted East-West across the submarine basin. The Totten catchment is also consistently deglaciated, with the Aurora subglacial

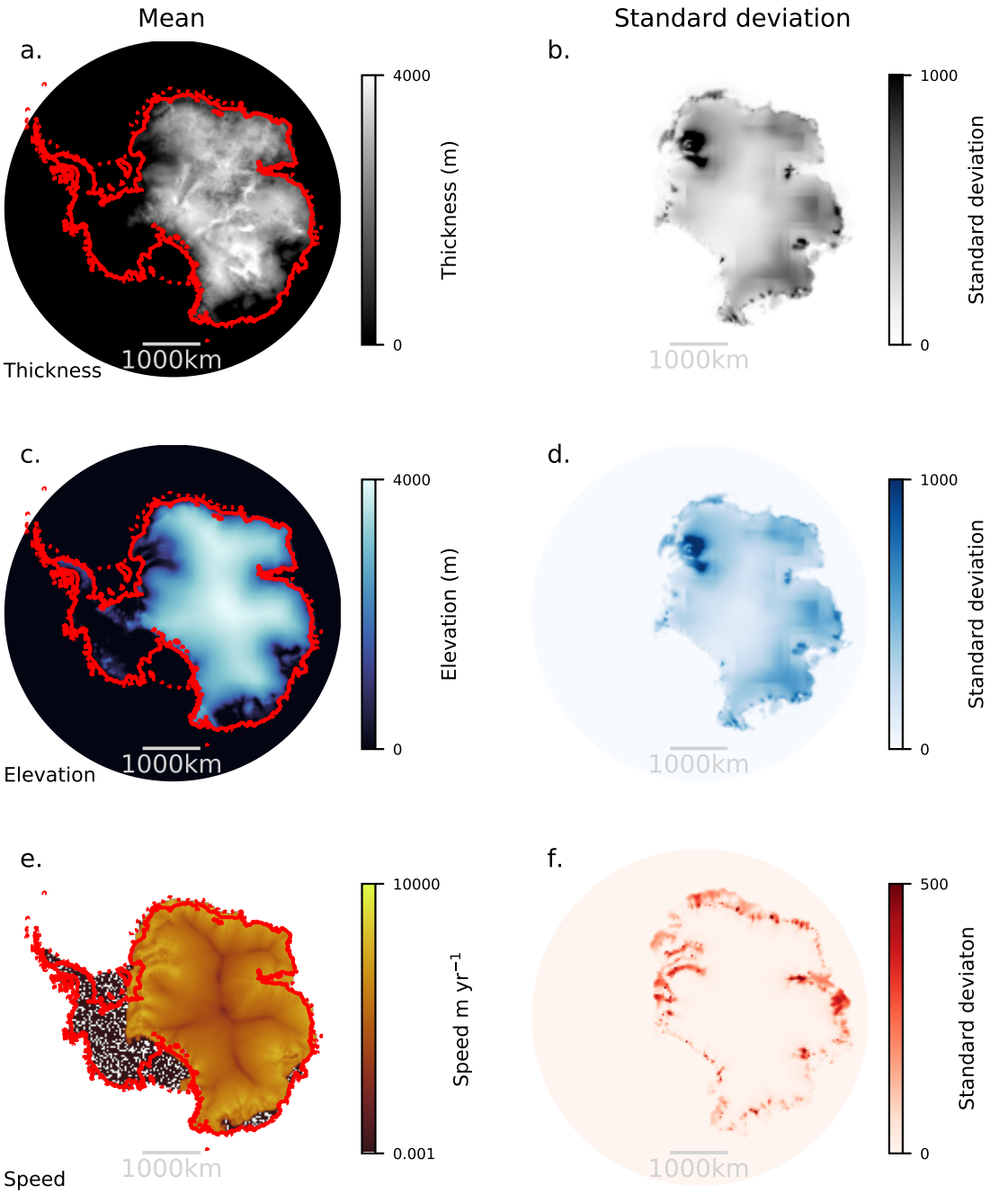


Fig. 5.22 Average thickness, surface elevation and ice velocity fields for the PRISM initialised simulations. Also shown are standard deviation for these fields across the ensemble. Red solid contours show initial grounding line position, with red dashed lines showing initial shelf extent. Linear patterns in standard deviation fields for thickness and elevation are an artefact of BISICLES adaptive mesh grid: simulations with thicker, less mobile ice have a larger domain area with 16km base resolution compared with simulations with a more active ice flow regime. Boundaries between regions of higher and lower resolution are accentuated where fields from simulations with different grid refinement regions are combined. In individual simulations, the same lineations are not visible, and do not impact ice flow.

basin open water and the Sabrina subglacial basin rebounded above sea level as in the PRISM initial geometry (Fig. 5.2). However, grounding lines advance across exposed bedrock along the Sabrina coast over the 10,000 year simulation period (Fig. 5.23 **b**) and the ice sheet thickens (Fig. 5.23 **a**) Recovery, Slessor and Bailey ice streams undergo variable retreat, as in the $Plio_{modern}$ ensemble, indicated by thickness variability in Fig. 5.22, with average thinning across the ensemble (Fig. 5.23 **a**) consistent with grounding line retreat at these ice streams (Fig. 5.23 **b**).

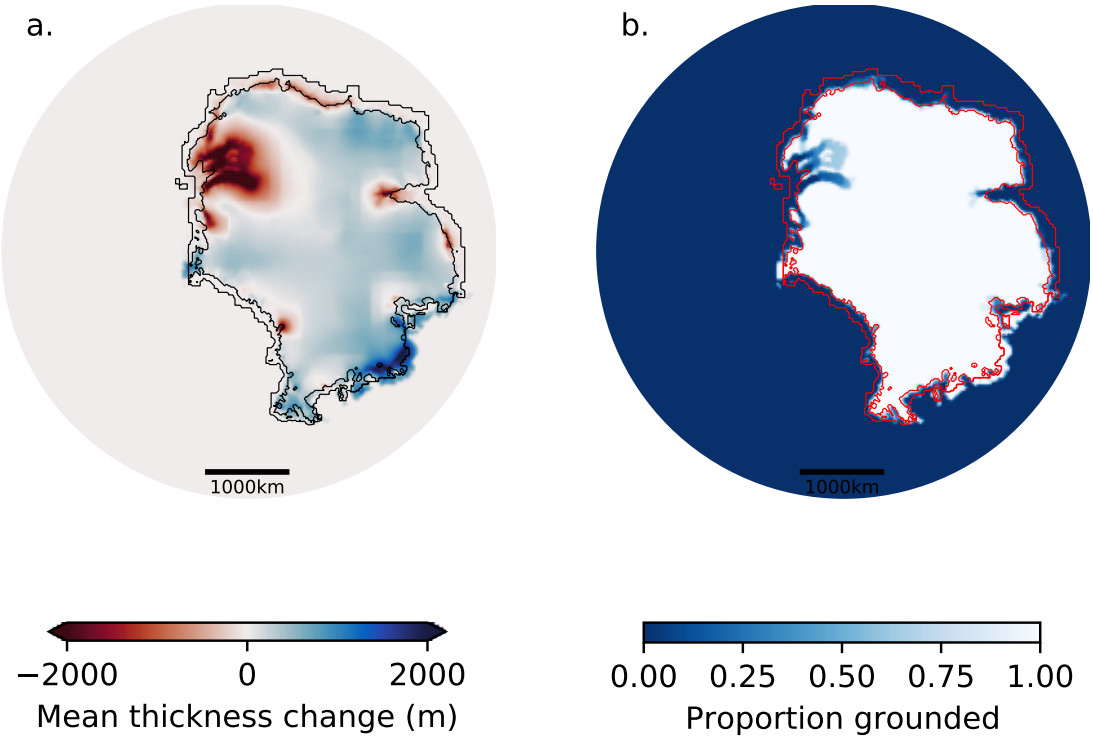


Fig. 5.23 Average thickness change of $Plio_{PRISM}$ after 10,000 years (**a**). Also shown is the proportion of runs that remain grounded across the domain (**b**). Red contours show the initial grounding line and ice shelf position.

We next explore the 5,000 year sea level contribution from our PRISM initialised ensemble relative to the equivalent control simulations. The $Plio_{PRISM}$ simulations have a much larger contribution to modern sea level than their equivalent $Control_{modern}$ simulation. For the $Plio_{PRISM}$ ensemble after 5,000 years, mean sea level contribution relative to the default control is 10.31 ± 5.03 m, with a range from 2.80 m to 18.75 m SLE. This means the $Plio_{PRISM}$ ice sheet response relative to the control is much larger than for $Plio_{modern}$: in fact, the ranges do not overlap. The mean difference between the PRISM initialised ensemble and the control ensemble sea level contribution is 15.25 ± 1.33m, with a range of 12.82 m to 17.41 m.

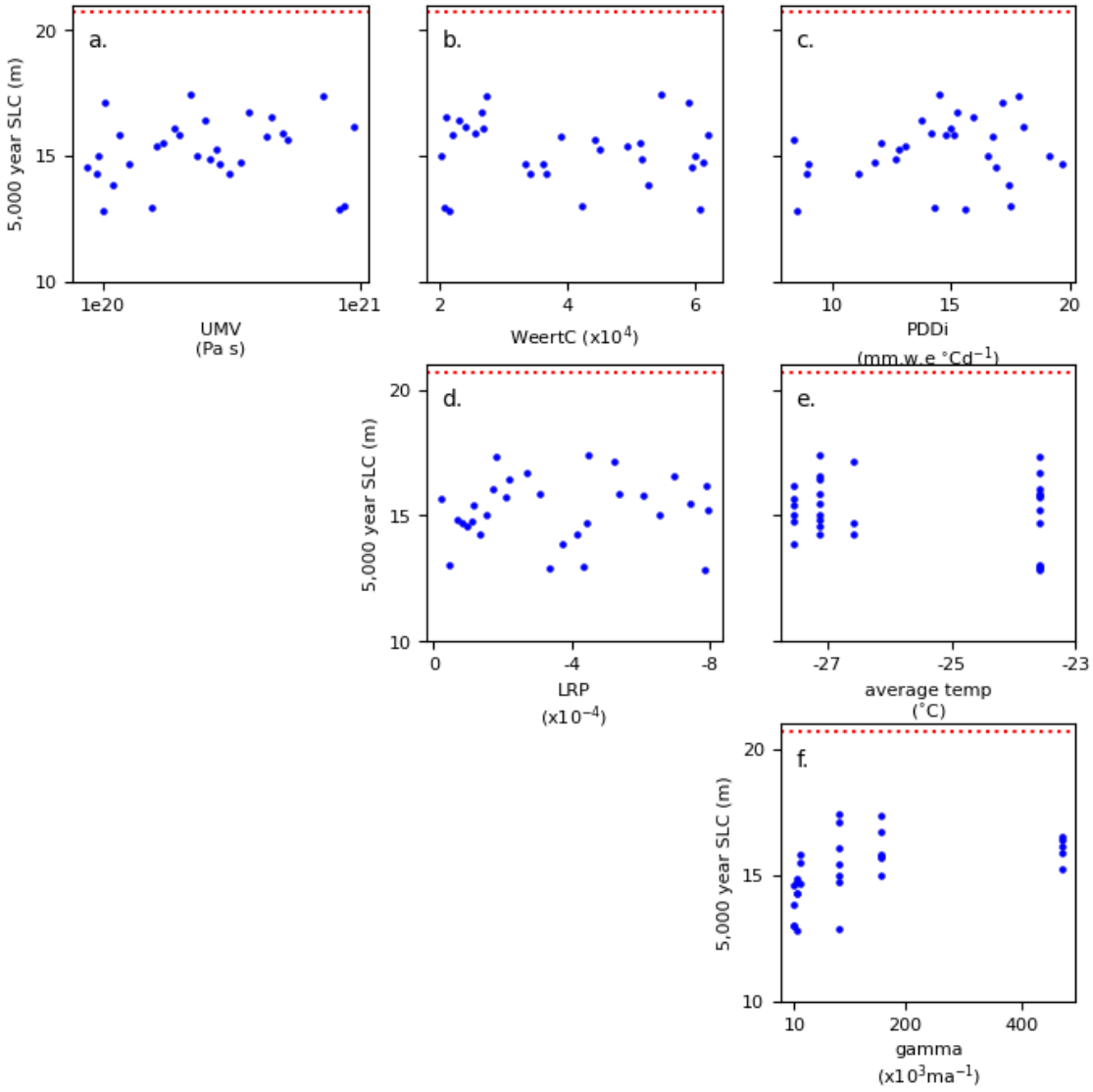


Fig. 5.24 Sensitivity of sea level contribution for PRISM initialised simulations minus the control ensemble ($Plio_{PRISM-control}$) to perturbed parameters and climate model. Red contours indicate reconstructed Pliocene sea level range.

### 5.3.5 All ensemble results

Figure 5.25 shows histograms and kernel density estimates for Pliocene ensemble results, including sea level contributions for ensemble members that pass both data comparison steps (subplots **g.** and **h.**). For $Plio_{PRISM}$ and $Plio_{PRISM-control}$ all ensemble members have a grounding line retreated into the Wilkes basin, and a sea level contribution within our reconstructed range. For these ensembles, the data comparison steps do not constrain the projected sea level range. Number of ensemble members, mean sea level contribution, standard deviations and ensemble ranges are shown in Table 5.4

| Ensemble | Year | Calibration | N | Mean SLC(m) | SD | min | max |
|---|---|---|---|---|---|---|---|
| $Plio_{modern}$ | 10,000 | - | 110 | 1.85 | 9.28 | -15.89 | 28.27 |
| $Plio_{modern}$ | 10,000 | SL | 71 | 4.76 | 6.31 | -3.25 | 20.48 |
| $Plio_{modern}$ | 10,000 | Wilkes | 58 | -1.53 | 7.52 | -13.23 | 28.27 |
| $Plio_{modern}$ | 10,000 | Wilkes + SL | 31 | 1.46 | 3.64 | -3.11 | 8.29 |
| $Plio_{modern}$ | 5,000 | - | 110 | 2.35 | 7.37 | -9.16 | 24.53 |
| $Plio_{modern}$ | 5,000 | Wilkes | 57 | -1.03 | 5.24 | -9.16 | 24.53 |
| $Plio_{modern}$ | 5,000 | Wilkes + SL | 38 | 0.56 | 2.97 | -3.08 | 7.32 |
| $Plio_{modernsubsample}$ | 5,000 | - | 27 | -0.90 | 5.98 | -9.16 | 8.23 |
| $Plio_{PRISM}$ | 10,000 | - | 30 | 9.10 | 6.74 | -1.28 | 19.96 |
| $Plio_{PRISM}$ | 5,000 | - | 30 | 10.31 | 5.03 | 2.80 | 18.75 |
| $Control_{ensemble}$ | 5,000 | - | 30 | -4.93 | 4.65 | -11.30 | 2.40 |
| $Plio_{modern-control}$ | 5,000 | - | 27 | 4.44 | 2.19 | 0.31 | 8.41 |
| $Plio_{modern-control}$ | 5,000 | Wilkes | 19 | 4.47 | 2.24 | 0.80 | 8.41 |
| $Plio_{modern-control}$ | 5,000 | Wilkes + SL | 19 | 4.70 | 2.24 | 0.80 | 8.41 |
| $Plio_{PRISM-control}$ | 5,000 | - | 30 | 15.25 | 1.33 | 12.82 | 17.41 |

Table 5.4 Ensemble results presented in this chapter. Subscript indicates ensemble name, or subtraction of the control ensemble e.g. modern - control indicates $Plio_{modern}$ minus $Control_{modern}$. Calibration refers to the calibration approach, where '-' indicates no calibration, SL indicates that only the sea level constraint has been applied, Wilkes indicates calibration only with Wilkes retreat, and Wilkes + SL is the combination of these two. N indicates the number of simulations on which each set of results is based. SD is standard deviation.

## 5.4 Discussion

### 5.4.1 Main Ensemble Patterns of retreat

WAIS collapse is consistent with previous modelling studies of Antarctica in the warm Pliocene (DeConto and Pollard, 2016, DeConto et al., 2021, Dolan et al., 2018, Austermann et al., 2015) and sedimentological evidence for a collapsed WAIS during peak Pliocene warmth (Naish et al., 2009). It underlines the vulnerability of the submarine grounded

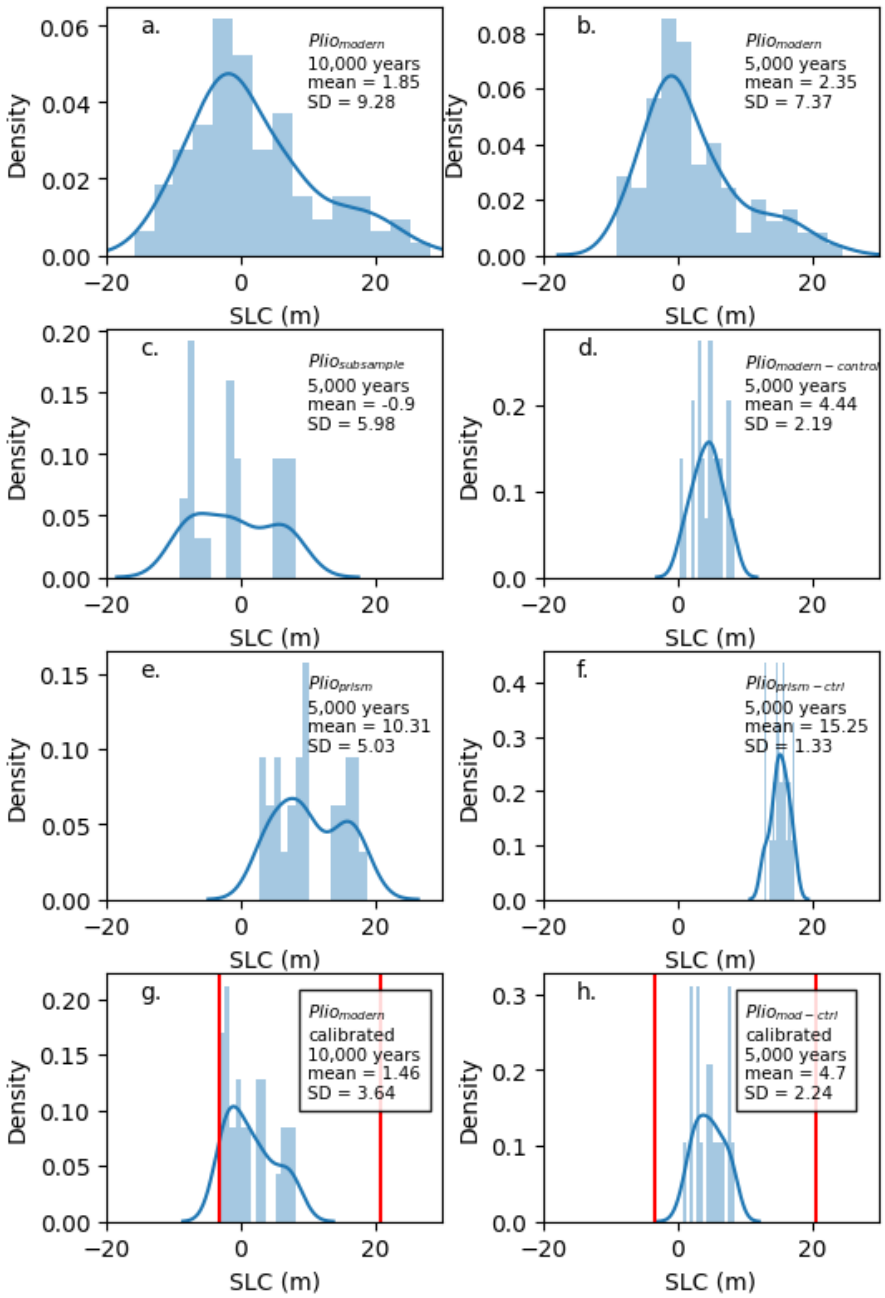


Fig. 5.25 Histograms and kernel density estimates for Pliocene sea level simulations for **a.** Pliocene simulations from a modern initial condition relative to control ($Plio_{modern}$) after 10,000 years. **b.** The same as a. but after 5,000 years **c.** Sea level contribution for the 30 ensemble members that are run in the PRISM and control ensembles. **d.** Pliocene simulations with modern initial condition subtracting the control ensemble ($Plio_{modern-control}$) **e.** Pliocene simulations with PRISM initial condition relative to control ($Plio_{PRISM}$) after 5,000 years **f.** The same as e. but subtracting the control ensemble **g.** $Plio_{modern}$ after 10,000 years showing the effect of Wilkes basin retreat and sea level constraints **h.** $Plio_{modern-control}$ showing the effect of Wilkes basin retreat and sea level constraints. Red vertical lines in **g.** and **h.** show the bounds of the sea level constraint (-3.3 m, 20.7 m).

WAIS to ocean forcing. And, in our simulations, retreat of the major ice shelves and ice sheet margins was also enhanced through surface melting.

For the EAIS, as well as the Wilkes basin undergoing retreat in some ensemble members, thinning and grounding line retreat also occur along the Sabrina coast, and the Totten glacier - though extensive grounding line retreat into the interior Aurora subglacial basin is limited to a few ensemble members in $Plio_{modern}$ experiments. Ice thinning and mass loss equivalent to 4 m SLE has been proposed for Totten in the Pliocene (Aitken et al., 2016). Evidence for grounding line retreat into the Aurora Subglacial Basin (ASB) in the warm Pliocene is limited (Section 1.4.2). Gulick et al. (2017) infer maximum grounding line retreat of 150 km in the Aurora subglacial basin (ASB) over the past 7 million years, based on patterns of erosion in the ASB and sediments associated with a polar glacial depositional environment on the shelf at the Sabrina coast. With reconstructions of Pliocene retreat in the region of the Totten glacier, this region could provide a second spatial data comparison to complement the Wilkes retreat constraint.

With large uncertainties in Pliocene sea level and ice sheet margin reconstructions, but small variation across model simulations, WAIS collapse is limited as a constraint on model performance: it is too broad to favour particular modelling approaches. EAIS retreat is more variable across studies. Exploration of climate and ice sheet model uncertainties here has resulted in simulations both with and without EAIS retreat, allowing the possibility of discriminating between different modeling choices using EAIS data constraints.

### 5.4.2 Parameter sensitivities

#### Weertman friction coefficient

The Weertman sliding coefficient predominantly controls sliding velocity in the interior of the ice sheet. Other studies (Yan et al., 2016) find a similar dependence of thickness and ice sheet volume on parameters related to ice discharge. Yan et al. (2016) find that flow enhancement factors in a SIA-SSA hybrid model have a clearer influence on ΔVAF than climate parameters in the mid-Piacenzian. They find that perturbing flow enhancement factors has a strong influence on Pliocene sea level contribution, with a range of 10.8 m SLE across their ensemble perturbing flow enhancement factors and PDD factors. Although flow enhancement factors are not directly analogous to the Weertman friction coefficient, the impact of directly perturbing discharge compared with climate parameters in both Yan et al. (2016) and in this study, underlines the ice sheets sensitivity to changes in the flow regime.

As well as facilitating more flux of ice through slow moving regions of the ice sheet, perturbing the Weertman friction can also indirectly impact ice stream formation and evolution. Through the two component, hydrology coupled sliding law, under higher Weertman friction coefficient, sliding will switch to Coulomb type at a lower velocity threshold. Nias et al. (2018) test the influence of the Tsai et al. (2015) Weertman-Coulomb sliding law in BISICLES, finding more grounding line retreat under coulomb type sliding. Weak negative correlation between Weertman friction coefficient and grounded area for $Plio_{modern}$ and $Control_{ensemble}$ could in part be related to switching from Weertman sliding to Coulomb sliding at a lower velocity threshold in simulations where the Weertman friction coefficient is higher. Coulomb sliding over a larger area of the ice sheet could then facilitate more extensive grounding line retreat (Nias et al., 2018). However, a similar correlation is not clear in $Plio_{PRISM}$ simulations, suggesting that other processes or interactions could convolute this interpretation. Lower Weertman friction coefficient simulations have faster sliding over more of the domain, resulting in frictional heating - producing more water at the bed. Figure 5.26 shows the percentage of grounded ice sheet area where water is present at the base (till water depth > 0). At lower Weertman friction coefficient values, with faster sliding, frictional heating contributes to water production at the base, promoting ice streaming.

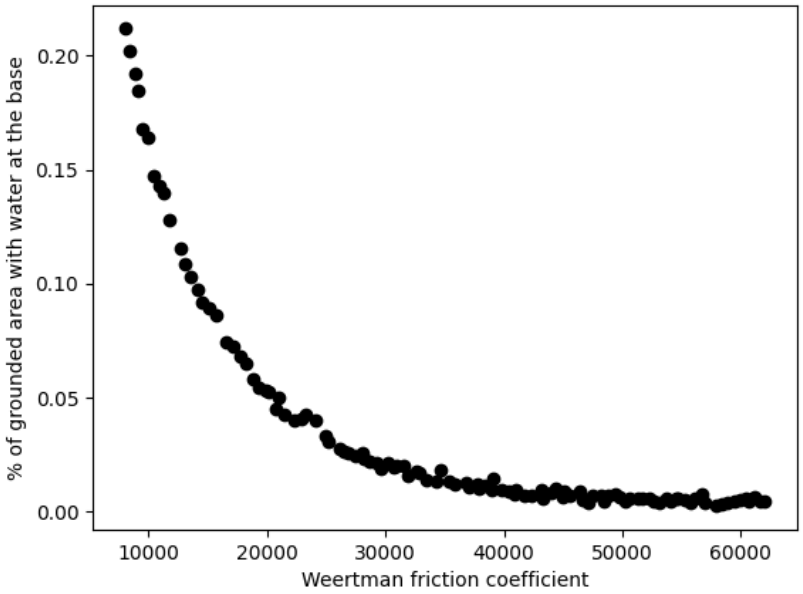


Fig. 5.26 Percentage of grounded ice sheet area with water at the base at year 10 of $Plio_{modern}$ simulations.

### Lapse rate precipitation

As noted in Section 4.1.1, PlioMIP2 models used a reduced Antarctic ice sheet in the Pliocene (Dowsett et al., 2016), with extensive ice-free regions in the Wilkes and Aurora subglacial basins. In PlioMIP2 Eoi400 simulations, these warmer, low elevation areas receive greater precipitation than cold, high regions of the EAIS. Using a higher value of LRP drives a more negative precipitation correction at higher (cooler) elevations. Lower LRP runs therefore retain more accumulation from the GCM. This can drive high surface mass balance where BISICLES elevation diverges significantly from the GCM Pliocene ice sheet boundary condition (i.e. along Wilkes Land Coast, at the start of runs). The higher surface mass balance in low LRP ensemble members therefore results in lower net sea level contributions.

### Positive degree day Factors

The positive degree day factor for ice is weakly negatively correlated with grounded ice sheet area in our main ensemble. A similar dependency was found in Chapter 4, Section 4.3.2. However, in our main ensemble, despite the denser sampling of (*PDDi*), a significant correlation doesn't emerge between *PDDi* and sea level contribution at 10,000 years. A key difference between the simulations presented here, and those in section 4.3.2 is the use of a GIA model. That higher positive degree day factor for ice drives smaller ice sheet grounded area, but not a concomitant increase in sea level contribution, could suggest a feedback with the GIA - though stabilisation of grounded volume is associated with lower mantle viscosity in this model for the Pine Island catchment (Kachuck et al., 2020). We also note the strong dependency of ice sheet shape on the Weertman friction coefficient, which could limit apparent sensitivity to *PDDi*. In our perturbed parameter design, simulations with high *PDDi* may undergo more retreat, as illustrated through the correlation with area. However, if the Weertman friction coefficient is high, this could limit volume loss in the interior to a greater extent than mass loss at the margins. The expected relationship between *PDDi*, seen in Chapter 4 with unperturbed Weertman friction coefficient, is therefore not seen.

### Upper mantle viscosity

Slight negative correlation between UMV and grounded area in simulations initialised from modern and PRISM ice sheet configuration reflects the stabilising impact of lower mantle viscosity (Konrad et al., 2015, Kachuck et al., 2020, Adhikari et al., 2014, Gomez

et al., 2015)(Section 3.2.1), although as previously stated, there is no correlation with sea level. A less viscous mantle responds to changing load more quickly, allowing the ice sheet to stabilise and maintain more grounded area as the ice sheet remains in contact with the bed across a greater area. The reason for lack of a relationship between UMV and sea level contribution is somewhat less clear, as we would expect greater grounded ice area to facilitate retention or growth of volume above floatation. However, with the strong dependency of ice sheet volume on the Weertman friction coefficient, this could negate any correlation between UMV and sea level contribution.

#### Ice shelf basal melt

Sea level contribution has weak positive correlation with ice shelf basal melt sensitivity to thermal forcing ($\gamma_0$) across the ensembles. Under higher $\gamma_0$, ice shelves are more vulnerable to retreat and are less able to persist - as reflected in the lower floating ice shelf area under higher $\gamma_0$ for the modern and PRISM initialised Pliocene ensembles (not shown), as well as the control ensemble (Figure 5.19). Moreover, under higher $\gamma_0$ and sustained thermal forcing, the ocean will more efficiently remove any ice transported across the grounding line. Under the range of $\gamma_0$ values used here and Pliocene thermal forcing, the ice sheet only gains mass through accumulation of mass in the interior, not through increasing the grounded area over which mass is accumulated.

#### Climate model

The role of climate model in driving variations in ice sheet response is explored through the relationship between mean Antarctic air temperature at the start of the simulation and ice sheet summary outputs. This is does not, however, capture the full complexity of surface mass balance, which is driven by climate model temperature, precipitation and surface elevation (through the lapse rate corrections). Climate model choice also determines thermal forcing at the base of ice shelves. The clearest relationships across Pliocene ensembles are between average temperature and ice sheet area, both floating and grounded, with no apparent correlations with sea level contribution. Lack of correlation between average temperature and sea level contribution may reflect the nonlinear nature of surface mass balance scaling with temperature. In the ice sheet accumulation zone, large increases in temperature will only affect ablation if they cause temperature to rise above the melting point. However, increases in precipitation with warming occur below 0°C. Conversely, higher air temperatures at the margin will increase melting. Warmer climate

models could therefore reduce ice sheet area at the margins through melting, but increase volume in the interior.

### 5.4.3 Wilkes basin retreat

As discussed in Section 5.4.1, collapse of the WAIS is a consistent feature of the simulations presented here, and also found across studies of the Pliocene. In comparison, grounding line retreat into the Wilkes subglacial basin has proved more challenging to reproduce in ice sheet models and is sensitive to initial conditions (Dolan et al., 2018) and the inclusion of model physics (DeConto and Pollard, 2016).

The Ninnis basin is not the explicit focus of Wilkes basin provenance studies (Cook et al., 2013, Bertram et al., 2018). Our screening approach is insensitive to deglaciation into the Ninnis catchment in the absence of retreat into the central Wilkes basin, defined in Bertam et al. (2018). The regions bounded by the central Wilkes basin contour closer to the coast (Fig. 5.12), as well as those in the interior, coincide with the Ferrar Large Igneous Province (FLIP), which geochemical provenance analysis (Cook et al., 2013, 2014, Bertram et al., 2018) indicate as the source for Pliocene sediments at the drill site off shore from the Wilkes basin indicated in Figure 1.4. Including ensemble members that retreat just inside the Cook catchment, with small grounded area change, reflects a conservative approach to the Wilkes retreat constraint. Whilst Bertram et al. (2018) suggest that Pliocene productivity increases are indicative of large scale grounding line retreat into the Wilkes basin, the outer edge of our bounded pink region broadly coincides with coastal regions of FLIP bedrock. Modest retreat onto it could therefore provide source material to ocean sediments with geochemical fingerprints found in Cook et al. (2013), though it does not reflect the broad scale retreat posited in Bertram et al. (2018).

As shown in Figure 5.9, CCSM4-Utr has large negative surface mass balance around the margins of EAIS, including at the terminus of the Cook and Ninnis ice streams in the Wilkes basin. Similarly, average upper ocean temperature is higher in the Wilkes basin for CCSM4-Utr compared with other models used (Fig. 4.2). These could both have contributed to the greater fraction of simulations showing retreat in this region. Mengel and Leverman (2014) find that retreat into the Wilkes basin is partially conditional on removal of an ‘Ice plug’ in simulations with the PISM ice sheet model. Under sustained surface melt in CCSM4-Utr forced scenarios, surface lowering of the ice towards floatation thickness will drive grounding line retreat in concert with strong ocean forcing. This demonstrates that both the magnitude of warming, and its location within the atmosphere and ocean, are important factors for driving retreat in the Wilkes catchment.

As well as favouring CCSM4-Utr, the Wilkes calibration preferentially removes low Weertman friction coefficient simulations from the ensemble. As previously shown, this parameter is positively correlated with ice sheet thickness. Low Weertman friction ensemble members have a thinner profile across the whole ice sheet. Thinner ice sheets exert smaller load on the bed, and ice sheets that rapidly thin under low Weertman friction and advection of mass to the oceans will undergo greater uplift compared with simulations where high thickness is maintained. Rate of bedrock response is dependent on mantle viscosity (lower viscosity, faster uplift) with elastic bedrock response also impacting stability. Following Mengel and Leverman's finding of a stabilising ice plug at the termini of glaciers draining the Wilkes basin (Mengel and Levermann, 2014), we posit that lower Weertman friction, thinned ice sheets favour stability on the ridge at the outer edge of the basin, maintaining this ice plug. Figure 5.27 shows transects through the Wilkes basin for all $Plio_{modern}$ ensemble members at 10,000 years. The tendency for thinner grounded ice in the Wilkes basin with lower Weertman friction (whiter profiles) demonstrates the tendency for thinned ice sheets, with more deflected and therefore shallower beds to maintain contact with the ridge indicated by the black dashed line. There is, however, no clear correlation between upper mantle viscosity and change in Wilkes basin grounded area (not shown). If lower mantle viscosities facilitate maintenance of grounded area in the Wilkes basin when the ice sheet undergoes broad scale thinning, we would expect more grounded area in the basin to be maintained under lower upper mantle viscosity. This could suggest that our interpretation is overly simplistic, or that elastic response of pinning points underlying the critical ice plug (Mengel and Levermann, 2014) maintains stability in the basin and prevents retreat. Stabilisation by elastic bedrock is consistent with Larour et al. (2019), who find a negative feedback between elastic bedrock uplift and grounding line retreat.

### 5.4.4 Initial condition uncertainty

Choice of ice sheet and bedrock initial condition has a large impact on our ensemble, with the PRISM-initialised simulations having a mean volume ~7 m SLE smaller than those initialised from the modern ice sheet (Table 5.4). For the $Plio_{modern}$ subset compared with $Plio_{PRISM}$, the difference is much larger: ~10 m SLE (compare Fig. 5.25 (**e.**) vs (**c.**) and (**f.**) vs (**d.**)

However, high Weertman friction coefficient simulations in the $Plio_{PRISM}$ ensemble are continuing to gain volume above floatation at 10,000 years (Fig. 5.21). We could therefore expect the mean sea level contribution to decrease with increased simulation length.

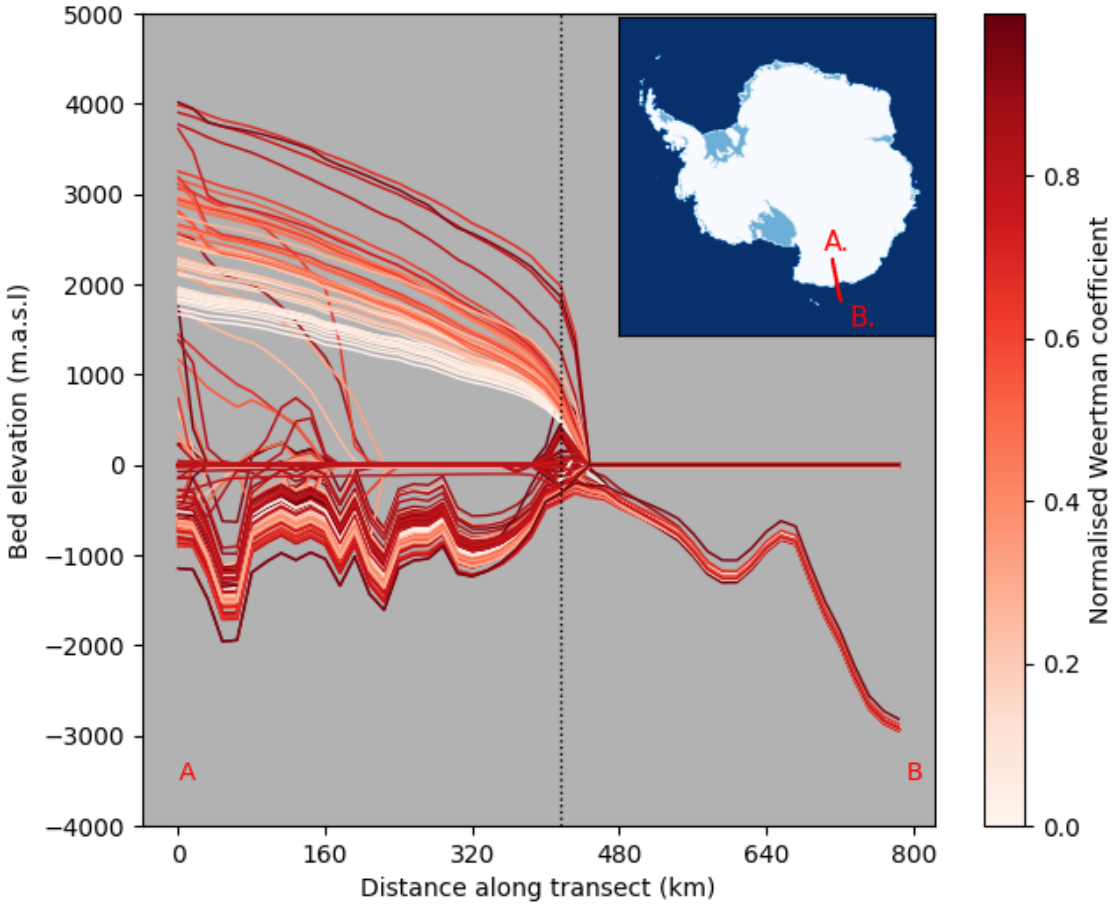


Fig. 5.27 Transect for all $Plio_{modern}$ simulations through the Wilkes subglacial basin at 10,000 years. Line color shows normalised Weertman friction coefficient, with darker reds corresponding to higher Weertman friction coefficient. Black dashed line indicates the stabilising ridge at the entrance to the Wilkes basin. The red line on the inset axis shows the cross section, with A and B corresponding to the ends of the transect in the main figure.

In a similar exploration of initial condition uncertainty, de Boer et al. (2015) find a similar difference of ~12 m between their modern-initialised and PRISM-initialised ice sheet multi-model mean under a single GCM. This is however lower than the initial condition uncertainty found in Dolan et al. (2018), who found a difference in multi-model mean for their PRISM-initialised and modern-initialised ensembles of ~5 m. The majority of previous warm Pliocene Antarctic ice sheet modelling studies initialise their simulations from a modern ice sheet, or an ice sheet simulated to equilibrium under modern conditions (DeConto and Pollard, 2016, DeConto et al., 2021, Golledge et al., 2017b, Yan et al., 2016, Pollard et al., 2017). Our results further highlight the influence of initial conditions in simulations of the Pliocene Antarctic ice sheet. Moreover, they highlight the need for more robust, high temporal resolution reconstructions of the Antarctic ice sheet configuration during Pliocene interglacials. Ice sheet configuration prior to and during the warm Pliocene is poorly constrained. In their study of an early Pliocene interglacial, Golledge et al. (2017b) initialise their ice sheet from modern geometry based on the finding of Naish et al. (2009) that the Pliocene ice sheet was more extensive than modern during Pliocene glacials. Transitioning from a cool Pliocene glacial, with a larger-than-modern AIS, to an interglacial, reduced AIS state would therefore necessitate the ice sheet shrinking through an approximately present day configuration. The modern initial condition therefore mainly impacts time to equilibrium as opposed to equilibrium configuration itself (Golledge et al., 2017b). We note however that ice sheets in our ensemble are not at equilibrium. Others have used a modern initial condition for transient Pliocene simulations however (DeConto and Pollard, 2016, DeConto et al., 2021, Pollard et al., 2015), with simulation length justified on the basis of the time window within which modern-like, Pliocene orbital configuration would have persisted (approximately 5,000 years).

The Pliocene initial condition significantly increases sea level contribution in our experiments, consistent with previous ensemble studies (Dolan et al., 2018, de Boer et al., 2015). In terms of other modern-initialised Pliocene ice sheet modelling studies (DeConto and Pollard, 2016, DeConto et al., 2021, Pollard and DeConto, 2020a), whether equivalent reduced Pliocene initialisation experiments would simulate a larger sea level contribution is unclear. Using an earlier version (Pollard and DeConto, 2012) of the model used in DeConto et al. (2016, 2021), without MICI, De Boer et al. (2015) find a Pliocene sea level contribution ~11 m higher for simulations initialised from PRISM3 compared with simulations initialised from Bedmap2. However, the inclusion of MICI in subsequent studies (DeConto and Pollard, 2016, DeConto et al., 2021) removes ice in East Antarctic submarine basins that remain glaciated when MICI is not included in their model (DeConto et al., 2021). We might not therefore expect as significant an effect if DeConto et

al. (2016, 2021) simulations were initialised from a reduced Pliocene ice sheet, though additional experiments would be required to explore this.

Another interpretation is that the PRISM ice sheet used in PLISMIP studies (Dolan et al., 2018, de Boer et al., 2017b), and modified for use here with BISICLES, already represents an ice sheet that has shrunk towards equilibrium with a steady-state fixed Pliocene climate, and further loss of volume would be reversed once the climate state transitioned out of Pliocene warmth.

### 5.4.5 Evidence of thickening

Across ensembles, the EAIS underwent thickening. Evidence for extensive East Antarctic thickening across the warm Pliocene is limited. Shakun et al. (2018) find evidence that the EAIS persisted throughout most of the past 8 Ma. Moreover, Yamane et al. (2015) compile cosmogenic exposure ages from sites in the Trans-Antarctic Mountains at the edge of the Wilkes subglacial basin, the Lambert glacier catchment, the Shackleton range in Coats land and Dronning Maud Land. From these, they infer thickening of the EAIS of up to ~600 m prior to 3 Ma (Yamane et al., 2015). However, EAIS thickening on a scale that counteracts collapse of the WAIS – which is well supported in the proxy record (Naish et al., 2009) – and loss of the Greenland ice sheet is likely incompatible with reconstructions of Pliocene sea level (Grant et al., 2019, Dumitru et al., 2019). The spatial distribution and age range uncertainty of the sites sampled by Yamane et al. ( 2015) preclude their use as a strong constraint on simulations of the warm Pliocene ice sheet. However, the use of an ice sheet model in conjunction with the proxy data in the same study supports the suggestion that the EAIS could have been up to 600m higher in the warm Pliocene Florindo et al. (2021). Following the interpretation of 600m as an approximate upper bound on mPWP EAIS thickening, we could infer that thickening in excess of this, over large areas of the ice sheet, is incompatible with this interpretation of Yamane et al. (2015).

### 5.4.6 EAIS retreat

Retreat of Recovery ice stream, as seen in both $Plio_{modern}$ and $Plio_{PRISM}$ ensembles, is consistent with a previous simulation by Pollard et al. (2015). Scherer et al. (2016) cite the simulated ice sheet of Pollard et al. (2015), with retreat into the recovery basin, as an intermediate configuration for the EAIS between instability postulated in some early Pliocene studies (Webb and Harwood, 1991, Harwood and Webb, 1998, Wilson, 1995)

and a stable configuration advocated elsewhere (Sugden et al., 1993, Denton et al., 1993, Clapperton and Sugden, 1990).

Using the PISM SIA-SSA hybrid ice sheet model, Golledge et al. (2017a) explore the response of the Antarctic ice sheet to sustained (10,000 years) warming thresholds in the ocean and atmosphere. They find uniform collapse of WAIS under an imposed 1°C of ocean warming above modern (Golledge et al., 2017a). Conversely, they find stability of the Wilkes and Aurora basins under all ocean warming scenarios if surface air temperature anomaly is <4 °C. Of all the East Antarctic catchments, Golledge et al. (2017a) find the Recovery basin catchment most sensitive to ocean driven warming, due to it's inland deepening bed topography and lack of pinning points compared with the Aurora and Wilkes basins. This leads to large volumes of ice close to floatation in the Recovery basin, which can be destabilised by ingress of warm ocean waters and basal melting.

Previous studies, have been unable to reproduce retreat in the Wilkes basin from a modern initial grounding line (Dolan et al., 2018, de Boer et al., 2015), unless they include MICI processes (DeConto and Pollard, 2016, DeConto et al., 2021) or ice shelf melt parameterisations that favour grounding line retreat (Golledge et al., 2017b). Moreover, Cornford et al. (2016) have shown that retreat on the George V margin, where the Wilkes basin is located, shows less retreat with lower resolution.

For our calibration step, we reject ensemble members that do not undergo retreat into the Wilkes subglacial basin. This follows the interpretation of geochemical provenance analysis, iceberg rafted debris and productivity indicators from IODP site U1361A in Bertram et al. (2018). Analysis of younger sections of the same core have been interpreted as evidence of similar retreat into the Wilkes basin in the Last Interglaciation (Wilson et al., 2018). However, ice core derived isotopic records and ice sheet modelling suggest that the Wilkes subglacial basin remained glaciated through this period (Blackburn et al., 2020, Goursaud et al., 2021, Sutter et al., 2020). In light of these conflicting records, Golledge et al. (2021) suggest that the record presented in Wilson et al. (2018) is more consistent with increased ice stream velocity and discharge, as opposed to extensive grounding line retreat. If the records presented in Bertram et al. (2018) are the result of the same processes and do not indicate grounding line retreat, our spatial calibration may be inappropriate. However, without strong countervailing geochemical evidence in support of a glaciated Wilkes basin in the Pliocene, we adopt the interpretation of Bertram et al. (2018) in our calibration approach.

### 5.4.7 Comparison with other studies

We now compare our simulated Pliocene sea level contributions (Section 5.3.5) with previous studies of the Antarctic ice sheet in Pliocene. Across three ice sheet models, forced with multiple PlioMIP1 GCMs, Dolan et al. (2018) find a mean of 2.43 ± 3.53 m SLE initialised from modern, with a range of -3.99 m to 7.97 m. In their perturbed parameter ensemble initialised from a modern ice sheet, sampling uncertainty in surface mass balance and ice sheet model parameters, Yan et al. (2016) simulate a range of Antarctic Pliocene sea level contributions from -4.2 to 6.6 m. The mean $Plio_{modern}$ contribution is similar to Dolan et al. (2018), but the range is far broader than both studies (mean: 1.85 ± 9.28 m; range -15.89 to 28.27 m). Compared with Dolan et al. (2018), $Plio_{modern}$ explored a wider range of uncertainties than their multi-model ensemble. Alongside using a range of PlioMIP2 models, $Plio_{modern}$ perturbed surface mass balance parameters, which Chapter 4 showed drove variation in simulated sea level contribution comparable with GCM choice. Perturbing parameters across a large range, in particular the Weertman friction coefficient, drove a large simulated Pliocene Antarctic sea level range compared with previous studies. After calibration, the $Plio_{modern}$ mean decreases slightly and standard deviation decreases substantially, bringing the range into line with previous studies (1.46 ± 3.64 m; range -3.11 to 8.29 m). The 30-member subset of $Plio_{modern}$ that was run in $Control_{modern}$ (and $Plio_{PRISM}$) has a lower mean after 5,000 years than the full ensemble at 10,000 years (-0.90 ± 7.84 m), due to the exclusion of low Weertman C and to a lesser extent the shorter simulation length. Subtracting a control ensemble from these increases the mean by around 5 m (4.44 ± 2.19 m), increasing slightly more after calibration (Table 5.4). This suggests that using the full control ensemble (10,000 year simulations for all 120 ensemble members) would likely increase the ensemble mean above that of Dolan et al. (2018).

As well as comparing to Dolan et al. (2018) and Yan et al. (2016), we can also make comparisons with studies implementing MICI (DeConto and Pollard, 2016, DeConto et al., 2021). In the first study to implement MICI in an ice sheet model, DeConto and Pollard (2016) simulate a range of Pliocene sea level contributions from 3.52 m to 12.41 m. The low end of this range has low ocean melt, and hydro-fracturing and MICI are not activated. The upper end of this range has high ocean melt, with hydro-fracturing and MICI activated. Moreover, they use two calibration ranges, < 5 m and < 10 m Antarctic Pliocene sea level contribution. In a more recent study implementing MICI in an updated version of their model, DeConto et al. (2021) simulate an Antarctic Pliocene sea level contribution range from 3.07 m to 20.85 m, with a mean and standard deviation of 15.98 m ± 5.73 m. Again, with the low end again having inactive hydro-fracture and MICI. For

their calibration, they exclude simulations outside an 11-21 m range based on Dumitru et al. (2019). The simulated $Plio_{modern}$ ensemble range is much wider than these studies, showing that uncertain parameters lead to very high sea level contributions (> 20 m) without invoking MICI.

However, all but two of the simulations that show Wilkes retreat have SLC less than ~10 m. Contributions above 20 m are also rejected by the sea level constraint. So in this model and ensemble design, the initially wide range is strongly reduced by the two data constraints, giving a much lower maximum than DeConto et al. (2021) (8.29 m compared with 20.85 m). A larger Latin Hypercube ensemble (or different parameter perturbations and ranges) might result in simulations with 10 - 20 m SLC and Wilkes retreat, which would increase the upper end of the range to be more consistent with DeConto et al. (2021).

Finally, comparisons can be made with PRISM initialised simulations on Dolan et al. (2018). For their simulations initialised from the reduce Pliocene PRISM ice sheet, Dolan et al. (2018) simulate a mean sea level contribution of 7.79 ±4.06 m, with a range of 2.24 m to 14.57 m across their ensemble. The multi-model ensemble mean sea level contribution of Dolan et al. (2018) is around 5 m higher when initialised from PRISM than from modern, slightly smaller than the 7 m difference found here and leading to a slightly lower mean in their study compared with the $Plio_{PRISM}$ ensemble (mean 9.10 ± 6.74 m; range -1.28 to 19.96 m). The range is again wider in the ensemble presented here, despite the small ensemble size (N=30). Subtracting the control ensemble again increases the mean by ~5 m, as in $Plio_{modern}$ (Table 5.4). This suggests that subtracting the full control ensemble would also increase the mean even further above that of Dolan et al. (2018).

### 5.4.8 Limitations

We simulated the Antarctic ice sheet with a minimum resolution of 4 km. This is higher than previous studies of the Pliocene, and comparable with the maximum resolution of fixed grid models used in ISMIP6 (Seroussi et al., 2020). However, it has been shown that BISICLES retreat is resolution dependent in some regions under modern climate and extreme idealised ocean forcing (Cornford et al., 2016), such as the George V coast as outlined above - where retreat increases with finer resolution.

Cornford et al. (2016) highlight the importance of resolution dependence in BISICLES, and the need to demonstrate resolution convergence in ice sheet modelling experiments. In their study of British-Irish and Fennoscandian ice sheet retreat using BISICLES, Gandy et al. (2021) simulate the ice sheet complex with a minimum horizontal resolution of 8 km, for a 70-member ensemble. To explore resolution convergence, they re-simulate two

episodes of rapid retreat for the Norwegian Channel ice stream for one of their ensemble members at 1 km minimum resolution (Gandy et al., 2021). For rapid retreat across retrograde sloping bedrock, Gandy et al. 2021 find broad agreement in rate of grounding line retreat for lower (8 km) and higher (1 km) model resolution, though grounding line retreats further (< 10 km) for the latter. In the first study to implement basal hydrology coupled ice stream evolution, Gandy et al. (2019) find comparable ice streaming behaviour at 4 km and below for the British-Irish ice sheet. There are key differences between the experiments presented in Gandy et al. (2019, 2021) and the work presented here, including climate forcing and ice sheet geometry - with the Fennoscandian and British-Irish ice sheets resting on shallower marine bedrock compared to submarine regions of Antarctica. A previous palaeo-ice sheet study of the Laurentide ice sheet in BISICLES found limited resolution dependence from 10 km down to 2.5 km (Matero et al., 2020). However, with a limited marine marine margin compared to West Antarctica, the Laurentide ice sheet provides limited insight for the work presented here in terms of resolution dependence.

Based on the resolution dependence of ice stream dynamics in Gandy et al. (Gandy et al., 2019, 2021), we could infer that our 4 km minimum resolution can broadly capture ice stream processes. Considering those studies alongside Cornford et al. (2016), our modelling framework is likely conservative in terms of magnitude and timing of grounding line retreat. This would suggest that simulated sea level contribution would be larger at higher resolution. However, a more thorough assessment of resolution dependency for our modelling framework would require experiments at higher model resolution.

Simulating the ice sheet, or regions such as the Wilkes basin, at higher resolution would be an improvement on the work presented here. If the same resolution dependence for the George V region (Wilkes basin) as seen in Cornford et al. (2016) applies, we could expect more ensemble members to retreat into the Wilkes basin.

This chapter applied the GIA model developed by Kachuck et al. (2020) to continental scale simulations for the first time, using two viscous mantle layers in the GIA model. Whilst the use of this GIA model is an advance of the work in this chapter, we note that viscosity in the two mantle layers did not vary spatially, which is a limitation of our approach. Whilst a lower viscosity upper mantle layer can simulate faster uplift where ice retreats, such as in WAIS, it does not capture spatially varying mantle viscosity under Antarctica (Section 3.2.1). An improvement on this work would be an exploration of the role 3D variability in mantle properties such as that undertaken by Coulon et al. (2021) using an ELRA model.

We sampled a subset of PlioMIP2 GCMs - COSMOS, HadCM3, CCSM4-UofT and CCSM4-Utr. However, this does not comprehensively sample all published PlioMIP2

GCMs (Haywood et al., 2020)(n = 16). Though results for all PlioMIP2 GCMs were not available to us at the time this work was undertaken, an improvement on this work would be a more comprehensive sampling of PlioMIP2, as Dolan et al. (2018) did for PlioMIP1.

Another limitation of this work is the limited ensemble sizes for $Plio_{modern}$ and $Plio_{control}$. Full 120-member ensembles for $Plio_{modern}$ and $Control_{modern}$ would allow for a more thorough exploration of initialisation uncertainty and parametric uncertainty in the control ensemble.

A limitation of the work presented here is that the $Control_{modern}$ ensemble was only run for 5,000 years. Future work would extend all control ensemble simulations to 10,000 years, so that simulations can approach equilibrium. The $Plio_{modern}$ minus $Control_{modern}$ is likely a conservative estimate of maximum contribution for our ensemble, as we do not include lower Weertman friction coefficient simulations. Moreover, the simulations have not equilibrated after 5,000 years.

We also note the lack of accumulation in WAIS for $Plio_{PRISM}$ simulations. Future work would initialise simulations with some ice sheet thickness in WAIS, to explore whether the lack of ice here in the initial condition, though consistent with PRISM, is limiting ice sheet growth. However, if the initial condition is driving under-prediction of ice volume in WAIS in $Plio_{PRISM}$ simulations, even with a WAIS at its largest volume amongst $Plio_{modern}$ simulations, the mean contribution for $Plio_{PRISM}$ simulations would still be many meters above the $Plio_{modern}$ contribution.

Finally, comparing ice sheet summaries with metrics other than mean Antarctic temperature at the start of the simulation may provide a more in-depth exploration climate-ice sheet interactions, or reveal stonger correlations.

## 5.5 Conclusions

We have presented three ensembles exploring Pliocene Antarctic ice sheet evolution initialised from modern ($Plio_{modern}$) and ($Plio_{PRISM}$). Alongside these, we provide an exploration of the control simulation sensitivity to perturbed parameters under modern climate ($Control_{modern}$).

Our modern initialisation Pliocene ensemble ($Plio_{modern}$) simulated a range of sea level contribution, relative to a default control, from -15.89 m to +28.27 m, with a mean of 1.85 ± 9.28 m over 10,000 years (Table 5.4). With a reduced Pliocene initial ice sheet, a subset of simulations from our $Plio_{modern}$ ensemble simulated sea level contributions of -1.28 m to +19.96 m over the same period, with a mean of 9.10 ± 6.74 (table 5.4). This underlines

the role of a smaller initial ice sheet in driving a larger sea level contribution relative to modern, consistent with previous studies (Dolan et al., 2018, de Boer et al., 2015).

Under a modern climate, initialised from the modern ice sheet, the $Control_{modern}$ ensemble underlined the sensitivity of the control simulation to perturbed parameters - with sea level contribution from -11.30 m to +2.40 m over a 5,000 year simulation period, and a mean of -4.93 ± 4.65 m (Table 5.4). The magnitude of negative sea level contributions showed a strong dependence on Weertman friction coefficient (Fig. 5.8). In order to partially account for sea level variability due to parameter perturbations, and the strong influence of the Weertman friction coefficient, we subtracted the $Control_{ensemble}$ results from 5,000 year $Plio_{modern}$ and $Plio_{PRISM}$ results. For $Plio_{modern}$, this resulted in a mean simulated sea level contribution of 4.44 ± 2.19 m, and reduced the range to 0.31 m to 8.41 m (Table 5.4). For $Plio_{PRISM}$, subtracting $Control_{ensemble}$ also increased the mean, to 15.25 ± 1.33 m contribution to sea level, and narrowed the range to 12.82 m to 17.41 m (Table 5.4).

We also compared our ensemble results to reconstructions of Wilkes basin Pliocene deglacial history (Cook et al., 2013, Bertram et al., 2018). This data comparison step slightly favours CCSM4-Utr, the warmest surface air temperature model. CCSM4-Utr also has high ocean thermal forcing in the Wilkes basin, which contributes to basal melting alongside more negative surface mass balance in this region - promoting retreat of ice streams. In addition, we compared our ensemble results with a reconstructed Pliocene sea level range (Grant and Naish, 2021). Subtracting $Control_{modern}$ from equivalent $Plio_{modern}$ simulations, and calibrating against Wilkes margin retreat and Pliocene sea level range gave a mean sea level contribution of 4.70 ± 2.24 m, with a range from 0.80 m to 8.41 m.

As outlined elsewhere (Section 1.4.2), Pliocene sea level reconstructions have large uncertainties. The use of the Wilkes margin data comparison proves to be more informative than comparing to sea level reconstructions alone in ruling out ensemble members in our modelling framework, with more ruled out by the Wilkes calibration alone compared with the sea level data comparison alone. For generally lower order physics, lower resolution models used to simulate Pliocene Antarctica, the Wilkes basin data comparison we apply here may exclude less simulations, where model resolution and less comprehensive physics do not capture Wilkes retreat (Section 5.4.6). We also note that 29 of the ensemble members passing the Wilkes calibration in our main ensemble fall outside the reconstructed sea level range. The Wilkes calibration favours higher Weertman friction coefficient simulations. With high Weertman friction showing a strong association with lower sea level contributions, this has the residual effect that the Wilkes calibration decreases mean simulated sea level contribution. Sensitivity to the Weertman friction coefficient, seen across ensembles in this chapter, may be an artefact of our elevation-dependent basal

friction scheme. We based our scheme on previous palaeo-Antarctic studies (Martin et al., 2011, Blasco et al., 2021), however, had we used an alternative elevation dependence (e.g. of the form used in Matero et al. 2020) we could have expected a different Weertman friction dependence. With a constant friction coefficient for bedrock above sea level, this likely made the ice sheet more sensitive to Weertman friction coefficient perturbed across a wide range. Specifically, regions of East Antarctica grounded high above sea level have spatially invariant Weertman friction coefficients in our scheme. In ensemble members with high Weertman friction coefficients, this reduces export of ice from the interior. Over millennium time scales, this can cause the ice sheet to thicken substantially. With an alternative Weertman friction elevation-dependence, we could expect a stronger relationship between Wilkes retreat and sea level contribution, as the latter would not be as strongly dependent on this parameter.

The sensitivity of the control ensemble to parameter perturbations under a modern climate lends support to the use of control ensembles in future Pliocene perturbed parameter ensembles. Whilst exploration of parametric uncertainty is a primary function of perturbed parameter ensembles, subtracting a control ensemble is a useful approach to partially account for potentially unphysical behaviour, such as model drift, as well as calculate equilibrium responses to forcings (e.g. Murphy et al. 2004). Given the large sea level variability in our control ensemble, which likely reflects an overly large range for the Weertman friction coefficient, simulations relative to a single default control simulation do reflect ice sheet response to Pliocene climate forcing, but are strongly influenced by the Weertman coefficient. Partially accounting for this through the use of the control ensemble moves the majority of ensemble members into the reconstructed sea level range, particularly at the low end. We conclude therefore that the difference between Pliocene simulations and the control ensemble gives a better indication of Pliocene sea level than Pliocene simulations relative to the default control.

# 5.6 Appendix

## 5.6.1 Selection of Ensemble subset for further tests

To select a subset of simulations to run with for the $Plio_{PRISM}$ and $Control_{modern}$ ensembles, we assess the $Plio_{modern}$ ensemble at 5,000 simulation years. In this first step however, we simply repeat the ten largest negative change in VAF, the ten smallest (sea level fall) and ten intermediate. We assess which ensemble members to prioritise based on a judgement of whether some parameter values drive an overly fast initial ice sheet and large sea level contribution. Most ensemble members (n=118) completed 5,000 simulation years.

Looking at the $5^{th}$ percentile of modelled ice sheet speed from BISICLES at the start of each ice sheet simulation, we can assess whether some parameter values, specifically the Weertman friction coefficient, result in ice speeds faster than we would judge to be reasonable for the slow moving interior of the ice sheet. Comparing modelled ice sheet velocity at the start of the run to observations gives a clearer insight into the behaviour of interior regions in a configuration closest to modern.

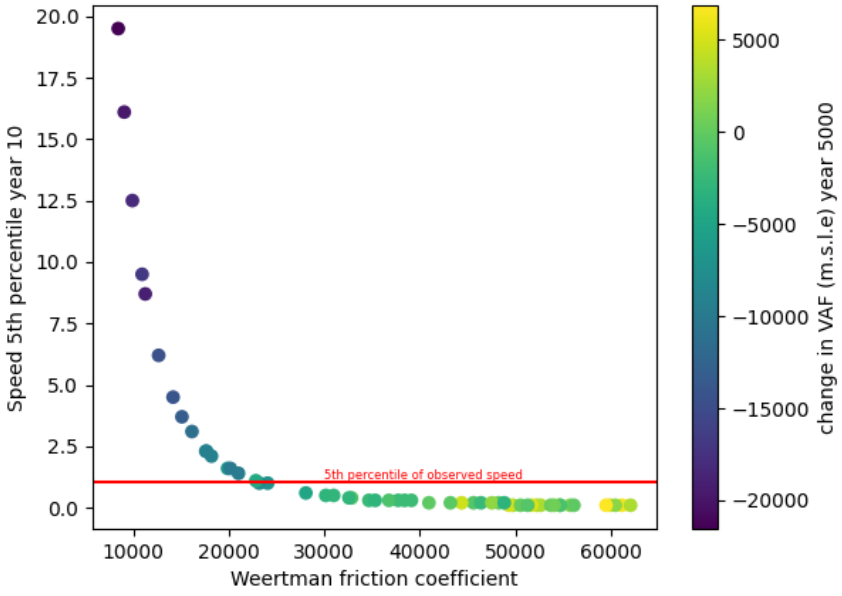


Fig. 5.28 $5^{th}$ percentile of ice speed at year 10 as a function of Weertman friction coefficient.

Figure 5.28 shows the relationship between the 5th percentile of modelled ice speed and Weertman friction coefficient, with marker color corresponding to change in volume above flotation in metres sea level equivalent. The red horizontal line indicates the $5^{th}$ percentile of speed observations for Antarctica in the modern (Mouginot et al., 2019).

This shows a very strong and non-linear relationship between the two, with values of C < 10,000 leading to a $5^{th}$ percentile ice speed up to an order of magnitude faster than that of current observations. The low C simulations show large decreases in volume above floatation after 5,000 years (marker color, Figure 5.28).

Although the model setup does allow dynamic ice streaming during the simulation (Section 3.2.3), such rapid minimum ice speeds (i.e. those of the interior of the ice sheet) are likely unrealistic. We therefore select from simulations with Weertman friction coefficient higher than 20,000 to run under our control climate and PRISM initial geometry conditions.

### 5.6.2 Experiment list

| Run | $\gamma_0$ | *UMV* | *LRP* | *PDDi* | *WeertC* | *GCM* |
|---|---|---|---|---|---|---|
| run001 | 9.619E+03 | 2.058E+20 | 7.158E-04 | 1.959E-02 | 2.230E+04 | COSMOS |
| run002 | 1.592E+05 | 7.970E+20 | 5.273E-04 | 1.682E-02 | 1.311E+04 | COSMOS |
| run003 | 1.592E+05 | 2.366E+19 | 3.960E-04 | 1.198E-02 | 1.659E+04 | COSMOS |
| run004 | 4.713E+05 | 6.491E+20 | 6.618E-04 | 1.355E-02 | 3.157E+04 | COSMOS |
| run005 | 1.592E+05 | 3.212E+20 | 1.022E-04 | 1.815E-02 | 3.984E+04 | COSMOS |
| run006 | 8.698E+04 | 1.489E+20 | 3.444E-04 | 1.993E-02 | 2.820E+04 | COSMOS |
| run007 | 1.592E+05 | 8.871E+20 | 2.139E-05 | 1.271E-02 | 4.400E+04 | COSMOS |
| run008 | 8.698E+04 | 6.578E+20 | 2.943E-04 | 1.727E-02 | 5.022E+04 | COSMOS |
| run009 | 8.698E+04 | 1.077E+20 | 5.213E-04 | 1.718E-02 | 5.887E+04 | COSMOS |
| run010 | 1.592E+05 | 7.192E+19 | 6.474E-04 | 1.974E-02 | 1.456E+04 | COSMOS |
| run011 | 9.619E+03 | 2.562E+20 | 1.771E-04 | 1.574E-02 | 5.798E+04 | COSMOS |
| run012 | 8.698E+04 | 9.920E+20 | 4.776E-04 | 8.197E-03 | 4.498E+04 | COSMOS |
| run013 | 8.698E+04 | 6.587E+20 | 9.126E-06 | 1.582E-02 | 3.785E+04 | COSMOS |
| run014 | 2.101E+04 | 8.665E+20 | 3.862E-04 | 1.031E-02 | 2.864E+04 | COSMOS |
| run015 | 8.698E+04 | 3.972E+20 | 6.733E-04 | 1.365E-02 | 1.179E+04 | COSMOS |
| run016 | 2.101E+04 | 3.947E+18 | 2.749E-04 | 9.265E-03 | 5.533E+04 | COSMOS |
| run017 | 8.698E+04 | 3.859E+20 | 4.898E-04 | 8.248E-03 | 4.671E+04 | COSMOS |
| run018 | 2.101E+04 | 1.175E+19 | 7.475E-04 | 1.924E-02 | 3.369E+04 | COSMOS |
| run019 | 1.592E+05 | 1.104E+20 | 3.487E-04 | 9.456E-03 | 3.589E+04 | COSMOS |
| run020 | 9.619E+03 | 3.777E+20 | 6.325E-04 | 1.173E-02 | 1.354E+04 | COSMOS |
| run021 | 1.592E+05 | 6.006E+20 | 5.156E-04 | 1.147E-02 | 4.047E+04 | COSMOS |
| run022 | 4.713E+05 | 5.980E+20 | 7.068E-04 | 1.857E-02 | 5.773E+04 | COSMOS |
| run023 | 1.448E+04 | 9.729E+20 | 2.881E-04 | 1.894E-02 | 4.851E+04 | COSMOS |
| run024 | 9.619E+03 | 6.383E+19 | 2.215E-04 | 1.405E-02 | 2.923E+04 | COSMOS |
| run025 | 1.448E+04 | 7.759E+19 | 1.319E-04 | 8.877E-03 | 3.426E+04 | COSMOS |
| run026 | 4.713E+05 | 9.410E+20 | 8.699E-05 | 9.948E-03 | 1.715E+04 | COSMOS |
| run027 | 4.713E+05 | 2.644E+20 | 1.649E-04 | 1.833E-02 | 5.672E+04 | COSMOS |
| run028 | 1.448E+04 | 1.941E+20 | 4.451E-04 | 8.974E-03 | 3.628E+04 | COSMOS |
| run029 | 1.448E+04 | 7.648E+20 | 7.798E-05 | 8.540E-03 | 4.169E+04 | COSMOS |
| run030 | 1.448E+04 | 9.841E+20 | 7.633E-04 | 1.661E-02 | 6.171E+04 | COSMOS |
| run031 | 4.713E+05 | 3.061E+20 | 4.996E-04 | 1.169E-02 | 3.065E+04 | CCSM4-Utr |
| run032 | 4.713E+05 | 7.298E+20 | 5.362E-04 | 1.415E-02 | 2.560E+04 | CCSM4-Utr |
| run033 | 9.619E+03 | 9.661E+20 | 4.020E-04 | 1.541E-02 | 4.717E+04 | CCSM4-Utr |
| run034 | 1.448E+04 | 8.405E+20 | 4.621E-04 | 1.152E-02 | 9.529E+03 | CCSM4-Utr |
| run035 | 9.619E+03 | 8.458E+20 | 5.650E-04 | 1.628E-02 | 5.698E+04 | CCSM4-Utr |
| run036 | 1.592E+05 | 1.590E+20 | 6.058E-04 | 1.514E-02 | 2.209E+04 | CCSM4-Utr |
| run037 | 1.448E+04 | 7.519E+20 | 5.826E-04 | 1.449E-02 | 5.843E+04 | CCSM4-Utr |

| Run | $\gamma_0$ | *UMV* | *LRP* | *PDDi* | *WeertC* | *GCM* |
|---|---|---|---|---|---|---|
| run038 | 1.592E+05 | 6.106E+20 | 2.714E-04 | 1.523E-02 | 2.652E+04 | CCSM4-Utr |
| run039 | 1.592E+05 | 6.721E+20 | 2.082E-04 | 1.678E-02 | 3.897E+04 | CCSM4-Utr |
| run040 | 9.619E+03 | 9.446E+20 | 4.466E-05 | 1.753E-02 | 4.236E+04 | CCSM4-Utr |
| run041 | 9.619E+03 | 2.694E+20 | 4.362E-04 | 1.433E-02 | 2.072E+04 | CCSM4-Utr |
| run042 | 2.101E+04 | 4.688E+20 | 2.358E-04 | 1.703E-02 | 2.962E+04 | CCSM4-Utr |
| run043 | 8.698E+04 | 6.340E+20 | 5.500E-06 | 1.905E-02 | 3.190E+04 | CCSM4-Utr |
| run044 | 2.101E+04 | 5.121E+20 | 8.177E-05 | 1.970E-02 | 3.346E+04 | CCSM4-Utr |
| run045 | 4.713E+05 | 2.326E+20 | 3.178E-04 | 1.617E-02 | 2.522E+04 | CCSM4-Utr |
| run046 | 1.448E+04 | 4.137E+20 | 3.024E-04 | 1.237E-02 | 4.085E+04 | CCSM4-Utr |
| run047 | 8.698E+04 | 3.491E+20 | 1.715E-04 | 1.499E-02 | 2.682E+04 | CCSM4-Utr |
| run048 | 1.592E+05 | 8.715E+20 | 1.802E-04 | 1.787E-02 | 2.743E+04 | CCSM4-Utr |
| run049 | 9.619E+03 | 2.984E+20 | 2.434E-04 | 9.676E-03 | 1.927E+04 | CCSM4-Utr |
| run050 | 4.713E+05 | 1.855E+20 | 2.032E-04 | 1.001E-02 | 1.883E+04 | CCSM4-Utr |
| run051 | 1.592E+05 | 5.249E+20 | 3.331E-04 | 1.946E-02 | 4.334E+04 | CCSM4-Utr |
| run052 | 1.448E+04 | 8.830E+20 | 3.575E-04 | 1.014E-02 | 1.045E+04 | CCSM4-Utr |
| run053 | 8.698E+04 | 5.662E+20 | 7.056E-04 | 1.093E-02 | 7.978E+03 | CCSM4-Utr |
| run054 | 4.713E+05 | 4.958E+20 | 7.963E-04 | 1.281E-02 | 4.510E+04 | CCSM4-Utr |
| run055 | 4.713E+05 | 7.728E+20 | 5.446E-04 | 1.984E-02 | 3.705E+04 | CCSM4-Utr |
| run056 | 1.448E+04 | 9.962E+19 | 7.853E-04 | 8.484E-03 | 2.147E+04 | CCSM4-Utr |
| run057 | 2.101E+04 | 9.131E+20 | 4.972E-05 | 1.083E-02 | 2.612E+04 | CCSM4-Utr |
| run058 | 4.713E+05 | 7.052E+20 | 7.369E-04 | 1.055E-02 | 2.492E+04 | CCSM4-Utr |
| run059 | 9.619E+03 | 1.754E+20 | 5.911E-04 | 1.075E-02 | 5.318E+04 | CCSM4-Utr |
| run060 | 8.698E+04 | 9.293E+20 | 3.359E-04 | 1.558E-02 | 6.070E+04 | CCSM4-Utr |
| run061 | 1.448E+04 | 1.807E+20 | 5.064E-04 | 1.503E-02 | 2.364E+04 | CCSM4-UofT |
| run062 | 9.619E+03 | 5.885E+19 | 5.489E-04 | 1.861E-02 | 1.267E+04 | CCSM4-UofT |
| run063 | 8.698E+04 | 5.832E+20 | 1.084E-04 | 1.181E-02 | 6.116E+04 | CCSM4-UofT |
| run064 | 1.592E+05 | 1.294E+20 | 7.774E-04 | 1.312E-02 | 3.841E+04 | CCSM4-UofT |
| run065 | 9.619E+03 | 1.350E+20 | 3.745E-04 | 1.746E-02 | 5.266E+04 | CCSM4-UofT |
| run066 | 8.698E+04 | 5.061E+20 | 6.251E-04 | 1.766E-02 | 4.563E+04 | CCSM4-UofT |
| run067 | 9.619E+03 | 5.583E+20 | 7.285E-04 | 1.337E-02 | 4.826E+04 | CCSM4-UofT |
| run068 | 8.698E+04 | 8.245E+20 | 5.842E-05 | 9.776E-03 | 4.976E+04 | CCSM4-UofT |
| run069 | 4.713E+05 | 6.213E+20 | 4.692E-04 | 1.888E-02 | 3.468E+04 | CCSM4-UofT |
| run070 | 1.448E+04 | 6.848E+20 | 5.086E-04 | 1.068E-02 | 9.071E+03 | CCSM4-UofT |
| run071 | 1.592E+05 | 7.481E+20 | 1.934E-05 | 8.387E-03 | 4.438E+04 | CCSM4-UofT |
| run072 | 8.698E+04 | 4.324E+20 | 1.544E-04 | 1.658E-02 | 5.992E+04 | CCSM4-UofT |
| run073 | 2.101E+04 | 7.176E+20 | 6.165E-04 | 1.938E-02 | 5.371E+04 | CCSM4-UofT |
| run074 | 9.619E+03 | 2.810E+20 | 3.733E-04 | 1.048E-02 | 9.925E+03 | CCSM4-UofT |
| run075 | 4.713E+05 | 7.396E+20 | 7.250E-04 | 1.299E-02 | 3.913E+04 | CCSM4-UofT |
| run076 | 1.592E+05 | 4.489E+20 | 1.257E-04 | 1.346E-02 | 1.418E+04 | CCSM4-UofT |

| Run | $\gamma_0$ | *UMV* | *LRP* | *PDDi* | *WeertC* | *GCM* |
|---|---|---|---|---|---|---|
| run077 | 1.448E+04 | 8.006E+20 | 2.563E-04 | 1.483E-02 | 5.224E+04 | CCSM4-UofT |
| run078 | 2.101E+04 | 9.035E+20 | 1.975E-04 | 1.424E-02 | 8.443E+03 | CCSM4-UofT |
| run079 | 2.101E+04 | 4.857E+20 | 4.839E-04 | 1.400E-02 | 5.463E+04 | CCSM4-UofT |
| run080 | 1.448E+04 | 5.352E+20 | 2.826E-04 | 1.535E-02 | 3.287E+04 | CCSM4-UofT |
| run081 | 8.698E+04 | 2.872E+20 | 1.133E-04 | 1.306E-02 | 4.936E+04 | CCSM4-UofT |
| run082 | 1.448E+04 | 1.582E+20 | 2.285E-04 | 1.633E-02 | 1.989E+04 | CCSM4-UofT |
| run083 | 4.713E+05 | 9.823E+20 | 7.923E-04 | 1.805E-02 | 2.408E+04 | CCSM4-UofT |
| run084 | 1.592E+05 | 7.764E+20 | 4.133E-04 | 1.027E-02 | 1.511E+04 | CCSM4-UofT |
| run085 | 9.619E+03 | 6.314E+20 | 6.463E-04 | 1.847E-02 | 5.575E+04 | CCSM4-UofT |
| run086 | 2.101E+04 | 6.817E+20 | 4.289E-04 | 9.097E-03 | 1.094E+04 | CCSM4-UofT |
| run087 | 2.101E+04 | 2.182E+20 | 6.287E-05 | 8.068E-03 | 1.769E+04 | CCSM4-UofT |
| run088 | 9.619E+03 | 8.528E+20 | 4.249E-04 | 1.770E-02 | 4.199E+04 | CCSM4-UofT |
| run089 | 1.592E+05 | 4.093E+19 | 3.104E-05 | 1.468E-02 | 1.616E+04 | CCSM4-UofT |
| run090 | 1.448E+04 | 4.361E+20 | 6.870E-04 | 9.581E-03 | 3.017E+04 | CCSM4-UofT |
| run091 | 2.101E+04 | 5.258E+20 | 3.886E-04 | 1.384E-02 | 4.096E+04 | HadCM3 |
| run092 | 4.713E+05 | 2.464E+20 | 1.893E-04 | 8.611E-03 | 1.568E+04 | HadCM3 |
| run093 | 1.448E+04 | 4.759E+20 | 6.947E-05 | 1.265E-02 | 5.173E+04 | HadCM3 |
| run094 | 4.713E+05 | 5.846E+20 | 1.343E-04 | 1.321E-02 | 1.127E+04 | HadCM3 |
| run095 | 2.101E+04 | 3.672E+20 | 3.085E-04 | 1.477E-02 | 6.206E+04 | HadCM3 |
| run096 | 8.698E+04 | 4.066E+20 | 4.486E-04 | 1.451E-02 | 5.471E+04 | HadCM3 |
| run097 | 1.592E+05 | 4.179E+20 | 1.528E-04 | 1.794E-02 | 3.260E+04 | HadCM3 |
| run098 | 1.448E+04 | 8.285E+20 | 5.698E-04 | 1.640E-02 | 5.406E+04 | HadCM3 |
| run099 | 1.592E+05 | 8.471E+19 | 6.533E-04 | 1.912E-02 | 2.018E+04 | HadCM3 |
| run100 | 4.713E+05 | 1.189E+20 | 5.781E-04 | 1.872E-02 | 8.866E+03 | HadCM3 |
| run101 | 4.713E+05 | 4.561E+20 | 2.189E-04 | 1.376E-02 | 2.321E+04 | HadCM3 |
| run102 | 9.619E+03 | 7.847E+20 | 6.102E-04 | 1.244E-02 | 6.046E+04 | HadCM3 |
| run103 | 2.101E+04 | 3.287E+20 | 3.205E-04 | 8.784E-03 | 1.820E+04 | HadCM3 |
| run104 | 2.101E+04 | 3.639E+20 | 7.574E-04 | 9.333E-03 | 5.613E+04 | HadCM3 |
| run105 | 1.592E+05 | 4.662E+20 | 2.486E-04 | 1.129E-02 | 4.641E+04 | HadCM3 |
| run106 | 4.713E+05 | 6.925E+20 | 6.962E-04 | 1.594E-02 | 2.103E+04 | HadCM3 |
| run107 | 2.101E+04 | 7.161E+20 | 2.641E-04 | 1.251E-02 | 4.754E+04 | HadCM3 |
| run108 | 2.101E+04 | 2.411E+20 | 6.822E-04 | 1.736E-02 | 3.774E+04 | HadCM3 |
| run109 | 1.448E+04 | 3.566E+20 | 4.564E-04 | 1.113E-02 | 3.099E+04 | HadCM3 |
| run110 | 9.619E+03 | 8.096E+20 | 7.679E-04 | 9.164E-03 | 5.056E+04 | HadCM3 |
| run111 | 8.698E+04 | 3.130E+19 | 3.620E-04 | 1.568E-02 | 4.321E+04 | HadCM3 |
| run112 | 8.698E+04 | 3.411E+20 | 5.538E-04 | 1.131E-02 | 3.534E+04 | HadCM3 |
| run113 | 1.448E+04 | 5.458E+20 | 4.161E-04 | 1.108E-02 | 3.677E+04 | HadCM3 |
| run114 | 2.101E+04 | 8.984E+20 | 1.414E-04 | 1.829E-02 | 1.760E+04 | HadCM3 |
| run115 | 8.698E+04 | 5.686E+20 | 6.383E-04 | 1.214E-02 | 4.884E+04 | HadCM3 |

| Run | $\gamma_0$ | *UMV* | *LRP* | *PDDi* | *WeertC* | *GCM* |
|---|---|---|---|---|---|---|
| run116 | 4.713E+05 | 2.146E+20 | 6.670E-04 | 1.608E-02 | 1.216E+04 | HadCM3 |
| run117 | 2.101E+04 | 9.571E+20 | 5.969E-04 | 1.224E-02 | 2.808E+04 | HadCM3 |
| run118 | 9.619E+03 | 9.250E+20 | 3.875E-05 | 9.879E-03 | 2.285E+04 | HadCM3 |
| run119 | 2.101E+04 | 3.116E+20 | 7.431E-04 | 1.203E-02 | 5.130E+04 | HadCM3 |
| run120 | 9.619E+03 | 4.374E+19 | 9.523E-05 | 1.690E-02 | 5.950E+04 | HadCM3 |

Table 5.5 Parameter values for all simulations in the 120-member perturbed parameter ensemble, as well as forcing model from PlioMIP2 (*GCM*).

| Run | $Plio_{mod}$ 5ka $\Delta V$ ($m^3$) | $Plio_{mod}$ 10ka $\Delta V$ ($m^3$) | $Ctrl_{mod}$ 5ka $\Delta V$ ($m^3$) | $Plio_{prism}$ 5ka $\Delta V$ ($m^3$) | $Plio_{prism}$ 10ka $\Delta V$ ($m^3$) |
|---|---|---|---|---|---|
| run001 | -4.101E+15 | -4.097E+15 | | | |
| run002 | -7.443E+15 | -8.276E+15 | | | |
| run003 | -5.809E+15 | -6.182E+15 | | | |
| run004 | -3.285E+15 | -4.522E+15 | | | |
| run005 | -1.118E+15 | 7.976E+13 | | | |
| run006 | -3.065E+15 | -2.606E+15 | | | |
| run007 | -9.474E+14 | -1.289E+15 | | | |
| run008 | -1.912E+15 | -2.087E+15 | | | |
| run009 | -1.502E+15 | -7.799E+14 | 3.516E+15 | 1.398E+15 | 2.706E+15 |
| run010 | -7.044E+15 | -7.613E+15 | | | |
| run011 | 5.484E+14 | 1.956E+15 | | | |
| run012 | -2.194E+15 | -2.496E+15 | | | |
| run013 | -9.243E+14 | 3.679E+14 | | | |
| run014 | -2.517E+15 | -2.076E+15 | | | |
| run015 | -7.864E+15 | -8.607E+15 | | | |
| run016 | 6.533E+14 | 2.971E+15 | | | |
| run017 | -2.019E+15 | -1.489E+15 | | | |
| run018 | | | | | |
| run019 | -1.888E+15 | -2.625E+15 | | | |
| run020 | -6.052E+15 | -6.955E+15 | | | |
| run021 | -3.071E+15 | -3.093E+15 | | | |
| run022 | -2.357E+15 | | | | |
| run023 | -1.198E+15 | -6.344E+14 | | | |
| run024 | -1.943E+15 | -1.180E+15 | | | |
| run025 | -8.976E+14 | 3.578E+14 | 2.010E+15 | 1.102E+15 | 1.851E+15 |
| run026 | -5.561E+15 | -6.007E+15 | | | |
| run027 | -6.907E+14 | 4.559E+14 | | | |
| run028 | -1.476E+15 | | 1.928E+15 | 8.984E+14 | 1.608E+15 |
| run029 | 1.177E+14 | 1.812E+15 | | | |

| Run | $Plio_{mod}$ 5ka $\Delta V$ ($m^3$) | $Plio_{mod}$ 10ka $\Delta V$ ($m^3$) | $Ctrl_{mod}$ 5ka $\Delta V$ ($m^3$) | $Plio_{prism}$ 5ka $\Delta V$ ($m^3$) | $Plio_{prism}$ 10ka $\Delta V$ ($m^3$) |
|---|---|---|---|---|---|
| run030 | -1.483E+15 | -1.253E+15 | | | |
| run031 | -2.312E+15 | -2.815E+15 | | | |
| run032 | -3.602E+15 | | 9.018E+13 | -2.001E+15 | -2.146E+15 |
| run033 | -6.049E+14 | -1.350E+14 | | | |
| run034 | -8.526E+15 | -1.041E+16 | | | |
| run035 | -2.187E+14 | 9.123E+14 | | | |
| run036 | -5.043E+15 | | -4.226E+14 | -2.114E+15 | -2.294E+15 |
| run037 | -3.429E+14 | 6.615E+14 | | | |
| run038 | -4.310E+15 | -4.598E+15 | 5.100E+14 | -1.511E+15 | -1.907E+15 |
| run039 | -1.361E+15 | -1.599E+15 | 2.115E+15 | 4.985E+14 | 1.054E+15 |
| run040 | 9.626E+14 | 2.629E+15 | 2.889E+15 | 2.420E+15 | 3.351E+15 |
| run041 | -4.525E+15 | -4.645E+15 | -6.750E+14 | -1.155E+15 | -1.256E+15 |
| run042 | -2.554E+15 | -2.843E+15 | | | |
| run043 | -2.336E+15 | -2.806E+15 | | | |
| run044 | -1.195E+15 | -9.163E+14 | 1.798E+15 | 6.223E+14 | 9.918E+14 |
| run045 | -3.142E+15 | -2.785E+15 | | | |
| run046 | -6.248E+14 | -4.122E+14 | | | |
| run047 | -3.694E+15 | -4.191E+15 | 6.508E+14 | -1.112E+15 | -1.127E+15 |
| run048 | -4.135E+15 | -4.943E+15 | 6.564E+14 | -1.652E+15 | -1.805E+15 |
| run049 | -3.419E+15 | -3.429E+15 | | | |
| run050 | -4.296E+15 | -4.446E+15 | | | |
| run051 | -1.091E+15 | -7.465E+14 | | | |
| run052 | -7.808E+15 | -8.402E+15 | | | |
| run053 | -1.133E+16 | -1.251E+16 | | | |
| run054 | -1.514E+15 | -6.039E+14 | 2.129E+15 | 7.926E+14 | 1.489E+15 |
| run055 | -2.297E+15 | -1.735E+15 | | | |
| run056 | -4.015E+15 | -3.883E+15 | -4.338E+14 | -8.689E+14 | -9.241E+14 |
| run057 | -1.577E+15 | -1.028E+15 | | | |
| run058 | -3.465E+15 | -3.934E+15 | | | |
| run059 | -1.009E+14 | 1.274E+15 | | | |
| run060 | 8.181E+14 | 2.518E+15 | 3.750E+15 | 3.328E+15 | 4.805E+15 |
| run061 | | | | | |
| run062 | -6.141E+15 | -7.096E+15 | | | |
| run063 | 1.813E+15 | 3.073E+15 | 4.236E+15 | 3.161E+15 | 4.471E+15 |
| run064 | -1.551E+15 | -8.920E+14 | | | |
| run065 | 8.602E+14 | 2.394E+15 | 3.485E+15 | 2.795E+15 | 4.082E+15 |
| run066 | -1.078E+15 | -1.840E+15 | | | |
| run067 | -6.061E+14 | -2.786E+14 | | | |

| Run | $Plio_{mod}$ 5ka $\Delta V$ ($m^3$) | $Plio_{mod}$ 10ka $\Delta V$ ($m^3$) | $Ctrl_{mod}$ 5ka $\Delta V$ ($m^3$) | $Plio_{prism}$ 5ka $\Delta V$ ($m^3$) | $Plio_{prism}$ 10ka $\Delta V$ ($m^3$) |
|---|---|---|---|---|---|
| run068 | 3.497E+14 | 7.762E+14 | | | |
| run069 | -1.599E+15 | -1.148E+15 | | | |
| run070 | -8.303E+15 | -9.185E+15 | | | |
| run071 | 1.279E+15 | 2.415E+15 | 2.837E+15 | 1.402E+15 | 1.692E+15 |
| run072 | 1.208E+15 | 2.205E+15 | 4.029E+15 | 2.841E+15 | 4.042E+15 |
| run073 | -6.909E+14 | -4.306E+13 | | | |
| run074 | -7.579E+15 | -8.517E+15 | | | |
| run075 | -1.556E+15 | -1.209E+15 | | | |
| run076 | -6.256E+15 | -6.868E+15 | | | |
| run077 | 6.673E+14 | 1.447E+15 | | | |
| run078 | -9.160E+15 | -9.820E+15 | | | |
| run079 | -1.287E+14 | 6.062E+14 | | | |
| run080 | -6.973E+14 | 1.892E+13 | | | |
| run081 | 1.472E+15 | 3.074E+15 | 3.342E+15 | 1.973E+15 | 3.009E+15 |
| run082 | -3.073E+15 | -3.262E+15 | | | |
| run083 | -3.479E+15 | -3.678E+15 | -1.969E+14 | -1.854E+15 | -2.497E+15 |
| run084 | -5.922E+15 | -6.493E+15 | | | |
| run085 | -1.370E+14 | 6.574E+14 | | | |
| run086 | -7.133E+15 | -7.909E+15 | | | |
| run087 | -3.560E+15 | -3.919E+15 | | | |
| run088 | | | | | |
| run089 | -5.135E+15 | | | | |
| run090 | -1.664E+15 | -1.238E+15 | | | |
| run091 | -6.879E+14 | 3.527E+14 | | | |
| run092 | -6.031E+15 | -6.814E+15 | | | |
| run093 | 1.605E+15 | 3.769E+15 | 3.733E+15 | 2.779E+15 | 3.870E+15 |
| run094 | -8.356E+15 | -9.355E+15 | | | |
| run095 | 6.427E+14 | 1.487E+15 | 4.007E+15 | 2.613E+15 | 3.898E+15 |
| run096 | -1.504E+15 | -1.019E+15 | 3.237E+15 | 1.069E+15 | 1.493E+15 |
| run097 | -1.921E+15 | -1.795E+15 | | | |
| run098 | -3.971E+14 | 4.425E+12 | | | |
| run099 | -4.752E+15 | -5.069E+15 | -8.849E+14 | -2.172E+15 | -2.554E+15 |
| run100 | -1.030E+16 | -1.136E+16 | | | |
| run101 | -3.848E+15 | -4.076E+15 | -3.595E+14 | -2.123E+15 | -2.527E+15 |
| run102 | 2.176E+14 | 1.232E+15 | | | |
| run103 | -4.105E+15 | -4.494E+15 | | | |
| run104 | -8.280E+14 | -2.016E+14 | | | |
| run105 | -1.928E+15 | -1.555E+15 | | | |

| Run | $Plio_{mod}$ 5ka $\Delta$V ($m^3$) | $Plio_{mod}$ 10ka $\Delta$V ($m^3$) | $Ctrl_{mod}$ 5ka $\Delta$V ($m^3$) | $Plio_{prism}$ 5ka $\Delta$V ($m^3$) | $Plio_{prism}$ 10ka $\Delta$V ($m^3$) |
|---|---|---|---|---|---|
| run106 | -4.691E+15 | -5.200E+15 | -8.486E+14 | -2.670E+15 | -3.126E+15 |
| run107 | 2.716E+14 | 1.817E+15 | | | |
| run108 | -1.512E+15 | -8.172E+14 | | | |
| run109 | -1.703E+15 | -1.181E+15 | | | |
| run110 | -5.500E+14 | 7.415E+13 | | | |
| run111 | -7.740E+14 | 3.658E+14 | | | |
| run112 | -1.961E+15 | -1.729E+15 | | | |
| run113 | -9.908E+14 | -4.231E+14 | 1.939E+15 | 1.198E+15 | 1.418E+15 |
| run114 | -4.249E+15 | | | | |
| run115 | -2.269E+15 | -2.164E+15 | | | |
| run116 | | | | | |
| run117 | -2.462E+15 | -2.232E+15 | | | |
| run118 | -2.085E+15 | -1.920E+15 | | | |
| run119 | -1.048E+15 | -7.243E+14 | 2.859E+15 | 1.584E+15 | 2.273E+15 |
| run120 | 2.502E+15 | 5.598E+15 | 4.637E+15 | 3.718E+15 | 5.608E+15 |

Table 5.6 Total volume change ($\Delta$ V $m^3$) from the initial ice sheet for $Plio_{modern}$ at 5,000 and 10,000 years, $Control_{modern}$ at 5,000 years, and $Plio_{PRISM}$ at 5,000 and 10,000 years. Blank entries indicate that the simulation failed before reaching the run-time indicated in the column header.

| Run | Wilkes Pass or fail 5,000 years | Wilkes Pass or fail 10,000 years | Run | Wilkes Pass or fail 5,000 years | Wilkes Pass or fail 10,000 years |
|---|---|---|---|---|---|
| run001 | fail | fail | run060 | pass | pass |
| run002 | fail | fail | run061 | | |
| run003 | fail | fail | run062 | fail | fail |
| run004 | pass | pass | run063 | pass | pass |
| run005 | fail | fail | run064 | fail | fail |
| run006 | fail | fail | run065 | pass | pass |
| run007 | pass | pass | run066 | pass | pass |
| run008 | pass | pass | run067 | pass | pass |
| run009 | pass | pass | run068 | pass | pass |
| run010 | fail | fail | run069 | fail | fail |
| run011 | pass | pass | run070 | fail | fail |
| run012 | pass | pass | run071 | fail | fail |
| run013 | fail | fail | run072 | pass | pass |
| run014 | fail | fail | run073 | pass | pass |
| run015 | fail | fail | run074 | fail | fail |
| run016 | pass | pass | run075 | fail | fail |

| Run | Wilkes Pass or fail 5,000 years | Wilkes Pass or fail 10,000 years | Run | Wilkes Pass or fail 5,000 years | Wilkes Pass or fail 10,000 years |
|---|---|---|---|---|---|
| run017 | pass | pass | run076 | fail | fail |
| run018 | | | run077 | pass | pass |
| run019 | pass | pass | run078 | fail | fail |
| run020 | fail | fail | run079 | pass | pass |
| run021 | pass | pass | run080 | fail | fail |
| run022 | | | run081 | fail | fail |
| run023 | pass | pass | run082 | fail | fail |
| run024 | fail | fail | run083 | fail | fail |
| run025 | fail | fail | run084 | fail | fail |
| run026 | fail | fail | run085 | pass | pass |
| run027 | pass | pass | run086 | fail | fail |
| run028 | | | run087 | fail | fail |
| run029 | fail | fail | run088 | | |
| run030 | pass | pass | run089 | | |
| run031 | pass | pass | run090 | fail | fail |
| run032 | | | run091 | fail | fail |
| run033 | pass | pass | run092 | fail | fail |
| run034 | fail | pass | run093 | pass | pass |
| run035 | pass | pass | run094 | fail | fail |
| run036 | | | run095 | pass | pass |
| run037 | pass | pass | run096 | pass | pass |
| run038 | pass | pass | run097 | fail | fail |
| run039 | pass | pass | run098 | pass | pass |
| run040 | pass | pass | run099 | fail | fail |
| run041 | pass | pass | run100 | fail | fail |
| run042 | pass | pass | run101 | fail | fail |
| run043 | pass | pass | run102 | pass | pass |
| run044 | pass | pass | run103 | fail | fail |
| run045 | pass | pass | run104 | pass | pass |
| run046 | pass | pass | run105 | pass | pass |
| run047 | pass | pass | run106 | fail | fail |
| run048 | pass | pass | run107 | fail | pass |
| run049 | fail | fail | run108 | fail | fail |
| run050 | fail | fail | run109 | fail | fail |
| run051 | pass | pass | run110 | pass | pass |
| run052 | fail | fail | run111 | fail | fail |
| run053 | pass | pass | run112 | fail | fail |
| run054 | pass | pass | run113 | fail | fail |

| Run | Wilkes Pass or fail 5,000 years | Wilkes Pass or fail 10,000 years | Run | Wilkes Pass or fail 5,000 years | Wilkes Pass or fail 10,000 years |
|---|---|---|---|---|---|
| run055 | pass | pass | run114 | | |
| run056 | pass | pass | run115 | pass | pass |
| run057 | fail | fail | run116 | | |
| run058 | pass | pass | run117 | fail | fail |
| run059 | pass | pass | run118 | fail | fail |
| run060 | pass | pass | run119 | pass | pass |
| run061 | | | run120 | pass | fail |

Table 5.7 Results of the Wilkes retreat calibration at 5,000 and 10,000 years

# Chapter 6

# Summary

## 6.1 Introduction

This thesis aimed to explore uncertainties in Antarctic ice sheet evolution under projected $21^{st}$ century climate, and in the warm Pliocene, using the BISICLES ice sheet model. It presented the BISICLES contribution to the Ice Sheet Mode Intercomparison Project for the Climate Model Intercomparison Phase 6 (ISMIP6), complementing previous ISMIP6 studies (Seroussi et al., 2020, Payne et al., 2021). Moreover, Chapter 2 presented simulations that contributed key findings to the synthesis of Edwards et al. (2021)(see below).

The work in this thesis is the first application of the BISICLES ice sheet model to the Pliocene Antarctic ice sheet. It presented a new approach to simulating the Pliocene Antarctic ice sheet, capturing processes of Glacial Isostatic Adjustment (GIA)(Section 3.2.2; Kachuck et al. 2020), ice stream evolution (Section 3.2.3; Gandy et al. 2019) and Pliocene climate (Sections 3.2.4, 3.3.5, 4.2.3; Seguinot 2013) within a single modelling framework. It used bias-corrected climate forcing from the Pliocene Model Intercomparison Project Phase 2 (PlioMIP2) (Haywood et al., 2020) (Chapters 4 and 5) for the first time. These developments facilitated an exploration of uncertainty in climate and ice sheet dynamics in simulating the Pliocene Antarctic ice sheet. In this chapter we summarise key findings from each chapter, cross chapter findings and recommendations for future work.

## 6.2 Chapter 2: Century scale projections of the Antarctic contribution to Sea level

Chapter 2 presented projections of the Antarctic contribution to sea level rise by 2100 (Table 2.2, Figure 2.4) under low and very high emissions scenarios (RCP2.6/ SSP1-2.6 and RCP8.5/ SSP5-8.5), exploring the impact of multiple modelling choices - climate model, basal melt sensitivity to ocean forcing, and ice shelf collapse - on the results to contribute to the ISMIP6 intercomparison project (Nowicki et al., 2016). These were performed with the BISICLES ice sheet model; 11 of the 19 were performed by the author. One particular aim of these 11 simulations was to determine the importance of interactions between modelling choices, to inform the synthesis of ISMIP6 projections by Edwards et al. (2021)

The range of projected sea level contributions from 2015 to 2100, relative to the control, is -53 mm SLE to +125 mm SLE for RCP8.5/SSP5-8.5 (N=14), and -17 mm SLE to +62 mm SLE for RCP2.6/SSP1-2.6 (N=4). Basal melt sensitivity determines the balance between dynamical mass loss and increased accumulation, i.e. the sign of net sea level contribution. Under the very high emissions scenarios, some models (CNRM-CM6-1, CCSM4) have increased surface mass balance. Under low basal melt sensitivity, dynamic mass loss can be slower than mass gain through increased accumulation occurring over large areas of the ice sheet – particularly the EAIS. Where mass gain through increased surface mass balance is greater than dynamic losses, overall sea level contribution is negative by 2100.

Whilst sea level contribution is generally larger for higher basal melt sensitivity, the increase in sea level contribution does not scale directly with increase in basal melt sensitivity. For example, NorESM1-M forced simulations for RCP2.6 contribute less to sea level for the highest basal melt sensitivity ($PIGL_{95}$) compared with the next highest basal melt sensitivity ($PIGL_{50}$)(Figure 2.4).

Chapter 2 supports the result in Edwards et al. (2021) that there is a smaller spread of sea level contribution across different basal melt parameter values under RCP2.6 compared wit RCP8.5. It also supports the finding in Edwards et al. (2021) that ice shelf collapse and basal melt sensitivity have limited interaction: i.e. ice shelf collapse sea level contribution is very similar under the basal melt parameter sensitivity values sampled.

## 6.3 Chapter 3: Uncertainties at the base of the ice sheet

Chapter 3 aimed to develop BISICLES for palaeo-ice sheet simulations, and to explore modelling uncertainties related to processes at the base of the ice sheet. This work explored the extent to which modelling uncertainties related to processes at the base of the ice sheet - sensitivity of the bed to changing surface load, ice stream evolution as a function of bed hydrology, bed conditions in slow flowing regions of the domain, and sensitivity of the ice shelves to ocean melt - affected simulations of the Pine Island Glacier under Pliocene climate.

A major advance in this chapter is the implementation of technical advances needed for the application of BISICLES to simulate the Pliocene Antarctic ice sheet for the first time. This involved implementing GIA, surface mass balance and sub shelf melt calculations for the Pliocene and testing assumptions about the representation of basal sliding for ice sheets different from the modern. We tested this new Pliocene BISICLES set up for the Amundsen Sea Embayment, a larger domain than in previous publications with GIA-enabled BISICLES (GIANT-BISICLES) (Kachuck et al., 2020). We perturbed five parameters relating to GIA, basal sliding, and the ISMIP6 basal melt parameterisation used in Chapter 2 in a 30-member Latin Hypercube ensemble design.

Our focus on the Amundsen Sea Embayment allowed for high model resolution in the Pine Island Glacier (PIG) catchment and an exploration of uncertainty using a perturbed parameter ensemble design, over a reasonably long interval. This allowed us to explore the influence of model parameters and their interactions. Whilst this ensemble sought to assess the relative importance of basal process parameters in rate of mass loss from the PIG, it had some limitations. Specifically, focusing on a largely marine-grounded glacier catchment may have obscured the role of high Weertman friction coefficient values in mass gain in the ice sheet interior, that was seen in Chapter 5.

We found an error in the GIA implementation that meant that all simulations underwent background subsidence. Despite this, we were able to discern a stronger influence of Weertman friction coefficient on mass loss than till water depth under the range of values used, setting the priorities for parameter perturbations in the final ensemble, presented in Chapter 5. Subsequent simulations, with the run time configuration amended to avoid unphysical bedrock subsidence, support this conclusion - with Weertman friction coefficient exerting a primary control on the rate of glacier scale mass loss.

Identifying the GIA error, and using Pliocene climate surface mass balance and ocean forcing, hydrology-coupled basal sliding and elevation-dependent bed friction for non-

streaming regions, paves the way for whole Antarctic ice sheet Pliocene simulations in Chapter 5.

## 6.4 Chapter 4: Uncertainties in Pliocene climate

Chapter 4 aimed to investigate the sensitivity of the Antarctic ice sheet to uncertainties in the Pliocene climate and calculations of surface mass balance through a series of scoping experiments. This was to inform the design of a large (120-member) perturbed parameter ensemble of Pliocene Antarctic ice sheet simulations (Chapter 5), that co-sampled uncertainties in the climate, surface mass balance and ice sheet dynamics. In this chapter, we also tested the effect of uncertainty in the bedrock topography by contrasting simulations run with different bedrock boundary conditions.

Chapter 4 first explored the ice sheet response to five of the latest generation Pliocene climate model simulations from PlioMIP2, with two modern initial conditions derived from Bedmap2 (Fretwell et al., 2013, Cornford et al., 2016) and BedMachine (Morlighem et al., 2020). GIA was not enabled for the experiments in this chapter. These ten experiments demonstrate that under Pliocene climates, the choice of model drives larger differences in sea level contribution than initial bedrock topography and ice sheet thickness. However, localised differences in bedrock elevation between Bedmap2 and BedMachine can modulate change in grounded area in response to thermal forcing, such as in the Lambert glacier catchment. Here, a deeper trough at the grounding zone in the BedMachine bedrock is associated with greater thinning compared with Bedmap2 simulations. East Antarctic grounding line retreat is limited in all simulations, consistent with previous studies of the Pliocene initialised from modern (de Boer et al., 2015, Dolan et al., 2018). These experiments also demonstrate the impact of different GCM spatial patterns of Pliocene climate response on the ice sheet. For four of the five climate model forcings, significant ice shelf melting at the start of the simulation period drives rapid collapse of WAIS. But for MIROC4m forced simulations, lower ocean thermal forcing allows ice shelves to persist for longer – buttressing upstream ice. The Filchner-Ronne ice shelf is able to persist for the duration of the 5,000 year simulation period. Negative sea level contribution in MIROC4m-forced simulations shows that even over long time scales, with less basal melt forcing, increased surface mass balance under Pliocene warming can drive a sea level fall. In other words, the net mass gain shown in Chapter 2 under century-scale warming could also persist over millennial timescales, under certain combinations of climate and ice sheet response. This highlights the importance of better estimating changes in Antarctic precipitation both in the past and the future.

The second set of experiments presented in Chapter 4 explore the sensitivity of modelled sea level contribution to 4 surface mass balance parameters, in a 9-member one-at-a-time ensemble design (single parameter perturbations). We find that the parameters controlling ice melt per positive degree day (*PDDi*) and the lapse rate for precipitation with change in temperature (*LRP*) drove the largest range in sea level contribution for the ranges sampled, with *LRP* having the greatest effect. The importance of *LRP* again highlights the sensitivity of the ice sheet to increased surface mass balance across the interior under Pliocene warming.

These results were used to choose the climate forcings: COSMOS, CCSM4-Utr, CCSM4-UofT and HadCM3 for climate model forcing; and parameter perturbations: positive degree day factor for ice (*PDDi*), and precipitation lapse rate (*LRP*) in the surface mass balance calculation; for the final ensemble presented in Chapter 5.

## 6.5 Chapter 5: Perturbed Parameter Ensemble of the Antarctic ice sheet in the Pliocene

Chapter 5 aimed to address two topics. First, the influence of climate and ice sheet modelling choices on simulations of the Pliocene Antarctic ice sheet. The modelling choices encompassed: parameters from the GIA, hydrology-coupled basal sliding, ocean melt, and PDD schemes; climate model forcing; the initial state of the ice sheet; and choices for subtracting a control simulation. Second, how these simulations compare with reconstructions of Pliocene sea level and grounding line retreat in the Wilkes basin of East Antarctica. We perform simulations of the whole Antarctic ice sheet using the modelling framework developed in previous chapters.

Chapter 5 presents three ensembles of simulations (Table 5.4; Figure 5.25):

- $Plio_{modern}$ – a 120-member perturbed parameter ensemble, forced with 4 PlioMIP2 GCMs, perturbing 5 model parameters – Weertman friction coefficient, ice shelf basal melt sensitivity, upper mantle viscosity, precipitation lapse rate and positive degree day factor for ice.
- $Plio_{PRISM}$ – a 30-member subset of the $Plio_{modern}$ ensemble, but initialised from a reduced Pliocene ice sheet derived from the PRISM Antarctic ice sheet used in PLISMIP.

- $Control_{modern}$ – a 30-member ensemble with the same set of parameter values as the $Plio_{PRISM}$ ensemble, initialised from the same thickness and bedrock as $Plio_{modern}$, forced with modern climate.

Firstly, we find a large range of simulated sea level contributions relative to a single control simulation for the $Plio_{modern}$ ensemble: 1.85 ± 9.28 m, with a range from -15.89 m to 28.27 m.

Many of our experiments simulate Wilkes basin retreat from a modern initial ice sheet configuration – in contrast to Chapter 4 and Dolan et al. (2018) and de Boer et al (2015). This likely reflects strong ocean melt forcing and destabilisation through surface ablation at the Wilkes margin, with the warmest GCM (CCSM4-Utr) driving retreat into the Wilkes basin in more simulations than other models.

We found a strong dependence on the Weertman friction coefficient, which dominates ice sheet volume change and thickening – with higher Weertman friction coefficient driving larger sea level fall across all ensemble members. This largely explains the large range in $Plio_{modern}$. The other parameters do not show a systematic relationship with sea level contribution, at least over the ranges sampled.

$Plio_{PRISM}$ simulations contribute more to sea level than simulations initialised from modern ($Plio_{modern}$) as in previous studies (Dolan et al., 2018, de Boer et al., 2015). This underlines the importance of ice sheet initialisation on millennium-scale sea level contribution.

$Control_{modern}$ provides a first exploration of the role of perturbed parameters under modern climate forcing. We find that the control ensemble simulations show a very wide range of sea level contributions (-11.30 m to +2.40 m after 5000 years), with the most negative contributions driven by high values of the Weertman friction coefficient.

Subtracting the control perturbed parameter ensemble from the (subset of the) $Plio_{modern}$ ensemble shifts the range of sea level contributions to higher values, leading to better agreement with reconstructed Pliocene sea level ranges. This approach is equivalent to the anomaly approach used in palaeo-climate studies to remove the effect of biases at modern day (Murphy et al., 2004). For the $Plio_{PRISM}$ simulations, subtracting the control ensemble narrows the sea level contribution range significantly. The influence of the control ensemble in narrowing the sea level contribution range, and improving agreement with reconstructions, underlines the importance of perturbed control ensembles in simulating Pliocene Antarctic sea level contribution. It suggests that future studies should adopt this approach in order to account for the role of parameter perturbations. A further conclusion that can be drawn from the the large impact of parameters in $Control_{modern}$, is that combining modern and palaeo-data constraints could narrow the range of Pliocene

reconstructions. As suggested in future work, applying modern constraints to a control ensemble, designed to simulate the modern ice sheet, could identify parameter values in our Pliocene ensemble that drive unreasonable ice sheet evolution in the modern.

We compare the Pliocene ensembles to reconstructions of Pliocene sea level, and Pliocene deglacial history of the Wilkes subglacial basin based on proxy data. For $Plio_{PRISM}$ simulations, these data comparison steps have no effect – all 30 ensemble members fall within the reconstructed sea level contribution range, and have a retreated Wilkes subglacial basin. For the $Plio_{modern}$ ensemble, the Wilkes basin retreat constraint rules out more ensemble members than the sea level comparison. We note that the large sea level range used (-3.3 m SLE to 22.7 m SLE) reflects uncertainty in Pliocene reconstructions. This demonstrates that requiring Wilkes retreat may be a more effective constraint (rule out more ensemble members) than comparison with sea level reconstructions alone.

Overall, we are able to simulate Pliocene EAIS retreat from a modern initial ice sheet without the need for additional processes such as MICI (DeConto and Pollard, 2016, DeConto et al., 2021). Previous studies have not simulated this retreat from a modern initial condition (Dolan et al., 2018, de Boer et al., 2015), unless additional warming is added to Pliocene climate (Yan et al., 2016). This likely reflects our sampling of uncertainties in climate, perturbing both the surface mass balance calculation, and the climate model forcing itself. We also reproduce Pliocene sea level without MICI, however, high end sea level contributions are more a function of low Weertman friction coefficient.

## 6.6 Cross chapter conclusions

Across future and Pliocene simulation ensembles, marine grounded regions of the West Antarctic ice sheet thin to floatation or collapse entirely, underscoring WAIS vulnerability to ocean-driven warming. WAIS collapse drives a multi-metre sea level contribution from the region, and collapse of EAIS basins may further increase sea level contribution.

However, contributions driven by WAIS collapse can be offset to varying degrees and rates by surface mass balance changes driven by accumulation in the interior. A recurring feature of the warmer-than-modern climates used to force both century-scale Antarctic simulations (Chapter 2) and Pliocene millennium-scale simulations is enhanced precipitation in higher elevation regions of the ice sheet under warming. For Chapter 2 simulations, under some scenarios and low basal melt sensitivity, mass gain through increased precipitation drives an overall sea level fall. For some Chapter 5 simulations, increased precipitation can also offset mass loss through discharge – driving an overall sea level fall in some simulations

even after 10,000 years, though ice sheet model parameters are also influential. After the majority of submarine grounded ice has been lost, warming-driven increases in interior ice sheet SMB can drive sea level fall. In both $Plio_{PRISM}$ and $Plio_{modern}$ ensembles, mean sea level contribution relative to the default control is smaller at 10,000 years compared with at 5,000 years. Similarly, for Chapter 4 simulations forced with multiple GCMs, sea level contribution peaks after 1000 years for most simulations, followed by gradual sea level fall. This shows that under sustained forcing, when the ice sheet has become less sensitive to ocean driven warming through loss of shelf ice and vulnerable submarine ice mass, increased accumulation drives sea level fall.

The overarching aim of this thesis was to assess the sensitivity of the Antarctic ice sheet to uncertain processes under warmer-than-modern climates. To address this, we completed a suite of simulations with a model capable of capturing key ice sheet processes, at relatively high resolution for studies of this kind at continental scale. These experiments explored future emissions scenarios to 2100, and a range of warm Pliocene climates on millennium time scales. We found that, under both periods and time scales, ocean driven change in the West Antarctic ice sheet dominates mass loss. Conversely, warming driven surface mass balance increases can drive mass gain - particularly on longer time scales. For our future projections, we explored a range of climates, ice shelf collapse scenarios and sensitivities to ocean thermal forcing. In these simulations, basal friction coefficients were inferred from modern velocity observations. For our Pliocene simulations, we also explored uncertainty in climate, as well as uncertainty in processes at the base of the ice sheet. We achieved this by perturbing the Weertman friction coefficient, in a modelling framework capable of approximating ice stream evolution. Under Pliocene and modern-observation-based climates, bed friction uncertainty dominated the Antarctic sea level response. Comparing our Pliocene results to palaeo-data, we found a sea level response consistent with the low end of Pliocene reconstructions when initialised from modern. When initialising from a reduced Pliocene ice sheet, sea level response was closer to the high end of sea level reconstructions for the period. A key difference between future projections and our ensembles in Chapter 5, was the exploration of bed friction uncertainty in the latter. Whilst the edges of the basal friction parameter range were ruled out by our comparison to Pliocene data, for sea level relative to the default control with a modern initial ice sheet, the constrained ensemble range remained considerable. This highlights model sensitivity to bed friction uncertainty. Considered alongside future projections in Chapter 1, we might expect that perturbing bed friction increases the sea level range in future projections. To further explore our approach to perturbing basal friction, assess its validity, and quantify its potential impact on uncertainty in future projections, an informative next step would be to apply our modelling framework to the relatively data rich pre-industrial (see Section 6.7).

We have demonstrated the role of perturbed bed friction in driving modelled Antarctic variability, and compared our results to uncertain Pliocene sea level and margin retreat reconstructions. Applying our modelling framework to the pre-industrial would help assess the validity of our approach, and provide an additional constraint on the basal friction parameter range. This would pave the way for a more thorough exploration of projected sea level contribution variability under future emissions scenarios, accounting for basal friction uncertainty. It could help quantify the extent to which the Antarctic sea level contribution range is underestimated, when uncertainty at the base is not explored alongside other uncertain ice sheet processes.

## 6.7 Recommendations for Future work

Our control ensemble in chapter 5 revealed a significant sea level fall with higher Weertman friction coefficient at 5,000 years. This sea level was likely implausible, but judging the plausibility of simulations under quasi-equilibriation with modern climate forcing is challenging. Future work could use a control ensemble of the recent historical period and compare with observations. With the high temporal and spatial resolution of the observational record, particularly compared with the Pliocene, it would provide a stronger constraint on our modelling approach. This could assess whether our modelling framework can simulate Antarctic mass change consistent with historical trends. It would allow us to try and narrow, for example, the plausible Weertman friction range.

For whole Antarctic ice sheet Pliocene simulations, we use a minimum resolution of 4 km. Cornford et al. (2016) have demonstrated the resolution-dependence of BISICLES under extreme ocean forcing, showing that retreat is delayed or absent in some Antarctic glacier catchments unless resolution of 1 km is used. Whilst 4 km is higher resolution than previous Pliocene studies, future work could provide an exploration of resolution-dependence in simulated Pliocene ice sheet dynamics. To make this computationally feasible, one approach would be to focus on specific catchments as we do for the Pine Island glacier in Chapter 3. Simulating individual catchments at high resolution, particularly those overlying the Wilkes basin – which is the focus of our Chapter 5 data comparison, would be an informative first step. Moreover, assessing resolution-dependence for regions of the ice sheet before simulating the whole AIS could allow a more efficient approach. For example, grid resolution could be increased only in regions that show resolution-dependence, and lower resolution could be used in those that do not in subsequent whole Antarctic ice sheet simulations.

We explored only a limited subset of PlioMIP2 GCMs in Chapters 4 and 5. Future work could explore more of the PlioMIP2 ensemble. Further to this, future work could apply a model selection process, as for ISMIP6 CMIP5 GCMs used in Chapter 2. This could identify a diverse subset of PlioMIP2 models with which to force BISICLES simulations. Model selection could also follow the approach of Dolan et al. (2018) – for example forcing BISICLES with control simulation climates to identify any that produce an implausible modern ice sheet. We note, however, that our use of a climate anomaly approach aims to reduce errors due to climate model biases. It is therefore sensitive to the difference between simulated Pliocene and modern control climates, as opposed to the simulated Pliocene or control climate individually.

The work presented in this thesis uses the most simple approach for simulating surface climate forcing – a positive degree day model forced with average monthly temperature and precipitation based on equilibrated Pliocene climate simulations. Moreover, our results are sensitive to the precipitation lapse rate. A more sophisticated approach to calculating SMB and climate-ice feedbacks could help narrow the Pliocene contribution range. Moreover, future work could implement time-evolving climate fields, in order to better capture the temporal aspect of the Antarctic ice sheet warming into the Pliocene, and to explore reversibility of retreat as the climate cools.

# References


Abe-Ouchi, A., Saito, F., Kawamura, K., Raymo, M. E., Okuno, J., Takahashi, K., and Blatter, H. (2013). Insolation-driven 100,000-year glacial cycles and hysteresis of ice-sheet volume. *Nature*, 500(7461):190–193. Number: 7461 Publisher: Nature Publishing Group.

Adhikari, S., Ivins, E. R., Larour, E., Seroussi, H., Morlighem, M., and Nowicki, S. (2014). Future Antarctic bed topography and its implications for ice sheet dynamics. *Solid Earth*, 5(1):569–584. Publisher: Copernicus GmbH.

Adusumilli, S., Fricker, H. A., Medley, B., Padman, L., and Siegfried, M. R. (2020). Interannual variations in meltwater input to the Southern Ocean from Antarctic ice shelves. *Nature Geoscience*, 13(9):616–620. Bandiera_abtest: a Cg_type: Nature Research Journals Number: 9 Primary_atype: Research Publisher: Nature Publishing Group Subject_term: Cryospheric science;Physical oceanography Subject_term_id: cryospheric-science;physical-oceanography.

Aitken, A. R. A., Roberts, J. L., Ommen, T. D. v., Young, D. A., Golledge, N. R., Greenbaum, J. S., Blankenship, D. D., and Siegert, M. J. (2016). Repeated large-scale retreat and advance of Totten Glacier indicated by inland bed erosion. *Nature*, 533(7603):385–389. Number: 7603 Publisher: Nature Publishing Group.

Albrecht, T., Winkelmann, R., and Levermann, A. (2020). Glacial-cycle simulations of the Antarctic Ice Sheet with the Parallel Ice Sheet Model (PISM) – Part 1: Boundary conditions and climatic forcing. *The Cryosphere*, 14(2):599–632. Publisher: Copernicus GmbH.

Alley, R. B. (2000). Continuity comes first: recent progress in understanding subglacial deformation. *Geological Society, London, Special Publications*, 176(1):171–179. Publisher: Geological Society of London Section: Sub-Glacial Deformation.

Alley, R. B., Blankenship, D. D., Bentley, C. R., and Rooney, S. T. (1986). Deformation of till beneath ice stream B, West Antarctica. *Nature*, 322(6074):57–59. Number: 6074 Publisher: Nature Publishing Group.

Alley, R. B., Cuffey, K. M., Evenson, E. B., Strasser, J. C., Lawson, D. E., and Larson, G. J. (1997). How glaciers entrain and transport basal sediment: Physical constraints. *Quaternary Science Reviews*, 16(9):1017–1038.

Anandakrishnan, S., Blankenship, D. D., Alley, R. B., and Stoffa, P. L. (1998). Influence of subglacial geology on the position of a West Antarctic ice stream from seismic observations. *Nature*, 394(6688):62–65. Number: 6688 Publisher: Nature Publishing Group.

Arthern, R. J., Hindmarsh, R. C. A., and Williams, C. R. (2015). Flow speed within the Antarctic ice sheet and its controls inferred from satellite observations. *Journal of Geophysical Research: Earth Surface*, 120(7):1171–1188. _eprint: https://onlinelibrary.wiley.com/doi/pdf/10.1002/2014JF003239.

Arthern, R. J., Winebrenner, D. P., and Vaughan, D. G. (2006). Antarctic snow accumulation mapped using polarization of 4.3-cm wavelength microwave emission. *Journal of Geophysical Research: Atmospheres*, 111(D6). _eprint: https://onlinelibrary.wiley.com/doi/pdf/10.1029/2004JD005667.

Aschwanden, A., Aðalgeirsdóttir, G., and Khroulev, C. (2013). Hindcasting to measure ice sheet model sensitivity to initial states. *The Cryosphere*, 7(4):1083–1093. Publisher: Copernicus GmbH.

Aschwanden, A., Bueler, E., Khroulev, C., and Blatter, H. (2012). An enthalpy formulation for glaciers and ice sheets. *Journal of Glaciology*, 58(209):441–457. Publisher: Cambridge University Press.

Austermann, J., Mitrovica, J. X., Huybers, P., and Rovere, A. (2017). Detection of a dynamic topography signal in last interglacial sea-level records. *Science Advances*, 3(7):e1700457. Publisher: American Association for the Advancement of Science.

Austermann, J., Pollard, D., Mitrovica, J. X., Moucha, R., Forte, A. M., DeConto, R. M., Rowley, D. B., and Raymo, M. E. (2015). The impact of dynamic topography change on Antarctic ice sheet stability during the mid-Pliocene warm period. *Geology*, 43(10):927–930.

Baatsen, M. L. J., von der Heydt, A. S., Kliphuis, M. A., Oldeman, A. M., and Weiffenbach, J. E. (2021). Warm mid-Pliocene conditions without high climate sensitivity: the CCSM4-Utrecht (CESM 1.0.5) contribution to the PlioMIP2. *Climate of the Past Discussions*, pages 1–30. Publisher: Copernicus GmbH.

Baatsen, M. L. J., von der Heydt, A. S., Kliphuis, M. A., Oldeman, A. M., and Weiffenbach, J. E. (2022). Warm mid-Pliocene conditions without high climate sensitivity: the CCSM4-Utrecht (CESM 1.0.5) contribution to the PlioMIP2. *Climate of the Past*, 18(4):657–679. Publisher: Copernicus GmbH.

Bahadory, T., Tarasov, L., and Andres, H. (2021). Last glacial inception trajectories for the Northern Hemisphere from coupled ice and climate modelling. *Climate of the Past*, 17(1):397–418. Publisher: Copernicus GmbH.

Ballantyne, A., Greenwood, D., Sinninghe Damsté, J., Csank, A., Eberle, J., and Rybczynski, N. (2010). Significantly warmer Arctic surface temperatures during the Pliocene indicated by multiple independent proxies. *Geology*, 38(7):603–606.

Bamber, J. L., Griggs, J. A., Hurkmans, R. T. W. L., Dowdeswell, J. A., Gogineni, S. P., Howat, I., Mouginot, J., Paden, J., Palmer, S., Rignot, E., and Steinhage, D. (2013). A new bed elevation dataset for Greenland. *The Cryosphere*, 7(2):499–510.

Bamber, J. L., Vaughan, D. G., and Joughin, I. (2000). Widespread Complex Flow in the Interior of the Antarctic Ice Sheet. *Science*, 287(5456):1248–1250. Publisher: American Association for the Advancement of Science.

Barletta, V. R., Bevis, M., Smith, B. E., Wilson, T., Brown, A., Bordoni, A., Willis, M., Khan, S. A., Rovira-Navarro, M., Dalziel, I., SmalleyJr, R., Kendrick, E., Konfal, S., CaccamiseII, D. J., Aster, R. C., Nyblade, A., and Wiens, D. A. (2018). Observed rapid bedrock uplift in Amundsen Sea Embayment promotes ice-sheet stability. *Science*. Publisher: American Association for the Advancement of Science.

Barthel, A., Agosta, C., Little, C. M., Hattermann, T., Jourdain, N. C., Goelzer, H., Nowicki, S., Seroussi, H., Straneo, F., and Bracegirdle, T. J. (2020). CMIP5 model selection for ISMIP6 ice sheet model forcing: Greenland and Antarctica. *The Cryosphere*, 14(3):855–879. Publisher: Copernicus GmbH.

Bassis, J. N., Berg, B., Crawford, A. J., and Benn, D. I. (2021). Transition to marine ice cliff instability controlled by ice thickness gradients and velocity. *Science*, 372(6548):1342–1344. Publisher: American Association for the Advancement of Science.

Bassis, J. N. and Walker, C. C. (2012). Upper and lower limits on the stability of calving glaciers from the yield strength envelope of ice. *Proceedings of the Royal Society A: Mathematical, Physical and Engineering Sciences*, 468(2140):913–931. Publisher: Royal Society.

Bell, R. E., Blankenship, D. D., Finn, C. A., Morse, D. L., Scambos, T. A., Brozena, J. M., and Hodge, S. M. (1998). Influence of subglacial geology on the onset of a West Antarctic ice stream from aerogeophysical observations. *Nature*, 394(6688):58–62. Number: 6688 Publisher: Nature Publishing Group.

Benn, D. I., Warren, C. R., and Mottram, R. H. (2007). Calving processes and the dynamics of calving glaciers. *Earth-Science Reviews*, 82(3):143–179.

Benn, D. I., Åström, J., Zwinger, T., Todd, J., Nick, F. M., Cook, S., Hulton, N. R. J., and Luckman, A. (2017). Melt-under-cutting and buoyancy-driven calving from tidewater glaciers: new insights from discrete element and continuum model simulations. *Journal of Glaciology*, 63(240):691–702. Publisher: Cambridge University Press.

Bennett, M. R. (2003). Ice streams as the arteries of an ice sheet: their mechanics, stability and significance. *Earth-Science Reviews*, 61(3):309–339.

Bennike, O. and Böcher, J. (1990). Forest-Tundra Neighbouring the North Pole: Plant and Insect Remains from the Plio-Pleistocene Kap København Formation, North Greenland. *Arctic*, 43(4):331–338. Publisher: Arctic Institute of North America.

Berends, C. J., de Boer, B., Dolan, A. M., Hill, D. J., and van de Wal, R. S. W. (2019). Modelling ice sheet evolution and atmospheric $CO_2$ during the Late Pliocene. *Climate of the Past*, 15(4):1603–1619. Publisher: Copernicus GmbH.

Bertram, R. A., Wilson, D. J., van de Flierdt, T., McKay, R. M., Patterson, M. O., Jimenez-Espejo, F. J., Escutia, C., Duke, G. C., Taylor-Silva, B. I., and Riesselman, C. R. (2018). Pliocene deglacial event timelines and the biogeochemical response offshore Wilkes Subglacial Basin, East Antarctica. *Earth and Planetary Science Letters*, 494:109–116.

Bindschadler, R., Choi, H., Wichlacz, A., Bingham, R., Bohlander, J., Brunt, K., Corr, H., Drews, R., Fricker, H., Hall, M., Hindmarsh, R., Kohler, J., Padman, L., Rack, W., Rotschky, G., Urbini, S., Vornberger, P., and Young, N. (2011). Getting around Antarctica: new high-resolution mappings of the grounded and freely-floating boundaries

of the Antarctic ice sheet created for the International Polar Year. *The Cryosphere*, 5(3):569–588. Publisher: Copernicus GmbH.

Bindschadler, R. A., Nowicki, S., Abe-Ouchi, A., Aschwanden, A., Choi, H., Fastook, J., Granzow, G., Greve, R., Gutowski, G., Herzfeld, U., Jackson, C., Johnson, J., Khroulev, C., Levermann, A., Lipscomb, W. H., Martin, M. A., Morlighem, M., Parizek, B. R., Pollard, D., Price, S. F., Ren, D., Saito, F., Sato, T., Seddik, H., Seroussi, H., Takahashi, K., Walker, R., and Wang, W. L. (2013). Ice-sheet model sensitivities to environmental forcing and their use in projecting future sea level (the SeaRISE project). *Journal of Glaciology*, 59(214):195–224. Publisher: Cambridge University Press.

Bingham, R. G., Vaughan, D. G., King, E. C., Davies, D., Cornford, S. L., Smith, A. M., Arthern, R. J., Brisbourne, A. M., De Rydt, J., Graham, A. G. C., Spagnolo, M., Marsh, O. J., and Shean, D. E. (2017). Diverse landscapes beneath Pine Island Glacier influence ice flow. *Nature Communications*, 8(1):1618. Number: 1 Publisher: Nature Publishing Group.

Blackburn, T., Edwards, G. H., Tulaczyk, S., Scudder, M., Piccione, G., Hallet, B., McLean, N., Zachos, J. C., Cheney, B., and Babbe, J. T. (2020). Ice retreat in Wilkes Basin of East Antarctica during a warm interglacial. *Nature*, 583(7817):554–559. Number: 7817 Publisher: Nature Publishing Group.

Blackmon, M., Boville, B., Bryan, F., Dickinson, R., Gent, P., Kiehl, J., Moritz, R., Randall, D., Shukla, J., Solomon, S., Bonan, G., Doney, S., Fung, I., Hack, J., Hunke, E., Hurrell, J., Kutzbach, J., Meehl, J., Otto-Bliesner, B., Saravanan, R., Schneider, E. K., Sloan, L., Spall, M., Taylor, K., Tribbia, J., and Washington, W. (2001). The Community Climate System Model. *Bulletin of the American Meteorological Society*, 82(11):2357–2376. Publisher: American Meteorological Society Section: Bulletin of the American Meteorological Society.

Blankenship, D. D., Bentley, C. R., Rooney, S. T., and Alley, R. B. (1986). Seismic measurements reveal a saturated porous layer beneath an active Antarctic ice stream. *Nature*, 322(6074):54–57. Number: 6074 Publisher: Nature Publishing Group.

Blankenship, D. D., Morse, D. L., Finn, C. A., Bell, R. E., Peters, M. E., Kempf, S. D., Hodge, S. M., Studinger, M., Behrendt, J. C., and Brozena, J. M. (2001). Geologic Controls on the Initiation of Rapid Basal Motion for West Antarctic Ice Streams: A Geophysical Perspective Including New Airborne Radar Sounding and Laser Altimetry Results. In *The West Antarctic Ice Sheet: Behavior and Environment*, pages 105–121. American Geophysical Union (AGU). _eprint: https://onlinelibrary.wiley.com/doi/pdf/10.1029/AR077p0105.

Blasco, J., Alvarez-Solas, J., Robinson, A., and Montoya, M. (2021). Exploring the impact of atmospheric forcing and basal drag on the Antarctic Ice Sheet under Last Glacial Maximum conditions. *The Cryosphere*, 15(1):215–231. Publisher: Copernicus GmbH.

Blatter, H. (1995). Velocity and stress fields in grounded glaciers: a simple algorithm for including deviatoric stress gradients. *Journal of Glaciology*, 41(138):333–344. Publisher: Cambridge University Press.

Bradley, S. L., Milne, G. A., Shennan, I., and Edwards, R. (2011). An improved glacial isostatic adjustment model for the British Isles. *Journal of Quaternary Science*, 26(5):541–552. _eprint: https://onlinelibrary.wiley.com/doi/pdf/10.1002/jqs.1481.

Brigham-Grette, J., Melles, M., Minyuk, P., Andreev, A., Tarasov, P., DeConto, R., Koenig, S., Nowaczyk, N., Wennrich, V., Rosén, P., Haltia, E., Cook, T., Gebhardt, C., Meyer-Jacob, C., Snyder, J., and Herzschuh, U. (2013). Pliocene Warmth, Polar Amplification, and Stepped Pleistocene Cooling Recorded in NE Arctic Russia. *Science*, 340(6139):1421–1427. Publisher: American Association for the Advancement of Science.

Brotchie, J. F. and Silvester, R. (1969). On crustal flexure. *Journal of Geophysical Research (1896-1977)*, 74(22):5240–5252. _eprint: https://onlinelibrary.wiley.com/doi/pdf/10.1029/JB074i022p05240.

Brovkin, V., Raddatz, T., Reick, C. H., Claussen, M., and Gayler, V. (2009). Global biogeophysical interactions between forest and climate. *Geophysical Research Letters*, 36(7). _eprint: https://onlinelibrary.wiley.com/doi/pdf/10.1029/2009GL037543.

Brown, S. J. and Elderfield, H. (1996). Variations in Mg/Ca and Sr/Ca ratios of planktonic foraminifera caused by postdepositional dissolution: Evidence of shallow Mg-dependent dissolution. *Paleoceanography*, 11(5):543–551. _eprint: https://onlinelibrary.wiley.com/doi/pdf/10.1029/96PA01491.

Bueler, E. and Brown, J. (2009). Shallow shelf approximation as a "sliding law" in a thermomechanically coupled ice sheet model. *Journal of Geophysical Research: Earth Surface*, 114(F3). _eprint: https://onlinelibrary.wiley.com/doi/pdf/10.1029/2008JF001179.

Bueler, E., Lingle, C. S., and Brown, J. (2007). Fast computation of a viscoelastic deformable Earth model for ice-sheet simulations. *Annals of Glaciology*, 46:97–105. Publisher: Cambridge University Press.

Bulthuis, K., Arnst, M., Sun, S., and Pattyn, F. (2019). Uncertainty quantification of the multi-centennial response of the Antarctic ice sheet to climate change. *The Cryosphere*, 13(4):1349–1380. Publisher: Copernicus GmbH.

Burke, K. D., Williams, J. W., Chandler, M. A., Haywood, A. M., Lunt, D. J., and Otto-Bliesner, B. L. (2018). Pliocene and Eocene provide best analogs for near-future climates. *Proceedings of the National Academy of Sciences*, 115(52):13288–13293. Publisher: Proceedings of the National Academy of Sciences.

Calov, R. and Ganopolski, A. (2005). Multistability and hysteresis in the climate-cryosphere system under orbital forcing. *Geophysical Research Letters*, 32(21). _eprint: https://onlinelibrary.wiley.com/doi/pdf/10.1029/2005GL024518.

Canals, M., Urgeles, R., and Calafat, A. M. (2000). Deep sea-floor evidence of past ice streams off the Antarctic Peninsula. *Geology*, 28(1):31–34.

Caron, L., Métivier, L., Greff-Lefftz, M., Fleitout, L., and Rouby, H. (2017). Inverting Glacial Isostatic Adjustment signal using Bayesian framework and two linearly relaxing rheologies. *Geophysical Journal International*, 209(2):1126–1147.

Carter, S. P. and Fricker, H. A. (2012). The supply of subglacial meltwater to the grounding line of the Siple Coast, West Antarctica. *Annals of Glaciology*, 53(60):267–280. Publisher: Cambridge University Press.

Cathles, L. M. (2015). *Viscosity of the Earth's Mantle*. Princeton University Press. Publication Title: Viscosity of the Earth's Mantle.

Chan, W.-L. and Abe-Ouchi, A. (2020). Pliocene Model Intercomparison Project (PlioMIP2) simulations using the Model for Interdisciplinary Research on Climate (MIROC4m). *Climate of the Past*, 16(4):1523–1545. Publisher: Copernicus GmbH.

Chandan, D. and Peltier, W. R. (2017). Regional and global climate for the mid-Pliocene using the University of Toronto version of CCSM4 and PlioMIP2 boundary conditions. *Climate of the Past*, 13(7):919–942. Publisher: Copernicus GmbH.

Chandan, D. and Peltier, W. R. (2018). On the mechanisms of warming the mid-Pliocene and the inference of a hierarchy of climate sensitivities with relevance to the understanding of climate futures. *Climate of the Past*, 14(6):825–856. Publisher: Copernicus GmbH.

Chen, B., Haeger, C., Kaban, M. K., and Petrunin, A. G. (2018). Variations of the effective elastic thickness reveal tectonic fragmentation of the Antarctic lithosphere. *Tectonophysics*, 746:412–424.

Choudhury, D., Timmermann, A., Schloesser, F., Heinemann, M., and Pollard, D. (2020). Simulating Marine Isotope Stage 7 with a coupled climate–ice sheet model. *Climate of the Past*, 16(6):2183–2201. Publisher: Copernicus GmbH.

Clapperton, C. M. and Sugden, D. E. (1990). Late cenozoic glacial history of the ross embayment, antarctica. *Quaternary Science Reviews*, 9(2):253–272.

Clark, P. U. (1994). Unstable Behavior of the Laurentide Ice Sheet over Deforming Sediment and Its Implications for Climate Change. *Quaternary Research*, 41(1):19–25.

Clark, P. U., He, F., Golledge, N. R., Mitrovica, J. X., Dutton, A., Hoffman, J. S., and Dendy, S. (2020). Oceanic forcing of penultimate deglacial and last interglacial sea-level rise. *Nature*, 577(7792):660–664. Number: 7792 Publisher: Nature Publishing Group.

Clarke, G. K. C., Nitsan, U., and Paterson, W. S. B. (1977). Strain heating and creep instability in glaciers and ice sheets. *Reviews of Geophysics*, 15(2):235–247. _eprint: https://onlinelibrary.wiley.com/doi/pdf/10.1029/RG015i002p00235.

Clerc, F., Minchew, B. M., and Behn, M. D. (2019). Marine Ice Cliff Instability Mitigated by Slow Removal of Ice Shelves. *Geophysical Research Letters*, 46(21):12108–12116. _eprint: https://onlinelibrary.wiley.com/doi/pdf/10.1029/2019GL084183.

Cook, A. J. and Vaughan, D. G. (2010). Overview of areal changes of the ice shelves on the Antarctic Peninsula over the past 50 years. *The Cryosphere*, 4(1):77–98. Publisher: Copernicus GmbH.

Cook, C. P., Hill, D. J., van de Flierdt, T., Williams, T., Hemming, S. R., Dolan, A. M., Pierce, E. L., Escutia, C., Harwood, D., Cortese, G., and Gonzales, J. J. (2014). Sea surface temperature control on the distribution of far-traveled Southern Ocean ice-rafted detritus during the Pliocene. *Paleoceanography*, 29(6):533–548. _eprint: https://onlinelibrary.wiley.com/doi/pdf/10.1002/2014PA002625.

Cook, C. P., van de Flierdt, T., Williams, T., Hemming, S. R., Iwai, M., Kobayashi, M., Jimenez-Espejo, F. J., Escutia, C., González, J. J., Khim, B.-K., McKay, R. M., Passchier, S., Bohaty, S. M., Riesselman, C. R., Tauxe, L., Sugisaki, S., Galindo, A. L., Patterson, M. O., Sangiorgi, F., Pierce, E. L., Brinkhuis, H., Klaus, A., Fehr, A., Bendle, J. A. P.,

Bijl, P. K., Carr, S. A., Dunbar, R. B., Flores, J. A., Hayden, T. G., Katsuki, K., Kong, G. S., Nakai, M., Olney, M. P., Pekar, S. F., Pross, J., Röhl, U., Sakai, T., Shrivastava, P. K., Stickley, C. E., Tuo, S., Welsh, K., and Yamane, M. (2013). Dynamic behaviour of the East Antarctic ice sheet during Pliocene warmth. *Nature Geoscience*, 6(9):765–769. Number: 9 Publisher: Nature Publishing Group.

Cornford, S. L., Martin, D. F., Graves, D. T., Ranken, D. F., Le Brocq, A. M., Gladstone, R. M., Payne, A. J., Ng, E. G., and Lipscomb, W. H. (2013). Adaptive mesh, finite volume modeling of marine ice sheets. *Journal of Computational Physics*, 232(1):529–549.

Cornford, S. L., Martin, D. F., Lee, V., Payne, A. J., and Ng, E. G. (2016). Adaptive mesh refinement versus subgrid friction interpolation in simulations of Antarctic ice dynamics. *Annals of Glaciology*, 57(73):1–9. Publisher: Cambridge University Press.

Cornford, S. L., Martin, D. F., Payne, A. J., Ng, E. G., Le Brocq, A. M., Gladstone, R. M., Edwards, T. L., Shannon, S. R., Agosta, C., van den Broeke, M. R., Hellmer, H. H., Krinner, G., Ligtenberg, S. R. M., Timmermann, R., and Vaughan, D. G. (2015). Century-scale simulations of the response of the West Antarctic Ice Sheet to a warming climate. *The Cryosphere*, 9(4):1579–1600. Publisher: Copernicus GmbH.

Cornford, S. L., Seroussi, H., Asay-Davis, X. S., Gudmundsson, G. H., Arthern, R., Borstad, C., Christmann, J., Dias dos Santos, T., Feldmann, J., Goldberg, D., Hoffman, M. J., Humbert, A., Kleiner, T., Leguy, G., Lipscomb, W. H., Merino, N., Durand, G., Morlighem, M., Pollard, D., Rückamp, M., Williams, C. R., and Yu, H. (2020). Results of the third Marine Ice Sheet Model Intercomparison Project (MISMIP+). *The Cryosphere*, 14(7):2283–2301. Publisher: Copernicus GmbH.

Coulon, V., Bulthuis, K., Whitehouse, P. L., Sun, S., Haubner, K., Zipf, L., and Pattyn, F. (2021). Contrasting Response of West and East Antarctic Ice Sheets to Glacial Isostatic Adjustment. *Journal of Geophysical Research: Earth Surface*, 126(7):e2020JF006003. _eprint: https://onlinelibrary.wiley.com/doi/pdf/10.1029/2020JF006003.

Cox, P. M., Betts, R. A., Bunton, C. B., Essery, R. L. H., Rowntree, P. R., and Smith, J. (1999). The impact of new land surface physics on the GCM simulation of climate and climate sensitivity. *Climate Dynamics*, 15(3):183–203.

Crawford, A. J., Benn, D. I., Todd, J., Åström, J. A., Bassis, J. N., and Zwinger, T. (2021). Marine ice-cliff instability modeling shows mixed-mode ice-cliff failure and yields calving rate parameterization. *Nature Communications*, 12(1):2701. Number: 1 Publisher: Nature Publishing Group.

Cuffey, K. M. and Paterson, W. S. B. (2010). *The Physics of Glaciers*. Academic Press. Google-Books-ID: Jca2v1u1EKEC.

Currier, J. H. and Schulson, E. M. (1982). The tensile strength of ice as a function of grain size. *Acta Metallurgica*, 30(8):1511–1514.

Danabasoglu, G., Large, W. G., and Briegleb, B. P. (2010). Climate impacts of parameterized Nordic Sea overflows. *Journal of Geophysical Research: Oceans*, 115(C11). _eprint: https://onlinelibrary.wiley.com/doi/pdf/10.1029/2010JC006243.

Dansgaard, W. (1964). Stable isotopes in precipitation. *Tellus*, 16(4):436–468. _eprint: https://onlinelibrary.wiley.com/doi/pdf/10.1111/j.2153-3490.1964.tb00181.x.

de Boer, B., Dolan, A. M., Bernales, J., Gasson, E., Goelzer, H., Golledge, N. R., Sutter, J., Huybrechts, P., Lohmann, G., Rogozhina, I., Abe-Ouchi, A., Saito, F., and van de Wal, R. S. W. (2015). Simulating the Antarctic ice sheet in the late-Pliocene warm period: PLISMIP-ANT, an ice-sheet model intercomparison project. *The Cryosphere*, 9(3):881–903. Publisher: Copernicus GmbH.

de Boer, B., Haywood, A. M., Dolan, A. M., Hunter, S. J., and Prescott, C. L. (2017a). The Transient Response of Ice Volume to Orbital Forcing During the Warm Late Pliocene: PLIOCENE TRANSIENT ICE VOLUME. *Geophysical Research Letters*, 44(20):10,486–10,494.

de Boer, B., Stocchi, P., and van de Wal, R. S. W. (2014). A fully coupled 3-D ice-sheet–sea-level model: algorithm and applications. *Geoscientific Model Development*, 7(5):2141–2156. Publisher: Copernicus GmbH.

de Boer, B., Stocchi, P., Whitehouse, P. L., and van de Wal, R. S. W. (2017b). Current state and future perspectives on coupled ice-sheet – sea-level modelling. *Quaternary Science Reviews*, 169:13–28.

de la Vega, E., Chalk, T. B., Wilson, P. A., Bysani, R. P., and Foster, G. L. (2020). Atmospheric CO2 during the Mid-Piacenzian Warm Period and the M2 glaciation. *Scientific Reports*, 10(1):11002.

De Rydt, J., Holland, P. R., Dutrieux, P., and Jenkins, A. (2014). Geometric and oceanographic controls on melting beneath Pine Island Glacier. *Journal of Geophysical Research: Oceans*, 119(4):2420–2438. _eprint: https://onlinelibrary.wiley.com/doi/pdf/10.1002/2013JC009513.

De Schepper, S., Gibbard, P. L., Salzmann, U., and Ehlers, J. (2014). A global synthesis of the marine and terrestrial evidence for glaciation during the Pliocene Epoch. *Earth-Science Reviews*, 135:83–102.

DeConto, R. M. and Pollard, D. (2016). Contribution of Antarctica to past and future sea-level rise. *Nature*, 531(7596):591–597. Bandiera_abtest: a Cg_type: Nature Research Journals Number: 7596 Primary_atype: Research Publisher: Nature Publishing Group Subject_term: Climate and Earth system modelling;Climate sciences;Cryospheric science Subject_term_id: climate-and-earth-system-modelling;climate-sciences;cryospheric-science.

DeConto, R. M., Pollard, D., Alley, R. B., Velicogna, I., Gasson, E., Gomez, N., Sadai, S., Condron, A., Gilford, D. M., Ashe, E. L., Kopp, R. E., Li, D., and Dutton, A. (2021). The Paris Climate Agreement and future sea-level rise from Antarctica. *Nature*, 593(7857):83–89. Bandiera_abtest: a Cg_type: Nature Research Journals Number: 7857 Primary_atype: Research Publisher: Nature Publishing Group Subject_term: Climate and Earth system modelling;Climate-change impacts;Cryospheric science Subject_term_id: climate-and-earth-system-modelling;climate-change-impacts;cryospheric-science.

Dee, D. P., Uppala, S. M., Simmons, A. J., Berrisford, P., Poli, P., Kobayashi, S., Andrae, U., Balmaseda, M. A., Balsamo, G., Bauer, P., Bechtold, P., Beljaars, A. C. M., van de

Berg, L., Bidlot, J., Bormann, N., Delsol, C., Dragani, R., Fuentes, M., Geer, A. J., Haimberger, L., Healy, S. B., Hersbach, H., Hólm, E. V., Isaksen, L., Kållberg, P., Köhler, M., Matricardi, M., McNally, A. P., Monge-Sanz, B. M., Morcrette, J.-J., Park, B.-K., Peubey, C., de Rosnay, P., Tavolato, C., Thépaut, J.-N., and Vitart, F. (2011). The ERA-Interim reanalysis: configuration and performance of the data assimilation system. *Quarterly Journal of the Royal Meteorological Society*, 137(656):553–597. _eprint: https://onlinelibrary.wiley.com/doi/pdf/10.1002/qj.828.

Denton, G. H., Sugden, D. E., Marchant, D. R., Hall, B. L., and Wilch, T. I. (1993). East Antarctic Ice Sheet Sensitivity to Pliocene Climatic Change from a Dry Valleys Perspective. *Geografiska Annaler: Series A, Physical Geography*, 75(4):155–204. Publisher: Taylor & Francis _eprint: https://doi.org/10.1080/04353676.1993.11880393.

Depoorter, M. A., Bamber, J. L., Griggs, J. A., Lenaerts, J. T. M., Ligtenberg, S. R. M., van den Broeke, M. R., and Moholdt, G. (2013). Calving fluxes and basal melt rates of Antarctic ice shelves. *Nature*, 502(7469):89–92. Number: 7469 Publisher: Nature Publishing Group.

deVernal, A. and Mudie, P. (1989). Pliocene and Pleistocene Palynostratigraphy at ODP Sites 646 and 647, Eastern and Southern Labrador Sea. *Proc., scientific results, ODP, Leg 105, Baffin Bay and Labrador Sea*, 105.

De Rydt, J. and Gudmundsson, G. H. (2016). Coupled ice shelf-ocean modeling and complex grounding line retreat from a seabed ridge. *Journal of Geophysical Research: Earth Surface*, 121(5):865–880.

Dissard, D., Nehrke, G., Reichart, G. J., and Bijma, J. (2010). The impact of salinity on the Mg/Ca and Sr/Ca ratio in the benthic foraminifera Ammonia tepida: Results from culture experiments. *Geochimica et Cosmochimica Acta*, 74(3):928–940.

Dodson, J. R. and Macphail, M. K. (2004). Palynological evidence for aridity events and vegetation change during the Middle Pliocene, a warm period in Southwestern Australia. *Global and Planetary Change*, 41(3):285–307.

Dolan, A. M., de Boer, B., Bernales, J., Hill, D. J., and Haywood, A. M. (2018). High climate model dependency of Pliocene Antarctic ice-sheet predictions. *Nature Communications*, 9(1):2799. Bandiera_abtest: a Cc_license_type: cc_by Cg_type: Nature Research Journals Number: 1 Primary_atype: Research Publisher: Nature Publishing Group Subject_term: Cryospheric science;Palaeoclimate Subject_term_id: cryospheric-science;palaeoclimate.

Dolan, A. M., Haywood, A. M., Hill, D. J., Dowsett, H. J., Hunter, S. J., Lunt, D. J., and Pickering, S. J. (2011). Sensitivity of Pliocene ice sheets to orbital forcing. *Palaeogeography, Palaeoclimatology, Palaeoecology*, 309(1):98–110.

Dolan, A. M., Hunter, S. J., Hill, D. J., Haywood, A. M., Koenig, S. J., Otto-Bliesner, B. L., Abe-Ouchi, A., Bragg, F., Chan, W.-L., Chandler, M. A., Contoux, C., Jost, A., Kamae, Y., Lohmann, G., Lunt, D. J., Ramstein, G., Rosenbloom, N. A., Sohl, L., Stepanek, C., Ueda, H., Yan, Q., and Zhang, Z. (2015). Using results from the PlioMIP ensemble to investigate the Greenland Ice Sheet during the mid-Pliocene Warm Period. *Climate of the Past*, 11(3):403–424. Publisher: Copernicus GmbH.

Dolan, A. M., Koenig, S. J., Hill, D. J., Haywood, A. M., and DeConto, R. M. (2012). Pliocene Ice Sheet Modelling Intercomparison Project (PLISMIP) – experimental design. *Geoscientific Model Development*, 5(4):963–974. Publisher: Copernicus GmbH.

Dowsett, H., Dolan, A., Rowley, D., Moucha, R., Forte, A. M., Mitrovica, J. X., Pound, M., Salzmann, U., Robinson, M., Chandler, M., Foley, K., and Haywood, A. (2016). The PRISM4 (mid-Piacenzian) paleoenvironmental reconstruction. *Climate of the Past*, 12(7):1519–1538. Publisher: Copernicus GmbH.

Dowsett, H., Robinson, M., Haywood, A. M., Salzmann, U., Hill, D., Sohl, L. E., Chandler, M., Williams, M., Foley, K., and Stoll, D. K. (2010). The PRISM3D paleoenvironmental reconstruction. *Stratigraphy*, 7(2-3):123–139. Number: 2-3 Publisher: Micropaleontology Press.

Dowsett, H. J. (2007). The PRISM palaeoclimate reconstruction and Pliocene sea-surface temperature.

Dowsett, H. J. and Cronin, T. M. (1990). High eustatic sea level during the middle Pliocene:Evidence from the southeastern U.S. Atlantic Coastal Plain. *Geology*, 18(5):435–438.

Dowsett, H. J., Foley, K. M., Stoll, D. K., Chandler, M. A., Sohl, L. E., Bentsen, M., Otto-Bliesner, B. L., Bragg, F. J., Chan, W.-L., Contoux, C., Dolan, A. M., Haywood, A. M., Jonas, J. A., Jost, A., Kamae, Y., Lohmann, G., Lunt, D. J., Nisancioglu, K. H., Abe-Ouchi, A., Ramstein, G., Riesselman, C. R., Robinson, M. M., Rosenbloom, N. A., Salzmann, U., Stepanek, C., Strother, S. L., Ueda, H., Yan, Q., and Zhang, Z. (2013). Sea Surface Temperature of the mid-Piacenzian Ocean: A Data-Model Comparison. *Scientific Reports*, 3(1):2013. Number: 1 Publisher: Nature Publishing Group.

Dowsett, H. J. and Poore, R. Z. (1991). Pliocene sea surface temperatures of the north atlantic ocean at 3.0 Ma. *Quaternary Science Reviews*, 10(2):189–204.

Dowsett, H. J. and Robinson, M. M. (2009). Mid-Pliocene equatorial Pacific sea surface temperature reconstruction: a multi-proxy perspective. *Philosophical Transactions of the Royal Society A: Mathematical, Physical and Engineering Sciences*, 367(1886):109–125. Publisher: Royal Society.

Dumitru, O. A., Austermann, J., Polyak, V. J., Fornós, J. J., Asmerom, Y., Ginés, J., Ginés, A., and Onac, B. P. (2019). Constraints on global mean sea level during Pliocene warmth. *Nature*, 574(7777):233–236. Bandiera_abtest: a Cg_type: Nature Research Journals Number: 7777 Primary_atype: Research Publisher: Nature Publishing Group Subject_term: Palaeoceanography;Physical oceanography Subject_term_id: palaeoceanography;physical-oceanography.

Durand, G., Gagliardini, O., de Fleurian, B., Zwinger, T., and Le Meur, E. (2009). Marine ice sheet dynamics: Hysteresis and neutral equilibrium. *Journal of Geophysical Research*, 114(F3):F03009.

Durand, G., Gagliardini, O., Favier, L., Zwinger, T., and le Meur, E. (2011). Impact of bedrock description on modeling ice sheet dynamics. *Geophysical Research Letters*, 38(20). _eprint: https://onlinelibrary.wiley.com/doi/pdf/10.1029/2011GL048892.

Dutton, A., Carlson, A. E., Long, A. J., Milne, G. A., Clark, P. U., DeConto, R., Horton, B. P., Rahmstorf, S., and Raymo, M. E. (2015). Sea-level rise due to polar ice-sheet mass loss during past warm periods. *Science*, 349(6244):aaa4019.

Dwyer, G. S. and Chandler, M. A. (2009). Mid-Pliocene sea level and continental ice volume based on coupled benthic Mg/Ca palaeotemperatures and oxygen isotopes. *Philosophical Transactions of the Royal Society A: Mathematical, Physical and Engineering Sciences*, 367(1886):157–168.

Edwards, T. L., Brandon, M. A., Durand, G., Edwards, N. R., Golledge, N. R., Holden, P. B., Nias, I. J., Payne, A. J., Ritz, C., and Wernecke, A. (2019). Revisiting Antarctic ice loss due to marine ice-cliff instability. *Nature*, 566(7742):58–64. Number: 7742 Publisher: Nature Publishing Group.

Edwards, T. L., Fettweis, X., Gagliardini, O., Gillet-Chaulet, F., Goelzer, H., Gregory, J. M., Hoffman, M., Huybrechts, P., Payne, A. J., Perego, M., Price, S., Quiquet, A., and Ritz, C. (2014a). Effect of uncertainty in surface mass balance–elevation feedback on projections of the future sea level contribution of the Greenland ice sheet. *The Cryosphere*, 8(1):195–208. Publisher: Copernicus GmbH.

Edwards, T. L., Fettweis, X., Gagliardini, O., Gillet-Chaulet, F., Goelzer, H., Gregory, J. M., Hoffman, M., Huybrechts, P., Payne, A. J., Perego, M., Price, S., Quiquet, A., and Ritz, C. (2014b). Probabilistic parameterisation of the surface mass balance–elevation feedback in regional climate model simulations of the Greenland ice sheet. *The Cryosphere*, 8(1):181–194. Publisher: Copernicus GmbH.

Edwards, T. L., Nowicki, S., Marzeion, B., Hock, R., Goelzer, H., Seroussi, H., Jourdain, N. C., Slater, D. A., Turner, F. E., Smith, C. J., McKenna, C. M., Simon, E., Abe-Ouchi, A., Gregory, J. M., Larour, E., Lipscomb, W. H., Payne, A. J., Shepherd, A., Agosta, C., Alexander, P., Albrecht, T., Anderson, B., Asay-Davis, X., Aschwanden, A., Barthel, A., Bliss, A., Calov, R., Chambers, C., Champollion, N., Choi, Y., Cullather, R., Cuzzone, J., Dumas, C., Felikson, D., Fettweis, X., Fujita, K., Galton-Fenzi, B. K., Gladstone, R., Golledge, N. R., Greve, R., Hattermann, T., Hoffman, M. J., Humbert, A., Huss, M., Huybrechts, P., Immerzeel, W., Kleiner, T., Kraaijenbrink, P., Le clec'h, S., Lee, V., Leguy, G. R., Little, C. M., Lowry, D. P., Malles, J.-H., Martin, D. F., Maussion, F., Morlighem, M., O'Neill, J. F., Nias, I., Pattyn, F., Pelle, T., Price, S. F., Quiquet, A., Radić, V., Reese, R., Rounce, D. R., Rückamp, M., Sakai, A., Shafer, C., Schlegel, N.-J., Shannon, S., Smith, R. S., Straneo, F., Sun, S., Tarasov, L., Trusel, L. D., Van Breedam, J., van de Wal, R., van den Broeke, M., Winkelmann, R., Zekollari, H., Zhao, C., Zhang, T., and Zwinger, T. (2021). Projected land ice contributions to twenty-first-century sea level rise. *Nature*, 593(7857):74–82. Bandiera_abtest: a Cg_type: Nature Research Journals Number: 7857 Primary_atype: Research Publisher: Nature Publishing Group Subject_term: Climate and Earth system modelling;Cryospheric science;Projection and prediction Subject_term_id: climate-and-earth-system-modelling;cryospheric-science;projection-and-prediction.

Elderfield, H., Yu, J., Anand, P., Kiefer, T., and Nyland, B. (2006). Calibrations for benthic foraminiferal Mg/Ca paleothermometry and the carbonate ion hypothesis. *Earth and Planetary Science Letters*, 250(3):633–649.

Emiliani, C. (1955). Pleistocene Temperatures. *The Journal of Geology*, 63(6):538–578. Publisher: The University of Chicago Press.

Engelhardt, H., Humphrey, N., Kamb, B., and Fahnestock, M. (1990). Physical Conditions at the Base of a Fast Moving Antarctic Ice Stream. *Science*, 248(4951):57–59. Publisher: American Association for the Advancement of Science.

Epstein, S., Buchsbaum, R., Lowenstam, H. A., and Urey, H. C. (1953). Revised carbonate-water isotopic temperature scale. *GSA Bulletin*, 64(11):1315–1326.

Escutia, C., DeConto, R., Dunbar, R., De Santis, L., Shevenell, A., and Nash, T. (2019). Keeping an Eye on Antarctic Ice Sheet Stability. *Oceanography*, 32(1):32–46.

Essery, R. L. H., Best, M. J., Betts, R. A., Cox, P. M., and Taylor, C. M. (2003). Explicit Representation of Subgrid Heterogeneity in a GCM Land Surface Scheme. *Journal of Hydrometeorology*, 4(3):530–543. Publisher: American Meteorological Society Section: Journal of Hydrometeorology.

Evans, D. J. A., Clark, C. D., and Rea, B. R. (2008). Landform and sediment imprints of fast glacier flow in the southwest Laurentide Ice Sheet. *Journal of Quaternary Science*, 23(3):249–272. _eprint: https://onlinelibrary.wiley.com/doi/pdf/10.1002/jqs.1141.

Fauquette, S., Suc, J.-P., Guiot, J., Diniz, F., Feddi, N., Zheng, Z., Bessais, E., and Drivaliari, A. (1999). Climate and biomes in the West Mediterranean area during the Pliocene. *Palaeogeography, Palaeoclimatology, Palaeoecology*, 152(1):15–36.

Favier, L., Durand, G., Cornford, S. L., Gudmundsson, G. H., Gagliardini, O., Gillet-Chaulet, F., Zwinger, T., Payne, A. J., and Le Brocq, A. M. (2014). Retreat of Pine Island Glacier controlled by marine ice-sheet instability. *Nature Climate Change*, 4(2):117–121. Number: 2 Publisher: Nature Publishing Group.

Favier, L., Jourdain, N. C., Jenkins, A., Merino, N., Durand, G., Gagliardini, O., Gillet-Chaulet, F., and Mathiot, P. (2019). Assessment of sub-shelf melting parameterisations using the ocean–ice-sheet coupled model NEMO(v3.6)–Elmer/Ice(v8.3). *Geoscientific Model Development*, 12(6):2255–2283. Publisher: Copernicus GmbH.

Favier, L., Pattyn, F., Berger, S., and Drews, R. (2016). Dynamic influence of pinning points on marine ice-sheet stability: a numerical study in Dronning Maud Land, East Antarctica. *The Cryosphere*, 10(6):2623–2635. Publisher: Copernicus GmbH.

Fedorov, A. V., Dekens, P. S., McCarthy, M., Ravelo, A. C., deMenocal, P. B., Barreiro, M., Pacanowski, R. C., and Philander, S. G. (2006). The Pliocene Paradox (Mechanisms for a Permanent El Niño). *Science*, 312(5779):1485–1489. Publisher: American Association for the Advancement of Science.

Flato, G., Marotzke, J., Abiodun, B., Braconnot, P., Chou, S. C., Collins, W., Cox, P., Driouech, F., Emori, S., Eyring, V., Forest, C., Gleckler, P., Guilyardi, E., Jakob, C., Kattsov, V., Reason, C., and Rummukainen, M. (2013). Evaluation of climate models. In Stocker, T. F., Qin, D., Plattner, G.-K., Tignor, M., Allen, S. K., Doschung, J., Nauels, A., Xia, Y., Bex, V., and Midgley, P. M., editors, *Climate Change 2013: The Physical Science Basis. Contribution of Working Group I to the Fifth Assessment Report of the Intergovernmental Panel on Climate Change*, pages 741–882. Cambridge University Press, Cambridge, UK.

Florindo, F., Siegert, M., Santis, L. D., and Naish, T. (2021). *Antarctic Climate Evolution*. Elsevier. Google-Books-ID: N8DvDwAAQBAJ.

Forester, R. M. (1991). Pliocene-climate history of the western united states derived from lacustrine ostracodes. *Quaternary Science Reviews*, 10(2):133–146.

Fox-Kemper, B., Hewitt, H. T., Xiao, C., Aðalgeirsdóttir, G., Drijfhout, S. S., Edwards, T. L., Golledge, N. R., Hemer, M., Kopp, R. E., Krinner, G., Mix, A., Notz, D., Nowicki, S., Nurhati, I. S., Ruiz, L., Sallée, J.-B., Slangen, A. B. A., and Yu, Y. (2021). Ocean, cryosphere, and sea level change. In Masson-Delmotte, V., Zhai, P., Pirani, A., Connors, S. L., Péan, C., Berger, S., Caud, N., Chen, Y., Goldfarb, L., Gomis, M. I., Huang, M., Leitzell, K., Lonnoy, E., Matthews, J. B. R., Maycock, T. K., Waterfield, T., Yelekçi, , Yu, R., and Zhou, B., editors, *Climate Change 2021: The Physical Science Basis. Contribution of Working Group I to the Sixth Assessment Report of the Intergovernmental Panel on Climate Change*. Cambridge University Press.

Fretwell, P., Pritchard, H. D., Vaughan, D. G., Bamber, J. L., Barrand, N. E., Bell, R., Bianchi, C., Bingham, R. G., Blankenship, D. D., Casassa, G., Catania, G., Callens, D., Conway, H., Cook, A. J., Corr, H. F. J., Damaske, D., Damm, V., Ferraccioli, F., Forsberg, R., Fujita, S., Gim, Y., Gogineni, P., Griggs, J. A., Hindmarsh, R. C. A., Holmlund, P., Holt, J. W., Jacobel, R. W., Jenkins, A., Jokat, W., Jordan, T., King, E. C., Kohler, J., Krabill, W., Riger-Kusk, M., Langley, K. A., Leitchenkov, G., Leuschen, C., Luyendyk, B. P., Matsuoka, K., Mouginot, J., Nitsche, F. O., Nogi, Y., Nost, O. A., Popov, S. V., Rignot, E., Rippin, D. M., Rivera, A., Roberts, J., Ross, N., Siegert, M. J., Smith, A. M., Steinhage, D., Studinger, M., Sun, B., Tinto, B. K., Welch, B. C., Wilson, D., Young, D. A., Xiangbin, C., and Zirizzotti, A. (2013). Bedmap2: improved ice bed, surface and thickness datasets for Antarctica. *The Cryosphere*, 7(1):375–393. Publisher: Copernicus GmbH.

Frieler, K., Clark, P. U., He, F., Buizert, C., Reese, R., Ligtenberg, S. R. M., van den Broeke, M. R., Winkelmann, R., and Levermann, A. (2015). Consistent evidence of increasing Antarctic accumulation with warming. *Nature Climate Change*, 5(4):348–352. Number: 4 Publisher: Nature Publishing Group.

Fürst, J. J., Durand, G., Gillet-Chaulet, F., Tavard, L., Rankl, M., Braun, M., and Gagliardini, O. (2016). The safety band of Antarctic ice shelves. *Nature Climate Change*, 6(5):479–482. Bandiera_abtest: a Cg_type: Nature Research Journals Number: 5 Primary_atype: Research Publisher: Nature Publishing Group Subject_term: Climate and Earth system modelling;Cryospheric science Subject_term_id: climate-and-earth-system-modelling;cryospheric-science.

Gandy, N., Gregoire, L. J., Ely, J. C., Clark, C. D., Hodgson, D. M., Lee, V., Bradwell, T., and Ivanovic, R. F. (2018). Marine ice sheet instability and ice shelf buttressing of the Minch Ice Stream, northwest Scotland. *The Cryosphere*, 12(11):3635–3651. Publisher: Copernicus GmbH.

Gandy, N., Gregoire, L. J., Ely, J. C., Cornford, S. L., Clark, C. D., and Hodgson, D. M. (2019). Exploring the ingredients required to successfully model the placement, generation, and evolution of ice streams in the British-Irish Ice Sheet. *Quaternary Science Reviews*, 223:105915.

Gandy, N., Gregoire, L. J., Ely, J. C., Cornford, S. L., Clark, C. D., and Hodgson, D. M. (2021). Collapse of the Last Eurasian Ice Sheet in the North Sea Modulated by Combined Processes of Ice Flow, Surface Melt, and Marine Ice Sheet Instabilities. *Journal of Geophysical Research: Earth Surface*, 126(4):e2020JF005755. _eprint: https://onlinelibrary.wiley.com/doi/pdf/10.1029/2020JF005755.

Ganopolski, A. and Brovkin, V. (2017). Simulation of climate, ice sheets and $CO_2$ evolution during the last four glacial cycles with an Earth system model of intermediate complexity. *Climate of the Past*, 13(12):1695–1716. Publisher: Copernicus GmbH.

Ganopolski, A., Calov, R., and Claussen, M. (2010). Simulation of the last glacial cycle with a coupled climate ice-sheet model of intermediate complexity. *Climate of the Past*, 6(2):229–244. Publisher: Copernicus GmbH.

Gardner, A. S., Moholdt, G., Scambos, T., Fahnstock, M., Ligtenberg, S., van den Broeke, M., and Nilsson, J. (2018). Increased West Antarctic and unchanged East Antarctic ice discharge over the last 7 years. *The Cryosphere*, 12(2):521–547. Publisher: Copernicus GmbH.

Gasson, E., DeConto, R. M., and Pollard, D. (2016). Modeling the oxygen isotope composition of the Antarctic ice sheet and its significance to Pliocene sea level. *Geology*, 44(10):827–830.

Gent, P. R., Danabasoglu, G., Donner, L. J., Holland, M. M., Hunke, E. C., Jayne, S. R., Lawrence, D. M., Neale, R. B., Rasch, P. J., Vertenstein, M., Worley, P. H., Yang, Z.-L., and Zhang, M. (2011). The Community Climate System Model Version 4. *Journal of Climate*, 24(19):4973–4991. Publisher: American Meteorological Society Section: Journal of Climate.

Gibbard, P. L., Head, M. J., Walker, M. J. C., and Stratigraphy, t. S. o. Q. (2010). Formal ratification of the Quaternary System/Period and the Pleistocene Series/Epoch with a base at 2.58 Ma. *Journal of Quaternary Science*, 25(2):96–102. _eprint: https://onlinelibrary.wiley.com/doi/pdf/10.1002/jqs.1338.

Giles, A. B. (2017). The Mertz Glacier Tongue, East Antarctica. Changes in the past 100years and its cyclic nature - Past, present and future. *Remote Sensing of Environment*, 191:30–37.

Gillet-Chaulet, F., Gagliardini, O., Seddik, H., Nodet, M., Durand, G., Ritz, C., Zwinger, T., Greve, R., and Vaughan, D. G. (2012). Greenland ice sheet contribution to sea-level rise from a new-generation ice-sheet model. *The Cryosphere*, 6(6):1561–1576. Publisher: Copernicus GmbH.

Gladstone, R. M., Lee, V., Rougier, J., Payne, A. J., Hellmer, H., Le Brocq, A., Shepherd, A., Edwards, T. L., Gregory, J., and Cornford, S. L. (2012). Calibrated prediction of Pine Island Glacier retreat during the 21st and 22nd centuries with a coupled flowline model. *Earth and Planetary Science Letters*, 333-334:191–199.

Goelzer, H., Coulon, V., Pattyn, F., de Boer, B., and van de Wal, R. (2020a). Brief communication: On calculating the sea-level contribution in marine ice-sheet models. *The Cryosphere*, 14(3):833–840. Publisher: Copernicus GmbH.

Goelzer, H., Huybrechts, P., Loutre, M.-F., and Fichefet, T. (2016). Last Interglacial climate and sea-level evolution from a coupled ice sheet–climate model. *Climate of the Past*, 12(12):2195–2213. Publisher: Copernicus GmbH.

Goelzer, H., Nowicki, S., Payne, A., Larour, E., Seroussi, H., Lipscomb, W. H., Gregory, J., Abe-Ouchi, A., Shepherd, A., Simon, E., Agosta, C., Alexander, P., Aschwanden, A., Barthel, A., Calov, R., Chambers, C., Choi, Y., Cuzzone, J., Dumas, C., Edwards,

T., Felikson, D., Fettweis, X., Golledge, N. R., Greve, R., Humbert, A., Huybrechts, P., Le clec'h, S., Lee, V., Leguy, G., Little, C., Lowry, D. P., Morlighem, M., Nias, I., Quiquet, A., Rückamp, M., Schlegel, N.-J., Slater, D. A., Smith, R. S., Straneo, F., Tarasov, L., van de Wal, R., and van den Broeke, M. (2020b). The future sea-level contribution of the Greenland ice sheet: a multi-model ensemble study of ISMIP6. *The Cryosphere*, 14(9):3071–3096. Publisher: Copernicus GmbH.

Goelzer, H., Noël, B. P. Y., Edwards, T. L., Fettweis, X., Gregory, J. M., Lipscomb, W. H., van de Wal, R. S. W., and van den Broeke, M. R. (2020c). Remapping of Greenland ice sheet surface mass balance anomalies for large ensemble sea-level change projections. *The Cryosphere*, 14(6):1747–1762. Publisher: Copernicus GmbH.

Goff, J. A., Powell, E. M., Young, D. A., and Blankenship, D. D. (2014). Conditional simulation of Thwaites Glacier (Antarctica) bed topography for flow models: Incorporating inhomogeneous statistics and channelized morphology. *Journal of Glaciology*, 60(222):635–646. Publisher: Cambridge University Press.

Gohl, K., Uenzelmann-Neben, G., Gille-Petzoldt, J., Hillenbrand, C.-D., Klages, J. P., Bohaty, S. M., Passchier, S., Frederichs, T., Wellner, J. S., Lamb, R., Leitchenkov, G., and Scientists, I. E. . (2021). Evidence for a Highly Dynamic West Antarctic Ice Sheet During the Pliocene. *Geophysical Research Letters*, 48(14):e2021GL093103. _eprint: https://onlinelibrary.wiley.com/doi/pdf/10.1029/2021GL093103.

Goldberg, D., Holland, D. M., and Schoof, C. (2009). Grounding line movement and ice shelf buttressing in marine ice sheets. *Journal of Geophysical Research: Earth Surface*, 114(F4). _eprint: https://onlinelibrary.wiley.com/doi/pdf/10.1029/2008JF001227.

Golledge, N. R., Clark, P. U., He, F., Dutton, A., Turney, C. S. M., Fogwill, C. J., Naish, T. R., Levy, R. H., McKay, R. M., Lowry, D. P., Bertler, N. a. N., Dunbar, G. B., and Carlson, A. E. (2021). Retreat of the Antarctic Ice Sheet During the Last Interglaciation and Implications for Future Change. *Geophysical Research Letters*, 48(17):e2021GL094513. _eprint: https://onlinelibrary.wiley.com/doi/pdf/10.1029/2021GL094513.

Golledge, N. R., Kowalewski, D. E., Naish, T. R., Levy, R. H., Fogwill, C. J., and Gasson, E. G. W. (2015). The multi-millennial Antarctic commitment to future sea-level rise. *Nature*, 526(7573):421–425. Number: 7573 Publisher: Nature Publishing Group.

Golledge, N. R., Levy, R. H., McKay, R. M., and Naish, T. R. (2017a). East Antarctic ice sheet most vulnerable to Weddell Sea warming. *Geophysical Research Letters*, 44(5):2343–2351. _eprint: https://onlinelibrary.wiley.com/doi/pdf/10.1002/2016GL072422.

Golledge, N. R., Thomas, Z. A., Levy, R. H., Gasson, E. G. W., Naish, T. R., McKay, R. M., Kowalewski, D. E., and Fogwill, C. J. (2017b). Antarctic climate and ice-sheet configuration during the early Pliocene interglacial at 4.23 Ma. *Climate of the Past*, 13(7):959–975. Publisher: Copernicus GmbH.

Gomez, N., Latychev, K., and Pollard, D. (2018). A Coupled Ice Sheet–Sea Level Model Incorporating 3D Earth Structure: Variations in Antarctica during the Last Deglacial Retreat. *Journal of Climate*, 31(10):4041–4054. Publisher: American Meteorological Society Section: Journal of Climate.

Gomez, N., Mitrovica, J. X., Huybers, P., and Clark, P. U. (2010). Sea level as a stabilizing factor for marine-ice-sheet grounding lines. *Nature Geoscience*, 3(12):850–853. Number: 12 Publisher: Nature Publishing Group.

Gomez, N., Pollard, D., and Holland, D. (2015). Sea-level feedback lowers projections of future Antarctic Ice-Sheet mass loss. *Nature Communications*, 6(1):8798. Number: 1 Publisher: Nature Publishing Group.

Gomez, N., Pollard, D., and Mitrovica, J. X. (2013). A 3-D coupled ice sheet – sea level model applied to Antarctica through the last 40 ky. *Earth and Planetary Science Letters*, 384:88–99.

Gomez, N., Pollard, D., Mitrovica, J. X., Huybers, P., and Clark, P. U. (2012). Evolution of a coupled marine ice sheet–sea level model. *Journal of Geophysical Research: Earth Surface*, 117(F1). _eprint: https://onlinelibrary.wiley.com/doi/pdf/10.1029/2011JF002128.

Gong, Y., Cornford, S. L., and Payne, A. J. (2014). Modelling the response of the Lambert Glacier–Amery Ice Shelf system, East Antarctica, to uncertain climate forcing over the 21st and 22nd centuries. *The Cryosphere*, 8(3):1057–1068. Publisher: Copernicus GmbH.

Gong, Y., Zwinger, T., Cornford, S., Gladstone, R., Schäfer, M., and Moore, J. C. (2017). Importance of basal boundary conditions in transient simulations: case study of a surging marine-terminating glacier on Austfonna, Svalbard. *Journal of Glaciology*, 63(237):106–117. Publisher: Cambridge University Press.

Good, P., Jones, C., Lowe, J., Betts, R., and Gedney, N. (2013a). Comparing Tropical Forest Projections from Two Generations of Hadley Centre Earth System Models, HadGEM2-ES and HadCM3LC. *Journal of Climate*, 26(2):495–511. Publisher: American Meteorological Society Section: Journal of Climate.

Good, S. A., Martin, M. J., and Rayner, N. A. (2013b). EN4: Quality controlled ocean temperature and salinity profiles and monthly objective analyses with uncertainty estimates. *Journal of Geophysical Research: Oceans*, 118(12):6704–6716. _eprint: https://onlinelibrary.wiley.com/doi/pdf/10.1002/2013JC009067.

Gordon, C., Cooper, C., Senior, C. A., Banks, H., Gregory, J. M., Johns, T. C., Mitchell, J. F. B., and Wood, R. A. (2000). The simulation of SST, sea ice extents and ocean heat transports in a version of the Hadley Centre coupled model without flux adjustments. *Climate Dynamics*, 16(2):147–168.

Goursaud, S., Holloway, M., Sime, L., Wolff, E., Valdes, P., Steig, E. J., and Pauling, A. (2021). Antarctic Ice Sheet Elevation Impacts on Water Isotope Records During the Last Interglacial. *Geophysical Research Letters*, 48(6):e2020GL091412. _eprint: https://onlinelibrary.wiley.com/doi/pdf/10.1029/2020GL091412.

Grant, G. and Naish, T. (2021). Pliocene sea level revisited: Is there more than meets the eye? *Past Global Changes Magazine*, 29(1):34–35.

Grant, G. R., Naish, T. R., Dunbar, G. B., Stocchi, P., Kominz, M. A., Kamp, P. J. J., Tapia, C. A., McKay, R. M., Levy, R. H., and Patterson, M. O. (2019). The amplitude and origin of sea-level variability during the Pliocene epoch. *Nature*,

574(7777):237–241. Bandiera_abtest: a Cg_type: Nature Research Journals Number: 7777 Primary_atype: Research Publisher: Nature Publishing Group Subject_term: Cryospheric science;Palaeoceanography;Palaeoclimate Subject_term_id: cryospheric-science;palaeoceanography;palaeoclimate.

Gregoire, L. J., Otto-Bliesner, B., Valdes, P. J., and Ivanovic, R. (2016). Abrupt Bølling warming and ice saddle collapse contributions to the Meltwater Pulse 1a rapid sea level rise. *Geophysical Research Letters*, 43(17):9130–9137. _eprint: https://onlinelibrary.wiley.com/doi/pdf/10.1002/2016GL070356.

Gregoire, L. J., Payne, A. J., and Valdes, P. J. (2012). Deglacial rapid sea level rises caused by ice-sheet saddle collapses. *Nature*, 487(7406):219–222. Number: 7406 Publisher: Nature Publishing Group.

Gregoire, L. J., Valdes, P. J., and Payne, A. J. (2015). The relative contribution of orbital forcing and greenhouse gases to the North American deglaciation. *Geophysical Research Letters*, 42(22):9970–9979. _eprint: https://onlinelibrary.wiley.com/doi/pdf/10.1002/2015GL066005.

Gregory, J. M., Griffies, S. M., Hughes, C. W., Lowe, J. A., Church, J. A., Fukimori, I., Gomez, N., Kopp, R. E., Landerer, F., Cozannet, G. L., Ponte, R. M., Stammer, D., Tamisiea, M. E., and van de Wal, R. S. W. (2019). Concepts and Terminology for Sea Level: Mean, Variability and Change, Both Local and Global. *Surveys in Geophysics*, 40(6):1251–1289.

Greve, R. and Blatter, H. (2009). Glacial Isostasy. In Greve, R. and Blatter, H., editors, *Dynamics of Ice Sheets and Glaciers*, Advances in Geophysical and Environmental Mechanics and Mathematics, pages 185–201. Springer, Berlin, Heidelberg.

Gudmundsson, G. H. (2013). Ice-shelf buttressing and the stability of marine ice sheets. *The Cryosphere*, 7(2):647–655. Publisher: Copernicus GmbH.

Gudmundsson, G. H., Krug, J., Durand, G., Favier, L., and Gagliardini, O. (2012). The stability of grounding lines on retrograde slopes. *The Cryosphere*, 6(6):1497–1505. Publisher: Copernicus GmbH.

Gulev, S. K., Thorne, P. W., Ahn, J., Dentener, F. J., Domingues, C. M., Gerland, S., Gong, D., Kaufman, D. S., Nnamchi, H. C., Quaas, J., Rivera, J. A., Sathyendranath, S., Smith, S. L., Trewin, B., von Shuckmann, K., and Vose, R. S. (2021). Changing state of the climate system. In Masson-Delmotte, V., Zhai, P., Pirani, A., Connors, S. L., Péan, C., Berger, S., Caud, N., Chen, Y., Goldfarb, L., Gomis, M. I., Huang, M., Leitzell, K., Lonnoy, E., Matthews, J. B. R., Maycock, T. K., Waterfield, T., Yelekçi, , Yu, R., and Zhou, B., editors, *Climate Change 2021: The Physical Science Basis. Contribution of Working Group I to the Sixth Assessment Report of the Intergovernmental Panel on Climate Change*. Cambridge University Press.

Gulick, S. P. S., Shevenell, A. E., Montelli, A., Fernandez, R., Smith, C., Warny, S., Bohaty, S. M., Sjunneskog, C., Leventer, A., Frederick, B., and Blankenship, D. D. (2017). Initiation and long-term instability of the East Antarctic Ice Sheet. *Nature*, 552(7684):225–229. Number: 7684 Publisher: Nature Publishing Group.

Hallegatte, S., Green, C., Nicholls, R. J., and Corfee-Morlot, J. (2013). Future flood losses in major coastal cities. *Nature Climate Change*, 3(9):802–806. Number: 9 Publisher: Nature Publishing Group.

Han, H. K., Gomez, N., Pollard, D., and DeConto, R. (2021). Modeling Northern Hemispheric Ice Sheet Dynamics, Sea Level Change, and Solid Earth Deformation Through the Last Glacial Cycle. *Journal of Geophysical Research: Earth Surface*, 126(4):e2020JF006040. _eprint: https://onlinelibrary.wiley.com/doi/pdf/10.1029/2020JF006040.

Hanson, B. and Hooke, R. L. (2000). Glacier calving: a numerical model of forces in the calving-speed/water-depth relation. *Journal of Glaciology*, 46(153):188–196. Publisher: Cambridge University Press.

Hanson, B. and Hooke, R. L. B. (2003). Buckling rate and overhang development at a calving face. *Journal of Glaciology*, 49(167):577–586. Publisher: Cambridge University Press.

Harwood, D. and Webb, P. (1998). Glacial transport of diatoms in the Antarctic Sirius Group: Pliocene refrigerator. *GSA Today*, 8(4):1–8.

Hasumi, H. and Emori, S. (2008). K-1 Coupled GCM ( MIROC ) Description K-1 model developers.

Haywood, A. M., Dowsett, H. J., and Dolan, A. M. (2016a). Integrating geological archives and climate models for the mid-Pliocene warm period. *Nature Communications*, 7(1):10646. Bandiera_abtest: a Cc_license_type: cc_by Cg_type: Nature Research Journals Number: 1 Primary_atype: Reviews Publisher: Nature Publishing Group Subject_term: Climate and Earth system modelling;Palaeoclimate Subject_term_id: climate-and-earth-system-modelling;palaeoclimate.

Haywood, A. M., Dowsett, H. J., Dolan, A. M., Rowley, D., Abe-Ouchi, A., Otto-Bliesner, B., Chandler, M. A., Hunter, S. J., Lunt, D. J., Pound, M., and Salzmann, U. (2016b). The Pliocene Model Intercomparison Project (PlioMIP) Phase 2: scientific objectives and experimental design. *Climate of the Past*, 12(3):663–675. Publisher: Copernicus GmbH.

Haywood, A. M., Dowsett, H. J., Otto-Bliesner, B., Chandler, M. A., Dolan, A. M., Hill, D. J., Lunt, D. J., Robinson, M. M., Rosenbloom, N., Salzmann, U., and Sohl, L. E. (2010). Pliocene Model Intercomparison Project (PlioMIP): experimental design and boundary conditions (Experiment 1). *Geoscientific Model Development*, 3(1):227–242. Publisher: Copernicus GmbH.

Haywood, A. M., Tindall, J. C., Dowsett, H. J., Dolan, A. M., Foley, K. M., Hunter, S. J., Hill, D. J., Chan, W.-L., Abe-Ouchi, A., Stepanek, C., Lohmann, G., Chandan, D., Peltier, W. R., Tan, N., Contoux, C., Ramstein, G., Li, X., Zhang, Z., Guo, C., Nisancioglu, K. H., Zhang, Q., Li, Q., Kamae, Y., Chandler, M. A., Sohl, L. E., Otto-Bliesner, B. L., Feng, R., Brady, E. C., von der Heydt, A. S., Baatsen, M. L. J., and Lunt, D. J. (2020). The Pliocene Model Intercomparison Project Phase 2: large-scale climate features and climate sensitivity. *Climate of the Past*, 16(6):2095–2123. Publisher: Copernicus GmbH.

Haywood, A. M., Valdes, P. J., and Sellwood, B. W. (2000). Global scale palaeoclimate reconstruction of the middle Pliocene climate using the UKMO GCM: initial results. *Global and Planetary Change*, 25(3):239–256.

Heeszel, D. S., Wiens, D. A., Anandakrishnan, S., Aster, R. C., Dalziel, I. W. D., Huerta, A. D., Nyblade, A. A., Wilson, T. J., and Winberry, J. P. (2016). Upper mantle structure of central and West Antarctica from array analysis of Rayleigh wave phase velocities. *Journal of Geophysical Research: Solid Earth*, 121(3):1758–1775. _eprint: https://onlinelibrary.wiley.com/doi/pdf/10.1002/2015JB012616.

Heinemann, M., Timmermann, A., Elison Timm, O., Saito, F., and Abe-Ouchi, A. (2014). Deglacial ice sheet meltdown: orbital pacemaking and $CO_2$ effects. *Climate of the Past*, 10(4):1567–1579. Publisher: Copernicus GmbH.

Hewitt, I. J. (2011). Modelling distributed and channelized subglacial drainage: the spacing of channels. *Journal of Glaciology*, 57(202):302–314. Publisher: Cambridge University Press.

Hewitt, I. J. (2013). Seasonal changes in ice sheet motion due to melt water lubrication. *Earth and Planetary Science Letters*, 371-372:16–25.

Hibler, W. D. (1979). A Dynamic Thermodynamic Sea Ice Model. *Journal of Physical Oceanography*, 9(4):815–846. Publisher: American Meteorological Society Section: Journal of Physical Oceanography.

Hill, D. (2009). *Modelling Earth's Cryosphere During Peak Pliocene Warmth*. PhD thesis, University of Bristol.

Hill, D. J., Haywood, A. M., Lunt, D. J., Hunter, S. J., Bragg, F. J., Contoux, C., Stepanek, C., Sohl, L., Rosenbloom, N. A., Chan, W.-L., Kamae, Y., Zhang, Z., Abe-Ouchi, A., Chandler, M. A., Jost, A., Lohmann, G., Otto-Bliesner, B. L., Ramstein, G., and Ueda, H. (2014). Evaluating the dominant components of warming in Pliocene climate simulations. *Climate of the Past*, 10(1):79–90.

Hock, R. (2003). Temperature index melt modelling in mountain areas. *Journal of Hydrology*, 282(1):104–115.

Hogg, A. E. and Gudmundsson, G. H. (2017). Impacts of the Larsen-C Ice Shelf calving event. *Nature Climate Change*, 7(8):540–542. Number: 8 Publisher: Nature Publishing Group.

Holland, P. R., Bracegirdle, T. J., Dutrieux, P., Jenkins, A., and Steig, E. J. (2019). West Antarctic ice loss influenced by internal climate variability and anthropogenic forcing. *Nature Geoscience*, 12(9):718–724. Number: 9 Publisher: Nature Publishing Group.

Hooke, R. (1981). Flow law for polycrystalline ice in glaciers: Comparison of theoretical predictions, laboratory data, and field measurements. *Reviews of Geophysics*, 19(4):664–672. _eprint: https://onlinelibrary.wiley.com/doi/pdf/10.1029/RG019i004p00664.

Hooke, R. L. (1989). Englacial and Subglacial Hydrology: A Qualitative Review. *Arctic and Alpine Research*, 21(3):221–233. Publisher: Taylor & Francis _eprint: https://www.tandfonline.com/doi/pdf/10.1080/00040851.1989.12002734.

Horwath, M., Gutknecht, B. D., Cazenave, A., Palanisamy, H. K., Marti, F., Marzeion, B., Paul, F., Le Bris, R., Hogg, A. E., Otosaka, I., Shepherd, A., Döll, P., Cáceres, D., Müller Schmied, H., Johannessen, J. A., Nilsen, J. E. , Raj, R. P., Forsberg, R., Sandberg Sørensen, L., Barletta, V. R., Simonsen, S. B., Knudsen, P., Andersen, O. B.,

Ranndal, H., Rose, S. K., Merchant, C. J., Macintosh, C. R., von Schuckmann, K., Novotny, K., Groh, A., Restano, M., and Benveniste, J. (2022). Global sea-level budget and ocean-mass budget, with a focus on advanced data products and uncertainty characterisation. *Earth System Science Data*, 14(2):411–447. Publisher: Copernicus GmbH.

Hulbe, C. (2017). Is ice sheet collapse in West Antarctica unstoppable? *Science*, 356(6341):910–911. Publisher: American Association for the Advancement of Science.

Hunke, E., Lipscomb, W., Jones, P., Turner, A., Jeffery, N., and Elliott, S. (2017). CICE, The Los Alamos Sea Ice Model. Technical Report CICE; 005315WKSTN00, Los Alamos National Lab. (LANL), Los Alamos, NM (United States).

Hunter, S. J., Haywood, A. M., Dolan, A. M., and Tindall, J. C. (2019). The HadCM3 contribution to PlioMIP phase 2. *Climate of the Past*, 15(5):1691–1713. Publisher: Copernicus GmbH.

Hutter, K. (1983). General Concepts. In Hutter, K., editor, *Theoretical Glaciology: Material Science of Ice and the Mechanics of Glaciers and Ice Sheets*, Mathematical Approaches to Geophysics, pages 3–47. Springer Netherlands, Dordrecht.

Huybrechts, P. and Oerlemans, J. (1990). Response of the Antarctic ice sheet to future greenhouse warming. *Climate Dynamics*, 5(2):93–102.

Huybrechts, P. and Wolde, J. d. (1999). The Dynamic Response of the Greenland and Antarctic Ice Sheets to Multiple-Century Climatic Warming. *Journal of Climate*, 12(8):2169–2188. Publisher: American Meteorological Society Section: Journal of Climate.

Ivins, E. R. and James, T. S. (2005). Antarctic glacial isostatic adjustment: a new assessment. *Antarctic Science*, 17(4):541–553. Publisher: Cambridge University Press.

Ivins, E. R. and Sammis, C. G. (1995). On lateral viscosity contrast in the mantle and the rheology of low-frequency geodynamics. *Geophysical Journal International*, 123(2):305–322.

Johnston, P. (1993). The effect of spatially non-uniform water loads on prediction of sea-level change. *Geophysical Journal International*, 114(3):615–634.

Joughin, I. and Alley, R. B. (2011). Stability of the West Antarctic ice sheet in a warming world. *Nature Geoscience*, 4(8):506–513. Number: 8 Publisher: Nature Publishing Group.

Joughin, I., Shean, D. E., Smith, B. E., and Floricioiu, D. (2020). A decade of variability on Jakobshavn Isbræ: ocean temperatures pace speed through influence on mélange rigidity. *The Cryosphere*, 14(1):211–227. Publisher: Copernicus GmbH.

Jourdain, N. C., Asay-Davis, X., Hattermann, T., Straneo, F., Seroussi, H., Little, C. M., and Nowicki, S. (2020). A protocol for calculating basal melt rates in the ISMIP6 Antarctic ice sheet projections. *The Cryosphere*, 14(9):3111–3134. Publisher: Copernicus GmbH.

Jourdain, N. C., Mathiot, P., Merino, N., Durand, G., Le Sommer, J., Spence, P., Dutrieux, P., and Madec, G. (2017). Ocean circulation and sea-ice thinning induced by melting ice shelves in the Amundsen Sea. *Journal of Geophysical Research: Oceans*, 122(3):2550–2573. _eprint: https://onlinelibrary.wiley.com/doi/pdf/10.1002/2016JC012509.

Kachuck, S. B., Martin, D. F., Bassis, J. N., and Price, S. F. (2020). Rapid Viscoelastic Deformation Slows Marine Ice Sheet Instability at Pine Island Glacier. *Geophysical Research Letters*, 47(10):e2019GL086446. _eprint: https://onlinelibrary.wiley.com/doi/pdf/10.1029/2019GL086446.

Kemp, A. C., Dutton, A., and Raymo, M. E. (2015). Paleo Constraints on Future Sea-Level Rise. *Current Climate Change Reports*, 1(3):205–215.

Kingslake, J., Scherer, R. P., Albrecht, T., Coenen, J., Powell, R. D., Reese, R., Stansell, N. D., Tulaczyk, S., Wearing, M. G., and Whitehouse, P. L. (2018). Extensive retreat and re-advance of the West Antarctic Ice Sheet during the Holocene. *Nature*, 558(7710):430–434. Number: 7710 Publisher: Nature Publishing Group.

Knott, J. R., Machette, M. N., Wan, E., Klinger, R. E., Liddicoat, J. C., Sarna-Wojcicki, A. M., Fleck, R. J., Deino, A. L., Geissman, J. W., Slate, J. L., Wahl, D. B., Wernicke, B. P., Wells, S. G., Tinsley, III, J. C., Hathaway, J. C., and Weamer, V. M. (2018). Late Neogene–Quaternary tephrochronology, stratigraphy, and paleoclimate of Death Valley, California, USA. *GSA Bulletin*, 130(7-8):1231–1255.

Koenig, S. J., Dolan, A. M., de Boer, B., Stone, E. J., Hill, D. J., DeConto, R. M., Abe-Ouchi, A., Lunt, D. J., Pollard, D., Quiquet, A., Saito, F., Savage, J., and van de Wal, R. (2015). Ice sheet model dependency of the simulated Greenland Ice Sheet in the mid-Pliocene. *Climate of the Past*, 11(3):369–381. Publisher: Copernicus GmbH.

Konrad, H., Sasgen, I., Pollard, D., and Klemann, V. (2015). Potential of the solid-Earth response for limiting long-term West Antarctic Ice Sheet retreat in a warming climate. *Earth and Planetary Science Letters*, 432:254–264.

Konrad, H., Shepherd, A., Gilbert, L., Hogg, A. E., McMillan, M., Muir, A., and Slater, T. (2018). Net retreat of Antarctic glacier grounding lines. *Nature Geoscience*, 11(4):258–262. Number: 4 Publisher: Nature Publishing Group.

Kozdon, R., Kelly, D. C., Kitajima, K., Strickland, A., Fournelle, J. H., and Valley, J. W. (2013). In situ 18O and Mg/Ca analyses of diagenetic and planktic foraminiferal calcite preserved in a deep-sea record of the Paleocene-Eocene thermal maximum. *Paleoceanography*, 28(3):517–528. _eprint: https://onlinelibrary.wiley.com/doi/pdf/10.1002/palo.20048.

Krantz, D. E. (1991). A chronology of Pliocene sea-level fluctuations: The U.S. Middle Atlantic Coastal Plain record. *Quaternary Science Reviews*, 10(2):163–174.

Kustowski, B., Ekström, G., and Dziewoński, A. M. (2008). Anisotropic shear-wave velocity structure of the Earth's mantle: A global model. *Journal of Geophysical Research: Solid Earth*, 113(B6). _eprint: https://onlinelibrary.wiley.com/doi/pdf/10.1029/2007JB005169.

Lambeck, K. (1998). On the choice of timescale in glacial rebound modelling: mantle viscosity estimates and the radiocarbon timescale. *Geophysical Journal International*, 134(2):647–651.

Lambeck, K., Rouby, H., Purcell, A., Sun, Y., and Sambridge, M. (2014). Sea level and global ice volumes from the Last Glacial Maximum to the Holocene. *Proceedings of the National Academy of Sciences*, 111(43):15296–15303.

Larour, E., Seroussi, H., Adhikari, S., Ivins, E., Caron, L., Morlighem, M., and Schlegel, N. (2019). Slowdown in Antarctic mass loss from solid Earth and sea-level feedbacks. *Science*. Publisher: American Association for the Advancement of Science.

Laskar, J., Robutel, P., Joutel, F., Gastineau, M., Correia, A. C. M., and Levrard, B. (2004). A long-term numerical solution for the insolation quantities of the Earth. *Astronomy & Astrophysics*, 428(1):261–285. Number: 1 Publisher: EDP Sciences.

Latychev, K., Mitrovica, J. X., Tromp, J., Tamisiea, M. E., Komatitsch, D., and Christara, C. C. (2005). Glacial isostatic adjustment on 3-D Earth models: a finite-volume formulation. *Geophysical Journal International*, 161(2):421–444.

Lawrence, D. M., Oleson, K. W., Flanner, M. G., Thornton, P. E., Swenson, S. C., Lawrence, P. J., Zeng, X., Yang, Z.-L., Levis, S., Sakaguchi, K., Bonan, G. B., and Slater, A. G. (2011). Parameterization improvements and functional and structural advances in Version 4 of the Community Land Model. *Journal of Advances in Modeling Earth Systems*, 3(1). _eprint: https://onlinelibrary.wiley.com/doi/pdf/10.1029/2011MS00045.

Le Brocq, A. M., Ross, N., Griggs, J. A., Bingham, R. G., Corr, H. F. J., Ferraccioli, F., Jenkins, A., Jordan, T. A., Payne, A. J., Rippin, D. M., and Siegert, M. J. (2013). Evidence from ice shelves for channelized meltwater flow beneath the Antarctic Ice Sheet. *Nature Geoscience*, 6(11):945–948. Number: 11 Publisher: Nature Publishing Group.

Lecavalier, B. S., Milne, G. A., Simpson, M. J. R., Wake, L., Huybrechts, P., Tarasov, L., Kjeldsen, K. K., Funder, S., Long, A. J., Woodroffe, S., Dyke, A. S., and Larsen, N. K. (2014). A model of Greenland ice sheet deglaciation constrained by observations of relative sea level and ice extent. *Quaternary Science Reviews*, 102:54–84.

Leroy, S. and Dupont, L. (1994). Development of vegetation and continental aridity in northwestern Africa during the Late Pliocene: the pollen record of ODP site 658. *Palaeogeography, Palaeoclimatology, Palaeoecology*, 109(2):295–316.

Levitus, S. and Boyer, T. (1994). World ocean atlas 1994. Vol. 4. Technical report, NOAA.

Lingle, C. S. and Clark, J. A. (1985). A numerical model of interactions between a marine ice sheet and the solid earth: Application to a West Antarctic ice stream. *Journal of Geophysical Research: Oceans*, 90(C1):1100–1114. _eprint: https://onlinelibrary.wiley.com/doi/pdf/10.1029/JC090iC01p01100.

Lipscomb, W. H., Leguy, G. R., Jourdain, N. C., Asay-Davis, X., Seroussi, H., and Nowicki, S. (2021). ISMIP6-based projections of ocean-forced Antarctic Ice Sheet evolution using the Community Ice Sheet Model. *The Cryosphere*, 15(2):633–661. Publisher: Copernicus GmbH.

Lisiecki, L. E. and Raymo, M. E. (2005). A Pliocene-Pleistocene stack of 57 globally distributed benthic $^{18}$ O records: PLIOCENE-PLEISTOCENE BENTHIC STACK. *Paleoceanography*, 20(1):n/a–n/a.

Liu, Y., Moore, J. C., Cheng, X., Gladstone, R. M., Bassis, J. N., Liu, H., Wen, J., and Hui, F. (2015). Ocean-driven thinning enhances iceberg calving and retreat of Antarctic ice shelves. *Proceedings of the National Academy of Sciences*, 112(11):3263–3268. Publisher: Proceedings of the National Academy of Sciences.

Locarnini, R., Mishonov, A., Baranova, O., Boyer, T., Zweng, M., Garcia, H., Reagan, J., Seidov, D., Weathers, K., Paver, C., and Smolyar, I. (2019). World Ocean Atlas 2018, Volume 1: Temperature, Tech. Rep. Atlas NESDIS 81, NOAA. Technical report.

Lowry, D. P., Krapp, M., Golledge, N. R., and Alevropoulos-Borrill, A. (2021). The influence of emissions scenarios on future Antarctic ice loss is unlikely to emerge this century. *Communications Earth & Environment*, 2(1):1–14. Bandiera_abtest: a Cc_license_type: cc_by Cg_type: Nature Research Journals Number: 1 Primary_atype: Research Publisher: Nature Publishing Group Subject_term: Cryospheric science;Projection and prediction Subject_term_id: cryospheric-science;projection-and-prediction.

Lunt, D. J., Haywood, A. M., Schmidt, G. A., Salzmann, U., Valdes, P. J., Dowsett, H. J., and Loptson, C. A. (2012). On the causes of mid-Pliocene warmth and polar amplification. *Earth and Planetary Science Letters*, 321-322:128–138.

Ma, Y., Tripathy, C. S., and Bassis, J. N. (2017). Bounds on the calving cliff height of marine terminating glaciers. *Geophysical Research Letters*, 44(3):1369–1375. _eprint: https://onlinelibrary.wiley.com/doi/pdf/10.1002/2016GL071560.

MacAyeal, D. R., Bindschadler, R. A., and Scambos, T. A. (1995). Basal friction of Ice Stream E, West Antarctica. *Journal of Glaciology*, 41(138):247–262. Publisher: Cambridge University Press.

Machette, M. N., Thompson, R. A., Marchetti, D. W., and Smith, R. S. U. (2013). Evolution of ancient Lake Alamosa and integration of the Rio Grande during the Pliocene and Pleistocene.

Magand, O., Frezzotti, M., Pourchet, M., Stenni, B., Genoni, L., and Fily, M. (2004). Climate variability along latitudinal and longitudinal transects in East Antarctica. *Annals of Glaciology*, 39:351–358. Publisher: Cambridge University Press.

Mai, D. H. M. a. (1995). *Tertiäre Vegetationsgeschichte Europas : Methoden und Ergebnisse*. G. Fischer Verlag, Jena.

Marsland, S. J., Haak, H., Jungclaus, J. H., Latif, M., and Röske, F. (2003). The Max-Planck-Institute global ocean/sea ice model with orthogonal curvilinear coordinates. *Ocean Modelling*, 5(2):91–127.

Martin, D. F., Cornford, S. L., and Payne, A. J. (2019). Millennial-Scale Vulnerability of the Antarctic Ice Sheet to Regional Ice Shelf Collapse. *Geophysical Research Letters*, 46(3):1467–1475. _eprint: https://onlinelibrary.wiley.com/doi/pdf/10.1029/2018GL081229.

Martin, M. A., Winkelmann, R., Haseloff, M., Albrecht, T., Bueler, E., Khroulev, C., and Levermann, A. (2011). The Potsdam Parallel Ice Sheet Model (PISM-PIK) – Part 2: Dynamic equilibrium simulation of the Antarctic ice sheet. *The Cryosphere*, 5(3):727–740. Publisher: Copernicus GmbH.

Matero, I. S. O., Gregoire, L. J., and Ivanovic, R. F. (2020). Simulating the Early Holocene demise of the Laurentide Ice Sheet with BISICLES (public trunk revision 3298). *Geoscientific Model Development*, 13(9):4555–4577. Publisher: Copernicus GmbH.

Matsuoka, K., Hindmarsh, R. C. A., Moholdt, G., Bentley, M. J., Pritchard, H. D., Brown, J., Conway, H., Drews, R., Durand, G., Goldberg, D., Hattermann, T., Kingslake, J., Lenaerts, J. T. M., Martín, C., Mulvaney, R., Nicholls, K. W., Pattyn, F., Ross, N., Scambos, T., and Whitehouse, P. L. (2015). Antarctic ice rises and rumples: Their properties and significance for ice-sheet dynamics and evolution. *Earth-Science Reviews*, 150:724–745.

McClymont, E. L., Ford, H. L., Ho, S. L., Tindall, J. C., Haywood, A. M., Alonso-Garcia, M., Bailey, I., Berke, M. A., Littler, K., Patterson, M. O., Petrick, B., Peterse, F., Ravelo, A. C., Risebrobakken, B., De Schepper, S., Swann, G. E. A., Thirumalai, K., Tierney, J. E., van der Weijst, C., White, S., Abe-Ouchi, A., Baatsen, M. L. J., Brady, E. C., Chan, W.-L., Chandan, D., Feng, R., Guo, C., von der Heydt, A. S., Hunter, S., Li, X., Lohmann, G., Nisancioglu, K. H., Otto-Bliesner, B. L., Peltier, W. R., Stepanek, C., and Zhang, Z. (2020). Lessons from a high-$CO_2$ world: an ocean view from 3 million years ago. *Climate of the Past*, 16(4):1599–1615. Publisher: Copernicus GmbH.

McDougall, T. and Barker, P. (2011). *Getting started with TEOS---10 and the Gibbs Seawater (GSW) Oceanographic Toolbox*. SCOR/IAPSO WG127.

McGregor, S., Gupta, A. S., and England, M. H. (2012). Constraining Wind Stress Products with Sea Surface Height Observations and Implications for Pacific Ocean Sea Level Trend Attribution. *Journal of Climate*, 25(23):8164–8176. Publisher: American Meteorological Society Section: Journal of Climate.

Medley, B. and Thomas, E. R. (2019). Increased snowfall over the Antarctic Ice Sheet mitigated twentieth-century sea-level rise. *Nature Climate Change*, 9(1):34–39. Bandiera_abtest: a Cg_type: Nature Research Journals Number: 1 Primary_atype: Research Publisher: Nature Publishing Group Subject_term: Climate-change impacts;Cryospheric science Subject_term_id: climate-change-impacts;cryospheric-science.

Meehl, G. A., Senior, C. A., Eyring, V., Flato, G., Lamarque, J.-F., Stouffer, R. J., Taylor, K. E., and Schlund, M. (2020). Context for interpreting equilibrium climate sensitivity and transient climate response from the CMIP6 Earth system models. *Science Advances*, 6(26):eaba1981.

Meier, M. F. and Post, A. (1987). Fast tidewater glaciers. *Journal of Geophysical Research: Solid Earth*, 92(B9):9051–9058. _eprint: https://onlinelibrary.wiley.com/doi/pdf/10.1029/JB092iB09p09051.

Mengel, M. and Levermann, A. (2014). Ice plug prevents irreversible discharge from East Antarctica. *Nature Climate Change*, 4(6):451–455. Number: 6 Publisher: Nature Publishing Group.

Mercer, J. H. (1978). West Antarctic ice sheet and CO2 greenhouse effect: a threat of disaster. *Nature*, 271(5643):321–325. Number: 5643 Publisher: Nature Publishing Group.

Meur, E. L. and Huybrechts, P. (1996). A comparison of different ways of dealing with isostasy: examples from modelling the Antarctic ice sheet during the last glacial cycle. *Annals of Glaciology*, 23:309–317. Publisher: Cambridge University Press.

Miller, K. G., Browning, J. V., Schmelz, W. J., Kopp, R. E., Mountain, G. S., and Wright, J. D. (2020). Cenozoic sea-level and cryospheric evolution from deep-sea geochemical and continental margin records. *Science Advances*, 6(20):eaaz1346.

Miller, K. G., Wright, J. D., Browning, J. V., Kulpecz, A., Kominz, M., Naish, T. R., Cramer, B. S., Rosenthal, Y., Peltier, W. R., and Sosdian, S. (2012). High tide of the warm Pliocene: Implications of global sea level for Antarctic deglaciation. *Geology*, 40(5):407–410.

Milne, G. A. and Mitrovica, J. X. (1998). Postglacial sea-level change on a rotating Earth. *Geophysical Journal International*, 133(1):1–19.

Mitrovica, J. X. and Forte, A. M. (1997). Radial profile of mantle viscosity: Results from the joint inversion of convection and postglacial rebound observables. *Journal of Geophysical Research: Solid Earth*, 102(B2):2751–2769. _eprint: https://onlinelibrary.wiley.com/doi/pdf/10.1029/96JB03175.

Mitrovica, J. X. and Forte, A. M. (2004). A new inference of mantle viscosity based upon joint inversion of convection and glacial isostatic adjustment data. *Earth and Planetary Science Letters*, 225(1):177–189.

Mitrovica, J. X., Gomez, N., Morrow, E., Hay, C., Latychev, K., and Tamisiea, M. E. (2011). On the robustness of predictions of sea level fingerprints. *Geophysical Journal International*, 187(2):729–742.

Mitrovica, J. X. and Milne, G. A. (2003). On post-glacial sea level: I. General theory. *Geophysical Journal International*, 154(2):253–267.

Morlighem, M., Rignot, E., Binder, T., Blankenship, D., Drews, R., Eagles, G., Eisen, O., Ferraccioli, F., Forsberg, R., Fretwell, P., Goel, V., Greenbaum, J. S., Gudmundsson, H., Guo, J., Helm, V., Hofstede, C., Howat, I., Humbert, A., Jokat, W., Karlsson, N. B., Lee, W. S., Matsuoka, K., Millan, R., Mouginot, J., Paden, J., Pattyn, F., Roberts, J., Rosier, S., Ruppel, A., Seroussi, H., Smith, E. C., Steinhage, D., Sun, B., Broeke, M. R. v. d., Ommen, T. D. v., Wessem, M. v., and Young, D. A. (2020). Deep glacial troughs and stabilizing ridges unveiled beneath the margins of the Antarctic ice sheet. *Nature Geoscience*, 13(2):132–137. Number: 2 Publisher: Nature Publishing Group.

Morlighem, M., Seroussi, H., Larour, E., and Rignot, E. (2013). Inversion of basal friction in Antarctica using exact and incomplete adjoints of a higher-order model. *Journal of Geophysical Research: Earth Surface*, 118(3):1746–1753. _eprint: https://onlinelibrary.wiley.com/doi/pdf/10.1002/jgrf.20125.

Mottram, R., Hansen, N., Kittel, C., van Wessem, J. M., Agosta, C., Amory, C., Boberg, F., van de Berg, W. J., Fettweis, X., Gossart, A., van Lipzig, N. P. M., van Meijgaard, E., Orr, A., Phillips, T., Webster, S., Simonsen, S. B., and Souverijns, N. (2021). What is the surface mass balance of Antarctica? An intercomparison of regional climate model estimates. *The Cryosphere*, 15(8):3751–3784. Publisher: Copernicus GmbH.

Mouginot, J., Rignot, E., and Scheuchl, B. (2019). Continent-Wide, Interferometric SAR Phase, Mapping of Antarctic Ice Velocity. *Geophysical Research Letters*, 46(16):9710–9718. _eprint: https://onlinelibrary.wiley.com/doi/pdf/10.1029/2019GL083826.

Muntjewerf, L., Sacks, W. J., Lofverstrom, M., Fyke, J., Lipscomb, W. H., Ernani da Silva, C., Vizcaino, M., Thayer-Calder, K., Lenaerts, J. T. M., and Sellevold, R. (2021). Description and Demonstration of the Coupled Community Earth System Model v2 – Community Ice Sheet Model v2 (CESM2-CISM2). *Journal of Advances in Modeling Earth Systems*, 13(6):e2020MS002356. _eprint: https://onlinelibrary.wiley.com/doi/pdf/10.1029/2020MS002356.

Murphy, J. M., Sexton, D. M. H., Barnett, D. N., Jones, G. S., Webb, M. J., Collins, M., and Stainforth, D. A. (2004). Quantification of modelling uncertainties in a large ensemble of climate change simulations. *Nature*, 430(7001):768–772. Number: 7001 Publisher: Nature Publishing Group.

Naish, T., Powell, R., Levy, R., Wilson, G., Scherer, R., Talarico, F., Krissek, L., Niessen, F., Pompilio, M., Wilson, T., Carter, L., DeConto, R., Huybers, P., McKay, R., Pollard, D., Ross, J., Winter, D., Barrett, P., Browne, G., Cody, R., Cowan, E., Crampton, J., Dunbar, G., Dunbar, N., Florindo, F., Gebhardt, C., Graham, I., Hannah, M., Hansaraj, D., Harwood, D., Helling, D., Henrys, S., Hinnov, L., Kuhn, G., Kyle, P., Läufer, A., Maffioli, P., Magens, D., Mandernack, K., McIntosh, W., Millan, C., Morin, R., Ohneiser, C., Paulsen, T., Persico, D., Raine, I., Reed, J., Riesselman, C., Sagnotti, L., Schmitt, D., Sjunneskog, C., Strong, P., Taviani, M., Vogel, S., Wilch, T., and Williams, T. (2009). Obliquity-paced Pliocene West Antarctic ice sheet oscillations. *Nature*, 458(7236):322–328. Number: 7236 Publisher: Nature Publishing Group.

Naish, T. R. and Wilson, G. S. (2009). Constraints on the amplitude of Mid-Pliocene (3.6–2.4 Ma) eustatic sea-level fluctuations from the New Zealand shallow-marine sediment record. *Philosophical Transactions of the Royal Society A: Mathematical, Physical and Engineering Sciences*, 367(1886):169–187.

Nakada, M. and Okuno, J. (2016). Inference of mantle viscosity for depth resolutions of GIA observations. *Geophysical Journal International*, 207(2):719–740.

Naughten, K. A., Meissner, K. J., Galton-Fenzi, B. K., England, M. H., Timmermann, R., Hellmer, H. H., Hattermann, T., and Debernard, J. B. (2018). Intercomparison of Antarctic ice-shelf, ocean, and sea-ice interactions simulated by MetROMS-iceshelf and FESOM 1.4. *Geoscientific Model Development*, 11(4):1257–1292. Publisher: Copernicus GmbH.

Neale, R. B., Richter, J., Park, S., Lauritzen, P. H., Vavrus, S. J., Rasch, P. J., and Zhang, M. (2013). The Mean Climate of the Community Atmosphere Model (CAM4) in Forced SST and Fully Coupled Experiments. *Journal of Climate*, 26(14):5150–5168. Publisher: American Meteorological Society Section: Journal of Climate.

Neumann, B., Vafeidis, A. T., Zimmermann, J., and Nicholls, R. J. (2015). Future Coastal Population Growth and Exposure to Sea-Level Rise and Coastal Flooding - A Global Assessment. *PLOS ONE*, 10(3):e0118571. Publisher: Public Library of Science.

Nias, I. J., Cornford, S. L., Edwards, T. L., Gourmelen, N., and Payne, A. J. (2019). Assessing Uncertainty in the Dynamical Ice Response to Ocean Warming in the Amundsen

Sea Embayment, West Antarctica. *Geophysical Research Letters*, 46(20):11253–11260. _eprint: https://onlinelibrary.wiley.com/doi/pdf/10.1029/2019GL084941.

Nias, I. J., Cornford, S. L., and Payne, A. J. (2016). Contrasting the modelled sensitivity of the Amundsen Sea Embayment ice streams. *Journal of Glaciology*, 62(233):552–562. Publisher: Cambridge University Press.

Nias, I. J., Cornford, S. L., and Payne, A. J. (2018). New Mass-Conserving Bedrock Topography for Pine Island Glacier Impacts Simulated Decadal Rates of Mass Loss. *Geophysical Research Letters*, 45(7):3173–3181. _eprint: https://onlinelibrary.wiley.com/doi/pdf/10.1002/2017GL076493.

Nick, F. M., Veen, C. J. V. D., Vieli, A., and Benn, D. I. (2010). A physically based calving model applied to marine outlet glaciers and implications for the glacier dynamics. *Journal of Glaciology*, 56(199):781–794. Publisher: Cambridge University Press.

Nick, F. M., Vieli, A., Howat, I. M., and Joughin, I. (2009). Large-scale changes in Greenland outlet glacier dynamics triggered at the terminus. *Nature Geoscience*, 2(2):110–114. Number: 2 Publisher: Nature Publishing Group.

Nield, G. A., Barletta, V. R., Bordoni, A., King, M. A., Whitehouse, P. L., Clarke, P. J., Domack, E., Scambos, T. A., and Berthier, E. (2014). Rapid bedrock uplift in the Antarctic Peninsula explained by viscoelastic response to recent ice unloading. *Earth and Planetary Science Letters*, 397:32–41.

Nield, G. A., Whitehouse, P. L., van der Wal, W., Blank, B., O'Donnell, J. P., and Stuart, G. W. (2018). The impact of lateral variations in lithospheric thickness on glacial isostatic adjustment in West Antarctica. *Geophysical Journal International*, 214(2):811–824.

Niu, L., Lohmann, G., Gierz, P., Gowan, E. J., and Knorr, G. (2021). Coupled climate-ice sheet modelling of MIS-13 reveals a sensitive Cordilleran Ice Sheet. *Global and Planetary Change*, 200:103474.

Nowicki, S. M. J., Payne, A., Larour, E., Seroussi, H., Goelzer, H., Lipscomb, W., Gregory, J., Abe-Ouchi, A., and Shepherd, A. (2016). Ice Sheet Model Intercomparison Project (ISMIP6) contribution to CMIP6. *Geoscientific Model Development*, 9(12):4521–4545. Publisher: Copernicus GmbH.

Numaguti, A., Takahashi, M., Nakajima, T., and Sumi, A. (1997). Description of CCSR-NIES atmospheric general circulation model Chapter 1. Technical Report 1341-4356, Japan. CGER–1025-97 INIS Reference Number: 39072469.

Nye, J. F. (1976). Water Flow in Glaciers: Jökulhlaups, Tunnels and Veins. *Journal of Glaciology*, 17(76):181–207. Publisher: Cambridge University Press.

Oerlemans, J. (1980). Model experiments on the 100,000-yr glacial cycle. *Nature*, 287(5781):430–432. Number: 5781 Publisher: Nature Publishing Group.

Oleson, K., Lawrence, D., Bonan, G., Flanner, M., Kluzek, E., Lawrence, P., Levis, S., Swenson, S., Thornton, P., Dai, A., Decker, M., Dickinson, R., Feddema, J., Heald, C., Hoffman, F., Lamarque, J.-F., Mahowald, N., Niu, G.-Y., Qian, T., Randerson, J., Running, S., Sakaguchi, K., Slater, A., Stockli, R., Wang, A., Yang, Z.-L., Zeng, X., and Zeng, X. (2010). Technical Description of version 4.0 of the Community Land

Model (CLM). Technical report, UCAR/NCAR. Artwork Size: 2612 KB Medium: application/pdf.

Palerme, C., Genthon, C., Claud, C., Kay, J. E., Wood, N. B., and L'Ecuyer, T. (2017). Evaluation of current and projected Antarctic precipitation in CMIP5 models. *Climate Dynamics*, 48(1):225–239.

Pan, L., Powell, E. M., Latychev, K., Mitrovica, J. X., Creveling, J. R., Gomez, N., Hoggard, M. J., and Clark, P. U. (2021). Rapid postglacial rebound amplifies global sea level rise following West Antarctic Ice Sheet collapse. *Science Advances*, 7(18):eabf7787. Publisher: American Association for the Advancement of Science.

Parizek, B. R., Christianson, K., Alley, R. B., Voytenko, D., Vaňková, I., Dixon, T. H., Walker, R. T., and Holland, D. M. (2019). Ice-cliff failure via retrogressive slumping. *Geology*, 47(5):449–452.

Paterson, W. S. B. (1994). *Physics of Glaciers*. Butterworth-Heinemann. Google-Books-ID: X75dmp9QFbgC.

Patterson, M. O., McKay, R., Naish, T., Escutia, C., Jimenez-Espejo, F. J., Raymo, M. E., Meyers, S. R., Tauxe, L., and Brinkhuis, H. (2014). Orbital forcing of the East Antarctic ice sheet during the Pliocene and Early Pleistocene. *Nature Geoscience*, 7(11):841–847. Bandiera_abtest: a Cg_type: Nature Research Journals Number: 11 Primary_atype: Research Publisher: Nature Publishing Group Subject_term: Palaeoceanography;Palaeoclimate Subject_term_id: palaeoceanography;palaeoclimate.

Pattyn, F. (2003). A new three-dimensional higher-order thermomechanical ice sheet model: Basic sensitivity, ice stream development, and ice flow across subglacial lakes. *Journal of Geophysical Research: Solid Earth*, 108(B8). _eprint: https://onlinelibrary.wiley.com/doi/pdf/10.1029/2002JB002329.

Pattyn, F. (2010). Antarctic subglacial conditions inferred from a hybrid ice sheet/ice stream model. *Earth and Planetary Science Letters*, 295(3):451–461.

Pattyn, F. (2017). Sea-level response to melting of Antarctic ice shelves on multi-centennial timescales with the fast Elementary Thermomechanical Ice Sheet model (f.ETISh v1.0). *The Cryosphere*, 11(4):1851–1878. Publisher: Copernicus GmbH.

Pattyn, F. and Durand, G. (2013). Why marine ice sheet model predictions may diverge in estimating future sea level rise. *Geophysical Research Letters*, 40(16):4316–4320. _eprint: https://onlinelibrary.wiley.com/doi/pdf/10.1002/grl.50824.

Pattyn, F., Favier, L., Sun, S., and Durand, G. (2017). Progress in Numerical Modeling of Antarctic Ice-Sheet Dynamics. *Current Climate Change Reports*, 3(3):174–184.

Pattyn, F. and Morlighem, M. (2020). The uncertain future of the Antarctic Ice Sheet. *Science*, 367(6484):1331–1335. Publisher: American Association for the Advancement of Science.

Pattyn, F., Perichon, L., Durand, G., Favier, L., Gagliardini, O., Hindmarsh, R. C. A., Zwinger, T., Albrecht, T., Cornford, S., Docquier, D., Fürst, J. J., Goldberg, D., Gudmundsson, G. H., Humbert, A., Hütten, M., Huybrechts, P., Jouvet, G., Kleiner, T., Larour, E., Martin, D., Morlighem, M., Payne, A. J., Pollard, D., Rückamp, M., Rybak,

O., Seroussi, H., Thoma, M., and Wilkens, N. (2013). Grounding-line migration in plan-view marine ice-sheet models: results of the ice2sea MISMIP3d intercomparison. *Journal of Glaciology*, 59(215):410–422. Publisher: Cambridge University Press.

Pattyn, F., Ritz, C., Hanna, E., Asay-Davis, X., DeConto, R., Durand, G., Favier, L., Fettweis, X., Goelzer, H., Golledge, N. R., Kuipers Munneke, P., Lenaerts, J. T. M., Nowicki, S., Payne, A. J., Robinson, A., Seroussi, H., Trusel, L. D., and van den Broeke, M. (2018). The Greenland and Antarctic ice sheets under 1.5 °C global warming. *Nature Climate Change*, 8(12):1053–1061. Number: 12 Publisher: Nature Publishing Group.

Pattyn, F., Schoof, C., Perichon, L., Hindmarsh, R. C. A., Bueler, E., de Fleurian, B., Durand, G., Gagliardini, O., Gladstone, R., Goldberg, D., Gudmundsson, G. H., Huybrechts, P., Lee, V., Nick, F. M., Payne, A. J., Pollard, D., Rybak, O., Saito, F., and Vieli, A. (2012). Results of the Marine Ice Sheet Model Intercomparison Project, MISMIP. *The Cryosphere*, 6(3):573–588. Publisher: Copernicus GmbH.

Payne, A. J., Nowicki, S., Abe-Ouchi, A., Agosta, C., Alexander, P., Albrecht, T., Asay-Davis, X., Aschwanden, A., Barthel, A., Bracegirdle, T. J., Calov, R., Chambers, C., Choi, Y., Cullather, R., Cuzzone, J., Dumas, C., Edwards, T. L., Felikson, D., Fettweis, X., Galton-Fenzi, B. K., Goelzer, H., Gladstone, R., Golledge, N. R., Gregory, J. M., Greve, R., Hattermann, T., Hoffman, M. J., Humbert, A., Huybrechts, P., Jourdain, N. C., Kleiner, T., Munneke, P. K., Larour, E., Le clec'h, S., Lee, V., Leguy, G., Lipscomb, W. H., Little, C. M., Lowry, D. P., Morlighem, M., Nias, I., Pattyn, F., Pelle, T., Price, S. F., Quiquet, A., Reese, R., Rückamp, M., Schlegel, N.-J., Seroussi, H., Shepherd, A., Simon, E., Slater, D., Smith, R. S., Straneo, F., Sun, S., Tarasov, L., Trusel, L. D., Van Breedam, J., van de Wal, R., van den Broeke, M., Winkelmann, R., Zhao, C., Zhang, T., and Zwinger, T. (2021). Future Sea Level Change Under Coupled Model Intercomparison Project Phase 5 and Phase 6 Scenarios From the Greenland and Antarctic Ice Sheets. *Geophysical Research Letters*, 48(16):e2020GL091741. _eprint: https://onlinelibrary.wiley.com/doi/pdf/10.1029/2020GL091741.

Pegler, S. S. (2016). The dynamics of confined extensional flows. *Journal of Fluid Mechanics*, 804:24–57. Publisher: Cambridge University Press.

Pelletier, C., Fichefet, T., Goosse, H., Haubner, K., Helsen, S., Huot, P.-V., Kittel, C., Klein, F., Le clec'h, S., van Lipzig, N. P. M., Marchi, S., Massonnet, F., Mathiot, P., Moravveji, E., Moreno-Chamarro, E., Ortega, P., Pattyn, F., Souverijns, N., Van Achter, G., Vanden Broucke, S., Vanhulle, A., Verfaillie, D., and Zipf, L. (2022). PARASO, a circum-Antarctic fully coupled ice-sheet–ocean–sea-ice–atmosphere–land model involving f.ETISh1.7, NEMO3.6, LIM3.6, COSMO5.0 and CLM4.5. *Geoscientific Model Development*, 15(2):553–594. Publisher: Copernicus GmbH.

Pelt, W. J. J. V. and Oerlemans, J. (2012). Numerical simulations of cyclic behaviour in the Parallel Ice Sheet Model (PISM). *Journal of Glaciology*, 58(208):347–360. Publisher: Cambridge University Press.

Peltier, W. (2004). GLOBAL GLACIAL ISOSTASY AND THE SURFACE OF THE ICE-AGE EARTH: The ICE-5G (VM2) Model and GRACE. *Annual Review of Earth and Planetary Sciences*, 32(1):111–149.

Peltier, W. R. (1998). Postglacial variations in the level of the sea: Implications for climate dynamics and solid-Earth geophysics. *Reviews of Geophysics*, 36(4):603–689. _eprint: https://onlinelibrary.wiley.com/doi/pdf/10.1029/98RG02638.

Peltier, W. R., Argus, D. F., and Drummond, R. (2015). Space geodesy constrains ice age terminal deglaciation: The global ICE-6G_c (VM5a) model. *Journal of Geophysical Research: Solid Earth*, 120(1):450–487. _eprint: https://onlinelibrary.wiley.com/doi/pdf/10.1002/2014JB011176.

Petelet, M., Iooss, B., Asserin, O., and Loredo, A. (2010). Latin hypercube sampling with inequality constraints. *AStA Advances in Statistical Analysis*, 94(4):325–339.

Pico, T., Robel, A., Powell, E., Mix, A. C., and Mitrovica, J. X. (2019). Leveraging the Rapid Retreat of the Amundsen Gulf Ice Stream 13,000 Years Ago to Reveal Insight Into North American Deglaciation. *Geophysical Research Letters*, 46(21):12101–12107. _eprint: https://onlinelibrary.wiley.com/doi/pdf/10.1029/2019GL084789.

Pollard, D. and DeConto, R. M. (2012). Description of a hybrid ice sheet-shelf model, and application to Antarctica. *Geoscientific Model Development*, 5(5):1273–1295.

Pollard, D. and DeConto, R. M. (2020a). Continuous simulations over the last 40 million years with a coupled Antarctic ice sheet-sediment model. *Palaeogeography, Palaeoclimatology, Palaeoecology*, 537:109374.

Pollard, D. and DeConto, R. M. (2020b). Improvements in one-dimensional grounding-line parameterizations in an ice-sheet model with lateral variations (PSUICE3D v2.1). *Geoscientific Model Development*, 13(12):6481–6500. Publisher: Copernicus GmbH.

Pollard, D., DeConto, R. M., and Alley, R. B. (2015). Potential Antarctic Ice Sheet retreat driven by hydrofracturing and ice cliff failure. *Earth and Planetary Science Letters*, 412:112–121.

Pollard, D., DeConto, R. M., and Alley, R. B. (2018). A continuum model (PSUMEL1) of ice mélange and its role during retreat of the Antarctic Ice Sheet. *Geoscientific Model Development*, 11(12):5149–5172. Publisher: Copernicus GmbH.

Pollard, D., Gomez, N., and Deconto, R. M. (2017). Variations of the Antarctic Ice Sheet in a Coupled Ice Sheet-Earth-Sea Level Model: Sensitivity to Viscoelastic Earth Properties. *Journal of Geophysical Research: Earth Surface*, 122(11):2124–2138. _eprint: https://onlinelibrary.wiley.com/doi/pdf/10.1002/2017JF004371.

Pope, V. D., Gallani, M. L., Rowntree, P. R., and Stratton, R. A. (2000). The impact of new physical parametrizations in the Hadley Centre climate model: HadAM3. *Climate Dynamics*, 16(2):123–146.

Pound, M. J., Tindall, J., Pickering, S. J., Haywood, A. M., Dowsett, H. J., and Salzmann, U. (2014). Late Pliocene lakes and soils: a global data set for the analysis of climate feedbacks in a warmer world. *Climate of the Past*, 10(1):167–180. Publisher: Copernicus GmbH.

Powell, E. M., Pan, L., Hoggard, M. J., Latychev, K., Gomez, N., Austermann, J., and Mitrovica, J. X. (2021). The impact of 3-D Earth structure on far-field sea level following interglacial West Antarctic Ice Sheet collapse. *Quaternary Science Reviews*, 273:107256.

Prescott, C. L., Haywood, A. M., Dolan, A. M., Hunter, S. J., Pope, J. O., and Pickering, S. J. (2014). Assessing orbitally-forced interglacial climate variability during the mid-Pliocene Warm Period. *Earth and Planetary Science Letters*, 400:261–271.

Price, S. F., Bindschadler, R. A., Hulbe, C. L., and Joughin, I. R. (2001). Post-stagnation behavior in the upstream regions of Ice Stream C, West Antarctica. *Journal of Glaciology*, 47(157):283–294. Publisher: Cambridge University Press.

Quiquet, A. and Dumas, C. (2021). The GRISLI-LSCE contribution to the Ice Sheet Model Intercomparison Project for phase 6 of the Coupled Model Intercomparison Project (ISMIP6) – Part 2: Projections of the Antarctic ice sheet evolution by the end of the 21st century. *The Cryosphere*, 15(2):1031–1052. Publisher: Copernicus GmbH.

Quiquet, A., Dumas, C., Ritz, C., Peyaud, V., and Roche, D. M. (2018). The GRISLI ice sheet model (version 2.0): calibration and validation for multi-millennial changes of the Antarctic ice sheet. *Geoscientific Model Development*, 11(12):5003–5025. Publisher: Copernicus GmbH.

Rack, W. and Rott, H. (2004). Pattern of retreat and disintegration of the Larsen B ice shelf, Antarctic Peninsula. *Annals of Glaciology*, 39:505–510. Publisher: Cambridge University Press.

Raddatz, T. J., Reick, C. H., Knorr, W., Kattge, J., Roeckner, E., Schnur, R., Schnitzler, K.-G., Wetzel, P., and Jungclaus, J. (2007). Will the tropical land biosphere dominate the climate–carbon cycle feedback during the twenty-first century? *Climate Dynamics*, 29(6):565–574.

Raymo, M. E., Kozdon, R., Evans, D., Lisiecki, L., and Ford, H. L. (2018). The accuracy of mid-Pliocene 18O-based ice volume and sea level reconstructions. *Earth-Science Reviews*, 177:291–302.

Raymo, M. E., Mitrovica, J. X., O'Leary, M. J., DeConto, R. M., and Hearty, P. J. (2011). Departures from eustasy in Pliocene sea-level records. *Nature Geoscience*, 4(5):328–332.

Reeh, N. (1991). Parameterization of Melt Rate and Surface Temperature in the Greenland Ice Sheet. ISSN: 0032-2490 Issue: 3 Number: 3 Pages: 113-128 Place: Bremerhaven Publisher: Alfred Wegener Institute for Polar and Marine Research & German Society of Polar Research Volume: 59.

Reese, R., Albrecht, T., Mengel, M., Asay-Davis, X., and Winkelmann, R. (2018a). Antarctic sub-shelf melt rates via PICO. *The Cryosphere*, 12(6):1969–1985. Publisher: Copernicus GmbH.

Reese, R., Albrecht, T., Mengel, M., Asay-Davis, X., and Winkelmann, R. (2018b). Antarctic sub-shelf melt rates via PICO. *The Cryosphere*, 12(6):1969–1985. Publisher: Copernicus GmbH.

Reese, R., Winkelmann, R., and Gudmundsson, G. H. (2018c). Grounding-line flux formula applied as a flux condition in numerical simulations fails for buttressed Antarctic ice streams. *The Cryosphere*, 12(10):3229–3242. Publisher: Copernicus GmbH.

Regenberg, M., Nürnberg, D., Schönfeld, J., and Reichart, G.-J. (2007). Early diagenetic overprint in Caribbean sediment cores and its effect on the geochemical composition of planktonic foraminifera. *Biogeosciences*, 4(6):957–973. Publisher: Copernicus GmbH.

Regenberg, M., Regenberg, A., Garbe-Schönberg, D., and Lea, D. W. (2014). Global dissolution effects on planktonic foraminiferal Mg/Ca ratios controlled by the calcite-saturation state of bottom waters. *Paleoceanography*, 29(3):127–142. _eprint: https://onlinelibrary.wiley.com/doi/pdf/10.1002/2013PA002492.

Reynolds, J. M. (1981). The distribution of mean annual temperatures in the Antarctic Peninsula. *British Antarctic Survey Bulletin*, 54:123–133. Publisher: British Antarctic Survey.

Rignot, E., Jacobs, S., Mouginot, J., and Scheuchl, B. (2013). Ice-Shelf Melting Around Antarctica. *Science*, 341(6143):266–270. Publisher: American Association for the Advancement of Science.

Rignot, E., Mouginot, J., Scheuchl, B., Broeke, M. v. d., Wessem, M. J. v., and Morlighem, M. (2019). Four decades of Antarctic Ice Sheet mass balance from 1979–2017. *Proceedings of the National Academy of Sciences*, 116(4):1095–1103. Publisher: National Academy of Sciences Section: Physical Sciences.

Ritz, C., Edwards, T. L., Durand, G., Payne, A. J., Peyaud, V., and Hindmarsh, R. C. A. (2015). Potential sea-level rise from Antarctic ice-sheet instability constrained by observations. *Nature*, 528(7580):115–118. Number: 7580 Publisher: Nature Publishing Group.

Ritz, C., Fabre, A., and Letréguilly, A. (1996). Sensitivity of a Greenland ice sheet model to ice flow and ablation parameters: consequences for the evolution through the last climatic cycle. *Climate Dynamics*, 13(1):11–23.

Robel, A. A. and Banwell, A. F. (2019). A Speed Limit on Ice Shelf Collapse Through Hydrofracture. *Geophysical Research Letters*, 46(21):12092–12100. _eprint: https://onlinelibrary.wiley.com/doi/pdf/10.1029/2019GL084397.

Robel, A. A., Seroussi, H., and Roe, G. H. (2019). Marine ice sheet instability amplifies and skews uncertainty in projections of future sea-level rise. *Proceedings of the National Academy of Sciences*, 116(30):14887–14892. Publisher: National Academy of Sciences Section: Physical Sciences.

Robel, A. A. and Tziperman, E. (2016). The role of ice stream dynamics in deglaciation. *Journal of Geophysical Research: Earth Surface*, 121(8):1540–1554. _eprint: https://onlinelibrary.wiley.com/doi/pdf/10.1002/2016JF003937.

Roberts, W. H. G., Valdes, P. J., and Payne, A. J. (2014). Topography's crucial role in Heinrich Events. *Proceedings of the National Academy of Sciences*, 111(47):16688–16693. Publisher: Proceedings of the National Academy of Sciences.

Robinson, A., Goldberg, D., and Lipscomb, W. H. (2022). A comparison of the stability and performance of depth-integrated ice-dynamics solvers. *The Cryosphere*, 16(2):689–709. Publisher: Copernicus GmbH.

Roeckner, E., Bäuml, G., Bonaventura, L., Brokopf, R., Esch, M., Giorgetta, M., Hagemann, S., Kirchner, I., Kornblueh, L., Manzini, E., Rhodin, A., Schlese, U., Schulzweida, U., and Tompkins, A. (2003). The atmospheric general circulation model ECHAM 5. PART I: Model description. Publisher: Max-Planck-Institut für Meteorologie.

Roquet, F., Williams, G., Hindell, M. A., Harcourt, R., McMahon, C., Guinet, C., Charrassin, J.-B., Reverdin, G., Boehme, L., Lovell, P., and Fedak, M. (2014). A Southern Indian Ocean database of hydrographic profiles obtained with instrumented elephant seals. *Scientific Data*, 1(1):140028. Number: 1 Publisher: Nature Publishing Group.

Roquet, F., Wunsch, C., Forget, G., Heimbach, P., Guinet, C., Reverdin, G., Charrassin, J.-B., Bailleul, F., Costa, D. P., Huckstadt, L. A., Goetz, K. T., Kovacs, K. M., Lydersen, C., Biuw, M., Nøst, O. A., Bornemann, H., Ploetz, J., Bester, M. N., McIntyre, T., Muelbert, M. C., Hindell, M. A., McMahon, C. R., Williams, G., Harcourt, R., Field, I. C., Chafik, L., Nicholls, K. W., Boehme, L., and Fedak, M. A. (2013). Estimates of the Southern Ocean general circulation improved by animal-borne instruments. *Geophysical Research Letters*, 40(23):6176–6180. _eprint: https://onlinelibrary.wiley.com/doi/pdf/10.1002/2013GL058304.

Rosenbloom, N. A., Otto-Bliesner, B. L., Brady, E. C., and Lawrence, P. J. (2013). Simulating the mid-Pliocene Warm Period with the CCSM4 model. *Geoscientific Model Development*, 6(2):549–561. Publisher: Copernicus GmbH.

Rosenthal, Y., Lear, C. H., Oppo, D. W., and Linsley, B. K. (2006). Temperature and carbonate ion effects on Mg/Ca and Sr/Ca ratios in benthic foraminifera: Aragonitic species Hoeglundina elegans. *Paleoceanography*, 21(1). _eprint: https://onlinelibrary.wiley.com/doi/pdf/10.1029/2005PA001158.

Rosenthal, Y., Lohmann, G. P., Lohmann, K. C., and Sherrell, R. M. (2000). Incorporation and preservation of Mg in Globigerinoides sacculifer: implications for reconstructing the temperature and 18O/16O of seawater. *Paleoceanography*, 15(1):135–145. _eprint: https://onlinelibrary.wiley.com/doi/pdf/10.1029/1999PA000415.

Rovere, A., Hearty, P., Austermann, J., Mitrovica, J., Gale, J., Moucha, R., Forte, A., and Raymo, M. (2015). Mid-Pliocene shorelines of the US Atlantic Coastal Plain — An improved elevation database with comparison to Earth model predictions. *Earth-Science Reviews*, 145:117–131.

Rovere, A., Raymo, M. E., Mitrovica, J. X., Hearty, P. J., OLeary, M. J., and Inglis, J. D. (2014). The Mid-Pliocene sea-level conundrum: Glacial isostasy, eustasy and dynamic topography. *Earth and Planetary Science Letters*, 387:27–33.

Rowley, D. B., Forte, A. M., Moucha, R., Mitrovica, J. X., Simmons, N. A., and Grand, S. P. (2013). Dynamic Topography Change of the Eastern United States Since 3 Million Years Ago. *Science*, 340(6140):1560–1563. Publisher: American Association for the Advancement of Science.

Salzmann, U., Dolan, A. M., Haywood, A. M., Chan, W.-L., Voss, J., Hill, D. J., Abe-Ouchi, A., Otto-Bliesner, B., Bragg, F. J., Chandler, M. A., Contoux, C., Dowsett, H. J., Jost, A., Kamae, Y., Lohmann, G., Lunt, D. J., Pickering, S. J., Pound, M. J., Ramstein, G., Rosenbloom, N. A., Sohl, L., Stepanek, C., Ueda, H., and Zhang, Z. (2013). Challenges in quantifying Pliocene terrestrial warming revealed by data–model discord. *Nature Climate Change*, 3(11):969–974. Number: 11 Publisher: Nature Publishing Group.

Salzmann, U., Haywood, A. M., Lunt, D. J., Valdes, P. J., and Hill, D. J. (2008). A new global biome reconstruction and data-model comparison for the Middle Pliocene. *Global Ecology and Biogeography*, 17(3):432–447. _eprint: https://onlinelibrary.wiley.com/doi/pdf/10.1111/j.1466-8238.2008.00381.x.

Salzmann, U., Williams, M., Haywood, A. M., Johnson, A. L. A., Kender, S., and Zalasiewicz, J. (2011). Climate and environment of a Pliocene warm world. *Palaeogeography, Palaeoclimatology, Palaeoecology*, 309(1):1–8.

Samakinwa, E., Stepanek, C., and Lohmann, G. (2020). Sensitivity of mid-Pliocene climate to changes in orbital forcing and PlioMIP's boundary conditions. *Climate of the Past*, 16(4):1643–1665. Publisher: Copernicus GmbH.

Santner, T. J., Williams, B. J., and Notz, W. I. (2003). *The Design and Analysis of Computer Experiments*. Springer Series in Statistics. Springer, New York, NY.

Scambos, T., Fricker, H. A., Liu, C.-C., Bohlander, J., Fastook, J., Sargent, A., Massom, R., and Wu, A.-M. (2009). Ice shelf disintegration by plate bending and hydro-fracture: Satellite observations and model results of the 2008 Wilkins ice shelf break-ups. *Earth and Planetary Science Letters*, 280(1):51–60.

Scambos, T. A., Bohlander, J. A., Shuman, C. A., and Skvarca, P. (2004). Glacier acceleration and thinning after ice shelf collapse in the Larsen B embayment, Antarctica. *Geophysical Research Letters*, 31(18). _eprint: https://onlinelibrary.wiley.com/doi/pdf/10.1029/2004GL020670.

Scherer, R. P., DeConto, R. M., Pollard, D., and Alley, R. B. (2016). Windblown Pliocene diatoms and East Antarctic Ice Sheet retreat. *Nature Communications*, 7(1):12957. Number: 1 Publisher: Nature Publishing Group.

Schlegel, N.-J., Seroussi, H., Schodlok, M. P., Larour, E. Y., Boening, C., Limonadi, D., Watkins, M. M., Morlighem, M., and van den Broeke, M. R. (2018). Exploration of Antarctic Ice Sheet 100-year contribution to sea level rise and associated model uncertainties using the ISSM framework. *The Cryosphere*, 12(11):3511–3534. Publisher: Copernicus GmbH.

Schlemm, T., Feldmann, J., Winkelmann, R., and Levermann, A. (2022). Stabilizing effect of mélange buttressing on the marine ice-cliff instability of the West Antarctic Ice Sheet. *The Cryosphere*, 16(5):1979–1996. Publisher: Copernicus GmbH.

Schlemm, T. and Levermann, A. (2019). A simple stress-based cliff-calving law. *The Cryosphere*, 13(9):2475–2488. Publisher: Copernicus GmbH.

Schlemm, T. and Levermann, A. (2021). A simple parametrization of mélange buttressing for calving glaciers. *The Cryosphere*, 15(2):531–545. Publisher: Copernicus GmbH.

Schmidt, C. W. (2015). Delta Subsidence: An Imminent Threat to Coastal Populations. *Environmental Health Perspectives*, 123(8):A204–A209. Publisher: Environmental Health Perspectives.

Schoof, C. (2007a). Ice sheet grounding line dynamics: Steady states, stability, and hysteresis. *Journal of Geophysical Research*, 112(F3):F03S28.

Schoof, C. (2007b). Marine ice-sheet dynamics. Part 1. The case of rapid sliding. *Journal of Fluid Mechanics*, 573:27–55. Publisher: Cambridge University Press.

Schoof, C. (2010). Ice-sheet acceleration driven by melt supply variability. *Nature*, 468(7325):803–806. Number: 7325 Publisher: Nature Publishing Group.

Schoof, C. (2012). Marine ice sheet stability. *Journal of Fluid Mechanics*, 698:62–72.

Schoof, C. and Hindmarsh, R. C. A. (2010). Thin-Film Flows with Wall Slip: An Asymptotic Analysis of Higher Order Glacier Flow Models. *The Quarterly Journal of Mechanics and Applied Mathematics*, 63(1):73–114.

Schoof, C., Rada, C. A., Wilson, N. J., Flowers, G. E., and Haseloff, M. (2014). Oscillatory subglacial drainage in the absence of surface melt. *The Cryosphere*, 8(3):959–976. Publisher: Copernicus GmbH.

Seguinot, J. (2013). Spatial and seasonal effects of temperature variability in a positive degree-day glacier surface mass-balance model. *Journal of Glaciology*, 59(218):1202–1204. Publisher: Cambridge University Press.

Seguinot, J., Rogozhina, I., Stroeven, A. P., Margold, M., and Kleman, J. (2016). Numerical simulations of the Cordilleran ice sheet through the last glacial cycle. *The Cryosphere*, 10(2):639–664. Publisher: Copernicus GmbH.

Semtner, A. J. (1976). A Model for the Thermodynamic Growth of Sea Ice in Numerical Investigations of Climate. *Journal of Physical Oceanography*, 6(3):379–389. Publisher: American Meteorological Society Section: Journal of Physical Oceanography.

Sergienko, O. and Macayeal, D. R. (2005). Surface melting on Larsen Ice Shelf, Antarctica. *Annals of Glaciology*, 40:215–218. Publisher: Cambridge University Press.

Sergienko, O. V. (2022). No general stability conditions for marine ice-sheet grounding lines in the presence of feedbacks. *Nature Communications*, 13(1):2265. Number: 1 Publisher: Nature Publishing Group.

Sergienko, O. V. and Wingham, D. J. (2019). Grounding line stability in a regime of low driving and basal stresses. *Journal of Glaciology*, 65(253):833–849. Publisher: Cambridge University Press.

Seroussi, H. and Morlighem, M. (2018). Representation of basal melting at the grounding line in ice flow models. *The Cryosphere*, 12(10):3085–3096. Publisher: Copernicus GmbH.

Seroussi, H., Nowicki, S., Payne, A. J., Goelzer, H., Lipscomb, W. H., Abe-Ouchi, A., Agosta, C., Albrecht, T., Asay-Davis, X., Barthel, A., Calov, R., Cullather, R., Dumas, C., Galton-Fenzi, B. K., Gladstone, R., Golledge, N. R., Gregory, J. M., Greve, R., Hattermann, T., Hoffman, M. J., Humbert, A., Huybrechts, P., Jourdain, N. C., Kleiner, T., Larour, E., Leguy, G. R., Lowry, D. P., Little, C. M., Morlighem, M., Pattyn, F., Pelle, T., Price, S. F., Quiquet, A., Reese, R., Schlegel, N.-J., Shepherd, A., Simon, E., Smith, R. S., Straneo, F., Sun, S., Trusel, L. D., Van Breedam, J., van de Wal, R. S. W., Winkelmann, R., Zhao, C., Zhang, T., and Zwinger, T. (2020). ISMIP6 Antarctica: a multi-model ensemble of the Antarctic ice sheet evolution over the 21st century. *The Cryosphere*, 14(9):3033–3070. Publisher: Copernicus GmbH.

Seroussi, H., Nowicki, S., Simon, E., Abe-Ouchi, A., Albrecht, T., Brondex, J., Cornford, S., Dumas, C., Gillet-Chaulet, F., Goelzer, H., Golledge, N. R., Gregory, J. M., Greve, R., Hoffman, M. J., Humbert, A., Huybrechts, P., Kleiner, T., Larour, E., Leguy, G., Lipscomb, W. H., Lowry, D., Mengel, M., Morlighem, M., Pattyn, F., Payne, A. J., Pollard, D., Price, S. F., Quiquet, A., Reerink, T. J., Reese, R., Rodehacke, C. B.,

Schlegel, N.-J., Shepherd, A., Sun, S., Sutter, J., Van Breedam, J., van de Wal, R. S. W., Winkelmann, R., and Zhang, T. (2019). initMIP-Antarctica: an ice sheet model initialization experiment of ISMIP6. *The Cryosphere*, 13(5):1441–1471. Publisher: Copernicus GmbH.

Sexton, P. F., Wilson, P. A., and Pearson, P. N. (2006). Microstructural and geochemical perspectives on planktic foraminiferal preservation: "Glassy" versus "Frosty". *Geochemistry, Geophysics, Geosystems*, 7(12). _eprint: https://onlinelibrary.wiley.com/doi/pdf/10.1029/2006GC001291.

Shackleton, N. (1967). Oxygen Isotope Analyses and Pleistocene Temperatures Re-assessed. *Nature*, 215(5096):15–17. Number: 5096 Publisher: Nature Publishing Group.

Shakun, J. D., Corbett, L. B., Bierman, P. R., Underwood, K., Rizzo, D. M., Zimmerman, S. R., Caffee, M. W., Naish, T., Golledge, N. R., and Hay, C. C. (2018). Minimal East Antarctic Ice Sheet retreat onto land during the past eight million years. *Nature*, 558(7709):284–287. Number: 7709 Publisher: Nature Publishing Group.

Shepherd, A., Ivins, E., Rignot, E., Smith, B., van den Broeke, M., Velicogna, I., Whitehouse, P., Briggs, K., Joughin, I., Krinner, G., Nowicki, S., Payne, T., Scambos, T., Schlegel, N., A, G., Agosta, C., Ahlstrøm, A., Babonis, G., Barletta, V., Blazquez, A., Bonin, J., Csatho, B., Cullather, R., Felikson, D., Fettweis, X., Forsberg, R., Gallee, H., Gardner, A., Gilbert, L., Groh, A., Gunter, B., Hanna, E., Harig, C., Helm, V., Horvath, A., Horwath, M., Khan, S., Kjeldsen, K. K., Konrad, H., Langen, P., Lecavalier, B., Loomis, B., Luthcke, S., McMillan, M., Melini, D., Mernild, S., Mohajerani, Y., Moore, P., Mouginot, J., Moyano, G., Muir, A., Nagler, T., Nield, G., Nilsson, J., Noel, B., Otosaka, I., Pattle, M. E., Peltier, W. R., Pie, N., Rietbroek, R., Rott, H., Sandberg-Sørensen, L., Sasgen, I., Save, H., Scheuchl, B., Schrama, E., Schröder, L., Seo, K.-W., Simonsen, S., Slater, T., Spada, G., Sutterley, T., Talpe, M., Tarasov, L., van de Berg, W. J., van der Wal, W., van Wessem, M., Vishwakarma, B. D., Wiese, D., Wouters, B., and The IMBIE team (2018). Mass balance of the Antarctic Ice Sheet from 1992 to 2017. *Nature*, 558(7709):219–222. Number: 7709 Publisher: Nature Publishing Group.

Shepherd, A., Wingham, D., Wallis, D., Giles, K., Laxon, S., and Sundal, A. V. (2010). Recent loss of floating ice and the consequent sea level contribution. *Geophysical Research Letters*, 37(13). _eprint: https://onlinelibrary.wiley.com/doi/pdf/10.1029/2010GL042496.

Slater, T., Lawrence, I. R., Otosaka, I. N., Shepherd, A., Gourmelen, N., Jakob, L., Tepes, P., Gilbert, L., and Nienow, P. (2021). Review article: Earth's ice imbalance. *The Cryosphere*, 15(1):233–246. Publisher: Copernicus GmbH.

Smith, G. I. (1984). Paleohydrologic Regimes in the Southwestern Great Basin, 0–3.2 my ago, Compared with Other Long Records of "Gobal" Climate. *Quaternary Research*, 22(1):1–17. Publisher: Cambridge University Press.

Smith, R., Jones, P., Briegleb, B., Bryan, F., and Danabasoglu, G. (2010). The Parallel Ocean Program (POP) reference manual: Ocean component of the Community Climate System Model (CCSM). Technical report.

Smith, R. S., Mathiot, P., Siahaan, A., Lee, V., Cornford, S. L., Gregory, J. M., Payne, A. J., Jenkins, A., Holland, P. R., Ridley, J. K., and Jones, C. G. (2021). Coupling the U.K.

Earth System Model to Dynamic Models of the Greenland and Antarctic Ice Sheets. *Journal of Advances in Modeling Earth Systems*, 13(10):e2021MS002520. _eprint: https://onlinelibrary.wiley.com/doi/pdf/10.1029/2021MS002520.

Sommers, A. N., Otto-Bliesner, B. L., Lipscomb, W. H., Lofverstrom, M., Shafer, S. L., Bartlein, P. J., Brady, E. C., Kluzek, E., Leguy, G., Thayer-Calder, K., and Tomas, R. A. (2021). Retreat and Regrowth of the Greenland Ice Sheet During the Last Interglacial as Simulated by the CESM2-CISM2 Coupled Climate–Ice Sheet Model. *Paleoceanography and Paleoclimatology*, 36(12):e2021PA004272. _eprint: https://onlinelibrary.wiley.com/doi/pdf/10.1029/2021PA004272.

Stap, L. B., van de Wal, R. S. W., de Boer, B., Bintanja, R., and Lourens, L. J. (2014). Interaction of ice sheets and climate during the past 800 000 years. *Climate of the Past*, 10(6):2135–2152. Publisher: Copernicus GmbH.

Steffen, H. and Wu, P. (2011). Glacial isostatic adjustment in Fennoscandia—A review of data and modeling. *Journal of Geodynamics*, 52(3):169–204.

Stepanek, C. and Lohmann, G. (2012). Modelling mid-Pliocene climate with COSMOS. *Geoscientific Model Development*, 5(5):1221–1243. Publisher: Copernicus GmbH.

Stepanek, C., Samakinwa, E., Knorr, G., and Lohmann, G. (2020). Contribution of the coupled atmosphere–ocean–sea ice–vegetation model COSMOS to the PlioMIP2. *Climate of the Past*, 16(6):2275–2323. Publisher: Copernicus GmbH.

Stevens, C., Robinson, N., O'Connor, G., and Grant, B. (2020). Dynamics of Large Pelagic Ice Crystals in an Antarctic Ice Shelf Water Plume Flowing Beneath Land-Fast Sea Ice. *The Cryosphere Discussions*, pages 1–30. Publisher: Copernicus GmbH.

Stokes, C. R. and Clark, C. D. (1999). Geomorphological criteria for identifying Pleistocene ice streams. *Annals of Glaciology*, 28:67–74. Publisher: Cambridge University Press.

Stone, E. J., Lunt, D. J., Rutt, I. C., and Hanna, E. (2010). Investigating the sensitivity of numerical model simulations of the modern state of the Greenland ice-sheet and its future response to climate change. *The Cryosphere*, 4(3):397–417. Publisher: Copernicus GmbH.

Stroeven, A. P., Prentice, M. L., and Kleman, J. (1996). On marine microfossil transport and pathways in Antarctica during the late Neogene: Evidence from the Sirius Group at Mount Fleming. *Geology*, 24(8):727–730.

Studinger, M., Bell, R. E., Blankenship, D. D., Finn, C. A., Arko, R. A., Morse, D. L., and Joughin, I. (2001). Subglacial sediments: A regional geological template for ice flow in West Antarctica. *Geophysical Research Letters*, 28(18):3493–3496. _eprint: https://onlinelibrary.wiley.com/doi/pdf/10.1029/2000GL011788.

Sugden, D. E., Marchant, D. R., and Denton, G. H. (1993). The Case for a Stable East Antarctic Ice Sheet: The Background. *Geografiska Annaler: Series A, Physical Geography*, 75(4):151–154. Publisher: Taylor & Francis _eprint: https://doi.org/10.1080/04353676.1993.11880392.

Sutter, J., Eisen, O., Werner, M., Grosfeld, K., Kleiner, T., and Fischer, H. (2020). Limited Retreat of the Wilkes Basin Ice Sheet During the Last Interglacial. *Geophysical Research Letters*, 47(13):e2020GL088131. _eprint: https://onlinelibrary.wiley.com/doi/pdf/10.1029/2020GL088131.

Sutter, J., Fischer, H., Grosfeld, K., Karlsson, N. B., Kleiner, T., Van Liefferinge, B., and Eisen, O. (2019). Modelling the Antarctic Ice Sheet across the mid-Pleistocene transition – implications for Oldest Ice. *The Cryosphere*, 13(7):2023–2041. Publisher: Copernicus GmbH.

Takata, K., Emori, S., and Watanabe, T. (2003). Development of the minimal advanced treatments of surface interaction and runoff. *Global and Planetary Change*, 38(1):209–222.

The IMBIE Team (2021). Antarctic and Greenland Ice Sheet mass balance 1992-2020 for IPCC AR6. Artwork Size: 12 files, 155.5 kB Medium: text/plain,text/csv Pages: 12 files, 155.5 kB Version Number: 1.0 Type: dataset.

Thomas, E. R., van Wessem, J. M., Roberts, J., Isaksson, E., Schlosser, E., Fudge, T. J., Vallelonga, P., Medley, B., Lenaerts, J., Bertler, N., van den Broeke, M. R., Dixon, D. A., Frezzotti, M., Stenni, B., Curran, M., and Ekaykin, A. A. (2017). Regional Antarctic snow accumulation over the past 1000 years. *Climate of the Past*, 13(11):1491–1513. Publisher: Copernicus GmbH.

Thomas, R. H. (1979). The Dynamics of Marine Ice Sheets. *Journal of Glaciology*, 24(90):167–177. Publisher: Cambridge University Press.

Thompson, R. S. (1991). Pliocene environments and climates in the western United States. *Quaternary Science Reviews*, 10(2):115–132.

Thompson, R. S. and Fleming, R. F. (1996). Middle Pliocene vegetation: reconstructions, paleoclimatic inferences, and boundary conditions for climate modeling. *Marine Micropaleontology*, 27(1):27–49.

Tierney, J. E., Haywood, A. M., Feng, R., Bhattacharya, T., and Otto-Bliesner, B. L. (2019). Pliocene Warmth Consistent With Greenhouse Gas Forcing. *Geophysical Research Letters*, 46(15):9136–9144. _eprint: https://onlinelibrary.wiley.com/doi/pdf/10.1029/2019GL083802.

Treasure, A., Roquet, F., Ansorge, I. J., Bester, M. N., Boehme, l., Bornemann, H., and et al. (2017). Marine Mammals Exploring the Oceans Pole to Pole: A Review of the MEOP Consortium. *Oceanography*, issue_volume.

Trusel, L. D., Frey, K. E., Das, S. B., Karnauskas, K. B., Kuipers Munneke, P., van Meijgaard, E., and van den Broeke, M. R. (2015). Divergent trajectories of Antarctic surface melt under two twenty-first-century climate scenarios. *Nature Geoscience*, 8(12):927–932. Number: 12 Publisher: Nature Publishing Group.

Tsai, V. C., Stewart, A. L., and Thompson, A. F. (2015). Marine ice-sheet profiles and stability under Coulomb basal conditions. *Journal of Glaciology*, 61(226):205–215. Publisher: Cambridge University Press.

Turner, J., Lu, H., White, I., King, J. C., Phillips, T., Hosking, J. S., Bracegirdle, T. J., Marshall, G. J., Mulvaney, R., and Deb, P. (2016). Absence of 21st century warming on Antarctic Peninsula consistent with natural variability. *Nature*, 535(7612):411–415. Number: 7612 Publisher: Nature Publishing Group.

Ultee, L., Meyer, C., and Minchew, B. (2020). Tensile strength of glacial ice deduced from observations of the 2015 eastern Skaftá cauldron collapse, Vatnajökull ice cap, Iceland. *Journal of Glaciology*, 66(260):1024–1033. Publisher: Cambridge University Press.

Utescher, T., Mosbrugger, V., and Ashraf, A. (2000). Terrestrial Climate Evolution in Northwest Germany Over the Last 25 Million Years. *PALAIOS*, 15(5):430–449.

Valdes, P. J., Armstrong, E., Badger, M. P. S., Bradshaw, C. D., Bragg, F., Crucifix, M., Davies-Barnard, T., Day, J. J., Farnsworth, A., Gordon, C., Hopcroft, P. O., Kennedy, A. T., Lord, N. S., Lunt, D. J., Marzocchi, A., Parry, L. M., Pope, V., Roberts, W. H. G., Stone, E. J., Tourte, G. J. L., and Williams, J. H. T. (2017). The BRIDGE HadCM3 family of climate models: HadCM3@Bristol v1.0. *Geoscientific Model Development*, 10(10):3715–3743. Publisher: Copernicus GmbH.

van de Berg, W. J., van den Broeke, M. R., Reijmer, C. H., and van Meijgaard, E. (2006). Reassessment of the Antarctic surface mass balance using calibrated output of a regional atmospheric climate model. *Journal of Geophysical Research: Atmospheres*, 111(D11). _eprint: https://onlinelibrary.wiley.com/doi/pdf/10.1029/2005JD006495.

van de Wal, R. S. W., Boot, W., van den Broeke, M. R., Smeets, C. J. P. P., Reijmer, C. H., Donker, J. J. A., and Oerlemans, J. (2008). Large and Rapid Melt-Induced Velocity Changes in the Ablation Zone of the Greenland Ice Sheet. *Science*, 321(5885):111–113. Publisher: American Association for the Advancement of Science.

van der Veen, C. J. (1999). Evaluating the performance of cryospheric models. *Polar Geography*, 23(2):83–96. Publisher: Taylor & Francis _eprint: https://doi.org/10.1080/10889379909377667.

van der Veen, C. J. (2002). Calving glaciers. *Progress in Physical Geography: Earth and Environment*, 26(1):96–122. Publisher: SAGE Publications Ltd.

van der Wal, W., Whitehouse, P. L., and Schrama, E. J. O. (2015). Effect of GIA models with 3D composite mantle viscosity on GRACE mass balance estimates for Antarctica. *Earth and Planetary Science Letters*, 414:134–143.

Vaughan, D. G. (1993). Relating the occurrence of crevasses to surface strain rates. *Journal of Glaciology*, 39(132):255–266. Publisher: Cambridge University Press.

Veen, J. V. D. (1996). Tidewater calving. *Journal of Glaciology*, 42(141):375–385. Publisher: Cambridge University Press.

Vizcaino, M., Mikolajewicz, U., Ziemen, F., Rodehacke, C. B., Greve, R., and Broeke, M. R. (2015). Coupled simulations of Greenland Ice Sheet and climate change up to A.D. 2300. *Geophysical Research Letters*, 42(10):3927–3935.

Wake, L. M. and Marshall, S. J. (2015). Assessment of current methods of positive degree-day calculation using in situ observations from glaciated regions. *Journal of Glaciology*, 61(226):329–344. Publisher: Cambridge University Press.

Walter, F., O'Neel, S., McNamara, D., Pfeffer, W. T., Bassis, J. N., and Fricker, H. A. (2010). Iceberg calving during transition from grounded to floating ice: Columbia Glacier, Alaska. *Geophysical Research Letters*, 37(15). _eprint: https://onlinelibrary.wiley.com/doi/pdf/10.1029/2010GL043201.

Wan, J. X. W., Gomez, N., Latychev, K., and Han, H. K. (2022). Resolving glacial isostatic adjustment (GIA) in response to modern and future ice loss at marine grounding lines in West Antarctica. *The Cryosphere*, 16(6):2203–2223. Publisher: Copernicus GmbH.

Wara, M. W., Ravelo, A. C., and Delaney, M. L. (2005). Permanent El Niño-Like Conditions During the Pliocene Warm Period. *Science*, 309(5735):758–761. Publisher: American Association for the Advancement of Science.

Wardlaw, B. R. and Quinn, T. (1991). The record of Pliocene sea-level change at Enewetak Atoll. *Quaternary Science Reviews*, 10(2-3):12. Code: Quaternary Science Reviews Type: Journal Article.

Webb, P.-N. and Harwood, D. M. (1991). Late Cenozoic glacial history of the Ross embayment, Antarctica. *Quaternary Science Reviews*, 10(2):215–223.

Weertman, J. (1957). On the Sliding of Glaciers. *Journal of Glaciology*, 3(21):33–38. Publisher: Cambridge University Press.

Weertman, J. (1974). Stability of the Junction of an Ice Sheet and an Ice Shelf. *Journal of Glaciology*, 13(67):3–11. Publisher: Cambridge University Press.

Wernecke, A. (2020). *Quantifying Century-Scale Uncertainties Of The Global Mean Sea Level Rise Contribution From The Amundsen Sea Sector, West Antarctica*. phd, The Open University.

Wernecke, A., Edwards, T. L., Holden, P. B., Edwards, N. R., and Cornford, S. L. (2022). Quantifying the Impact of Bedrock Topography Uncertainty in Pine Island Glacier Projections for This Century. *Geophysical Research Letters*, 49(6):e2021GL096589. _eprint: https://onlinelibrary.wiley.com/doi/pdf/10.1029/2021GL096589.

Wernecke, A., Edwards, T. L., Nias, I. J., Holden, P. B., and Edwards, N. R. (2020). Spatial probabilistic calibration of a high-resolution Amundsen Sea Embayment ice sheet model with satellite altimeter data. *The Cryosphere*, 14(5):1459–1474. Publisher: Copernicus GmbH.

Wessem, J. M. V., Reijmer, C. H., Morlighem, M., Mouginot, J., Rignot, E., Medley, B., Joughin, I., Wouters, B., Depoorter, M. A., Bamber, J. L., Lenaerts, J. T. M., Berg, W. J. V. D., Broeke, M. R. V. D., and Meijgaard, E. V. (2014). Improved representation of East Antarctic surface mass balance in a regional atmospheric climate model. *Journal of Glaciology*, 60(222):761–770. Publisher: Cambridge University Press.

Whitehouse, P. L. (2018). Glacial isostatic adjustment modelling: historical perspectives, recent advances, and future directions. *Earth Surface Dynamics*, 6(2):401–429. Publisher: Copernicus GmbH.

Whitehouse, P. L., Bentley, M. J., Milne, G. A., King, M. A., and Thomas, I. D. (2012). A new glacial isostatic adjustment model for Antarctica: calibrated and tested using observations of relative sea-level change and present-day uplift rates. *Geophysical Journal International*, 190(3):1464–1482.

Whitehouse, P. L., Gomez, N., King, M. A., and Wiens, D. A. (2019). Solid Earth change and the evolution of the Antarctic Ice Sheet. *Nature Communications*, 10(1):503. Number: 1 Publisher: Nature Publishing Group.

Willeit, M., Ganopolski, A., Calov, R., and Brovkin, V. Mid-Pleistocene transition in glacial cycles explained by declining CO2 and regolith removal. *Science Advances*, 5(4):eaav7337. Publisher: American Association for the Advancement of Science.

Wilson, D. J., Bertram, R. A., Needham, E. F., van de Flierdt, T., Welsh, K. J., McKay, R. M., Mazumder, A., Riesselman, C. R., Jimenez-Espejo, F. J., and Escutia, C. (2018). Ice loss from the East Antarctic Ice Sheet during late Pleistocene interglacials. *Nature*, 561(7723):383–386. Number: 7723 Publisher: Nature Publishing Group.

Wilson, G. S. (1995). The neogene east antarctic ice sheet: A dynamic or stable feature? *Quaternary Science Reviews*, 14(2):101–123.

Wilson, G. S., Barron, J. A., Ashworth, A. C., Askin, R. A., Carter, J. A., Curren, M. G., Dalhuisen, D. H., Friedmann, E. I., Fyodorov-Davidov, D. G., Gilichinsky, D. A., Harper, M. A., Harwood, D. M., Hiemstra, J. F., Janecek, T. R., Licht, K. J., Ostroumov, V. E., Powell, R. D., Rivkina, E. M., Rose, S. A., Stroeven, A. P., Stroeven, P., van der Meer, J. J. M., and Wizevich, M. C. (2002). The Mount Feather Diamicton of the Sirius Group: an accumulation of indicators of Neogene Antarctic glacial and climatic history. *Palaeogeography, Palaeoclimatology, Palaeoecology*, 182(1):117–131.

Winkelmann, R., Martin, M. A., Haseloff, M., Albrecht, T., Bueler, E., Khroulev, C., and Levermann, A. (2011). The Potsdam Parallel Ice Sheet Model (PISM-PIK) – Part 1: Model description. *The Cryosphere*, 5(3):715–726. Publisher: Copernicus GmbH.

Winnick, M. J. and Caves, J. K. (2015). Oxygen isotope mass-balance constraints on Pliocene sea level and East Antarctic Ice Sheet stability. *Geology*, 43(10):879–882.

Winsborrow, M. C. M., Clark, C. D., and Stokes, C. R. (2010). What controls the location of ice streams? *Earth-Science Reviews*, 103(1):45–59.

Wise, M. G., Dowdeswell, J. A., Jakobsson, M., and Larter, R. D. (2017). Evidence of marine ice-cliff instability in Pine Island Bay from iceberg-keel plough marks. *Nature*, 550(7677):506–510. Number: 7677 Publisher: Nature Publishing Group.

Woodward, R. S. (1886). On the Form and Position of the Sea-level as Dependent on Superficial Masses Symmetrically Disposed with Respect to a Radius of the Earth's Surface. *Annals of Mathematics*, 2(5):97–103. Publisher: Annals of Mathematics.

Wu, P. and van der Wal, W. (2003). Postglacial sealevels on a spherical, self-gravitating viscoelastic earth: effects of lateral viscosity variations in the upper mantle on the inference of viscosity contrasts in the lower mantle. *Earth and Planetary Science Letters*, 211(1):57–68.

Wu, P., Wang, H., and Steffen, H. (2013). The role of thermal effect on mantle seismic anomalies under Laurentia and Fennoscandia from observations of Glacial Isostatic Adjustment. *Geophysical Journal International*, 192(1):7–17.

Wuite, J., Rott, H., Hetzenecker, M., Floricioiu, D., De Rydt, J., Gudmundsson, G. H., Nagler, T., and Kern, M. (2015). Evolution of surface velocities and ice discharge of Larsen B outlet glaciers from 1995 to 2013. *The Cryosphere*, 9(3):957–969. Publisher: Copernicus GmbH.

Yamane, M., Yokoyama, Y., Abe-Ouchi, A., Obrochta, S., Saito, F., Moriwaki, K., and Matsuzaki, H. (2015). Exposure age and ice-sheet model constraints on Pliocene East Antarctic ice sheet dynamics. *Nature Communications*, 6:7016.

Yan, Q., Zhang, Z., and Wang, H. (2016). Investigating uncertainty in the simulation of the Antarctic ice sheet during the mid-Piacenzian. *Journal of Geophysical Research: Atmospheres*, 121(4):1559–1574. _eprint: https://onlinelibrary.wiley.com/doi/pdf/10.1002/2015JD023900.

Yan, Q., Zhang, Z., Wang, H., and Zhang, R. (2014). Simulation of Greenland ice sheet during the mid-Pliocene warm period. *Chinese Science Bulletin*, 59(2):201–211.

Young, D. A., Wright, A. P., Roberts, J. L., Warner, R. C., Young, N. W., Greenbaum, J. S., Schroeder, D. M., Holt, J. W., Sugden, D. E., Blankenship, D. D., van Ommen, T. D., and Siegert, M. J. (2011). A dynamic early East Antarctic Ice Sheet suggested by ice-covered fjord landscapes. *Nature*, 474(7349):72–75. Number: 7349 Publisher: Nature Publishing Group.

Yousefi, M., Wan, J., Pan, L., Gomez, N., Latychev, K., Mitrovica, J. X., Pollard, D., and DeConto, R. M. (2022). The Influence of the Solid Earth on the Contribution of Marine Sections of the Antarctic Ice Sheet to Future Sea-Level Change. *Geophysical Research Letters*, 49(15):e2021GL097525. _eprint: https://onlinelibrary.wiley.com/doi/pdf/10.1029/2021GL097525.

Ziemen, F. A., Kapsch, M.-L., Klockmann, M., and Mikolajewicz, U. (2019). Heinrich events show two-stage climate response in transient glacial simulations. *Climate of the Past*, 15(1):153–168. Publisher: Copernicus GmbH.

Zweng, M., Locarnini, R., Mishonov, A., Baranova, O., Boyer, T., Garcia, H., Reagan, J., Seidov, D., Weathers, K., Paver, C., and Smolyar, I. (2019). World Ocean Atlas 2018, Volume 1: Salinity, Tech. Rep. Atlas NESDIS 81, NOAA. Technical report.